HYDRODYNAMIC, ACOUSTIC, AND ELECTRICAL CHARACTERISTICS OF UNDERWATER SPARK DISCHARGES INITIATED BY DIFFERENT MECHANISMS

Ph.D Thesis

Ying Sun, BSc, MSc

Jun. 2018

Department of Electronic and Electrical Engineering
University of Strathclyde
Glasgow, UK

Declaration

This thesis is the result of the author's original research. It has been composed by the author and has not been previously submitted for examination which has led to the award of a degree.

Signed: Ying Sun

Date: 20/08/2018

Acknowledgments

I would like present my acknowledgments to some people for their helps during my entire Ph.D experience. The sincerest acknowledge is for my supervisor Dr Igor Timoshkin. I gratefully appreciate the top-level supervision and professional suggestions not only on all aspects of the work but also on my daily academic life. His great patience and responsibility to me and my work have helped me come through the Ph.D experience happily and joyfully. Communication with Dr Igor Timoshkin has shown me how to share information and how to solve academic issues. Without him, nothing could have been accomplished.

Significant acknowledgments have to be given to Dr Martin Given and Dr Mark Wilson, who have provided the best efforts and advices on examining this project progress and on our published papers. I would also like to thank Prof. Scott Macgregor and the entire High Voltage Technology group and Mrs Maureen Cooper for her best assistive support during my Ph.D. Great thanks have to be given to Dr Michelle Maclean and Dr Rachael Tomb for their efforts in organising ROLEST meetings to provide excellent opportunities for exchanging ideas and practicing oral presentations.

Big thanks are also given to the HVT mechanical workshop for their professional manufacture of all equipment used in this work and for their help in addressing design issues of the experimental setup in this work.

Thanks have to go to Zhongshu Zhang as my closest colleague and friend. Together we have achieved so many interesting academic discussion and wonderful casual lives which are unforgettable experience for me.

Special thanks and appreciation are for my family members, my father and mother and my lovely fiancé. They have supported me since the beginning of this project. Their love has granted me the greatest power and motivation in accomplishing my Ph.D. Love you forever!

Publication

Published and accepted for publication journal papers

Y. Sun, I. V. Timoshkin, M. J. Given, M. P. Wilson, T. Wang, S. J. MacGregor and N. Bonifaci, "Electrical and acoustic parameters of wire-Guided discharges in water: experimental determination and phenomenological scaling," *IEEE T. Plasma Sci.*, vol. 45, no. 10, pp. 2648-2655, Jun. 2017.

Y. Sun, I. V. Timoshkin, M. J. Given, M. P. Wilson, T. Wang, S. J. MacGregor and N. Bonifaci, "Impulsive discharges in water: acoustic and hydrodynamic parameters," *IEEE T. Plasma Sci.*, vol. 44, no. 10, pp. 2156-2166, Jul. 2016.

Y. Sun, I. V. Timoshkin, M. J. Given, M. P. Wilson, T. Wang, S. J. MacGregor and N. Bonifaci, "Acoustic impulses generated by air-bubble stimulated underwater spark discharges", *IEEE T. Dielect. El. In.*, accepted for publication, 2018.

Conference papers

Y. Sun, I. V. Timoshkin, M. J. Given, M. P. Wilson, T. Wang, S. J. MacGregor and N. Bonifaci, "Hydrodynamic parameters of air-bubble stimulated underwater spark discharges," in *IEEE 19th ICDL*, Manchester, UK, Jun. 25 – 29, 2017, pp. 1-4.

I. V. Timoshkin, Y. Sun, M. J. Given, M. P. Wilson, T. Wang, S. J. MacGregor and N. Bonifaci, "Impulsive breakdown in water: optimisation of energy delivery for high acoustic output," in *IEEE 19th ICDL*, Manchester, UK, Jun. 25 – 29, 2017, pp. 1-4.

Y. Sun, I. V. Timoshkin and S. J. MacGregor, "Optimisation of acoustic emission from transit plasma discharges in water," in *Technological Plasma Workshop*, Book of Abstracts, Coventry, UK, Oct. 2015, pp. 1.

Y. Sun, I. V. Timoshkin and S. J. MacGregor, "Impulsive Discharges in Water: plasma resistance and acoustic emission," in *UHVnet Colloquium*, Book of Abstracts, Stafford, UK, Jan. 2015, pp. 1.

Abstract

Underwater spark discharge is one of the most common methods to generate intense acoustic impulses in water for different purposes in practical applications. As compared with chemical explosion, the underwater spark discharges provide a number of advantages: they do not generate toxic compounds or species, no high explosives involved and they provide high degree of controllability. These features have led to a large number of studies of underwater spark discharge mechanisms and their potential practical utilisation.

This work is aimed at experimental investigation of the breakdown characteristics of underwater spark discharges with three different initiation mechanisms: free discharge, air-bubble-stimulated discharge and wire-guided discharge. Study on the electrical and acoustic parameters of the discharge process has conducted. A capacitive voltage impulse system was developed to energise three different electrode topologies. Acoustic and electrical parameters of underwater spark discharges were obtained from experimental results, such as acoustic magnitude, period of cavity oscillation, breakdown voltage, plasma resistance and energy delivered into the plasma channel. Phenomenological scaling relations were established for these parameters, which allowed for better understanding and prediction of the acoustic performance of underwater spark discharges. An analytical model, which describes the cavity oscillation, has been developed and comparison of the modelling and experimental results was conducted for all three types of discharges. This model allowed for accurate description of the time-dependent behaviour of different parameters during the underwater spark discharge process. The obtained results are important for optimising the circuit parameters for generation of tailored acoustic impulses for different practical applications.

Contents

1 Introduction

The concept of plasma goes back to almost a century ago when Irving Langmuir named this particular state of matter as ‘plasma’. Plasma is regarded as one of the four fundamental states of matter in which ionised particles (positive and negative ions and electrons) exist and their behaviour is governed by electrical and magnetic fields. Free elections present in plasma result in high electrical conductivity of plasma, which is close to metallic conductivity.

Plasma can be created in laboratory conditions and used in practical applications. The fundamental approach to develop plasma is to ionise atoms or molecules in order to achieve a mix of electrons, ions and neutral particles (plasma). Ionisation can be produced by using strong electrical field and this form of plasma is known as ‘electrical discharge’. Depending on the type of energisation electrode topology, electrical discharge can appear in different forms, such as corona discharge, glow discharge, spark discharge and other forms. All of these electrical discharges differ in many aspects, including their physical properties, like their chemical species, light and acoustic emission, plasma temperature, and plasma conductivity. Significant large amount of practical applications based on plasma itself or its relevant phenomena have been developed over last several decades, covering a wild range of technological and scientific areas including environmental and bio-medical applications [1]-[6].

An important research area in the plasma science is the electrical discharge (or breakdown) in liquid, including liquid water. As mentioned above, the state of dielectric materials is one of the primary factors that determines the discharge process. Generally, compared with gas, liquid requires stronger electrical field to initiate the electrical discharge. The electrical discharge in water results in the chemical reactions, which provides different chemical species, thus these discharges can be used in practical applications [7],[8]. Also, discharges in water can be used in industrial applications, for example, for water treatment and purification [9]-[14].

One of the significant phenomena of the spark discharge in water is the formation of a gas cavity, resulting in acoustic (pressure) impulse emitted into the surrounding water. Thus, underwater spark discharges can be used as a source of intensive acoustic impulses in practical applications.

In mineral engineering and material recycling [15]-[18], the spark discharges in water

and plasma generated pressure waves are used to treat the target material. For example, in [15], Andres and Timoshkin have reported on a novel treatment of ores and slags by using underwater spark discharges to extract valuable inclusions. This technique is based on the electrical breakdown in solid ores submerged in water. According to [16], for electrical pulse with rise time less than ~ 500 ns, the breakdown field strength for rock is lower than that for liquid water. Therefore, by placing the rock sample in between two electrodes in water (for example using a rod-plate configuration) and by applying short electrical pulses to them, underwater spark discharges are initiated within solid rock along the boundary between mineral components due to their different electrical properties (like the permittivity/conductivity ratio). The generated plasma expands and produces intense pressure waves emitting radically. These pressure waves fragment mineral components, completing the separation of the valuable inclusions in an ore.

Another example is the use of underwater spark discharges for smaller scale laboratorial material treatment. In Parker's work on methods for mineral liberation [17], he used a high voltage (HV) pulse power fragmentation machine, developed and manufactured by SELFRAG AG Co for comminution of ores. It has shown in [17] by using this electrical comminution technique that better recovery and concentrate grades were achieved for copper ores as compared with mechanical crushing. This technique is used not only for treatment of ores and slags but also for crushing material, like glass fibre composite [18]. Thus, pulsed power disintegration is an established method for material fragmentation and recycling [19]-[21]. Similar technique can be used for hole drilling without mechanical rotation. In [22], Timoshkin, Mackersie and Macgregor have demonstrated a novel design of a plasma drilling system based on underwater spark discharges to generate selective spark discharges, which penetrate through rocks and result in produced intense pressure waves for drilling. The tests conducted with sandstone samples confirmed the effectiveness of the designed system in drilling miniature holes (35 mm and 50 mm diameters in [22]), and lower energy requirement making this technique suitable for drilling operations.

In many environmental practical applications, the underwater spark discharges are used as an acoustic source. For example, in [23], the use of spark discharges in self-cleaning filtration system was discussed. A similar example of the use of spark

discharges for water well cleaning system was studied in [24]. In this research, Chung and Lee from South Korea developed a practical spark discharge generator, which can be placed into a water well and produces shock waves with magnitude of a few to tens of MPa energised by a capacitive pulsed power system. The slug tests were also conducted and the results showed that the improvement in the hydraulic conductivity in slug after the pulse treatment was almost three times of that before the treatment for the same water sample. All these results verify the effectiveness of the shock waves generated by underwater spark discharges in cleaning wells. Another example of plasma pressure is the use of underwater spark discharges in fossil extraction operation [25]. The conventional way to increase efficiency of extraction of fossils is to use intense hydraulic pressure to penetrate the fossil storage layer. However, there are several issues associated with this method: it does not increase permeability and introduces pollutants to the environment. Zhang and Qiu from Xi'an Jiaotong University in China [25] proposed a new method of the pre-operational treatment by using the underwater electrical sparks, which generate shock waves in the fossil storage layers. These researchers conducted tests on several sandstone samples to evaluate the performance of the underwater-discharge-generated shock waves in increasing permeability of the samples. The obtained results showed that the average permeability of samples has increased from 0.611×10^{-3} μm^2 to 2.579×10^{-3} μm^2, indicating the effective performance of the shock wave generated by electrical discharges in penetrating the fossil stone layers. Since 2009, this technique has been adopted in several practical fossil/oil/gas fields in China. The efficiency of the oil extraction has reached ~ 93 % for different discharge configurations, which confirms the advantage of this technique being used in practical applications. More examples of different applications of underwater spark discharges in water can be found in [26] and [27], which demonstrated that plasma-acoustic sources could be used in sea water and in liquids with high salinity in medical applications.

The United States Geological Survey (USGS [28]) used spark discharges as an acoustic sound source in their seismic profiling system. This system included pairs of point electrodes to produce broadband (50 Hz – 4000 Hz) pressure pulses, which will propagate hundreds of meters to the subsurface in the sea and before being reflected and received by hydrophones. According to [29], the spark discharge is one of the three

methods to generate shock waves to be used for extracorporeal shock wave lithotripsy (ESWL).

With a large amount of industrial and scientific aspects as introduced above, the pressure waves generated by underwater spark discharges have become one of the important topics in plasma science and engineering. However, to use underwater spark discharges in practical applications effectively and efficiently, an 'easy' question has to be asked: what is the optimal system setup to obtain desirable acoustic impulses? The aim of this research project is to provide further knowledge and information, which can help to answer this question. At first, some basic processes and mechanisms, which underpin complex underwater spark discharges, should be considered.

The strong acoustic impulse is generated after the plasma channel bridges the inter-electrode gap. This process of breakdown and generation of acoustic impulse can be divided into three stages: pre-breakdown stage, energy dissipation stage (conductive current flows through the plasma channel) and adiabatic expansion stage of the gas cavity formed by the discharges. Each of these stages is determined by not only the pulsed power source but also the structure and properties of the spark-generation system and the discharge environment (electrical parameters of water). For example, the breakdown field depends on the duration of the high voltage impulse [30]. For high voltage impulses with duration in the microsecond range, the critical electrical field for breakdown in water is ~ 0.1 MV/cm, the critical breakdown field increases up to ~ 1.5 MV/cm for the impulses with sub-microseconds duration. The discharges may have different forms, for example, slow bush-like mode at lower applied voltages and fast tree-like mode at higher voltages [31]. It has been reported that the magnitude of the acoustic impulse generated by underwater spark discharges strongly depends on the length of the gap between electrodes and on the energy delivered into the plasma channel [32]-[34]. However, not only these parameters govern the characteristics of the acoustic impulses, other factors, which should be considered, include the storage capacitance, the impedance of the external circuit and the conductivity of the water.

Back to the question on the optimal setup, the answer is never simple but complicated. In other words, there is no universal spark generation system fulfilling all requirements with so many parameters involved in consideration. However, the question can be narrowed down to as how to adjust the system parameters to generate required acoustic

impulses. Therefore, the relationships between underwater spark discharges and their acoustic emission should be established for optimisation of the underwater spark discharges to achieve the tailored acoustic impulses.

As mentioned above, one of the critical parameters determining the strength of acoustic impulses is the length of the gap distance between the electrodes. Increasing the inter-electrode gap can be an effective way to increase the acoustic strength. According to the research conducted by Mackersie, Timoshkin and MacGregor in [35], the magnitude of acoustic impulses was almost tripled at the same level of injected energy (~ 110 J) when the inter-electrode gap was increased from 2 mm to 12 mm. By increasing the injected energy from ~ 100 J to ~ 150 J, an increase in the acoustic strength was only less than ~ 10 % for the same inter-electrode gap. As a result of an increase in the inter-electrode gap, the required applied voltage has to increase to achieve the breakdown in water. However, while keeping inter-electrode gaps as long as possible in many practical cases, it is desirable to limit the operating voltage. Therefore, apart from the free spark discharges with plasma streamers propagating between electrodes in bulk of water, several trigger-assisted initiation mechanisms for initiation of underwater spark discharges have been developed to reduce the breakdown voltage for long-gap underwater spark discharges. These approaches included wire-guided underwater discharges [36]-[38], and injection of gas bubbles to trigger underwater spark discharges [39]-[41]. By using these triggering techniques, the achievable inter-electrode gap and the strength of acoustic impulses can be enhanced significantly without significant increase in the operating voltage. However, these special triggering techniques are needed to be investigated as there is a gap in understanding of the link between acoustic, hydrodynamic and electrical parameters of underwater spark discharges. It is important for any potential practical application to understand how to optimise the plasma-acoustic system. Therefore, it is necessary to conduct comprehensive investigation to answer these important questions.

This work focuses on the breakdown characterisation and on the acoustic characteristics of the underwater spark discharges. Three different mechanisms are taken into consideration in this study: free self-triggering discharge, the wire-guided discharge and the air-bubble-stimulated discharge. A series of experimental tests with different levels of circuit energisation have been conducted to obtain the characteristic

electrical and acoustic waveforms for all three discharges. The relationships between electrical, hydrodynamic and acoustic parameters are established and analysed. Novel scaling relationships are derived for all three types of discharges. An analytical model has been developed to study the time-dependent variation of above parameters and the acoustic efficiency of underwater spark discharges. The importance of this study is in provision of reliable relationships between parameters of the pulse driving circuit (energy source) and the acoustic output. This work also investigates the energy conversion from the energy dissipated in the plasma channel to the acoustic energy associated with the acoustic impulses. The developed scaling relationships are essential for practical applications and allow evaluation of the behaviour of the spark generation systems and prediction of the acoustic performance.

Chapter 2 introduces the background and the fundamental aspects of underwater spark discharges and related phenomena. This chapter starts with an introduction of different types of underwater spark discharges developing with and without pre-existing gas bubbles formed under the applied field either in nanosecond or microsecond regimes. The high voltage impulses used in the present work are within the microsecond range, thus the detailed mechanism of underwater spark discharges, which involve formation of micro-bubbles, will be discussed in detail. Also, formation and the propagation of steamers in water will be considered; this mechanism is based on Townsend's discharge theory. The hydrodynamic behaviour of the gas cavity formed after complete breakdown (number expansion/collapse cycles) is discussed within Rayleigh's bubble oscillation model. Emission and propagation of the pressure waves generated by oscillating plasma/gas cavity is also discussed including aspects such as mechanism of its generation and the energy balance equation.

Chapter 3 presents practical design of the spark generation system and includes information on the equipment used in this study. The detailed description of the experimental setup is given; this set up contains the pulsed power generation system, the electrode system and the diagnostic system. The pulse power system includes a high power DC generator, a set of charging resistor and a storage capacitor bank. Different energisation levels used in this study have been achieved by using different combinations of charging voltage and different capacitances. Three sets of electrodes topologies were designed and used in this study. Free spark discharges were generated

in a point-to-point electrode topology used for enhancement of the electrical field. The electrode topology used to generate the wire-guided spark discharges consists of two stainless steel crocodile clips (at high voltage and ground potentials) which were used to hold a fixed length of a copper wire. Air-bubble-stimulated spark discharges were generated in a point-to-rod electrode topology. An external air-bubble injection system was embedded within the ground rod electrode and air-bubbles were injected into inter-electrode gap during tests. The technical parameters of the plasma-acoustic system and the diagnostic system are provided.

Chapter 4 presents the experimental results and their analysis for free (self-triggered) underwater spark discharges. The electrical parameters of the plasma channel were obtained from the experimental voltage and current waveforms based on the lumped RLC circuit model. These parameters include the plasma resistance and the energy delivered into the plasma channel. The functional dependency of the acoustic and hydrodynamic parameters on the electrical parameters is obtained for a range of inter-electrode gap from 5 mm to maximum 15 mm. The magnitude of acoustic signals was found to be dependent on the inter-electrode gap and the discharge energy, while the period of cavity oscillation was only related to the energy available in discharge. Phenomenological scaling relationships were developed for these parameters in order to establish the link between electrical, hydrodynamic and acoustic parameters for underwater air-bubble triggered spark discharges.

Chapter 5 presents the experimental results obtained for the wire-guided spark discharges. This chapter provides discussion and analysis of the obtained results. The maximum inter-electrode gap used in the study for this particular discharge mechanism was 75 mm, which is significantly longer than that of free spark discharges. The phenomenological scaling relationships between the acoustic and electrical parameters for the wire-guided spark discharges were established. The wire-guided spark discharges demonstrated their advantage over other discharge types in enhancing the acoustic magnitude of the emitted pressure impulses. However, this type of discharge system can be operated only in a single shot regime.

Chapter 6 presents the experimental and analytical results for air-bubble-stimulated underwater spark discharges. The maximum inter-electrode gap achieved by the air-bubble-stimulated discharges is 25 mm. Although this gap is less than that achieved

with wire-guided discharges, it allows the discharge operation rate to be as high as in the case of free spark discharges. This is important for different practical applications, which require high operation rate, like plasma drilling discussed in [22].

Chapter 7 presents the development and implementation of the analytical model designed for the underwater spark discharges (regardless of their initiation mechanisms). This analytical model was developed based on the Gilmore bubble oscillation model with the consideration of the pressure-dependent water density and the acoustic approximation method. The time-dependent behaviour of the electrical and acoustic parameters was obtained using the developed model. The comparison between the simulated and experimental acoustic impulse profile and the period of the cavity oscillation has been conducted. This comparison verifies the validity of the proposed model. The calculated acoustic energy and the corresponding acoustic efficiency (defined as the ratio of the acoustic energy and the energy delivered into the plasma channel) are provided and discussed for all three discharge mechanisms. It was found that the maximum acoustic efficiency could reach ~50 % in all discharge cases. The relationships between the acoustic efficiency and the plasma resistance and the energy delivered into the plasma channel have been established.

Chapter 8 presents general conclusions and discussion of the main results obtained in this thesis. The experimental and analytical findings are reviewed; they include experimental results and the obtained relationships between different parameters for three different underwater spark discharge mechanisms used in this work. Suggestions and recommendations for future work are also included in this chapter, indicating more investigation possibilities in this research area, which could be conducted in order to achieve more efficient and effective utilisation of the underwater spark discharge energy in present and future practical applications.

2 Literature Review

As introduced in Chapter 1, electrical discharge is one of the most common methods to generate acoustic impulses for practical applications. The electrical breakdown can take place in gases, liquids and solids. The fundamental theory of the discharge in gas is the Townsend discharge theory (avalanche discharge), which was named after Sir John Sealy Townsend for his work between later 19th century and early 20th century. The Townsend discharge provides the basic mechanisms of electrical discharges, which is critical for investigation of electrical breakdown. This chapter discusses fundamental principles of discharges in gas, liquids and practical applications of discharges in water, especially related to the development of plasma-acoustic sources.

2.1 Gas discharges

2.1.1 Townsend discharges mechanism

Townsend's discharge theory describes the electron multiplication process in gas stressed with a uniform electrical field above specific critical (breakdown) value. Avalanche is the fundamental form of electron multiplication, which starts from pre-existing or newly created free electrons. These seed electrons can be a result of ionisation of gas in the vicinity of the cathode by external ionisation sources. After the application of the electrical field, these free electrons are accelerated and propagate along the electrical field lines. If the magnitude of the electrical field is high enough, the kinetic energy of an electron accumulated during its acceleration could exceed the ionising potential of molecules or atoms of the gas, resulting in collisional ionisation process. Together with the original electron, newly created free electrons are accelerated by the electrical field and collide with neutral particles, producing more free electrons propagating to the anode (electron multiplication mechanism).

To describe this election avalanche process mathematically, the first Townsend ionisation coefficient was introduced: α_1, which is a number of electron-ion pairs generated per unit length (m). The positive ions produced in this process drift into the opposite direction until they collide with the cathode to produce secondary electrons from the cathode. These secondary electrons support the development of the avalanche. Secondary electron emission is governed by the second Townsend ionisation

coefficient, γ_1, which is the number of electrons released from the cathode surface by a single positive ion. The physical movement of particles (electrons and ions) in the gap induces the appearance of the conductive current. Based on the coefficient α_1 and γ_1, the current through with an inter-electrode gap with a distance, d_1, during the avalanche discharge is given as [42]:

$$\frac{I}{I_{pho}} = \frac{e^{\alpha_1 d_1}}{1-\gamma_1\left(e^{\alpha_1 d_1}-1\right)} \tag{2.1}$$

where I_{pho} is the initial current generated by an external ionisation source (for example UV light which produces initial current due to the photoelectric effect) at the cathode.

To form a breakdown between the electrodes, it is not enough to apply the electrical field, which initiates and supports the avalanche. If there is no external ionisation source, i.e. $I_{pho} = 0$, the discharge can become a self-sustained discharge when the following condition is fulfilled [43]:

$$\gamma_1(e^{\alpha_1 d_1} - 1) = 1 \tag{2.2}$$

This condition is the Townsend breakdown criterion, it defines the critical breakdown voltage, required to maintain the existence of the conductive current between electrodes.

The Townsend breakdown can be converted into a spark breakdown, which is characterized by the voltage collapse and by the formation of the highly conductive plasma channel. Another coefficient is the electron attachment coefficient, which affects the discharge process and is critical for the discharge developing in electronegative gases, such as O_2, CO_2 and SF_6.

Based on the electron avalanche criterion, the voltage required to support a self-sustained discharge (breakdown) in gas is given by the Paschen's law in which the breakdown voltage, V_{bd}, is related to the product of the inter-electrode gap, d_1, and the pressure in the gas medium, p [43]:

$$V_{bd} = \frac{B_1 p d_1}{\ln(A_1 p d_1) - \ln(\ln(1/\gamma_1))} \tag{2.3}$$

where A_1, B_1 are experimental constant.

The Paschen's law has also defined the Paschen's curve for the variation of breakdown voltage with *pd*. An example of a Paschen's curve in air is shown in Fig. 2-1.

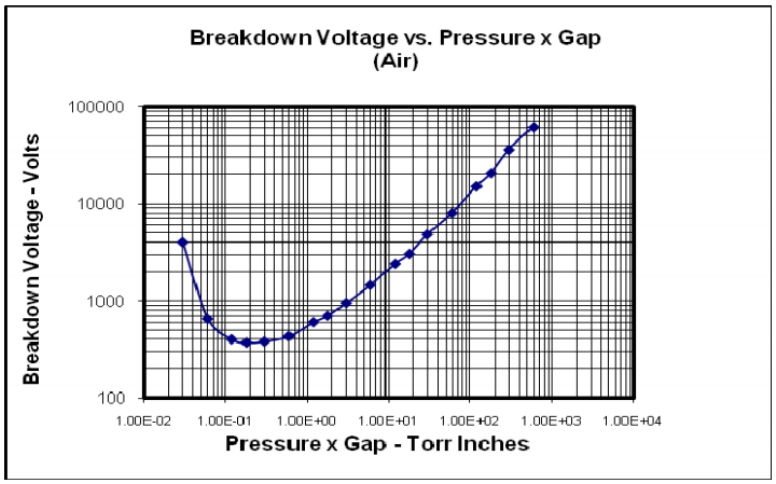

Figure 2-1. Example of Paschen's curve conducted for air with two flat parallel copper electrodes, separated by 1 inch and for pressure between 0.03 Torr and 760 Torr. (Picture taken from [44]).

It can be seen that there is a minimum point for the breakdown voltage, indicating the 'optimal' condition of *pd* combination to achieve a breakdown with minimum applied voltage. For both sides away from the minimum value (with lower or larger *pd*'s), the breakdown voltage has to be increased due to the lower probability of free electrons being energised enough to initiate avalanche.

2.1.2 Streamer discharges

Depending on the strength of the electrical field or electrode topology, different forms of discharges may be observed, not only the Townsend discharge introduced above. These forms of discharges include corona discharges and spark discharges. In many practical applications, the spark discharge is commonly used for generation of transient plasma and plasma streamers play an important role in initiating the spark breakdown.

As introduced in the previous section, the Townsend discharge is an electron multiplication process, which results in the development of electronic avalanche. If the following criterion is satisfied (the product of the inter-electrode gap, d_1, and the first Townsend ionisation coefficient, α, is more than 20), the amount of the charge carriers (space charge) in the avalanche head is sufficient to affect the original electrical field distribution established by the externally applied voltage:

$$\alpha_1 d_1 \geq (18\sim20) \tag{2.4}$$

If (2.4) is valid, the significant charge in the avalanche head distorts (enhances) the electrical field ahead of the avalanche and facilitates ionisation of the gas. Thus, the avalanche transforms into plasma steamer, which propagates between electrodes. Once the streamer bridges inter-electrode gap, a plasma channel filled with electrons and positive ions is formed. Afterwards, the appearance of the large conductive current through the plasma thermalizes the plasma in the channel.

This fundamental Townsend and streamer breakdown mechanisms are important for understanding development of the discharge in liquids including liquid water.

The following sections will discuss basic elements and characteristics of breakdown in water.

2.2 Underwater spark discharges

The spark discharge mechanism in water is a complex process. This mechanism depends on the magnitude of applied voltage, its duration and on the electrical properties of water. To initiate a streamer breakdown in liquid water, the required breakdown field depends on duration of the applied field and can be as high as ~1.2 MV/cm for impulses with duration shorter than 100 ns [45]. The link between the critical breakdown voltage or field and time to breakdown is called volt (field) - time characteristic.

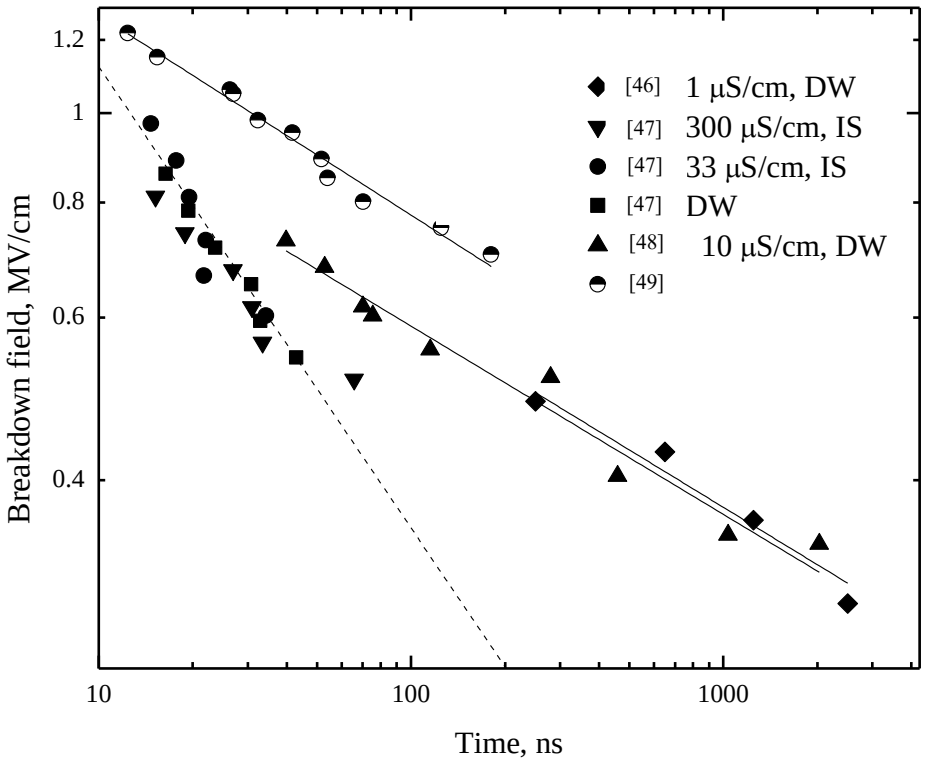

Figure 2-2. Volt-time characteristics of breakdown in water with different water conductivity. DW: distilled water, IS: water ionic solution. Dots: experimental data from papers [46]-[49]; solid lines: the analytical fit [30]. (Picture taken from [30]).

Fig. 2-2 shows the volt-time characteristic (the breakdown field $E_{field\text{-}br}$ and the pre-breakdown time t_{br}) for water with different conductivities together with analytical power fit lines:

$$E_{field-br} = C_1 \cdot t_{br}^{e} \tag{2.5}$$

where e and C_1 are empirical constants.

The results of C_1 and e obtained for the experimental results shown in Fig. 2-2 are given in Table. 2-1. It was found that the breakdown field was inversely proportional to the pre-breakdown time.

Table 2-1. Coefficients C_1 and e in (2.5) obtained using experimental results in Fig. 2-2

Data/ parameter	C_1	e
[46]	1.6	0.21
[47]	1.5	0.20
[48]	2.1	0.22
[49] (average values)	3.6	0.50

For successful breakdown in water with a relatively short pre-breakdown time, significant breakdown field has to be applied. Therefore, the selection of the applied voltage and the electrode topology is critical for achieving complete breakdown. In most cases of underwater breakdown applications [50], [51], an impulsive voltage source is preferred which results in reduction of Joule heating losses. Also it is easy to achieve voltage multiplication using impulsive (Marx) generators, thus water can be stressed with high electrical field and repetitive operation requirements can also be achieved.

In recent research papers on impulsive underwater spark discharge mechanisms, two theories have been frequently discussed and reported. One of them is the direct breakdown in water without the presence of gas bubbles [52], [57]. The other one discusses the breakdown mechanism, which is progresses through development of gas bubbles in water and consequent breakdown in these gas bubbles [31]. This mechanism is similar to the streamer breakdown in gas discussed in Section 2.1.2. These two mechanisms will be discussed in detail in Section 2.2.1 and Section 2.2.2.

2.2.1 Underwater spark discharges without presence of gas bubbles

This underwater direct breakdown mechanism is based on the electrostriction effect induced by the fast rising voltage impulse. As introduced in Section 2.1.1.1, the electron avalanche occurs when the applied electrical field is high enough to energise free electrons for effective ionisation collision. There are two deciding factors in this process, the electrical field strength and the density of the gas. The electrical field determines the velocity of free electrons; the density of gas provides a free mean path in which an electron can travel between collisions for accumulating its kinetic energy before next collision. For dielectric fluids (liquid water) which are significantly denser than a gas at normal conditions, the mean free path is very short and an electron is not able to gain sufficient energy for ionisation. Therefore, a straightforward solution to achieve breakdown is to increase the electrical field to energise an electron in such a limited space, which is in many cases not a practical solution. However, in the presence of an inhomogeneous electrical field in liquid water, the electrostriction effect can be the key factor in initiation of the breakdown. The electrostrictive force affects the bulk of water in the vicinity of the high voltage electrode. The stress is directed from the electrode into the bulk of water resulting in the "rupture" of the water (breakage of links between water molecules) and the formation of low pressure gas 'nano-pores' in the vicinity of high voltage electrode [52]. These gas filled nano-pores (dimensions of these nano-pores were assumed to be ~ 10 nm in longitude and ~ 1 nm in transversal radius in [57]) are stressed with high electric field which is concentrated in gas cavities due to dielectric permittivity mismatch between water and the gas. Thus, in this process, it is assumed that a streamer discharge initiates in this gas cavities region; the streamer will propagate in the bulk of water and will result in a complete breakdown.

It is worthy of note that this electrostriction breakdown mechanism is very sensitive to the rate of voltage rise, *dV/dt*. For example, in [52], an effective breakdown initiation has been recorded under the electrical field of 2.5 MV/cm by a positive voltage impulse with the rate rise of 5.77 kV/ns while no discharges were observed under a higher electrical field of 2.7 MV/cm by a voltage impulse with the rise rate of 4.5 kV/ns. Another example is given in [53] where the appearance of the underwater spark discharges without formation of gas bubbles has been obtained by using either short nanosecond voltage impulses with a rise time of < 5 ns or sub-nanosecond

voltage impulses. It was also shown in [53] that the underwater spark discharge mechanism in the picosecond time scale is similar to that in gases, indicating the direct formation of the electron avalanche.

2.2.2 Underwater spark discharges with formation of gas bubbles

The breakdown of water which involves formation of gas micro-bubbles is one of the common mechanisms of development of underwater spark discharges in microsecond and millisecond regimes [31], [39], [54]. As mentioned in Section 2.2, the electrical field required to initiate a direct breakdown in water has to be as high as ~1.2 MV/cm. Thus, the requirements for building a HV pulsed power system, which will be able to produce high voltage impulses with magnitude up to several hundreds of kV with a fast rising front (less than a few nanoseconds) may result in significant technical challenges. Therefore, considering potential applications of microsecond and millisecond HV impulses in practical cases, the injected gas bubble or gas micro-bubbles formed in water should be considered as they will play a critical role in initiating the spark discharges. Gas (micro)-bubbles can appear/may be generated in water stressed by HV impulses by different mechanisms, including the Joule heating of water, water movement/cavitation and injection of gas bubbles into water.

Joule heating is the main cause of appearance of the micro-bubbles when a voltage impulse is applied to a (sharp) electrode. The highly inhomogeneous enhanced electrical field in the vicinity of the electrode produces the field emission current, which vaporises the water to form gas bubble(s) in the vicinity of the electrode [45]. Even with a short voltage impulse with nanosecond duration and low magnitude, [31], such gas bubble(s) may appear in water at the pin electrode due to electrostriction and they will expand into micro-bubbles. With the presence of the gas micro-bubble at electrode, the local electrical field inside this bubble is enhanced due to difference in permittivity between the gas and water, and this field inside the bubble is given as:

$$E_g = \frac{3\varepsilon_l}{2\varepsilon_l + \varepsilon_g} E_l \tag{2.6}$$

where E_g is the enhanced electrical field in gas bubble, E_l is the external electrical field

in liquid; ε_l and ε_g are the permittivity of the liquid and the gas in bubble respectively. The enhanced electrical field in the gas bubble is likely to form a streamer in this bubble, which promotes the development of a breakdown in the inter-electrode gap. The mechanism of the streamer initiation process in these bubbles is similar to the breakdown process in air as introduced in Section 2.1.2. The streamer development by this bubble-aided mechanism depends on the polarity of the applied voltage.

2.2.2.1 Positive polarity

In the case of positive polarity of the applied voltage, two significant streamer modes in liquid water have been reported [54]: the primary mode and the secondary mode. They differ not only in their propagation morphology but also in their velocity of propagation. The appearance of either of these two propagation modes depends on the voltage magnitude. In general, the primary mode is often found at lower voltage level; the secondary mode usually appears with higher voltage impulse with sharp rising front. The probability of the appearance of either of these two streamer modes in water under a voltage impulse with increasing magnitude was studied in [31], which is illustrated in Fig. 2-3.

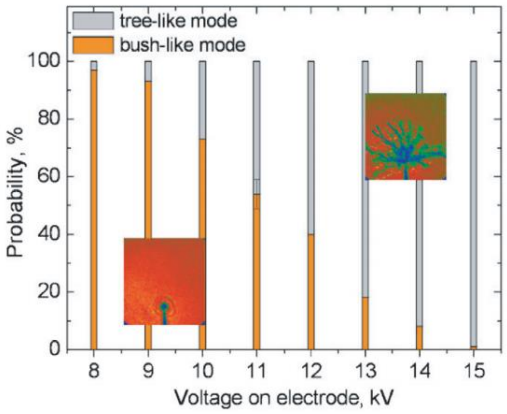

Figure 2-3. The probability of the appearance of different modes of discharge (tree-like mode and bush-like mode) as a function of applied voltage, conducted in pin-to-wire electrode topology in deionised water with conductivity of 5 μS/cm by using pulsed voltage with magnitude of maximum + 9.5 kV, 5 ns rise time and 30 ns duration. (Picture taken from [31]).

The inception probability of the primary and secondary streamer modes energised by rectangular pulses were also investigated in [55], it was found that with an increase in the applied voltage impulse, the inception probability of the primary streamer mode increased. When the voltage increased to a certain level, the secondary mode is observed and its inception probability increased to ~ 100 % with further increase in voltage while the inception probability of primary mode decreased until zero. It was also found that the voltage required for streamer initiation was higher in water with lower conductivity as less electrical charge was injected.

There is a possibility that the streamer is initiated as the primary mode and then it transfers into the secondary mode during its propagation, which has been reported in [41], [54].

The appearance of the primary mode streamer is a result of the electron multiplication process initiated in the bubble on the electrode after applying a voltage impulse with relatively low voltage level [31], [55], [56].

The development of the primary streamer mode features a hemispherical bush-like morphology with a large number of filaments. First filament streamers are initiated in the gas bubble and grow in all directions up their front. More filaments appear from the original ones and their development are accompanied by the propagation of a hemispherical shock wave away from the streamer head. The primary streamer develops during time duration from < 100 ns [54] to a few hundreds of nanoseconds [31] before it stops or enters into the transition to secondary mode. The length of the filaments could grow up to ~ 500 μm for microsecond discharge according to [31] and up to ~ 600 μm in [41]. The visualization of the primary mode development was conducted in [31], [41], [54] by using an ICCD camera or shadowgraph technique. Examples of the captured frames of the progress, conducted by [31], [54] for nanosecond voltage impulse, are shown in Fig. 2-4 and Fig. 2-5.

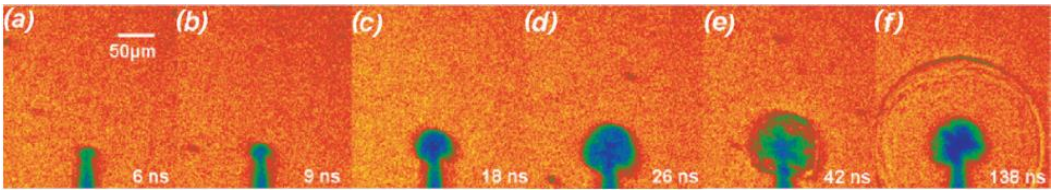

Figure 2-4. Shadowgraphs in false colour of the temporal development of bush-like discharge in deionised water with conductivity of 5 µS/cm using HV pulse with 14 kV magnitude. Camera gate is 2 ns. (Picture taken from [31]).

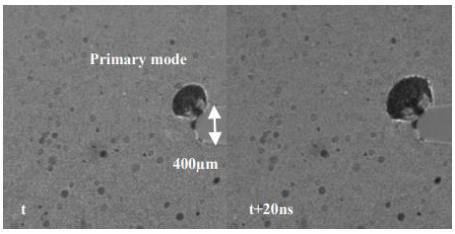

Figure 2-5. Successive ICCD camera shadow imagines taken for a primary mode discharge generated using voltage impulse with 40 kV peak magnitude and 20 ns rise time in water with conductivity of 100 µS/cm. (Picture taken from [54]).

The velocity of the primary streamer was supersonic ~ 2 km/s in [41]. This velocity was found to be constant during the propagation period and did not depend on variations in voltage and the pulse duration, [31]. The propagation velocity of the shock wave at the streamer front was found to be ~ 4 km/s [54] and it decayed to the local speed of sound (~1.45 km/s) during its propagation. For rectangular voltage impulse, the velocity of the primary streamer was found to be dependent on the applied voltage [55], [56], it increased from ~ 0.4 km/s to ~ 0.6 km/s with an increase in voltage from ~ 11 kV to ~ 14 kV with a low and stable water conductivity at 0.05 µS/cm.

The discharge current during this primary streamer mode has a repetitive pulsed profile with pulse magnitude in the range of mA [45], [54], [56]. The magnitude of individual current pulses keeps increasing during the streamer's propagation, indicating an increase of the plasma conductivity, which is important to the streamer's transition to the secondary mode as more electrical charge is injected into channel.

The secondary streamer mode may appear either as the direct discharge after applying a desirable voltage impulse or as a continuous stage of discharge following the primary mode streamer. The appearance of the secondary mode streamer directly at electrode surface requires the condition of a highly non-uniform electrical field present close to the electrode with rough surface or with small radii. The secondary mode streamer is a result of impact ionisation, photoionization and the generation of charge carries [57], especially for nanosecond discharges. The mechanism behind this phenomenon is similar to that of underwater spark discharges without the bubble formation. The electrostrictive force induced by the strong electrical field ruptures the bulk of water in the vicinity of the electrode, generating a low pressure region (low pressure gas-filled "crack") for electron multiplication and then initiates the streamer formation and propagation to the opposite electrode [57]-[59]. In these papers, it was also emphasised that the key to initiate secondary mode streamer is the use of impulsive voltage with a short rise time (typically less than 10 ns). However, in the most cases of microsecond and sub-millisecond discharges, the secondary mode is often observed as a continuous discharge stage after the primary mode streamer. From the previous introduction on the conditions of the primary and secondary mode streamers, it can be concluded that the major difference in the initiation stage of these two modes is the voltage impulse rise time and the voltage level, which is the strength of the electrical field. Also, as mentioned above, the appearance of the primary streamer causes the conductive current flowing through the filaments of the streamer and the current keeps increasing until streamer stops. Therefore, a hypothesis was proposed in [31] for the transition of the streamer from the primary mode to the secondary mode. Paper [31] proposed a possible explanation of this phenomenon: the plasma conductivity grows sufficiently to provide threshold electrical field (~ 10 MV/cm) at one of the filaments heads to initiate a secondary streamer after the pressure inside previous bush-like streamer channels relaxes down to a critical value.

Different from the bush-like primary mode, the secondary streamer mode features a tree-like structure with much less branches than the primary mode. Its initiation has shown intense luminescence at the electrode tip [31]. Several main branches appear from the initiation point and each of them is enveloped by conical shockwave emission. These branches of the streamer grow in random directions with a number of minor

branches developed on side of them. For a complete breakdown between electrodes, one of few of the main branches will bridge the opposite electrode. It is worthy of note that re-illumination happens as a re-start of the discharge in developed branch channel, which is observed in [45], [54]. This re-illumination occurs in one of the main streamer branch, which extends only a little further together with a shock wave emission.

The time-resolved dynamics of the secondary streamer has been recorded in [31], [54], [60] by using either ICCD camera or shadowgraph. A few of the examples, including discharge and breakdown conducted by [31], [60], are shown in Fig. 2-6 and Fig. 2-7

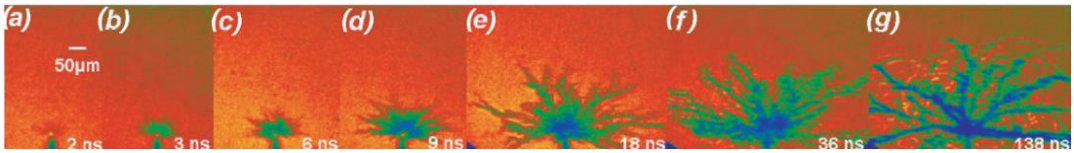

Figure 2-6. Shadowgraphs in false colour of the temporal development of tree-like discharge in deionised water with conductivity of 5 μS/cm using HV pulse with 14 kV magnitude. Camera gate is 2 ns. (Picture taken from [31]).

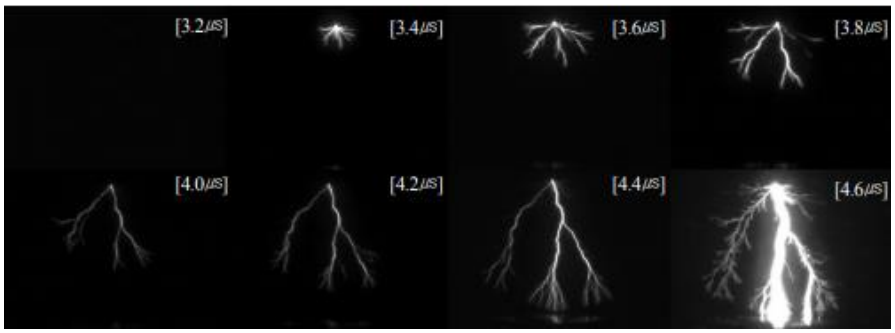

Figure 2-7. Time-integrated photographs of positive discharge using ICCD camera with 0.2 μs gate. (Voltage: 37 kV, conductivity of water: 100 μS/cm) (Picture taken from [60]).

The secondary streamer is a relatively fast process. The propagation velocity of this type of streamer can reach ~ 30 km/s [54]-[56] until the streamer is close to the stopping moment. This velocity was found to be almost constant during the steamer's

propagation in [31], [54]. In [55], [56], it was found that the propagation velocity was dependent on the applied voltage as was increasing with an increase in the voltage. According to [55], [56], for applied voltage increased at or beyond the breakdown level (> 30 kV), the streamer velocity would not increase further and was at ~ 30 km/s level under specific experimental conditions (rectangular pulse with fast rise and fall time (20 ns) for pin-to-plane electrode with 30 mm separation). The propagation length (the stopping moment) is related to the duration of the applied voltage impulse. The streamer stops when the voltage drops to a critical value that is not able to sustain the discharge. The velocity and the length of the secondary streamer propagation is independent on the water conductivity.

This fast and intense mode of streamer induces a conduction current impulse with a decaying slope. The initial magnitude of current in the secondary streamer can reach few of Amperes [55], which is much larger than the current in the primary streamer under a similar applied voltage. The current keeps decreasing during the propagation of the streamer until the streamer extension stops. An example of the current waveform containing the primary streamer, secondary streamer and the re-illumination spikes is shown in Fig. 2-8, [54].

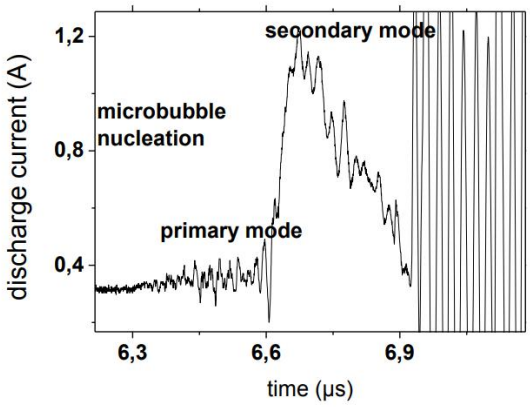

Figure 2-8. Waveform of current showing preinitiation, 300 mA, current ramp of the primary positive mode plasma, 100 mA, current increase of secondary mode plasma, 1 A, and re-illumination current. (Voltage: 40 kV; conductivity of water: 7 µS/cm). (Picture taken from [54]).

The propagation of streamers in water is also accompanied by light emission. Intensive light emission can be observed every time the secondary streamer propagates. In [55], [56], it was found that intense stepped light emission was detected for each duration of steamer propagation, indicating the stepped propagation progress of the secondary mode streamer. An example of the stepped propagation of streamer is shown in Fig. 2-9.

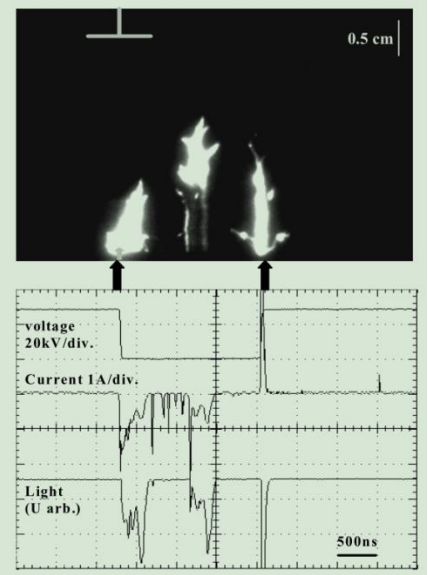

Figure 2-9. Example streak photograph, voltage, current and light emission of the stepped secondary model streamer propagation with applied voltage 28 kV for 30 mm separated pin-to-plane electrodes in pure water with 0.05 μS/cm. (Picture taken from [56]).

The length of each streamer propagation step was found to be dependent on the voltage [55], [56]. In a complete breakdown, several steps were expected for streamer propagation. For applied voltage larger than the critical value related to 100 % breakdown probability, only one unique step was observed for a streamer to reach the opposite electrode for a constant velocity (at 30 km/s).

2.2.2.2 Negative polarity

A negative streamer can be initiated by a negative voltage impulse with a relatively high magnitude. Different from the positive polarity case, only a single propagation mode was observed for the negative streamer. This propagation mode has a different structure and morphology as compared with the positive polarity case. To initiate a negative streamer breakdown in fluid (with high electron affinity), higher magnitude of field is required as compared with positive energisation condition. This is due to formation of the space charge, which modifies the electric field in the vicinity of the HV electrode. Thus, a negative impulse with higher magnitude is required to achieve complete breakdown in water as compared with a positive impulse.

The negative streamer in water has a unique morphology. The basic structure of negative streamers is similar to tree-like positive streamer having several main branches. However, a large number of tiny 'branches' is attached on the main body of the negative streamer, which is visually granular. During the propagation, the streamer region is non-transparent [41]. After completion of the breakdown, strong light emission is observed [60]. Fig. 2-10, Fig. 2-11 and Fig. 2-12 show three examples of the negative polarity streamer development in water, captured by shadowgraph and ICCD camera [41], [60], [61].

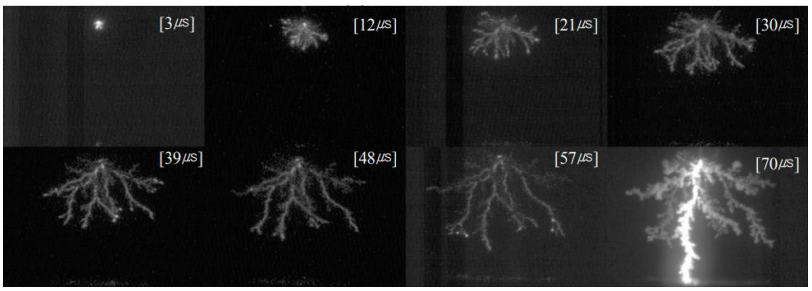

Figure 2-10. Time-integrated photographs of negative discharge using ICCD camera with 9 μs gate. (Voltage: 37 kV, conductivity of water: 100 μS/cm). (Picture taken from [60]).

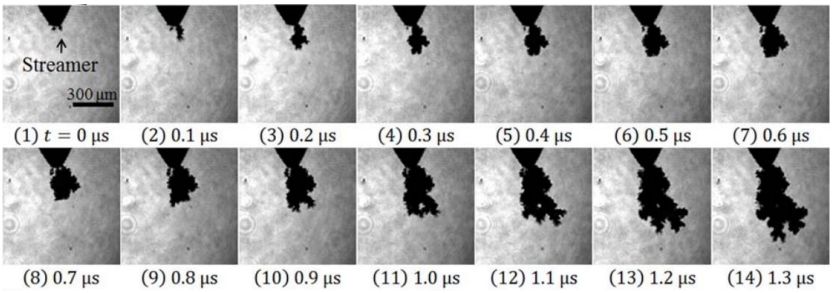

Figure 2-11. Shadowgraphs of negative streamer development taken using a high-speed camera with 50 ns exposure time for a voltage impulse (-23 kV and 100 ns rise time) applied to needle-to-wire electrodes with 2 mm separation in ultrapure water. (Picture taken from [61]).

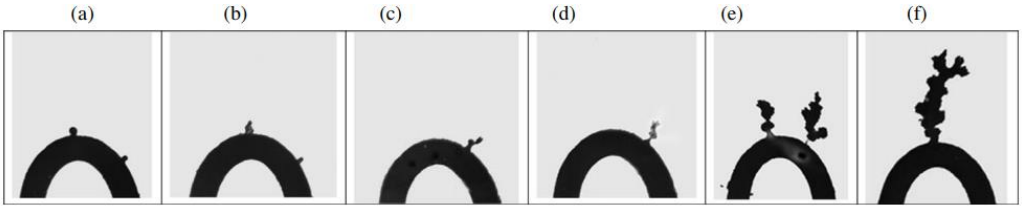

Figure 2-12. A series of negative discharge events taken using laser light pulses of ~3 ns with 800 kV/cm voltage:(a) initial bubbles; (b) deformed bubbles; (c) bubbles assuming an initial 'mushroom' shape; (d) bubbles with finished mushroom shape; (e) bubbles with bush-like development; (f) bush-like structure of bubble streamer channel. (Picture taken from [41]).

Typical propagation velocity of the negative streamer in water was found to be subsonic [41], [60]-[61]. However, it is not constant over the entire propagation duration. For example, it varied from ~ 200 m/s to ~ 800 m/s using a – 23 kV voltage impulse with 100 ns rise time in [61] and from ~ 100 m/s to ~ 400 m/s with maximum field intensity of 800 kV/cm in [41]. This phenomenon was linked to the discharge current in [61], which has a repetitive-pulses profile. The relatively high propagation velocity corresponds to the appearance of the current spikes in which the electrical field is concentrated at the tip of streamer due to the accumulation of electrical charge. Light emission during the propagation was observed only in these periods. The slower propagation velocity presents in the 'empty' durations of the current and is due to the

heat expansion of bubbles [61]. It is worthy of note that the average propagation velocity is irrelevant to the water conductivity and the propagation length of the negative streamer is proportional to the voltage magnitude.

As positive streamers are faster than negative streamers, the pre-breakdown time for negative polarity is generally lower than that for positive polarity. The breakdown voltage is higher for negative energisation of the HV electrode. The light emission by the breakdown in the case of positive polarity is more intense than in negative polarity.

2.3 Underwater spark discharges initiated with exploding wire

Apart from the breakdown initiation mechanisms described in Section 2.2, underwater spark discharges can be initiated by fast evaporation and disintegrating of a conductive wire placed between two electrodes. This initiation mechanism has been studied for over several decades [36], [62]-[68]. This 'unusual' mechanism does not involve pre-breakdown streamer's formation and propagation in the bulk of water. Instead, a thin conductive (metal) wire is placed between electrodes. By applying a voltage impulse to this wire, a conductive current through the metal wire closes the discharge circuit. Such current with a large magnitude produces intensive Joule heating of the wire. Thus, the wire is heated and it starts to melt. Finally, the wire disintegrates and a plasma channel filled with a mixture of hot metal droplets and water vapour is formed between electrodes. This channel is responsible for the following discharge development. An intense shock wave can be generated by the wire discharge. For example, using microsecond voltage impulse with energy up to 4.5 kJ, the resultant pressure of shock waves in water were in the range from ~ 3 to ~ 12 GPa for 50 mm and 100 mm wires [64].

Different from the streamer mechanism, the plasma path is well-defined by the wire which, in the most cases, produces a straight plasma channel. The initial shock wave generated at the vicinity of the plasma is cylindrical and propagates in the direction of channel expansion. The visualisation of the wire explosion process and the emitted shock wave was conducted in [36] using two CCD cameras. An example of the shadowgraph for a discharge channel generated by exploding a 50 mm long Cu wire with 100 μs diameter is shown in Fig. 2-13.

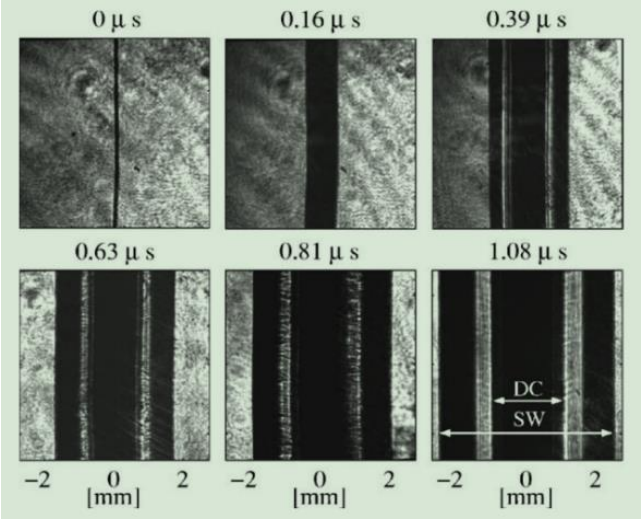

Figure 2-13. Shadow frames obtained for a discharge channel by electrically exploding a 50 mm long, and 100 μs diameter Cu wire using a negative, – 110 kV, voltage impulse. (Picture taken from [36]).

The magnitude (peak pressure) of the shock wave generated by wire-guided discharge depends on discharge circuit parameters and the wire configuration [67, 68]. The shock wave is generated as a result of the energy deposited into wire, thus, the discharge circuit parameters have significant influence on its magnitude. For example, in [67], microsecond and nanosecond voltage impulses, with energy of 4.5 kJ and 0.7 kJ respectively, were used to explode wires in water. It was found that the pressure of the shock wave obtained by wire-guided discharges showed almost a linear proportionality to the energy dissipated per unit length of wire. It was concluded that the energy density and the resultant shock waves could be substantially increased by increasing power, or energy deposition rate. Similar conclusion was also reached in [68] by using microsecond and sub-microsecond voltage impulses to explode Cu wires in water. It was found that the wire configuration and confinement of shock wave propagation play important role in determining the shock wave pressure. In [68], the shock waves obtained by exploding different wire configurations were obtained using current impulses with magnitude up to 75 kV with ~ 3 μs rise time. These configurations

included a single straight wire, a single zigzag wire, two parallel straight wires, two parallel zigzag wires and two zigzag wires with confined plates. It was found that the minimum shock pressure was ~ 0.55 kbar for the single straight wire configuration, followed by a single zigzag wire configuration produced 1.65 kbar. The maximum shock pressure was obtained for two zigzag wires with confined plates, 5.83 kbar.

2.4 Post-breakdown hydrodynamic and acoustic characteristics of underwater spark discharges

The post-breakdown period of underwater spark discharges can be divided into two stages, the energy deposition stage and the adiabatic expansion stage. The energy deposition stage refers to the stage during which the conductive current is present in the plasma channel formed between electrodes, and electrical energy is dissipated in the channel. Apart from the light emission and heat radiation at the early stage of the breakdown, most of the energy is transferred into the internal (or thermal) energy of the plasma [69]. This thermal energy causes the formation and expansion of a plasma/gas cavity due to an increase in the internal pressure, causing the consequent emission of the pressure impulse (or acoustic impulse). The adiabatic expansion stage refers to the period during which the gas cavity expands in the surrounding liquid. The strongest pressure impulse is emitted at the initial stage of cavity's expansion. All these parameters of the dynamic cavity, in terms of the pressure impulse intensity and the size of the cavity, is closely related to the initial energy injected into the plasma channel by discharging current, which is possible to establish links between the energisation conditions and the cavity dynamics.

2.4.1 Hydrodynamic characteristics of underwater spark discharges

The formation and collapse of a gas/plasma filled cavity between electrodes is one of the major phenomena in the post-breakdown period for underwater spark discharges. After the breakdown between electrodes, a part of the electrical energy from the discharging circuit is delivered into the plasma channel through the Joule heating mechanism. The partition of this amount of energy is governed by the relationship between the plasma resistance and the external circuit resistance. Regarding the high

conductivity of the plasma channel: the resistance of plasma channel between electrodes is relatively small, varying from few tens of milliohms to few Ohms [32], [70], resulting in the large magnitude of the oscillating current. For microsecond spark discharges, the current magnitude can reach thousands of Amperes [35], [71], and the transient power delivered into the plasma channel in is considerable, tens of MWs, [32], [72]. With such high electrical power released into the plasma channel, water near the plasma channel is vaporised to form a gas cavity filled with hot vapour and plasma. The resultant intense pressure inside the gas cavity leads to expansion of the water/gas interface. At the same time, the primary shock wave with magnitude of tens of MPa [73] is emitted into surrounding water. Depending on the energisation source, the energy deposition stage lasts for a few microseconds or even nanoseconds. Afterwards, the cavity enters the adiabatic expansion stage. During this stage, the cavity continues to expand as a result of the internal pressure until it reaches the maximum radius. At this moment, the internal pressure is much lower than the ambient hydrostatic pressure, causing the cavity to collapse. When the cavity reaches its minimum size, the internal pressure becomes high again resulting in the next cycle of expansion, which is accompanied by emission of the secondary shock wave. Several expansion-collapse cycles can be observed (2-3 cycles were registered in [74]). An example of the cavity evolution during the post-breakdown period, recorded for a spark with 720 J in [74], is demonstrated in Fig. 2-14.

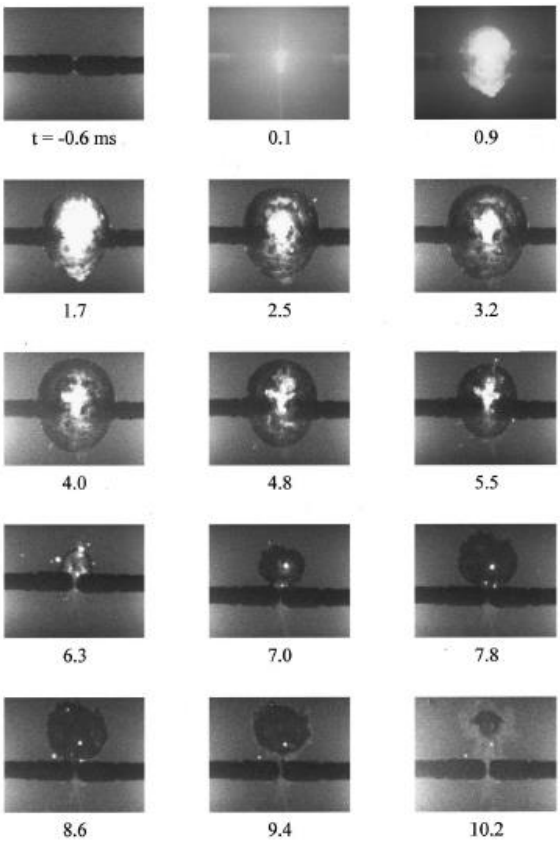

Figure 2-14. Selected frames captured by high-speed camera, Photec 16-mm full-frame rotating prism unit, of the expansion and collapse cycles for a 720 J spark discharge in 2 mm gap in water with conductivity of 0.06 S/m. Frame period: 154 μs. (Picture taken from [74]).

2.4.2 Modelling of cavity's dynamics

There are several models established to describe the dynamics of a transient gas cavity in a fluid, for example, the Rayleigh-Plesset model, Herring's model, Keller's model and the Gilmore model. These models are applicable to fluids with different viscosity, compressibility and density.

2.4.2.1 Rayleigh-Plesset Model

Rayleigh-Plesset (RP) model is the basic model used to describe the dynamic behaviour of a spherical cavity in the fluid with constant density ρ_∞, which is assumed to be incompressible and inviscid. This model was first derived by The Lord Rayleigh in 1917. The derivation of the model was based on the continuity and the momentum equations for a fluid. The gas in the cavity was assumed to be ideal:

$$P_i(t)V(t)^\gamma = constant \tag{2.7}$$

where $P_i(t)$ is the internal (gas) pressure of cavity, $V(t)$ is the volume of the cavity and γ is the ratio of specific heats.

The Rayleigh-Plesset model is given as, [74]:

$$r\ddot{r} + \frac{3}{2}\dot{r}^2 = \frac{1}{\rho_\infty}(P_L(t) - P_\infty - \frac{2\sigma}{r} - \frac{4\mu}{r}\dot{r}) \tag{2.8}$$

where $\dot{r}$ and $\ddot{r}$ are the first and second order derivatives of the time-dependent cavity radius r respectively, $P_L(t)$ is the pressure of the fluid at the cavity's interface and P_∞ is the fluid pressure far from the cavity. σ is the surface tension of the cavity in liquid and μ is the viscosity of the liquid.

2.4.2.2 Other cavity's dynamics models

Apart from the RP model, there are more available models to describe the dynamic oscillation of cavities generated in liquid, such as Herring's model, Keller-Miksis (KM) model and Gilmore's model. These models consider the compressibility of the liquid, where the expansion of the cavity will introduce the emission of acoustic pressure waves. Table. 2-2 shows the conditions in which these models are suitable to be used.

Figure 2-2 Conditions in which Herring's model, KM model and Gilmore's model are suitable to be used

Model	Conditions
Herring's model	Constant speed of sound, c_∞
KM's model	Constant speed of sound, c_∞ Viscosity, μ, with surface tension, σ
Gilmore's model	Pressure-dependent speed of sound, c

Herring's model and KM's model take the constant speed of sound in liquid into consideration. Also, the KM's model includes the viscosity of the liquid and the effect of the surface tension on the gas/water interface. Therefore, these two models are suitable to be used to describe (micro-) cavities with small and medium amplitudes. Detailed discussion of these models is given in [75].

Different from the Herring's model and the KM's model, Gilmore model is aimed to describe the dynamics of the cavity with large amplitude in fluid, which expands and collapses in a compressible fluid. Thus, the Tait's equation of state of this fluid is taken into account in this model. This results in variable speed of sound, which depends on pressure and density of the fluid. The development of this model was discussed in [76], [77]. The fluid density and the speed of sound are assumed to be dependent on the pressure and this dependence is given through the Tait's equation of state included in the enthalpy [78]. Mathematically the cavity dynamics in the Gilmore model is described as:

$$h = n_2 \left(\frac{P_\infty + B}{(n_2 - 1)\rho_\infty}\right)\left[\left(\frac{P_i + B}{P_{\infty + B}}\right)^{\frac{n_2 - 1}{n_2}} - 1\right] \tag{2.9}$$

$$c = c_\infty \left(1 + \frac{n_2 - 1}{{c_\infty}^2} h\right)^{1/2} \tag{2.10}$$

$$r\ddot{r}\left(1 - \frac{\dot{r}}{c}\right) + \frac{3}{2}\dot{r}^2\left(1 - \frac{\dot{r}}{3c}\right) = h\left(1 + \frac{\dot{r}}{c}\right) + \frac{r}{c} + \dot{h}\left(1 - \frac{\dot{r}}{c}\right) \tag{2.11}$$

where c and P_i are the pressure-dependent speed of sound at the gas/water interface and the gas pressure inside the cavity. h is the enthalpy difference of the liquid content (at the gas/water interface) at the pressure P_i and P_∞. c_∞ is the undisturbed speed of sound of the liquid. n_2 and B are constants used to calculate the local speed of sound, c, and were given as $n_2 = 7$ and $B = 3000$ atm by Gilmore [78]. More detailed description of this model will be given in Section 7.1.2.

The Gilmore model is suitable for description of a post-breakdown gas/plasma cavity in the case of underwater spark discharges with high enough energisation level. By considering the initial dynamic process of a high peak electrical power release in the plasma, the gas/water interface of the formed cavity could experience an intensive acceleration, resulting in the potential distortion of the water content in vicinity of the plasma channel. In this case, the water would be treated as a compressible liquid and the local speed of sound is considered to be pressure-dependent. As compared with this intense expansion of the cavity, the surface tension on the gas/water interface and viscosity of the water are not taken into consideration in the Gilmore's model. The feasibility of this model for description of the post-breakdown cavity dynamics was discussed in [35].

2.4.3 Acoustic emission by underwater spark discharges

Emission of acoustic impulses is an important phenomenon during the post-breakdown period of underwater spark discharges. Due to the large electrical power delivered by the conductive current, the thermalized plasma is formed in the cavity. As discussed in Section 2.4.3, the cavity expands and emits an intense pressure impulse. The magnitude of this pressure impulse depends on the energy available at breakdown and on the topology of the plasma-acoustic source (the length of the inter-electrode gap [35]). The acoustic impulse profile may show few oscillating cycles with a decaying envelope. Examples of typical waveforms of the pressure impulses registered by the acoustic transducer in [73], [79] are shown in Fig. 2-15 and Fig. 2-16.

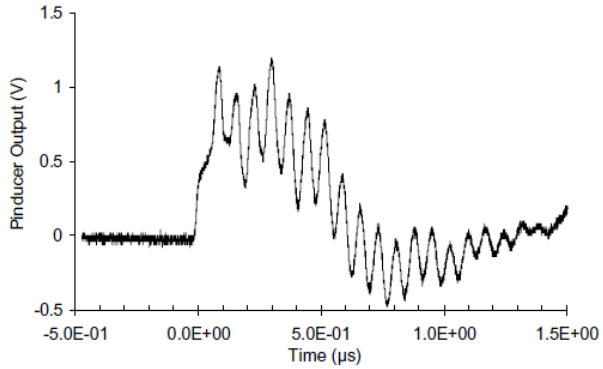

Figure 2-15. Output signal of Pinducer acoustic sensor for a shock wave generated in a 5 mm gap using 60 nF capacitive voltage in domestic tap water. (Picture taken from [79]).

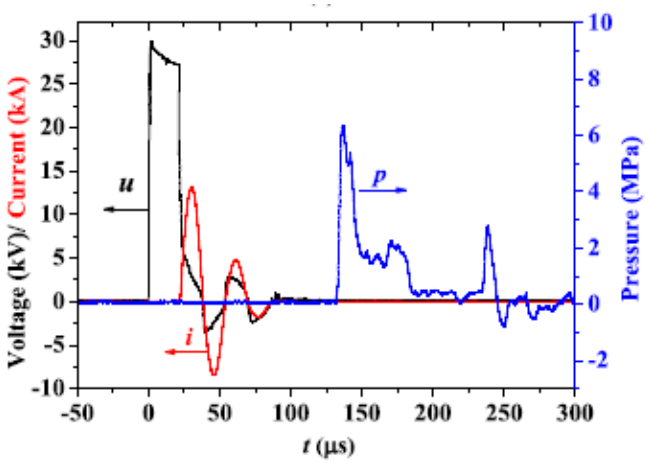

Figure 2-16. Example waveforms of voltage (black), current (red) and shock wave (blue) obtained for a discharge with pin to pin electrodes in a 15 mm inter-electrode gap (Voltage and capacitance: 30 kV, 3 µF; conductivity of water: 144.8 µS/cm), (Picture taken from [73]).

The initial strength of the impulsive pressure waves is intense (with magnitude up to few tens of MPa measured at 10 cm away from the source in [73]). Thus, this impulse can break the local sonic propagation limit and is considered to be a shock wave at distances close to the spark source [35], [79], [80]. However, it quickly develops into

a spherical acoustic impulse propagating outwards the source with a speed of sound. Fig. 2-17 shows an example of the time resolved shadowgraph visualization of the propagation of acoustic impulses, conducted in [80].

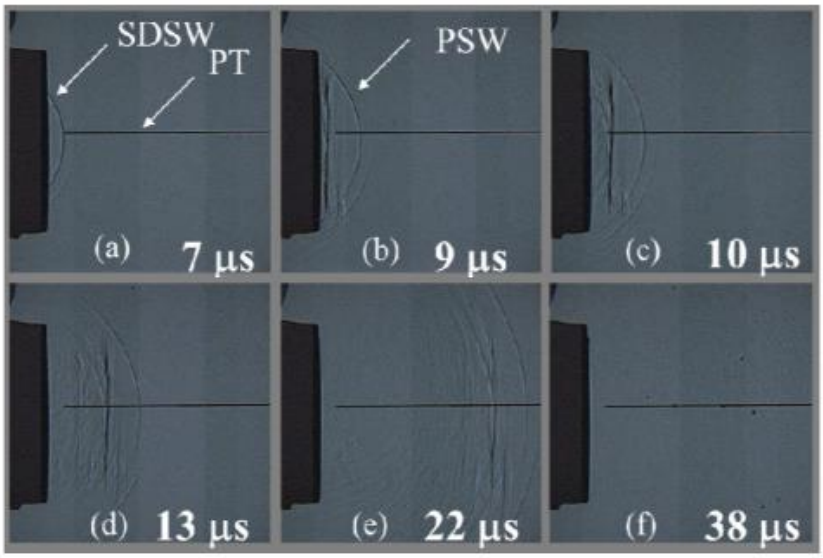

Figure 2-17. Shadowgraphs of parallel shock wave: SDSW, spherical diverging shock wave; PSW, parallel shock wave; PT, pressure transducer. High-speed camera, ULTRA Cam HS-106E, with frame rate 1.25 MHz. Conductivity of water: 62.5 μS/cm. (Picture taken from [80]).

The evolution of the pressure impulse introduced above only refers to a primary acoustic impulse emitted at the start of a cavity oscillation cycle. As discussed in Section 2.4.1, two to three complete cavity oscillation cycles may be observed. Therefore, the corresponding number of pressure impulses will also be expected to emit before the cavity stops its oscillation. An example of the successive pressure impulses emitted by the cavity in a single spark discharge is shown in Fig. 2-18. The solid line indicates the acoustic waveform captured by the acoustic sensor [81]. The primary pulse refers to the acoustic impulse emitted at the formation of the cavity and the secondary one refers to the acoustic impulse emitted at the collapse of the cavity. Due to the energy consumption of the cavity for each oscillation, the magnitude of the following pressure impulse is always weaker than previous one. It is worthy of note that there is a rarefaction pulse between two pulses [81].

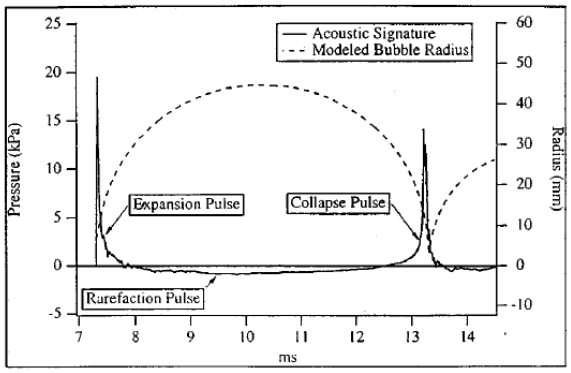

Figure 2-18. Example of measured acoustic signature showing shock waves generated by cavity expansion and collapse. (Picture taken from [81]).

2.4.4 Acoustic parameters

An acoustic impulse generated by the underwater spark discharges is a longitudinal mechanical wave propagating in a dense medium, water. Therefore, the propagation of the pressure impulse generated by the underwater spark discharges is expected to follow the established theories for the acoustic impulse and in many cases can be described by using the spherical acoustic wave model.

The propagation of a mechanical wave is characterised by the wave velocity and the acoustic pressure. The intrinsic properties of the medium, such as the density, ρ_∞, and the compressibility, χ_c, defines the acoustic propagation velocity, c_∞:

$$c_\infty = \sqrt{\frac{1}{x_c \rho_\infty}} \tag{2.12}$$

For water, the acoustic velocity is ~ 1500 m/s.

2.4.4.1 Wave equation

The linear wave equation describes the simplest propagation pattern of a mechanical wave. The general wave equation for the acoustic (pressure) plane waves in condensed media is given as, [76]:

$$\frac{\partial^2 p}{\partial x^2} + \frac{\partial^2 p}{\partial y^2} + \frac{\partial^2 p}{\partial z^2} = \frac{1}{c_\infty{}^2} \frac{\partial^2 p}{\partial t^2} \tag{2.13}$$

where p is the time-dependent acoustic pressure at any arbitrary point with coordinates (x,y,z); c_∞ is the local speed of sound. Speed of sound is the speed of the wave, which propagates in the media. This equation assumes that the density of media is constant.

For the case of a plane wave with a constant speed c_∞, a relationship between the particle velocities and pressure can be established, [76]:

$$p = \rho_\infty c_\infty v \tag{2.14}$$

where v is the particle velocity.

Equation (2.14) reveals the fact that the acoustic pressure depends on not only the particle movement but also on the nature of the medium. The term, $z_{ac} = \rho_\infty c_\infty$, is called the characteristic acoustic impedance, which defines the pressure reaction to the motion of particles.

The acoustic intensity for the wave is given as, [76]:

$$I_{ac} = \frac{p_{acoustic}{}^2}{z_{ac}} = \frac{p_{acoustic}{}^2}{\rho_\infty c_\infty} \tag{2.15}$$

where $P_{acoustic}$ is magnitude of the acoustic pressure. The acoustic intensity is in a unit of J/(m^{2}s). Therefore, the acoustic energy can be calculated by:

$$E_{ac} = F \int I_{ac} dt \tag{2.16}$$

where F is the surface area of the wave.

2.4.4.2 Spherical wave

The spherical wave is initiated from a point source and propagates spherically outwards this source. The propagation of a special wave is spatial and multi-directional. For a known observation position, the acoustic intensity and the energy of a spherical wave can be calculated using (2.15) and (2.16). The acoustic energy of a spherical wave can be calculated as, [81]:

$$E_{ac-sph} = F \int \frac{P_{acoustic}(d,t)^2}{\rho_\infty c_\infty} dt \quad (2.17)$$

$$F = 4\pi d^2 \quad (2.18)$$

where $P_{acoustic}(d, t)$ is the acoustic pressure at distance, d, and moment, t, and p_∞ is the ambient hydrostatic pressure.

2.5 Underwater spark discharges: Pulsed power driving circuits

The usability of the acoustic impulses generated by the underwater spark discharges in practical applications has drawn substantial attention since its discovery in the last few decades. Compared with other methods of generation of pressure impulses in water by using chemical explosives, the underwater spark discharges have important advantages as it provides better controllability and reproducibility. Also, it is environmental-friendly as it does not produces pollutant. The acoustic impulses generated by the underwater spark discharges are used in some industrial and environmental applications. Details and examples of some practical applications have been introduced in Chapter 1.

There are several aspects involved in this area, which requires attention, for example, the construction of the spark generation system and the dependency of the acoustic impulses on the discharging circuit. These aspects put forward a general question as how to generate desirable acoustic impulses by using optimal system in terms of the physical configuration and the energisation conditions.

A typical spark generation system consists of two parts, the voltage impulse generation system (pulsed power driving circuit) and the electrode topology. The

general form of the pulse power system is a capacitive pulse driving system, which includes a charging part and a power release (discharging) part. The electrode topology refers to the configuration of HV electrodes and the structure of the electrodes in terms of their shape and material.

2.5.1 Practical voltage impulse generation system

Typically, the high power voltage impulses used for development of spark discharges in water are generated by a pulse driving system based on the capacitive energy storage. The basic approach is to release electrical energy into the load within a relatively short period, usually in millisecond and microsecond ranges or sometimes in nanosecond range. The generation of a high voltage (HV) voltage impulse is a three-stage process, which includes charging capacitors, closing the gap switch and releasing the voltage impulse. The energy storage capacitor(s) are charged by a conventional high voltage DC power supply (or using an AC power supply together with a rectifier as in [32]) through a large (usually in MΩ) charging resistor for safety considerations. Then, by closing the spark gap switch, the energy stored in capacitors is released into the load.

The following parameters of a voltage impulse should be considered: voltage level, rise time, pulse duration and electrical energy per pulse. These properties of a voltage impulse are related to the selection of the capacitance, discharging resistance, triggering switch and circuit configuration. For different requirements, there are several available configurations for voltage impulse generation system.

2.5.1.1 Capacitive energy storage

A typical capacitive based pulsed power system consists of a HV DC power supply and a capacitor bank. The circuit is controlled by a plasma closing switch. The achievable peak voltage level of this configuration is determined by the charging voltage, which is usually in the range from a few kV to tens of kV for commercial systems. The capacitance of the circuit may consists of several capacitors connected in parallel. Therefore, this configuration is suitable to generate voltage impulse with magnitude from few kV to tens of kV and with long pulse duration (in the scale of microsecond and millisecond). An example schematic diagram of the parallel capacitor

bank pulse driving system [82] is shown in Fig. 2-19.

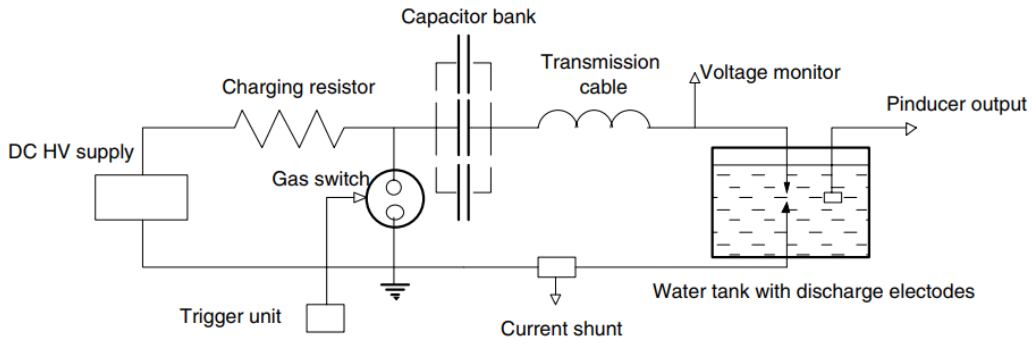

Figure 2-19. Example of schematic diagram capacitive voltage generation system used for underwater spark discharges. (Picture taken from [82]).

This pulse power system was developed by Timoshkin in [82] to conduct the investigation on the acoustic emission by underwater spark discharges. The capacitance used varied from 0.266 to 1.590 μF and the applied voltage could reach up to 35kV, resulting in the energy per pulse ranging from few J/pulse up to 1 kJ/pulse.

2.5.1.2 Marx high voltage impulsive generator

Marx generator is designed for voltage multiplication, by charging capacitors connected in parallel and discharging them in series. The voltage multiplication equals to the number of capacitors (charging stages). The Marx generator is suitable to produce short high voltage impulses with large peak magnitude (from hundreds of kV to a few MV). For example, a Marx generator was used for generation of HV impulses with magnitude up to ~ 460 kV to achieve electrical discharges between large gaps (tens of cm) in mineral oil in [83].

2.5.2 Topology of electrodes

The design of the electrode topology should be suitable to initiate the streamer's formation and propagation to achieve a successful breakdown between electrodes. As introduced in Section 2.2, the distribution of the electrical field is important to initiate streamers' formation and spark generation, as high electrical field strength is required to form a complete plasma channel. Therefore, topologies with almost uniform electrical field are not preferred.

The importance of an inhomogeneous electrical field has been enhanced in [57]. Therefore, electrode topologies, such as point/rod/sphere-to-plane and pin/rod/sphere-to-pin/rod/sphere, are commonly used for generation of underwater spark discharges [56]-[59], [69]-[73], In practical systems [16]-[19], due to their ability to produce inhomogeneous electrical field, these topologies result in the significant electrical field enhancement. Fig. 2-20 shows an example of the field enhancement effect in a point-like electrode topology [84]. It is shown that the electrical field is enhanced by an order of 3, as compared with the average field, E_0. The field enhancement increases with an increase in tip sharpness and with the decrease in electrode separation.

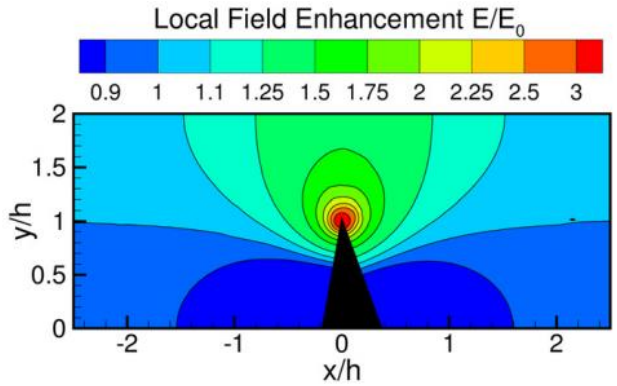

Figure 2-20. Example of contours of the field enhancement factor induced by a sharp asperity, solved using Schwarz–Christoffel transformation. *y/h* and *x/h* are dimensionless scale of the asperity. (Picture taken from [84]).

In order to achieve spark discharges in longer gaps, different approaches can be taken. It is not always practical to increase the magnitude of voltage impulses. Alternative approaches may include laser-triggering technique [85], [86], artificial bubble

injection [87], [88], electrical explosion of metallic wire [73], [89] and electrical explosion of chemical compound [25]. The gas bubble injection into the inter-electrode gap and the use of exploding wire are chosen in this work to initiate underwater sparks in order to investigate their acoustic performance.

2.5.2.1 Free self-triggering electrode topology

The 'free' self-triggering topology is the most common configuration used to achieve underwater spark discharges [2]-[4], [56]-[59], [69]-[72]. It is also often used to study development of the streamers in water [90]. The term 'free' refers to the free propagation path of the streamer from HV electrode to the ground electrode. The structure of this electrode topology is a pair of electrodes without any external triggering system(s). Fig. 2-21 shows an example of the free electrode topology used to monitor the pressure impulses during streamer propagation in water, [90].

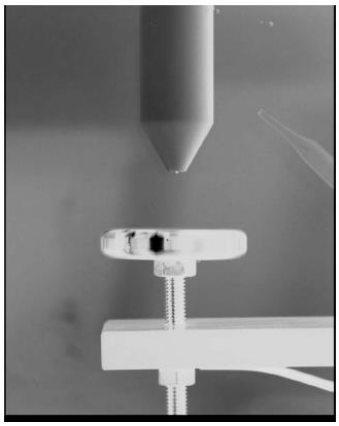

Figure 2-21. Example of a point-to-plane electrode topology for spark discharge with free plasma development path. (Picture taken from [90]).

This electrode topology allows changes in electrode separation and is 'ideal' for repetitive discharge operation. However, as mentioned above, a potential issue is the limited length of the inter-electrode gap for successful breakdowns in this

configuration. Another factor, which is difficult to control in the case of free discharges, is the path of the breakdown channel. An example of discharges with different paths between two electrodes in water are shown in Fig. 2-22, [32].

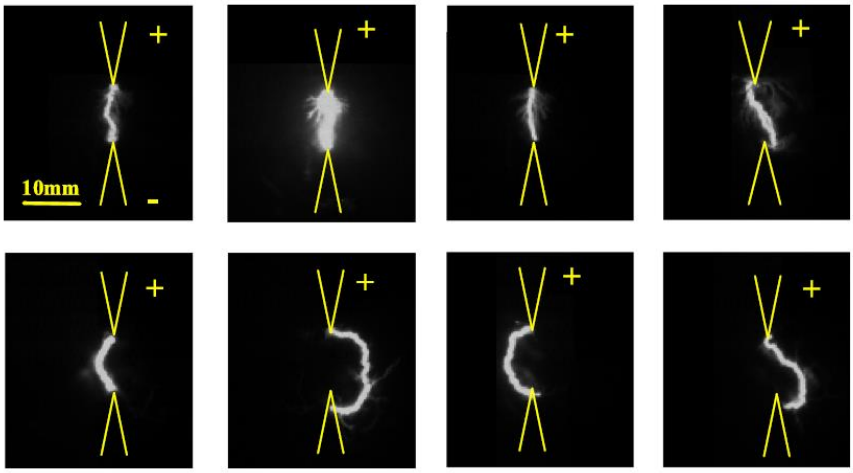

Figure 2-22. Imagines of various shapes of plasma channel, recorded using high-speed camera (Photron FASTCAM SA5) with 3 μs/frame and exposure time to be 0.37 μs. (Capacitance: 3μF; conductivity of water: 144.8 μS/cm). (Picture taken from [32]).

In an ideal case, the streamer develops a straight path from the HV electrode to the ground electrode. The randomness of the developed plasma channel between 'free' electrodes in practical cases increases the probability of energy consumption during streamer propagation, resulting in longer pre-breakdown time lag (time interval from the application of voltage impulse to breakdown). With further separation of electrodes, the randomness degree of the plasma channel path increases and unreliable performance of the underwater spark discharges in terms of generation of acoustic impulses can be expected. Therefore, in order to achieve stable and efficient acoustic emission in long inter-electrode gaps, modification on the electrode configuration is required.

2.5.2.2 Air-bubble stimulated electrode topology

The presence of gas bubble(s) in the inter-electrode gap can be critical for breakdown initiation [39]-[41], [91]-[96]. As introduced in Section 2.2.1, the direct streamer initiation by the electrostriction process is difficult to achieve unless voltage impulses with ns and sub-ns duration are used. For longer voltage impulses with microsecond duration, the formed gas bubble in the vicinity of the HV electrode provides a low-density region for streamer initiation and propagation in the enhanced electrical field within the bubble. In [91], the bubbled breakdown initiation mechanism has been visualized and an example is shown in Fig. 2-23. The bubble near the HV electrode acts as a 'shortcut' for the streamer, which propagates along the bubble/liquid surface interface.

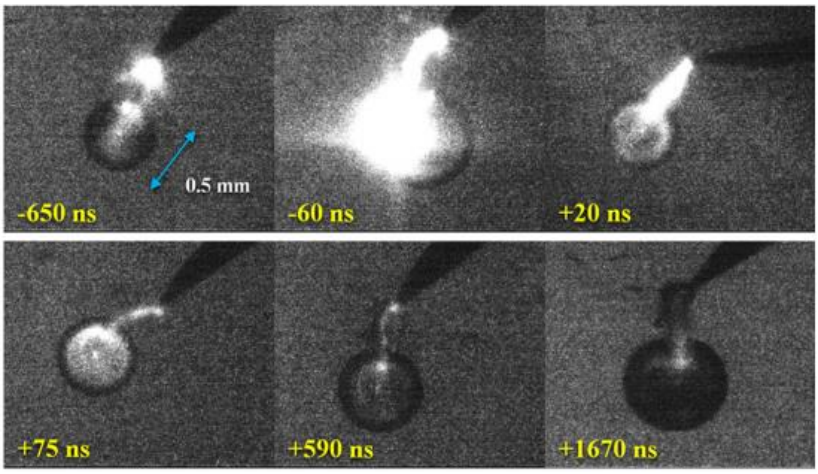

Figure 2-23. Development of the streamer along the bubble surface within 2μs during a breakdown event. Imagines obtained using ICCD camera. (Voltage: ~ 12 kV, conductivity of water: ~ 10 μS/cm to ~ 20 μS/cm). (Picture taken from [91]).

The importance of gas bubbles in decreasing of the breakdown voltage was investigated in [93]. It was reported that the initiation voltage for underwater spark discharges has decreased by ~ 25 % - ~ 50 % in the case of injection of bubbles as compared with the breakdown without gas bubbles. Low breakdown field in the presence of bubbles has been confirmed in [88]. Hamdan [87] used the injected gas

bubbles (Ar, CO_2, CH_4, C_3H_8) to promote the breakdown in distilled water. Therefore, to keep the breakdown voltage at a relatively low level in water for long inter-electrode gaps, gas bubbles can be injected between the electrodes.

2.5.2.3 Wire-guided electrode topology

The wire-guided electrode configuration is another promising method for generation of underwater spark discharges. It helps to produce stronger acoustic impulses and to achieve better acoustic efficiency in relatively long inter-electrode gaps. Therefore, wire-guided spark discharges are used in many applications [97] - [99]. The wire-guided spark discharge is implemented by electrically exploding a metallic wire fixed between the electrodes to directly form a plasma channel without relying on the streamer breakdown mechanism. The thin wire placed between electrodes melts and disintegrates into metal droplets, generating a channel filled with metal/water vapour. After wire disintegration, the circuit is open, resulting in the collapse of previous conductive current and the re-establishment of voltage across the inter-electrode gap. The presence of metallic droplets facilities the electron multiplication process between them and the plasma is formed through the channel, completing the breakdown. Then the electrical energy stored in the capacitor is released into the plasma channel. Thus, the gas cavity is formed. This gas cavity drives an acoustic impulse into water. An example of shadow imaging of exploding wire is shown in Fig. 2-24, [68].

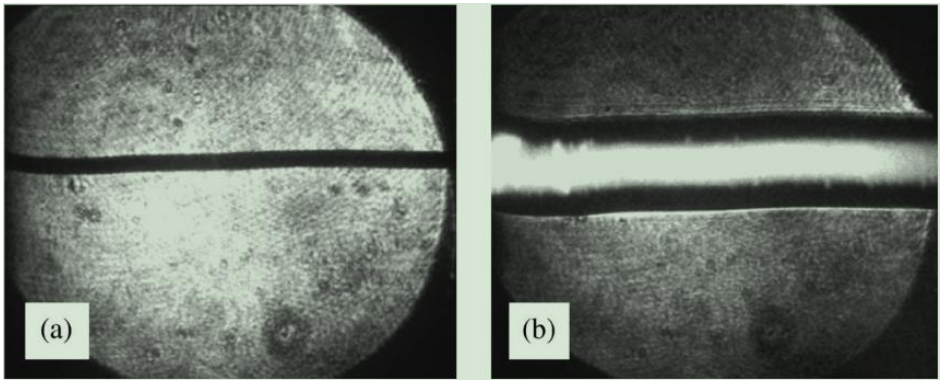

Figure 2-24. Shadow imaging of explosion of a Cu wire with 130 mm length and 0.4 mm diameter in tap water: (a) before explosion (b) ~1.5 μs after applied discharge current. Imagines obtained using fast-framing 4Quick05A camera with frame duration as 10 ns. (Current pulse: $I < 75$ kA with ~ 3 μs rise time). (Picture taken from [68]).

According to [89], the energy used for the wire disintegration only accounts for a small part of the total electrical energy stored in the circuit, depending on the length, diameter and melting energy of chosen metal. The remaining part of the electrical energy is released in the plasma channel. By using this wire-guided mechanism, the pre-breakdown time can be reduced significantly and the potential breakdown voltage will be relatively low. The magnitude of the shock wave generated by wire-guided discharges could reach ~ 1 GPa [100], and even ~ 400 GPa [101]. The energy transformation efficiency for this breakdown mechanism was found to be ~ 24 % [64] and can reach ~ (40 % - 50 %) [102]. The stability and consistency of the spark discharge performance is also enhanced by the wire-guided mechanism.

2.5.3 Modelling of pulsed power circuits

2.5.3.1 Dynamic resistance of the plasma channel

The development of the plasma channel is a complex and dynamic process. The time-dependent plasma resistance is a function of different parameters of the spark channel, such as its temperature, composition, the length of the channel. Therefore, corresponding to the dynamic process of the plasma channel development after the breakdown over time, its resistance is also time-dependent. Variation of the plasma

resistance over discharge period has been investigated and discussed in [103]-[109]. An example of the experimental plasma resistance over a period of 150 μs, conducted in [110], is shown in Fig. 2-25. The initial resistance between the electrodes before the complete breakdown is very high. After the plasma channel bridges the electrodes, a conductive current appears and energy is dissipated in the channel. The plasma thermalizes and the initial large resistance drops to its minimum value rapidly, within the first half or even quarter cycle of the current oscillation [110]. With the decrease of the current magnitude, the plasma channel is cooling down, resulting in the regrowth of the plasma resistance until the disappearance of current.

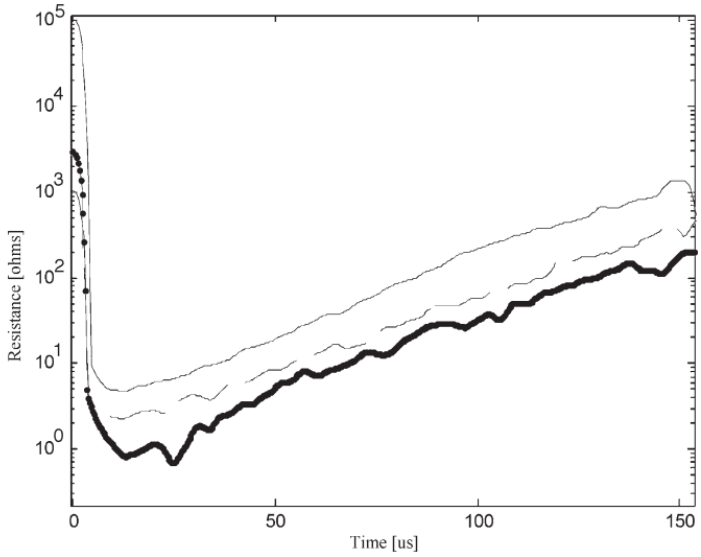

Figure 2-25. Examples of dynamic plasma resistance in 150 μs after breakdown for (solid line) peak current 0.62 kA, (dashed line) peak current 1.3 kA and (bold solid line) peak current 2.21 kA. Discharges obtained in a 12.8 cm air gap using output voltage ~ 300 kV to ~ 1 MV. (Picture taken from [110]).

To describe the time-dependent behaviour of the resistance of the spark breakdown channel, analytical models have been developed by several researchers, including Barannik [111], Demenik [112], Kushner [109], Rompe and Weizel (RW) [113], Toeple [114] and Vlastos [105]. Comparison between these models has been conducted in [110]. Among these approaches, the RW model is widely used for description of the resistance of spark discharges and has been proven to be effective in adequate

prediction of the transient spark resistance [108], [110], [115]. It relates the plasma resistance to the length of the plasma channel, *l*, and the discharging current, *I(t)*, which was developed based on the energy balance for the spark channel, [113]:

$$R_{plasma}(t) = \sqrt{2P_0 c_{co}} \cdot \frac{l}{\left(\int_0^t I(t)^2 dt\right)^{n_1}} \qquad (2.19)$$

where P_0 and c_{co} are the initial pressure of gas and model constant respectively; the model constant is a function of the electron temperature, electron mobility and ionisation potential and it was considered to be constant in a specific range of experimental conditions in [110]. The power coefficient, n_1, is equal to 1/2 in RW model and is 3/5 in Vlastos's energy equation model [105]. For both values of n_1 =1/2 and n_1 = 3/5, model (2.19) was used in [108], [115] to fit the transient spark resistance in air obtained from experimental data and have showed a reasonable agreement. Fig. 2-26 demonstrates an example of the comparison between the experimental data of a transient arc resistance generated by Marx generator and the fitting result of the RW model with n_1 = 1/2 in [110].

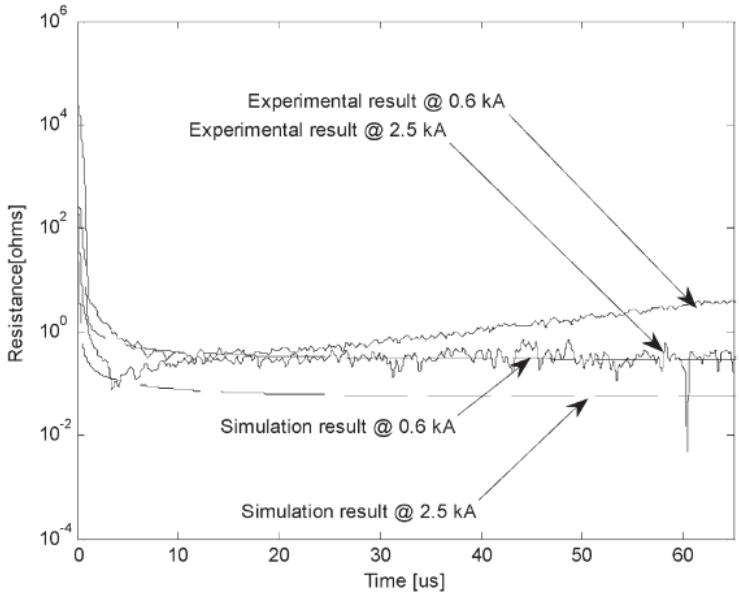

Figure 2-26. The comparison between the experimental results and computed results of the dynamic plasma resistance using Rompe and Weizel model (2.19) with $n_1 = 1/2$ for two discharges in 12.8 cm air gap with peak current 0.6 kA and 2.5 kA respectively. (Picture taken from [110]).

Although the RW model was originally developed for plasma channel in air, it only takes the energy delivered into the plasma channel into consideration. Therefore, the RW model can be applicable to the spark discharges in liquid. For example, in a case of spark in liquid hydrocarbons [115], Fehr and Schmidt successfully used (2.19) with $n_1 = 1/2$ to describe the transient resistance of the breakdown channel.

2.5.3.2 Discharge circuit with constant plasma resistance

The time-dependent behaviour of the plasma resistance demonstrates two significant regions in which initial significant decrease is followed by a relatively slow increase as shown in Fig. 2-27. The resistance in the second region increases almost linearly with time although some fluctuations are observed. By looking at the entire second region, the variation in the plasma resistance is not significant. This observation leads to a possibility to represent the plasma resistance with a constant value. This constant resistance can be obtained using the assumption that the constant resistance will result

in the release of the same amount of energy into the plasma as in the practical case of time-dependent plasma resistance. The constant plasma resistance model has been used in many papers [70], [71], [73], [82] in the analysis of the discharge processes.

The pulsed driving system used for impulsive breakdown studies consists of the energy storage capacitor bank, transmission line(s), spark plasma closing switch and the spark discharge (load) electrodes. This pulsed power driving circuit can be represented by lumped elements connected in series: capacitance, inductance and resistance, as a typical RLC circuit. It is worthy of note that the insignificant capacitance related to the discharging electrodes is negligible as compared with the main energy storage capacitance, [54]. The transmission line and the plasma channel contribute to the resistance and inductance of the circuit. Therefore, this RLC discharging circuit can be electrically solved by the Kirchhoff's law, which follows a second-order equation:

$$\frac{1}{C}\int I(t)dt + L\frac{dI(t)}{dt} + I(t)R = 0 \qquad (2.20)$$

where *I(t)* is the discharging current; *C, L, R* are the total capacitance, inductance and resistance of the circuit respectively. *R* is the combination of circuit resistance and the plasma resistance, which is given by:

$$R = R_{circuit} + R_{pl} \qquad (2.21)$$

Therefore, the time-dependent solution of the circuit can be calculated as, [82]:

$$I(t) = I_0 e^{-\alpha t}\sin(\omega t) \qquad (2.22)$$

$$I_0 = V_{bd}C\left(\frac{\alpha^2}{\omega} + \omega\right),\ \omega = \sqrt{\frac{1}{LC} - \frac{1}{\alpha^2}},\ \alpha = \frac{R}{2L} \qquad (2.23)$$

Followed by the extraction of the constant plasma resistance, the energy delivered into the plasma channel (as integration of the electrical power) is given by:

$$E_{pl}(t) = {R_{pl}}^2 \int_0^t I(t)^2 dt \quad (2.24)$$

The RLC circuit solution given by (2.22)-(2.23) have been used to fit the experimental discharge current waveform in [35], [73], [79], [82]. In these papers, it was shown that the calculated current waveform by (2.22) showed a good agreement with the experimental data and (2.24) was used in analysis of energy partition, verifying the feasibility of this approach in modelling the post-breakdown discharge circuit for underwater spark discharges.

2.6 Conclusions

Chapter 2 introduced the fundamental concepts of breakdown in fluids. The basic concepts of the Townsend avalanche discharge, streamer formation and propagation are discussed. These processes are considered to be involved as pre-breakdown mechanisms in the spark formation in water.

An overview of the discharge initiation processes in water is given. Different mechanisms of the streamer formation and propagation are discussed depending on energisation polarity and other parameters of HV impulses. A series of phenomena accompanying the streamer formation and development are also discussed based on examples of visualization of pre-breakdown process in water stressed with HV impulses with positive and negative polarities. The important role of the gas nano- and micro-bubbles formed in/near the HV electrode in water in initiation of streamers is emphasized. This analysis provides a basis for modification and optimisation of pulsed driving circuits and electrode topologies of underwater spark generation system to promote the successful breakdown under different conditions.

The discussion of post-breakdown plasma/gas cavity formation and evolution and emission of acoustic impulses is presented. Several models, which describe the cavity oscillation, are introduced and discussed in this chapter. An analysis of parameters and characteristics of the acoustic impulses is provided, allowing calculation of acoustic energy and analysis of the energy partition in the discharge. It was found that the acoustic magnitude is proportional to the length of the plasma channel, thus longer underwater sparks produces stronger pressure impulses. This analysis demonstrates an

importance of optimisation of the spark generation system for generation of the desirable acoustic impulses.

In order to effectively generate spark discharges in water, the basic pulsed power systems including capacitive energy storage pulsed driving circuit and Marx generator are discussed in this chapter. A detailed discussion and analysis of the advantages and limitations of different electrode topologies used to generate spark discharges in water is presented. Based on the literature information on the streamer development mechanisms, three electrode configurations, a topology for free self-triggering discharges, a topology with bubble injection and wire-guided topology are introduced. Two of these topologies (air-bubble stimulated discharges topology, and wire-guided discharges topology) will help to increase the inter-electrode gap at the same energisation parameters as compared with free self-triggering discharges. These three electrode topologies (free electrode topology, wire-guided topology and topology with injected bubbles) will be investigated comprehensively in following experimental chapters. Their performance in generating acoustic impulses will be studies and analysed. Links between the acoustic parameters and circuit energisation parameters are also proposed, which is crucial for the optimisation of these spark systems in their practical utilization.

For analytical analysis of underwater spark discharges, the method of modelling of the discharge circuit is introduced. The transient plasma resistance is discussed and the concept of the constant plasma resistance is introduced. For the purpose of the study present in this work, modelling of the pulsed driving circuit and the underwater plasma channel is achieved using the lumped parameters of the RLC circuit with a constant plasma resistance. The validity of this approach for engineering description of the practical underwater spark discharges is presented.

3 Design and development of the pulsed power and diagnostic systems for investigation of characteristics of underwater spark discharges

One of the defining factors in generation of underwater acoustic impulses is the topology of the underwater spark discharge generation system. A complete underwater spark discharge system, as introduced in Section 2.5, contains a voltage impulse generation system and a set of electrodes. The aim of this work is to investigate the breakdown characteristics and corresponding acoustic parameters of underwater spark discharges initiated by different mechanisms. Three electrode topologies are chosen for this study, including the free self-triggering discharges (FD's), the air-bubble stimulated discharges (ABSD's) and the wire-guided discharges (WGD's).

This chapter discusses and presents the design and the development of the experimental set-up used to generate underwater spark discharges and to conduct the experimental measurements. In the present work, a capacitive system was built to generate microsecond voltage impulses. Different values of capacitance and charging voltage have been used in the tests in order to create multi-levels of energisation conditions. Similar pulsed power driving circuit was also used in previous studies [35], [82]. The voltage and current waveforms during the discharge process were obtained by a high voltage probe and a resistive current shunt. The acoustic waveforms generated by underwater spark discharges were obtained by a piezo-electric acoustic sensor. Different electrode sets were designed for each type of initiation mechanism. The distance between the electrodes' tips was varying from 5 mm to 75 mm to study the acoustic generation in different scenarios (combinations of energisation levels and inter-electrode gaps).

For carrying out a comparison between different parameters of underwater spark discharges by three initiation methods, the energisation conditions selected for all tests have to be identical. Therefore, the same energy storage (voltage impulses generation system) and diagnostic system were used throughout this experimental work.

3.1 Design of the pulsed power driving circuit

The voltage impulse generation system built in the present work consists of a HV DC power supply, a series of charging resistors, a bank of storage capacitance, a manually-triggered spark-gap switch. The schematic diagram of the pulsed power driving circuit is shown in Fig. 3-1. This particular system is aimed to provide microsecond voltage impulses with adjustable magnitude and energy level. The HV DC power supply charges the storage capacitance to the pre-set voltage level by a stable output current through the charging resistors' bank. Afterwards, the spark-gap switch is closed by tester, resulting in a voltage impulse applied to the HV electrode. Once a complete plasma channel is formed between electrodes, spark breakdown occurs and the energy stored in capacitors is released into the conductive plasma channel. The total energy per impulse is determined by the charging voltage and storage capacitance as $CV_{ch}^2/2$. The detailed discussion of electrical parameters of the devices used in the voltage impulse generation system will be provided in the following section.

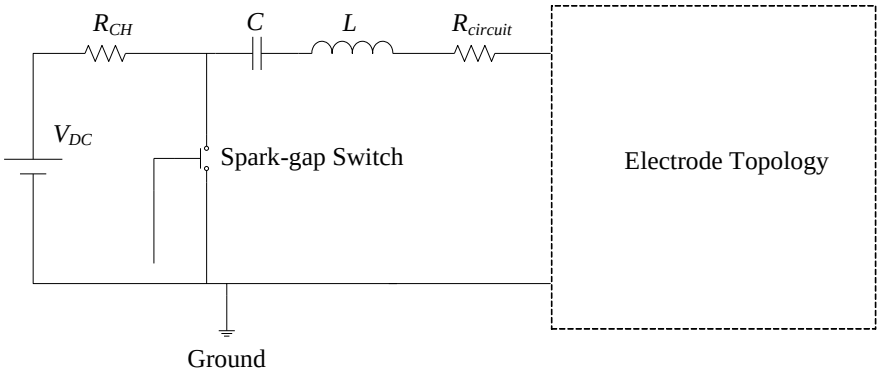

Figure 3-1. The schematic diagram of the voltage impulse generation system, consisting of: the DC voltage power supply, V_{DC}; the charging resistor bank, R_{CH}; the storage capacitor bank, C; the circuit inductance, L; the circuit resistance, $R_{circuit}$; the manually-triggered spark-gap switch.

3.1.1 HV DC power supply

The HV DC power supply was manufactured by GLASSMAN HIGH VOLTAGE, INC. with model number PS/EH60R01.5-22. This particular DC power model is capable of generating both positive and negative voltage with magnitude up to 60 kV; this output voltage was supplied to the capacitor(s) bank using RG-8U output HV cable.

3.1.2 Charging resistor

The charging resistor stack consists of 120 single MEGGITT CGS resistors (model SBCHE15). The resistance value of each individual resistor in the stack is 4.7 kΩ with 5% tolerance. Therefore, the total resistance of the charging resistor is ~ 0.56 MΩ.

3.1.3 Storage capacitance

The energy storage capacitances of the voltage impulse generation system used in the tests were 160 nF, 280 nF and 560 nF. These values of the capacitor(s) bank were given by three combinations of four individual HV capacitors, including two identical smaller ones and two identical larger ones in terms of their capacitances. These capacitors were made by Maxwell Laboratory Ltd, U.S.A. The catalogue number of the two small capacitors is 31190 with a nominal capacitance of 80 nF and maximum operating voltage of 100 kV; the catalogue number of two larger capacitors is 31857 with nominal capacitance of 280 nF with the maximum operating voltage of 65 kV. In the following mathematical analysis, the practical capacitance values of these capacitors were used: 77 nF, 78 nF, 266 nF and 267 nF. These values were obtained by using a VideoBridge 2160 (ES1-2160, Electro Scientific Instruments). Therefore, the actual values of capacitance used in the voltage impulse generation system for the tests were 155 nF, 266 nF and 533 nF.

3.1.4 Spark-gap switch

The spark-gap switch was made up of two brass balls and a circular brass plate, which were located within a transparent cylindrical nylon container. The two brass balls (with a diameter of 17 mm) were installed on the middle position of the wall inside the container and separated by 55 mm to avoid self-spark between them when applying a high voltage impulse. The circular brass plate was tied with a rope through its centre point and was placed at the bottom of the container; the rope was inserted passing through the top cap of the container for manual control. Once the rope is pulled up after capacitors get charged, the brass plate will rise and get in contact with the two brass balls and the spark generated between them will automatically close the switch.

3.1.5 Transmission cable

The high voltage transmission and the grounding cables used in the circuit were both obtained from the coaxial transmission lines. The inner core of the transmission lines, which contains the twisted conduction copper wires and a layer of nylon isolation, was used as the circuit conductor. The cylindrical outer layer of the cable is dense copper mesh, which was used as the grounding connection by being compressed flat.

As mentioned previously, serval energy levels are required to conduct the tests in order to investigate the breakdown characteristics of underwater spark discharges under different conditions. Three charging voltage levels were selected, including 25 kV, 30 kV and 35 kV, with the purpose of covering a wide range of energy levels. Thus, nine energy levels were used in this studied: 48 J, 70 J, 83 J, 120 J, 163 J, 167 J, 240 J and 326 J. Similar energies and charging voltage levels were used in a number of practical applications [22], [35], [79]. Therefore, these energy levels will be used to initiate the breakdown for each inter-electrode gap for all three underwater spark discharge types and the results can be compared with previously-published data on the acoustic, hydrodynamic and electrical parameters of underwater spark discharges, especially for FD's and WGD's.

3.2 Electrical and acoustic diagnostic devices and systems

The direct measurements conducted in the tests included the following electrical, hydrodynamic and acoustic parameters: voltage waveform, *V(t)*, breakdown voltage, V_{br}, current waveform, *I(t)*, acoustic signal waveform, peak acoustic magnitude, $P_{cav\text{-}max}$, and period of the cavity oscillation, T_{cavity}. The voltage across electrodes and the current through plasma channel were obtained by a high voltage probe and a current shunt. The voltage probe was a PVM-5 high voltage probe manufactured by NorthStar USA Inc. The maximum voltage, which can be measured by this HV probe is 100 kV (impulsive regime 80 MHz bandwidth), and 65 kV (steady state voltage). The voltage division ratio is 1000:1 and its input resistance is 400 MΩ. The current probe was a Samtech Ltd DE(CP)-01 resistive current shunt with resistance of 29.6 mΩ, voltage/current (V/A) ratio of 29.6 V/kA, and with a rise time of 3.6 ns.

The acoustic magnitude and the period of the cavity oscillation were obtained from the acoustic signal waveform measured by using a Valpey Fisher Pinducer VP1093 piezoelectric acoustic sensor. It was located 500 mm horizontally away from the spark source (the centre of the inter-electrodes' gap) by being attached on a slim stainless steel stick, which is fixed on a movable metal bar on top of the water tank for alignment between the Pinducer and the spark centre.

All measurement signals from these sensors are voltage signals displayed in unit Volts in oscilloscopes. The current signal can be converted into its original unit (Amperes) by using the V/A ratio. However, due to the fact that the calibration of the Pinducer between voltage and pressure is not given by the manufacturer, the acoustic magnitude will be represented in Volts.

The voltage and current signals were registered by a Tektronix TDS 2024 four-channel digital storage oscilloscope with 200 MHz bandwidth and 2 GS/s sampling rate. The time and voltage axis scales were set as 5 V/division and 20 μs/division in order to record the whole picture of the discharge process. Due to the limited space of the oscilloscope's screen display for current signal (not enlarged by signal-multiply setting of the oscilloscope), a Telegarther signal attenuator has been used where the attenuation coefficient is 20 dB ± 1 dB. The acoustic signals were recorded by a Tektronix TDS 3054B four-channel colour digital phosphor oscilloscope with 500 MHz bandwidth and 5 GS/s sampling rate. Two different sets of time scales were

used due to the different time intervals required to obtain $P_{cav\text{-}max}$ and T_{cavity}, which were 200 ns/division and 1000 µs/division respectively.

Due to a 500 mm distance between the acoustic sensor and the discharge centre, there is a time delay (t_{delay} = (0.5/1483) s = 337 µs) between the spark discharge and arriving of the pressure impulse to the detector location. Therefore, to capture the acoustic signal, the AB event triggering mode has been used in the Tektronix TDS 3054B oscilloscope. The A event is set to be triggered by the electromagnetic disturbance signal emitted when applying a voltage impulse to the discharging circuit while the B event is set 300 µs later. A flexible trigger level (from 500 mV to 1000 mV) was used to ensure the capture of the acoustic signals.

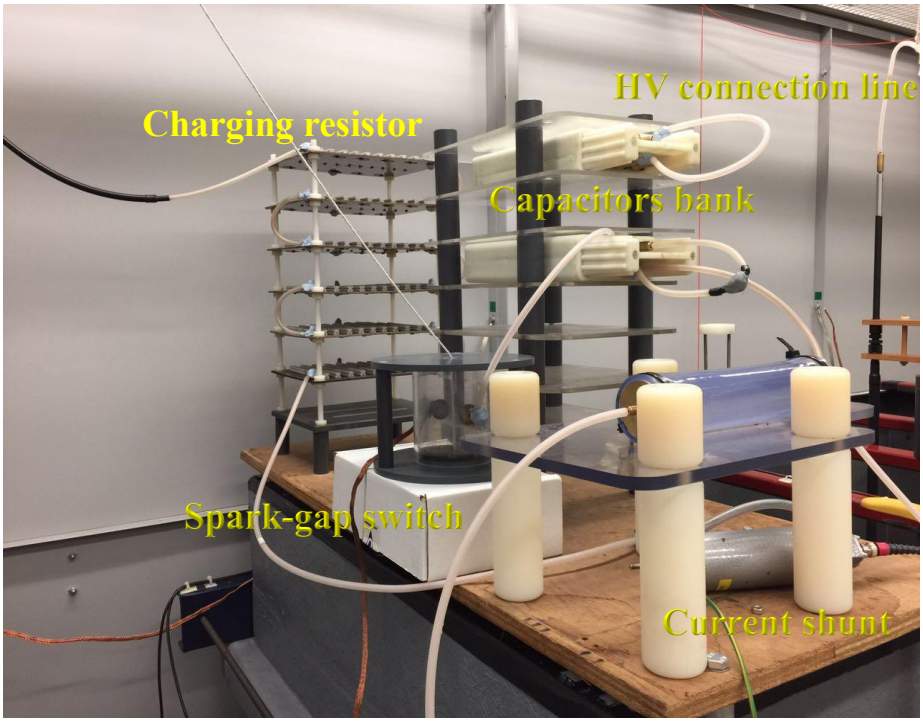

(a)

(b)

Figure 3-2. Photograph of (a) high voltage impulse generation system located on the water tank, and (b) digital oscilloscopes and HV DC supply in the control room.

Fig. 3-2 shows the photograph and layout of the voltage impulse generation system and the diagnostic system. These systems were placed separately in two individual rooms surrounded by metallic walls, control room and test room. These metallic walls provide electrostatic screening and prevent any potential signal interference.

The HV DC power supply and the oscilloscopes were placed in the control room for safe controlling and recording as shown in Fig. 3-2 (b). The impulse generation system and the diagnostic devices were located in the test room. The rope from the trigger switch was in the control room for manual triggering of the pulsed power system.

3.3 Design of the electrodes topology

The electrode topology is one of the key elements determining the development of the plasma channel between the HV and ground electrodes. The design of the electrode topology covers several aspects, such as the electrode shape, the electrode material, the electrode placement and external triggering devices. In the case of microsecond underwater spark discharges (which are under investigation in this work), gas bubbles/microbubbles play essential role in development of the discharges. Therefore, the major concept of the electrode topology design is based on facilitation of producing gas bubbles in the vicinity of HV electrode by either non-uniform electrical field or by gas bubble injection.

The FD's have a straightforward point-to-point electrode topology, providing highly inhomogeneous electrical field distribution. The ABSD's have a general point-to-plane topology with a modified ground electrode, embedded with air-bubble injection functionality. In terms of the WGD's, a pair of special stainless steel crocodile-like clips was used as electrodes where a thin metallic wire was fixed.

Given the fact that the same pulsed power circuit was used in all tests, significant efforts have been focused on the developing of the electrode configuration(s) with good movability and easy installation. For the purpose of providing long life time, all electrodes were made of stainless steel as discharges result in erosion of the sharp electrodes' tips as intensive conductive current passing through during post-breakdown discharge. Stainless steel resists this erosion and is not involved into direct chemical reactions with water. Therefore it does not produce by-products, which may potentially initiate the discharge and in turn influence the development of the plasma channel.

The magnitude of the acoustic impulses emitted from the spark source depends on the inter-electrode gap [35]. Therefore, in order to investigate the impact of inter-electrode gap on the acoustic impulse and energy partition of underwater spark discharges, the electrode configurations for all three types of underwater spark discharges were designed to be gap-length-adjustable.

3.3.1 Electrode topology for free self-triggering discharges

As discussed in Section 2.2, the electrical field required to initiate breakdown in water is much higher than that in air. Therefore, to facilitate the formation and propagation of streamers in water, electrodes with conical tips (featuring non-uniform electrical field distribution) were designed to achieve electric field enhancement in the vicinity of the electrode tips.

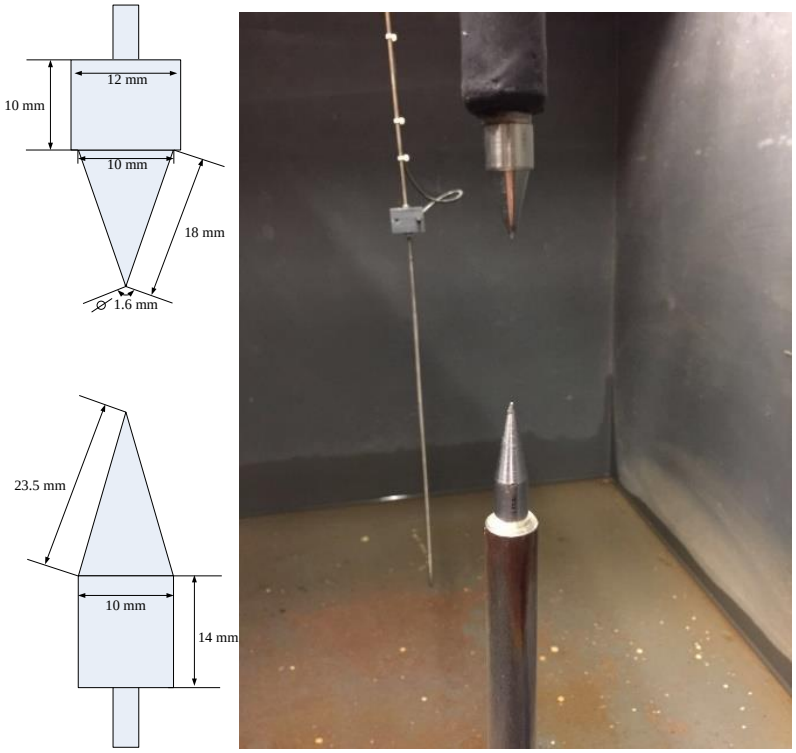

(a) (b)

(c)

Figure 3-3. The schematic diagram of (a) electrode topology for FD's, (b) the photograph of the electrode configuration and (c) the electrode stand.

The electrode topology for FD's is a point-to-point configuration. The photograph of the proposed electrodes and their configuration developed in this work is shown in Fig. 3-3. As shown in Fig. 3-3(a), the HV electrode has a conical shape with slant height of 18 mm, maximum radius of 5 mm and the tip radius of 0.8 mm; its cylindrical base bottom had a radius of 12 mm and a length of 10 mm. The ground electrode has a simple structure with solid base and the conical tip has a maximum radius of 5 mm and a slant height of 23.5 mm; the base bottom shares the same radius as 5 mm and was 14 mm in length. The tails of the HV and ground electrodes were designed for being inserted into and fitted tightly within the HV and ground rods for HV and ground connection. The HV and ground rods were both made up of stainless steel. The HV rod was covered with black rubber cover for electrical isolation. The other end of the HV tube was connected with a HV transmission line. The entire HV rod, installed with the HV electrode, was attached vertically to a plastic holder, which was a part of a metallic stand as shown in Fig. 3-3 (c). The plastic holder was connected with a motion gear, embedded within the stand, by which manual position tuning in vertical direction

is possible for inter-electrode gap adjustment. The ground tube was vertically fixed onto a heavy metal plate, being placed stably at the bottom of the water tank, which is movable for vertical alignment with the HV electrode.

3.3.2 Electrode topology for air-bubble stimulated discharges

The design of the ABSD's electrode topology is based on the bubble discharge mechanism. For long inter-electrode gaps in the FD's case, the propagation of the streamer may stop before a complete plasma channel is formed, causing the failure in developing of complete spark breakdown. Injecting air-bubbles between the electrodes is an effective method to initiate spark discharges and to decrease the breakdown voltage.

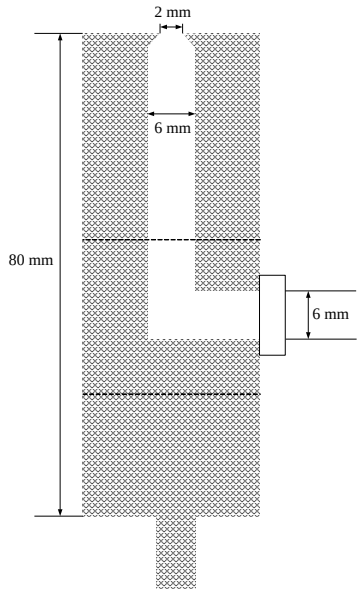

Figure 3-4. The schematic diagram of the ground electrode embedded with air-bubble channel.

The electrodes configuration for ABSD's contains a HV electrode and a modified ground electrode with an air-bubble injection system built in. The HV electrode and the HV rod with precise vertical-positional tuning structure, originally developed for

FD's, were also used in ABSD's tests. With the purpose of long-term use, the ground electrode for ABSD's was made in stainless steel and was designed with a three-piece structure with a diameter of 19 mm and a total length of 80 mm as shown in Fig. 3-4. The bottom piece features an outstanding stick, being used to connect the electrode with ground tube. The middle piece of the ground electrode had a built-in L-type air channel (with 6 mm inner diameter) whose one end was connected with the air tube by a brass push-in junction for external air injection and the other end guided the injected air to the top piece. With the consideration of constraining the output air bubbles within a reasonable size (not as big as that directly coming from the 6 mm air channel), the initial 6 mm air channel was tapered down to a smaller 2 mm (in diameter) port in the top piece. These three pieces were connected by screwing in each other with sealing tapes covered for air leaking-proof. The photograph of the electrode topology for ABSD's is shown in Fig. 3-5.

Figure 3-5. The photograph of the electrode configuration for ABSD's.

An Aqua Air AP1 fish tank air pump, manufactured by Interpet. Ltd, was used as the air- pumping source, which is capable of producing stable initial airflow at a speed of 120 litres/hour with pressure at 0.2 mbar. This air pump was seated in the control room and was connected to the ground electrode through a 6.6 m-long blue air transport tube

with a diameter of 6 mm. However, the direct output from the air pump is too strong to generate air bubbles, which are smoothly injected into the gap. In this case, a pair of flow regulators was introduced into the gas handling system to control airflow from the pump. These two airflow regulators with model numbers of FT257/2-14 and 1251 14, provided two-step fine tuning of airflow.

3.3.3 Electrode topology for wire guided discharges

The main requirement for the electrodes for WGD's is to hold a thin metallic wire firmly. An easy access to the wire holing system should allow straightforward replacement of the wire after each discharge. Therefore, instead of having the separate support structures as in the case of free and air-bubble stimulated discharges, the high voltage and ground connection rods for wire-guided discharges were assembled on a same electrode holder as shown in Fig. 3-6(a), where the HV rod is inserted within the stainless steel ground tube. Thus it is possible to handle these electrodes together which helps to replace wire easily. As the HV rod and ground tube had a coaxial structure, to avoid the direct spark discharge between them instead of exploding the metallic wire, there was plastic isolation filled between the HV rod and ground tube, which is indicated by the white nylon material in Fig. 3-6(a). The connection parts, such as nuts, screws and electrode bases, were mainly made up of nylon. A brass O-ring fixed on upper side of the ground tube was used to connect with the grounding cable. The total length of the ground tube is 720 mm and its internal diameter is 18 mm while the high voltage rod is 210 mm longer than it to prevent air sparks between the tube edge and the rod top. For additional insolation, a PVC cap is also fitted on the tube top. The nylon block together with a piece of red heavy metal is installed at a quarter length down from the tube top as a stable stand, to be fitted above the water tank, making the electrodes emerged in the water.

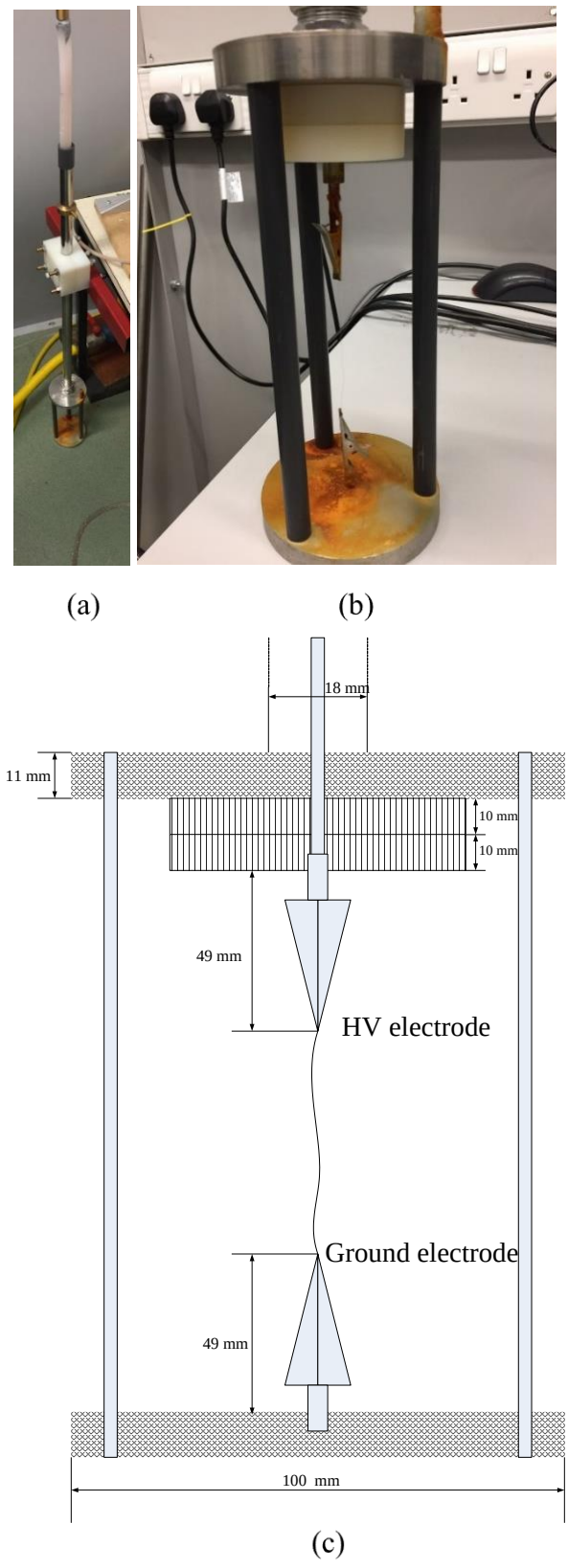

Figure 3-6. The photograph of (a) the electrode holder, (b) the electrode topology and (c) the schematic diagram of the electrode structure.

With the consideration of fast and safe wire exchange, two identical Hirschmann crocodile clips were modified to be used as the high voltage and ground electrodes. These Hirschmann AGF20 crocodile clips (shown in Fig. 3-6(b)) are made from nickel plated steel with body length of 49 mm. In order to fit them in the electrode topology used in this work, their front teeth have been removed for smooth grabbing of the thin wire and additional screw sections have also been attached at each end of these clips for easy installation into the base plates. The schematic diagram for the electrodes is also shown in Fig. 3-6(c). There are three plates (two 65 mm-diameter nylon ones and a 100 mm-diameter steel one) for the top base and one 100 mm-diameter steel plate for the bottom base. One of the clips (HV clip) was connected with the two nylon top plates though a small metal screwing-in connector with a diameter of 5 mm, where the end of high voltage brass rod was hidden within and got in touch with the clip electrically. These two nylons plates together with the high voltage clip were also fixed to the top steel plate by nylon screws and nuts. The other clip (ground clip) was directly screwed in the bottom base plate. The top and bottom steel plates were connected with each other to form a test cage by three plastic (PVC) columns, in one of which a long metallic screw was used for electrical ground connection. By this structure, the length of these columns determined the potential distance between electrodes (from head to head of the clips). Therefore, several sets of columns in different length have been made to achieve different inter-electrode gaps being conducted tests with.

The holder tube and the test cage were connected by using a Prestex 42CP brass adaptor with a size of 22 mm/0.75 in, which is manufactured by Pelger Yorkshire. Ltd. With this specific electrodes configuration design, the current will pass from the top of the high voltage brass rod down to the high voltage clip and then go back to ground through the ground clip together with the steel plates and the outer tube.

The thin metallic wire used to connect the electrodes is made up of copper because of the well-studied nature of it. The copper wire is manufactured by Goodfellow Cambridge, Ltd. The purity of the material is 99.9 % and its diameter is 0.1 mm.

3.3.4 Water tank

The water tank, shown in Fig. 3-7, was used in all three types of discharges' tests. It had a dimension of 2 m (length) × 1 m (width) × 1 m (height) and was made up of the mixture of nylon and fibre. The tank was filled with water to 90 % of its total volume (~ 1800 L) when conducting tests. By taking the consideration of potential contamination (dust from ambient atmosphere and potential chemical reactions in water) during the tests, the water tank was refilled with tap water every five days. The water was taken directly from the tap in the laboratory. Its conductivity was 66.00 μS/cm and pH value was 6.64 as measured by an Orion Star A215 pH/conductivity meter with Orion 013005MD conductivity cell and an Orion 8157BNUMD, manufactured by Thermo Scientific, Ltd. The conductivity of tap water used in University of Strathclyde in Scotland, supplied by Scottish Water, is relatively soft, as compared with other areas in England (hundreds of μS/cm). For example, typical water conductivity for the university's area for year Apr. 2017 to Mar. 2018, measured by Scottish Water, was in a range from 39 μS/cm to 59 μS/cm with a mean value of 52 μS/cm [116]. The electrodes in all spark discharges tests were located in the middle of the water tank.

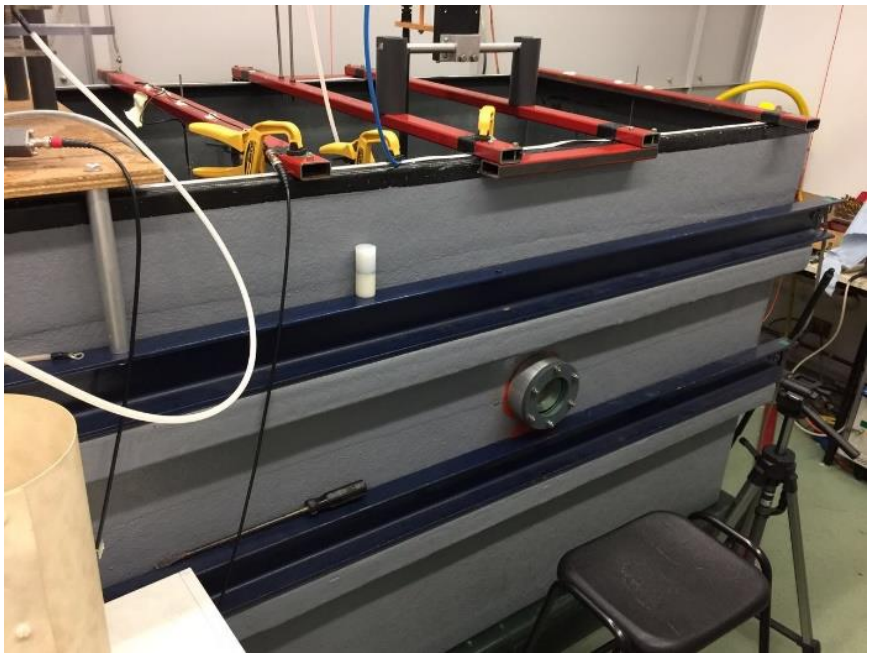

Figure 3-7. The photograph of the water tank used for all discharge tests.

3.4 Experimental methodology

The underwater spark discharge characteristics were obtained from experimental measurements and theoretical analysis. Statistical analysis of the data obtained in discharge tests was conducted. It is important to ensure that the number of conducted tests is sufficient to conduct reliable statistical analysis.

The controllable test parameters in the present work include the charging voltage, the storage capacitance and the inter-electrode gap. Three levels of charging voltage and three values of capacitance were used, resulting in nine energisation levels in total. The selection of the inter-electrode gap depends on the 'breakdown ability' in each type of discharge. The upper limit of the achievable inter-electrode gap for each type was obtained by conducing preliminary tests using the highest energisation level when the success rate of breakdown was lower than 50 % at specific inter-electrode gaps. The final selection of the inter-electrode gaps for FD's, ABSD's and WGD's is shown in Table. 3-1.

Table 3-1. The lengths of inter-electrode gap used for three types of discharges

Discharge mechanism	Inter-electrode gap (mm)
FD's	5, 7, 10, 12, 15
ABSD's	15, 20, 25
WGD's	15, 45, 75

By using combinations of the inter-electrode gap given in Table. 3-1 and the energisation levels mentioned in Section 3.1.5, the breakdown probability achieved for both FD's and ABSD's was above ~ 70 %.

Two major acoustic and hydrodynamic parameters were monitored during tests, the acoustic magnitude and the period of the cavity oscillation. For each combination of the charging voltage, the value of capacitance and the inter-electrode gap for FD's and ABSD's, ten independent measurements of the acoustic magnitude and the period of cavity oscillation were obtained. The voltage and current waveforms were monitored for all of these tests. With the consideration of the consistent performance of WGD's and its time-consuming wire exchange operation, the number of tests was reduced to

five for both acoustic magnitude and period of cavity oscillation. The plasma resistance and the energy delivered into the plasma channel were obtained from the current waveforms by using the RLC circuit analysis (2.22)-(2.24).

3.5 Conclusions

This chapter presented the design and development of the underwater spark discharge generation system used in the present work. The experimental set-up was divided into three sections, the voltage impulse generation system, the diagnostic system and the electrode topology. The detailed information and electrical parameters of all equipment used in the tests are provided. Different combinations of charging voltage (25 kV, 30 kV and 35kV) and storage capacitance (155 nF, 266 nF and 533 nF) were chosen to conduct the tests. The diagnostic system used in this work consists of voltage, current and acoustic monitoring probes. The corresponding oscilloscope settings were discussed in order to accurately capture and record the voltage, current and acoustic signals.

The design of the electrode topology for FD's, ABSD's and WGD's was explained. The dimensions and the materials used to construct the electrodes are also provided. The FD's and ABSD's used the same HV electrode to initiate the discharge. The ground electrode for ABSD's was modified so as to produce consistent air bubble injection in water during tests to increase the potential breakdown voltage.

A dedicated position tuning system was constructed for adjustment of inter-electrode gap, which was mounted on the top of the water tank. The electrodes for copper wires were hold by conductive crocodile clips, thus, it was easy to replace thin wires after each shot. Copper wire (99.9 % purity) was used in wire-guided discharge tests. For reducing potential interference from the acoustic waves reflected by the water surface and tank walls, the electrode configurations were located in the middle position in the water tank. The conductivity and PH values of water used in the tests were measured.

Different inter-electrode gaps for FD's, ABSD's and WGD's were chosen to conduct discharge tests. The inter-electrode gap varied from 5 mm to 75 mm depending on the amount of energy available in the discharge for different discharge mechanisms. A number of discharge tests were planned for each combination of charging voltage, capacitance and inter-electrode gap for better statistical accuracy.

The electrical parameters of the circuit, obtained from direct measurements and circuit analysis, were breakdown voltage, V_{br}, plasma resistance, R_{pl}, and the energy delivered into the plasma channel, E_{pl}, while the acoustic magnitude, $P_{cav\text{-}max}i$, and period of cavity oscillation, T_{cavity}, were obtained as the acoustic and hydrodynamic parameters. The acquisition of these parameters will be discussed in the following chapters. Fundamental relationships between these parameters will be investigated in following chapters. This analysis will allow the optimisation of the circuit parameter for generating desirable acoustic impulses. Also, this research will lead to further understanding of the mechanisms and parameters of underwater spark discharges.

4 Experimental results and analysis: Free self-triggering discharges

The free self-triggering discharge is one of the most common types of underwater spark discharges. This type of breakdown and its mechanism have been studied intensively from its pre-breakdown initiation process to post-breakdown phenomena. The advantages of this type of underwater spark discharge are the flexibility in configuration design and the ability to support high operation frequency (number of discharges per second). This chapter is aimed at investigation of the breakdown characteristics of the FD's for comprehensive analysis and understanding of the relationships between the discharge properties and the acoustic output characteristics, which is important for the optimisation of underwater spark discharge in practical cases.

This chapter presents the experimental results obtained in the point-to-point electrode topology designed in Chapter 2. These results include the breakdown voltage, V_{br}, the plasma resistance, R_{pl}, the energy delivered into the plasma channel, E_{pl}, the acoustic magnitude, $P_{cav\text{-}max}$, and the period of the cavity oscillation, T_{cavity}. The electrical properties of the plasma channel were obtained as the result of the discharging circuit being treated as a RLC circuit. These electrical parameters reveal the discharging conditions and the plasma channel properties. The acoustic magnitude and the period of cavity oscillation describe the strength of the acoustic impulse and the dynamic behaviour of the gas cavity after breakdown. The acoustic energy can be calculated with the help of the experimental acoustic profile. However, as mentioned in Section 3.2, the calibration of the acoustic sensor used in the diagnostic system is unknown and the actual pressure of the acoustic magnitude measurement is not obtainable. Therefore, only the magnitude of acoustic impulses and the period of the cavity oscillation are involved in the analysis within this chapter. The acquisition of the acoustic energy and its efficiency will be conducted by using an analytical model in Chapter 7.

The discussion of the dependency of the acoustic magnitude and the period of cavity oscillation on the obtained electrical parameters of the circuit is presented within this chapter. Their relationships are illustrated and statistical analysis is conducted to find scaling relations. The acoustic magnitude is shown as a function of the breakdown

voltage, the storage capacitance and the inter-electrode gap, while the period of cavity oscillation has weak dependency on the inter-electrode gap. It was found that the optimal acoustic output is also related to the electrical parameter of the external circuit, based on the non-linear relationship between the acoustic output parameters and the plasma resistance.

4.1 Experimental results

4.1.1 Voltage and current waveforms

The FD's were achieved by applying high voltage impulses directly to the HV and ground electrodes submerged in water. From initial tests, the streamers were propagating in a subsonic mode. The voltage and current waveforms were recorded covering the whole process of the spark discharge and examples of these waveforms for a specific free self-triggering discharge are shown in Fig. 4-1. The underdamped oscillations shown in these waveforms during post-breakdown discharges are similar to the waveforms obtained in [79].

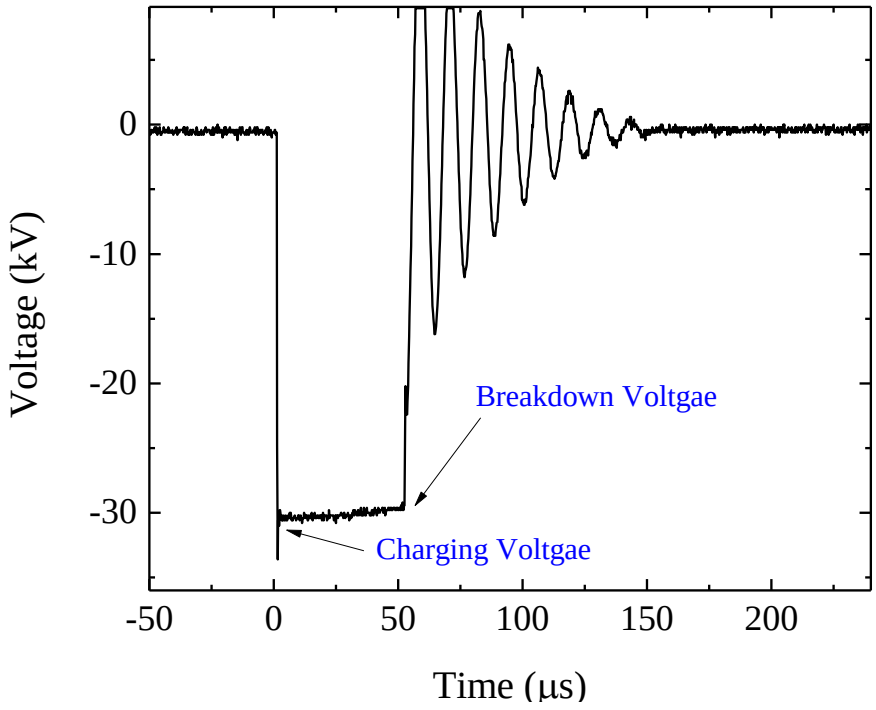

(a)

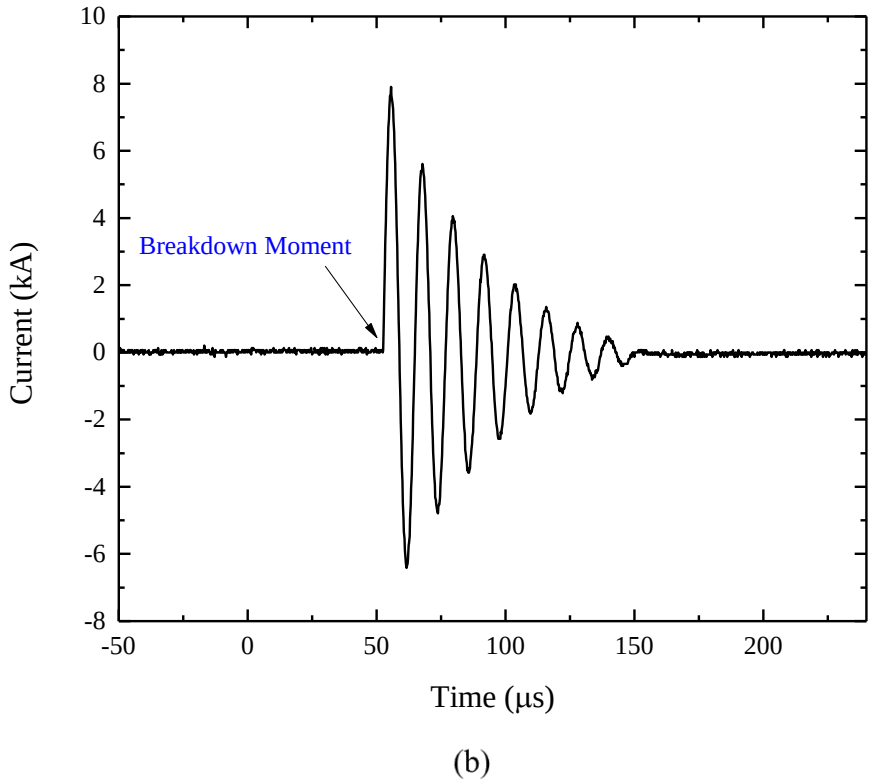

(b)

Figure 4-1. Example waveforms of (a) the voltage and (b) current, obtained for a free self-triggering discharge with the following parameters: 10 mm gap, 533 nF capacitance, ~ 29.8 kV breakdown voltage (30 kV nominal charging voltage).

Although the magnitude and the number of oscillation cycles in the waveforms can be different, the basic profile of these waveforms for different experimental conditions is similar. By taking Fig. 4-1 (a) as an example, the voltage impulse is applied to the electrodes at time 0 μs and the voltage across electrodes rapidly reaches the charging level. Due to the existence of the conductivity of water, the voltage starts to decay until the time reaches ~ 52 μs. The time interval between 0 μs to 52 μs is defined as the pre-breakdown time for the breakdown above when the formation and propagation of streamers take place. The general range of the pre-breakdown time for FD's is from ~ 25 μs to ~ 400 μs. The breakdown occurs at ~ 52 μs after streamers bridges the inter-electrode gap. The voltage present at this particular moment across the electrodes is the breakdown voltage, V_{br}. This voltage defines the total energy available at breakdown, E_{br}, part of which to be delivered into the plasma channel. The resistance

between electrodes dramatically decreases due to the establishment of highly conductive plasma channel. The conductive current, *I(t)*, appears at this moment, which is shown in Fig. 4-1 (b). The magnitude of the current, I_0, ranges from ~ 2 kA to ~ 12 kA in all FD's tests, depending on the energisation level used. During the post-breakdown period starting from ~ 52 µs, the current continues to inject electrical energy into the plasma until it disappears at ~ 155 µs. The voltage and current waveforms are in decaying sinusoidal forms during the discharge phase (energy deposition phase). These oscillations in voltage and current indicate the electrical dynamics of the system (RLC circuit) with presence of the capacitive and inductive elements in the circuit.

4.1.2 Hydrodynamic and acoustic signals

Examples of the acoustic signals recorded for FD's are shown in Fig. 4-2. Fig. 4-2(a) demonstrates typical waveforms of the primary acoustic impulses obtained for FD's in 5 mm, 7 mm, and 12 mm gaps, which show similar wave shapes but with different magnitudes. Similar experimentally obtained acoustic profiles were reported in [35].

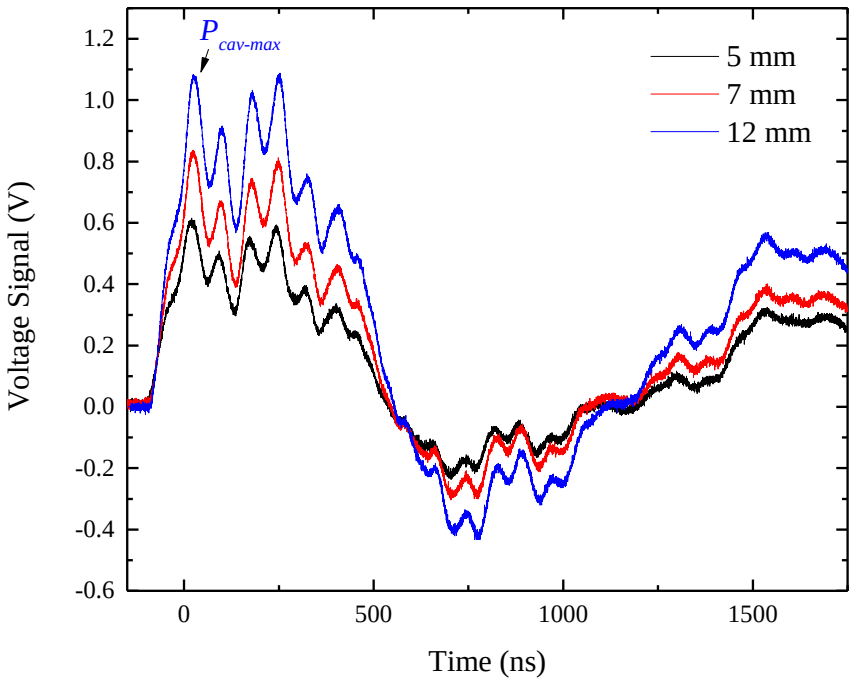

(a)

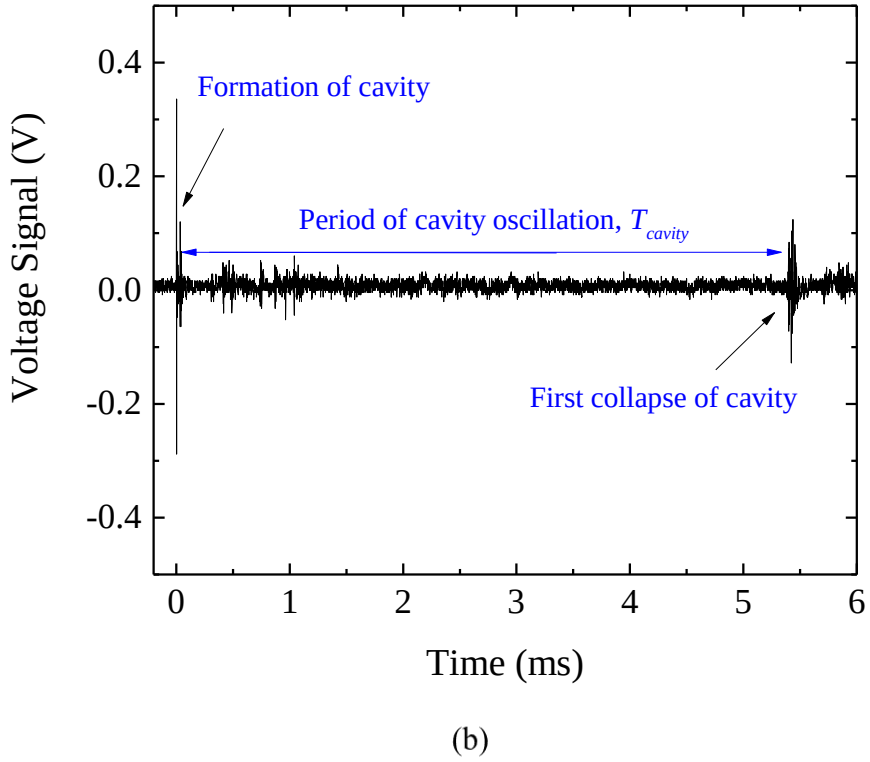

(b)

Figure 4-2. Acoustic signals obtained: (a) the profile of the acoustic magnitude for discharges in 5 mm, 7 mm and 12 mm gaps; (b) the primary and secondary acoustic impulses emitted at the formation and collapse of the cavity for a discharge in 7 mm gap. $P_{cav\text{-}max}$ is the first peak of the impulse and T_{cavity} indicates the time duration of the primary oscillation of the cavity.

As discussed in Section 2.4.3, a few number of acoustic impulses can be emitted during an underwater spark discharge. The acoustic signal in Fig. 4-2(a) refers to the primary acoustic impulse emitted from the spark source. The initial peak value of this signal will be used to represent the magnitude of the primary acoustic impulse emitted from the cavity, $P_{cav\text{-}max}$. The acoustic impulses generated by underwater spark discharges have short durations (< 1 μs).

Fig. 4-2(b) shows two successive acoustic impulses emitted during the gas cavity's oscillation (formation and first collapse of the cavity), which have different magnitudes due to energy dissipation. The first impulse indicates the formation of the cavity and the second impulse points out the end of its collapse. There are other visible acoustic 'spikes' with relatively small magnitudes present in Fig. 4-2(b). These minor acoustic signals are due to the reflective waves from the solid tank walls or from the

water-atmosphere interface. The position of the acoustic sensor (500 mm away from the spark source) guarantees that the first signal detected by the sensor must be the direct acoustic signal from spark rather than any reflection.

The hydrodynamic information obtained from the waveform is the period of cavity oscillation as illustrated in Fig. 4-2(b). In ideal case (no energy losses), the gas cavity oscillates with a period, researching its maximum size and then collapsing under the external hydrostatic pressure. These ideal oscillations are described by the Rayleigh model (2.8), which links T_{cavity} with the maximum radius of the cavity, r_{max}. In practical case, energy losses results in reduction of numbers of oscillations and thereby the shorter oscillating period of each new oscillation. In [117], the decaying cavity's oscillation period was discussed and was experimentally recorded as decreasing time interval between successive shockwave pulses. In the present work, the term T_{cavity} (the period of the cavity oscillation) only refers to the time interval from the formation of the cavity (after the breakdown) to its first collapse. Further potential oscillations are not considered is this work.

4.2 The period of cavity oscillation as a function of the breakdown voltage

The spark-generated cavity oscillation has previously been investigated to calculate the energy consumption for cavity expansion and the corresponding efficiency and to study the energy partition in the post-breakdown stage [74], [117], [118]. In present work, the cavity's oscillation was studied as one of the major post-breakdown hydrodynamic phenomena.

After completion of the pre-breakdown stage, a streamer bridges two electrodes and a gas cavity is formed in the centre of the spark. It expands due to the large initial pressure inside it and then collapses under the force of the external hydrostatic pressure. This characteristic of the cavity oscillation depends on the energy deposition in the early post-breakdown stage.

During this dynamic process, the mechanical work done to the ambient water by the cavity (the gas/water interface), W_m, by the time it reaches its maximum radius, r_{max}, can be expressed as:

$$W_m = (4\pi/3) r_{max}^3 p_\infty \quad (4.1)$$

where p_∞ is the ambient hydrostatic pressure.

The source of this work, W_m, is the energy delivered into the plasma channel, E_{pl}, which is proportional to the total energy available at breakdown, E_{br}, in the discharge circuit:

$$E_{pl} \propto E_{br} \quad (4.2)$$

Therefore, the mechanical work, W_m, can be related to E_{pl} by:

$$W_m = \delta E_{pl} \quad (4.3)$$

where δ is a proportionality coefficient, which will be investigated in details in Section 4.9.

E_{br} can be obtained by:

$$E_{br} = {}^{CV_{br}^2}/_2 \quad (4.4)$$

where V_{br} is the breakdown voltage and C is the storage capacitance.

Therefore, a relationship between W_m and V_{br} can be found as:

$$W_m \propto {}^{CV_{br}^2}/_2 \quad (4.5)$$

A model relating the collapse time of the cavity to the maximum cavity radius was derived by integrating the Rayleigh-Plesset equation, [119]-[122]:

$$T_{cavity} = 1.83 r_{max} (\rho_0 / p_\infty)^{1/2} \quad (4.6)$$

where ρ_0 is the density of water and p_∞ is the external hydrostatic pressure.

(4.6) is used to describe the relationship between T_{cavity} and r_{max} in this work with the

assumption that the viscosity and surface tension of the water can be neglected and no energy losses is included for an ideal case.

The combination of (4.1) and (4.6) links the period of cavity oscillation with the mechanical work, W_m:

$$T_{cavity} = 1.14\rho_0^{1/2} W_m^{1/3} p_\infty^{-5/6} \tag{4.7}$$

By substituting W_m with V_{br}, the result leads to a link between two experimentally obtained parameters, which are the period of cavity oscillation and the breakdown voltage:

$$T_{cavity} \propto V_{br}^{2/3} C^{1/3} \rho_0^{1/2} p_\infty^{-5/6} \tag{4.8}$$

Given the known values for the storage capacitance, water density and hydrostatic pressure, (4.8) can be simplified by using proportionality coefficient, m, to represent the links between T_{cavity} and V_{br} in all cases of the FD's tests:

$$T_{cavity} = mV_{br}^{2/3} \tag{4.9}$$

The dependency of T_{cavity} on V_{br} for different inter-electrode gaps is shown in Fig. 4-3 and they are classified by different values of the storage capacitance. Each data point shown in Fig. 4-3 indicates an individual breakdown event under corresponding experimental conditions. The main observations shown in three capacitance value cases are similar that the period of cavity oscillation increases with an increase in the breakdown voltage by a well-defined tendency, which can be used to accurately predict the cavity oscillation time for a given value of breakdown voltage.

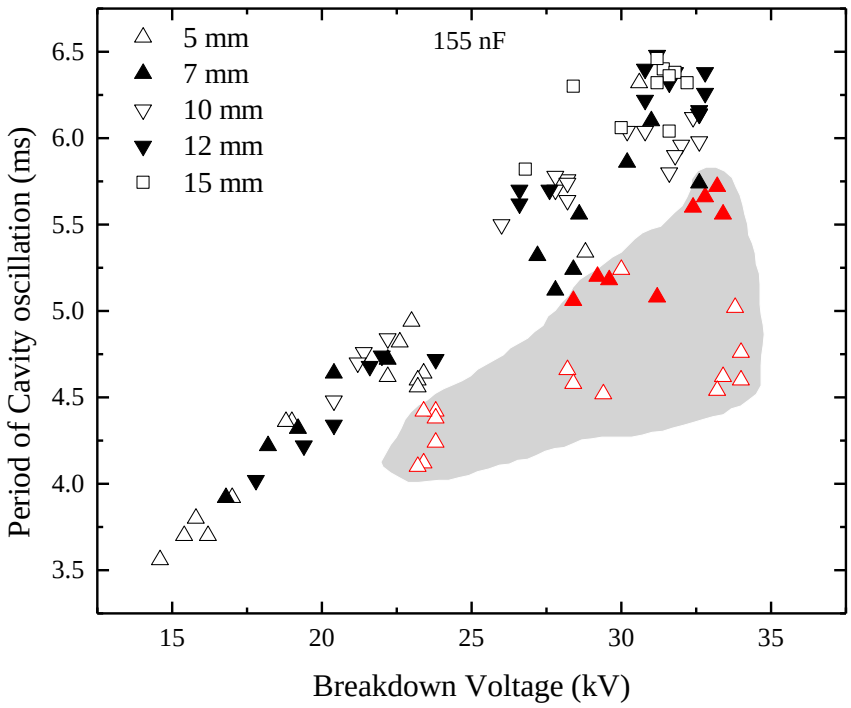
5 mm
7 mm
10 mm
12 mm
15 mm
155 nF
Period of Cavity oscillation (ms)
Breakdown Voltage (kV)
6.5
6.0
5.5
5.0
4.5
4.0
3.5
15
20
25
30
35

(a)

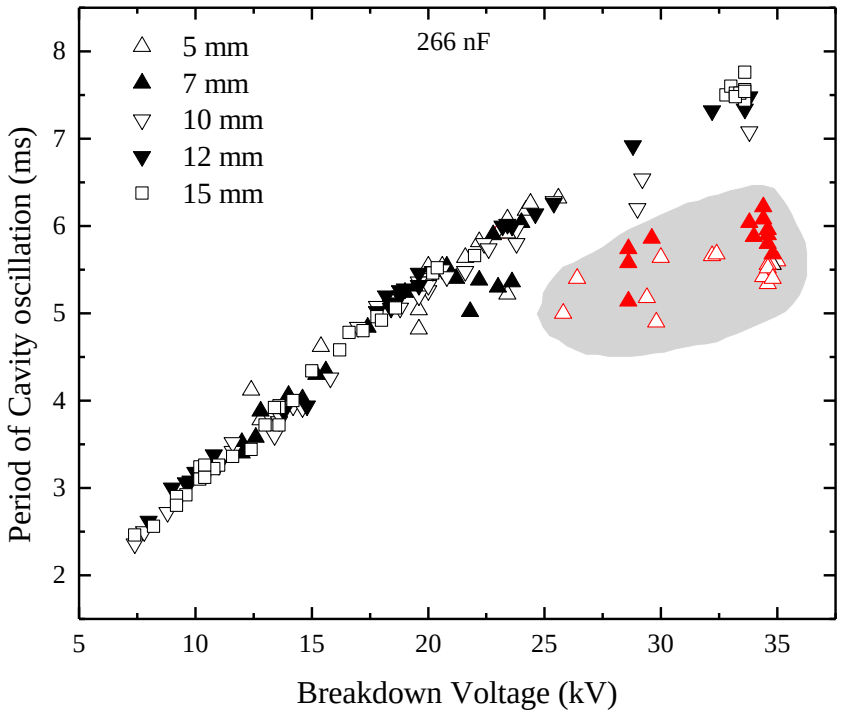
5 mm
7 mm
10 mm
12 mm
15 mm
266 nF
Period of Cavity oscillation (ms)
Breakdown Voltage (kV)
8
7
6
5
4
3
2
5
10
15
20
25
30
35

(b)

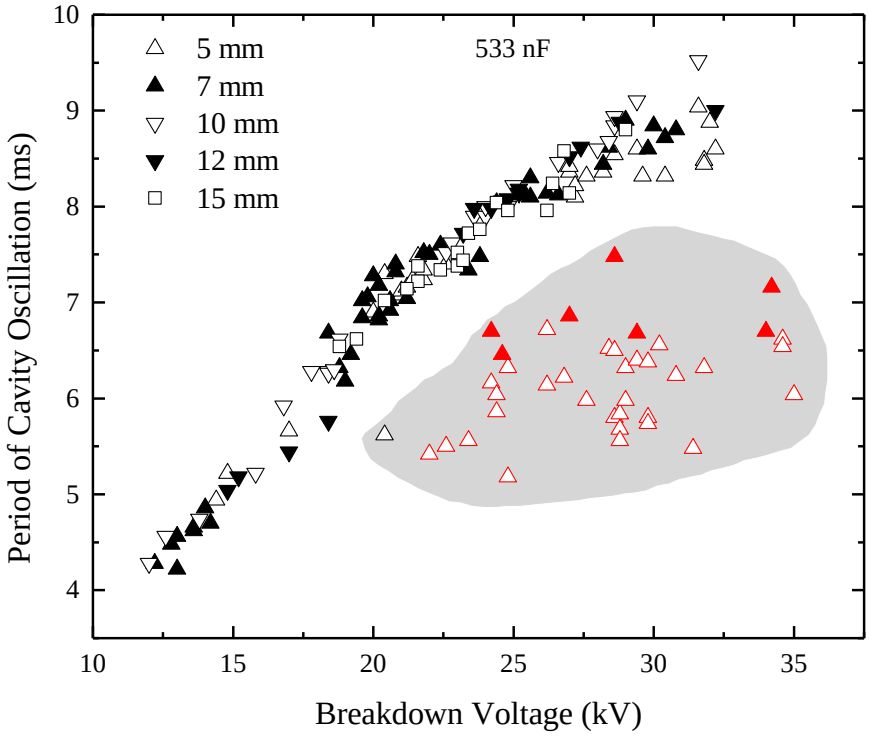

(c)

Figure 4-3. The period of cavity oscillation as a function of the breakdown voltage for (a) 155 nF, (b) 266 nF and (c) 533 nF. The red data points in grey areas indicate those discharges where $R_{pl} < R_{circuit}$.

However, there is a cluster of data points, which is located outside (below) the main trend for each capacitance case, showing lower increase in T_{cavity} with the increasing V_{br}, which is marked in red and covered in the grey area in Fig. 4-3. It should be noted that most of these points were obtained in short gaps (5 mm and 7 mm) with high breakdown voltages (> 20 kV), meaning the value of T_{cavity} in this situation will see no further significant increase even with breakdown voltages higher than 35 kV. Similar observation on the relationship between T_{cavity} and the breakdown energy ($CV_{br}^2/2$) was also obtained in [35]: T_{cavity} demonstrated no significant increase with an increase in the breakdown energy (> 40 J) for 5 mm inter-electrode gap. As discussed before, the expansion of the cavity depends on the amount of energy released into the plasma channel, E_{pl}. In other words, serval major factors determine the cavity oscillation period: the breakdown voltage, the energy delivered into the plasma channel and the

energy conversion efficiency (defined as ratio of the energy delivered into the plasma channel and the total energy available at breakdown). It is clear that that higher breakdown voltage produces larger energy available at breakdown according to (4.4). However, the energy conversion efficiency is different in different situations and is strongly related to the plasma resistance. Therefore, the plasma resistance will be used to explain these outlying clusters. The values of the constant plasma resistance have been obtained for all tests based on the RLC circuit solution as described by (2.22). It will be shown that the plasma resistance normally decreases with increasing breakdown voltage. The decreasing plasma resistance, in turn, results in lower energy conversion efficiency. Thus, the energy conversion efficiency will decrease with an increase in breakdown voltage.

It has been found that the plasma resistance of breakdowns (with high V_{br}) in the grey areas is lower than the circuit resistance, $R_{circuit}>R_{pl}$. For these discharges, low values of the energy conversion efficiency dominate the large amount of energy available in the circuit, resulting in less energy delivered into the plasma channel than expected. On the other hand, the discharges in the main trend, have values of the plasma resistance higher than the circuit resistance, $R_{circuit}<R_{pl}$. Thus, the increasing breakdown voltage overpowers the slowly-decreasing energy conversion efficiency, resulting in an increase in the energy delivered into in the plasma channel. As a summary, the difference between T_{cavity} in the main trend and in the grey areas in Fig. 4-3 can be explained by the inverse relationship between the electrical energy conversion efficiency and the breakdown voltage. More detailed discussion of the impact of the plasma resistance together with the energy conversion efficiency on the period of cavity oscillation will be demonstrated in Section 4.3.

Equation (4.9) has been used to fit the data points (T_{cavity}) in the main trend and the fitting results are shown as the solid lines in Fig. 4-4. The dashed lines indicate the upper and lower boundaries of the 9 % prediction intervals. This fitting procedure was conducted in OriginLab Pro 9.0 software. The proportionality coefficient, m, was used as a free fitting parameter. The values of breakdown voltage used in (4.9) were in kV.

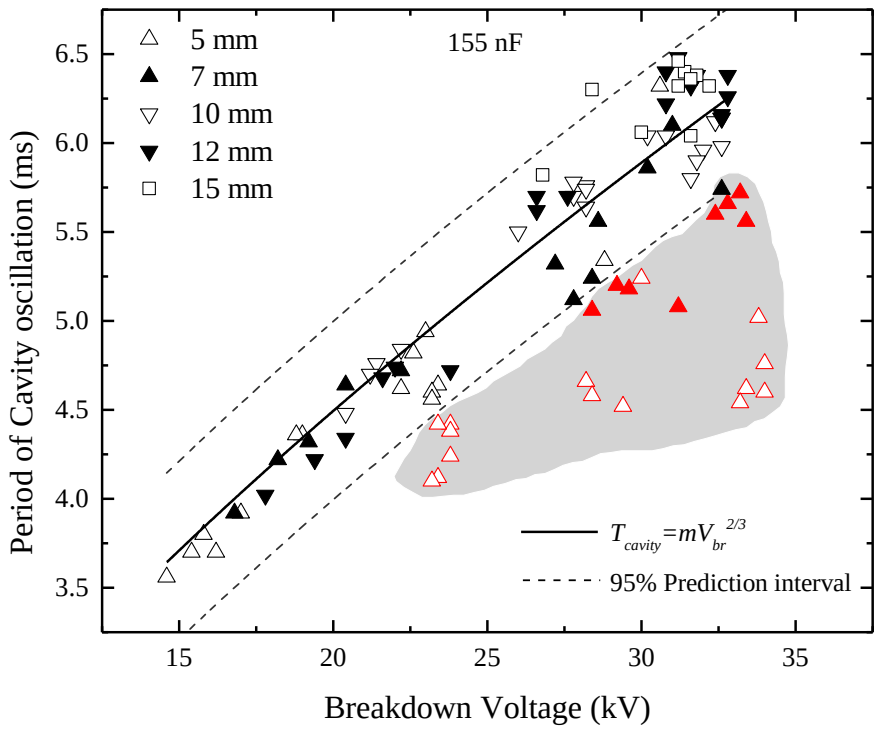
155 nF
5 mm
7 mm
10 mm
12 mm
15 mm
$T_{cavity}=mV_{br}^{2/3}$
95% Prediction interval
Period of Cavity oscillation (ms)
Breakdown Voltage (kV)
6.5
6.0
5.5
5.0
4.5
4.0
3.5
15
20
25
30
35

(a)

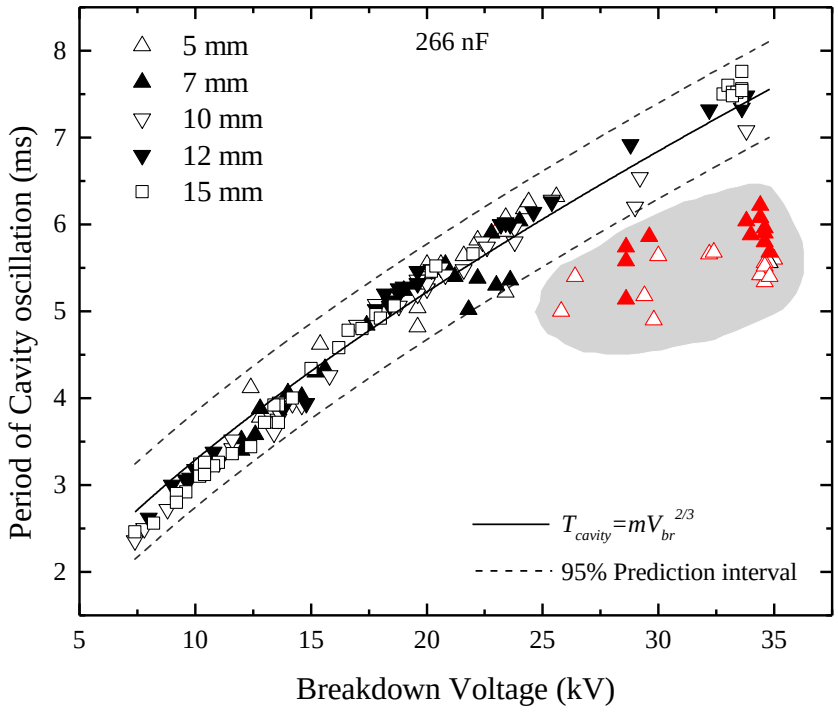
266 nF
5 mm
7 mm
10 mm
12 mm
15 mm
$T_{cavity}=mV_{br}^{2/3}$
95% Prediction interval
Period of Cavity oscillation (ms)
Breakdown Voltage (kV)
8
7
6
5
4
3
2
5
10
15
20
25
30
35

(b)

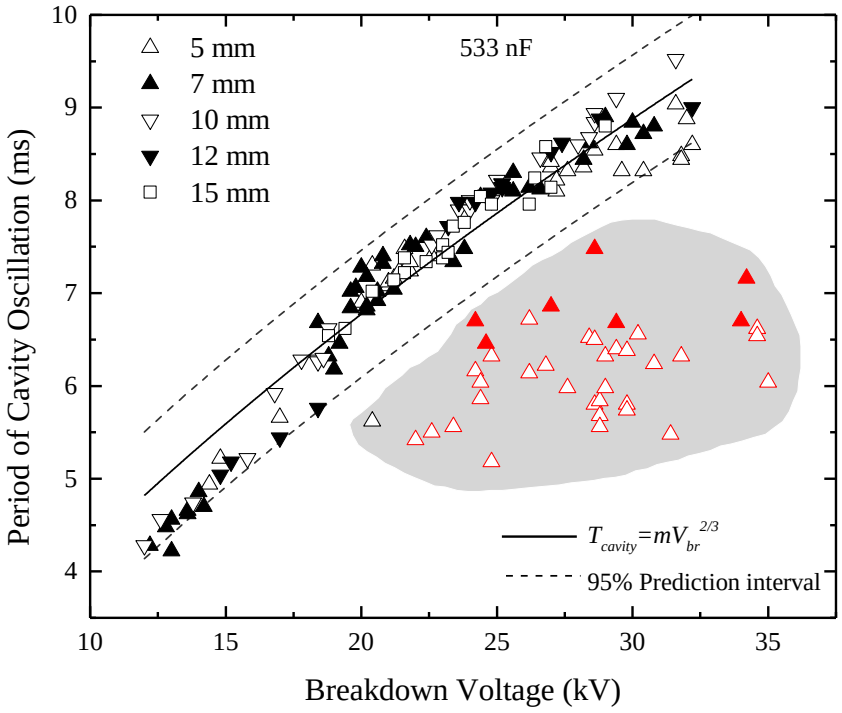

(c)

Figure 4-4. The period of cavity oscillation as a function of the breakdown voltage for (a) 155 nF, (b) 266 nF and (c) 533 nF, with the solid fitting lines given by (4.9). The dashed lines show the upper and lower boundaries of the 95 % prediction intervals.

Table 4-1. The coefficient, *m*, obtained for three values of capacitance by fitting (4.9) to data in Fig. 4-3

C	155 nF	266 nF	533 nF
m	0.61 ± 0.01	0.70 ± 0.01	0.92 ± 0.01

The numerical values of the fitting parameter, *m*, with their standard deviation are given in Table. 4.1 for all three values of storage capacitance. It was found that the fitting lines of (4.9) demonstrate a good agreement with the main trend of the experimental results for all capacitances. The upper and lower boundaries of the 95 % prediction intervals cover most of experimental data in the main trend, confirming the feasibility of (4.9) in predicting the T_{cavity} for a given value of breakdown voltages.

By implementing a non-linear fit to the calculated values of coefficient, *m*, in Table.

4-1 in software OriginPro 9.0, the fitting result turned out to be: $m \propto C^{0.34}$ as illustrated in Fig. 4.5 where m is represented as a function of C. The power coefficient of C, obtained using this fitting procedure is 0.34, which is close to its value 1/3 derived in (4.8). In the case of FD's, it can be said the behaviour of the cavity oscillation during the post-breakdown stage for different inter-electrode gaps will be the same for same energisation conditions.

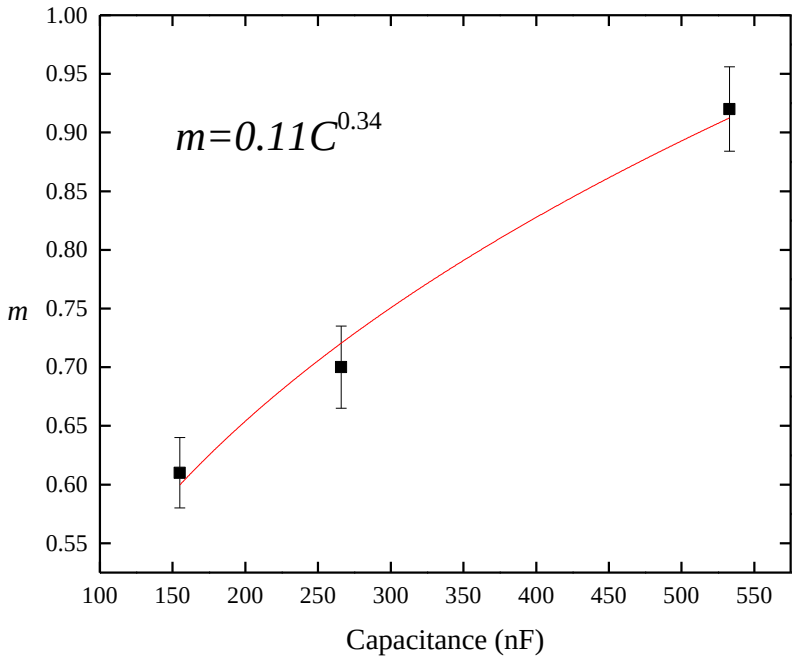

Figure 4-5. The coefficient, m, in (4.9) with its standard deviation as a function of the value of capacitance. The red curve shows the fitting result as $m = 0.11C^{0.34}$.

Based on the analysis conducted above, by substituting $m = 0.11C^{0.34}$ in (4.9), a general form of the scaling relationship can be obtained:

$$T_{cavity} = 0.11C^{0.34}{V_{br}}^{2/3} \tag{4.10}$$

Fig. 4-6 illustrates the combination of experimental data in the main trend for all three capacitance cases in FD's tests. The solid lines in Fig. 4-6 demonstrate the fitting of (4.10) to the experimental data. It was shown that (4.10) works well for all three

cases, confirming its validity to describe T_{cavity} as a function of V_{br} and C for FD's regardless of the inter-electrode gap.

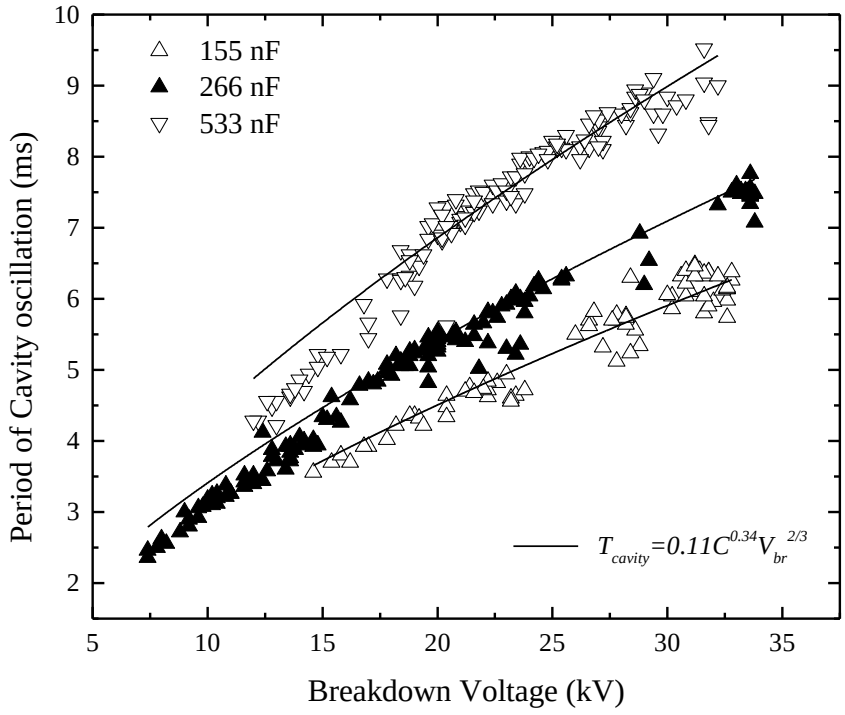

Figure 4-6. The period of cavity oscillation as a function of the breakdown voltage for all capacitance cases: (a) 155 nF, (b) 266 nF, (c) 533 nF. Solid lines show fitting results given by (4.10), excluding data points where $R_{pl} < R_{circuit}$.

4.3 The acoustic magnitude as a function of the breakdown voltage

The magnitude of the acoustic impulse emitted from the spark source is an essential parameter to be considered in practical underwater spark discharge applications as introduced in Chapter 1. Its dependency on the electrical parameters of the circuit and electrode topology has been investigated in [123]-[128]. Therefore, it is important to establish a link between the acoustic pressure and the discharge circuit parameters for straightforward evaluation of the acoustic performance of FD's. This section presents the discussion of the relationships between the acoustic magnitude and the breakdown voltage, capacitance and inter-electrode gap. Empirical scaling relations were

established.

A link between the acoustic magnitude and the breakdown voltage can be established by considering the energy partition in the discharge process. The mechanisms of propagation of acoustic impulses emitted by chemical explosion in water are similar to those produced by underwater spark discharges regardless of their initiation mechanisms. Therefore, the relationship between the acoustic magnitude, $P_{cav\text{-}max}$, the charge mass, M, and the distance between the charge and observation point, d, established for chemical underwater explosion, [129], can be applied to the underwater spark discharges:

$$P_{cav-max} \propto \left(M^{1/3}/d\right)^{\beta} \tag{4.11}$$

where β is an empirical constant parameter and is found to be 1.13 in [129].

In (4.11), in the case of underwater spark discharges, the charge mass, M, can be related to the energy available in spark breakdown, E_{br}. Therefore, the proposed link between M and V_{br} can be written as:

$$M \propto CV_{br}^2 / 2 \tag{4.12}$$

By combining (4.11) and (4.12), a simplified proportional relationship can be established for the acoustic magnitude, $P_{cav\text{-}max}$. This magnitude is proportional to the breakdown voltage to the power $2\beta/3$, $V_{br}^{2/3\beta}$ and to the capacitance to the power 1/3, $C^{1/3}$:

$$P_{cav-\max} \propto C^{\beta/3} V_{br}^{2\beta/3} \tag{4.13}$$

In the same manner, when dealing with the relationship between the period of cavity oscillation and the breakdown voltage, a proportionality coefficient, k, can be introduced, and (4.13) can be rewritten as:

$$P_{cav-\max} = kV_{br}^{2\beta/3} \tag{4.14}$$

where $P_{cav\text{-}max}$ is expressed in mV and V_{br} is in kV.

In [125], the peak pressure of the pressure impulse was found to be proportional to the breakdown energy, E_{br}, to the power $(0.46 - 0.14e^{-Ph/1.75})$ where P_h is hydrodynamic pressure in MPa. By using $E_{br} \propto V_{br}^2$, the power coefficient for V_{br} can be calculated for the FD's (for P_h ~0.1 MPa) in this work and it was found to be ~ 0.66, which is close to the value $2\beta/3 = 0.753$ obtained in (4.14). In [130], [131], an empirical scaling relationship was established between the peak pressure and the breakdown energy: the peak pressure was proportional to the breakdown energy to the power 0.35. By adopting $E_{br} \propto V_{br}^2$, it was found that the peak pressure was proportional to the breakdown voltage to the power ~ 0.7, which was also close to the phenomenological value, 0.753, obtained in this work.

It is worthy of note that the length of the acoustic source, (the inter-electrode gap, l,) is not taken into account in (4.14) as it is purely derived from the energy aspect in this case. Model (4.11) demonstrates that the effect of V_{br} on $P_{cav\text{-}max}$ is stronger than that of C as the power coefficient of V_{br}, $(2\beta/3)$, is twice of that of C, $(\beta/3)$.

The experimental acoustic magnitude as a function of the breakdown voltage for all three values of capacitance is plotted in Fig. 4-7. It was found that the magnitude of the acoustic magnitude increases with an increase in breakdown voltage. It is also established that for a given value of breakdown voltage for the same inter-electrode gap, the acoustic magnitudes obtained with higher capacitance normally have higher values. Both findings point to the same situation where larger amount of energy is delivered into the plasma channel and an enhancement in the acoustic magnitude can be expected. It was worthy of note that 'saturation' in the magnitude values was also observed for experimental data obtained for 5 mm and 7 mm gaps with high V_{br} (> 25 kV). This saturation of the peak pressure for high energy levels was also reported in [35] and a conclusion was made that both T_{cavity} and $P_{cav\text{-}max}$ saturate with higher applied pulse.

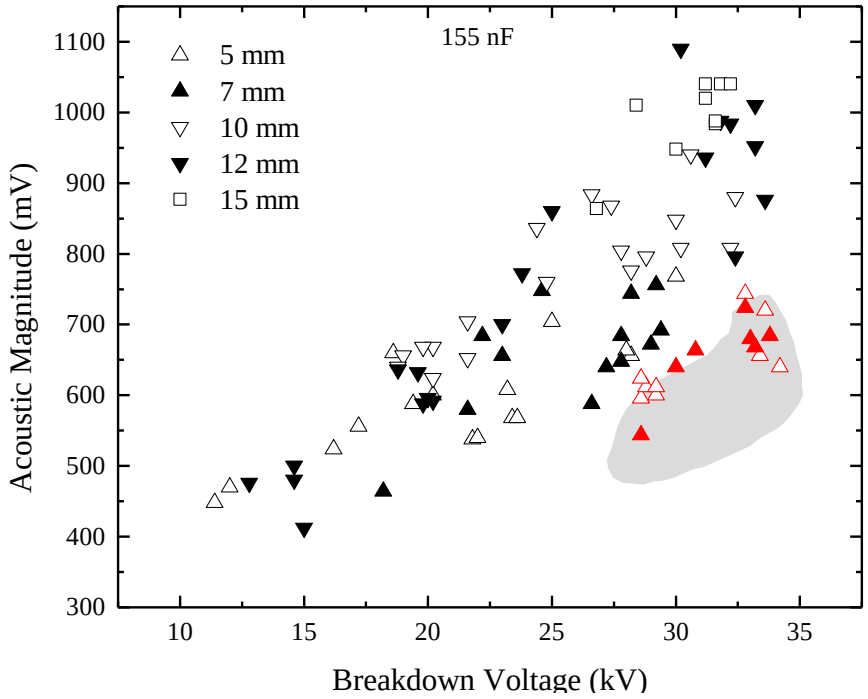
155 nF
5 mm
7 mm
10 mm
12 mm
15 mm
Acoustic Magnitude (mV)
Breakdown Voltage (kV)
300
400
500
600
700
800
900
1000
1100
10
15
20
25
30
35

(a)

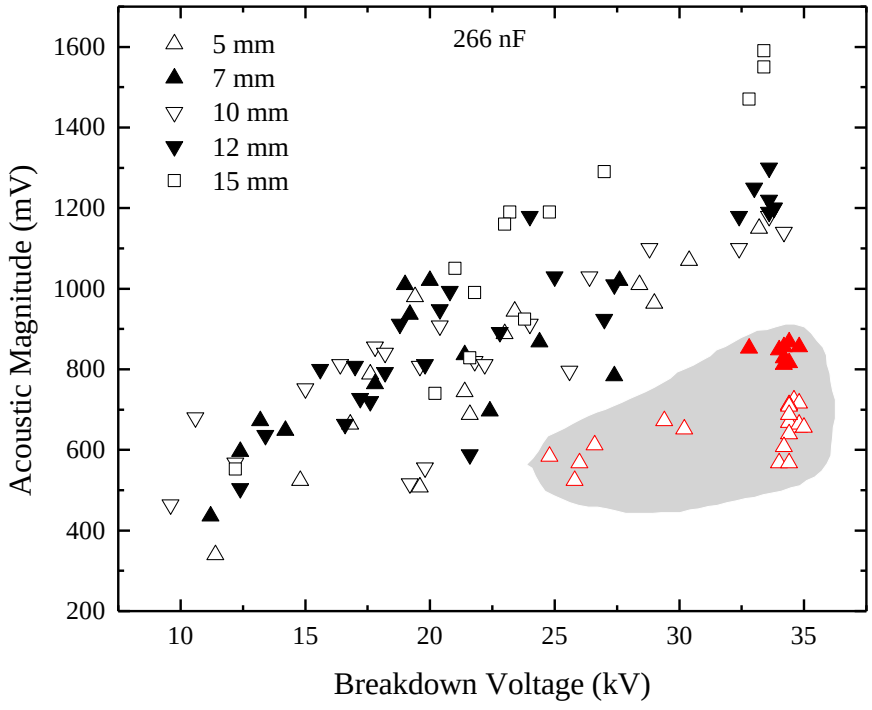
266 nF
5 mm
7 mm
10 mm
12 mm
15 mm
Acoustic Magnitude (mV)
Breakdown Voltage (kV)
200
400
600
800
1000
1200
1400
1600
10
15
20
25
30
35

(b)

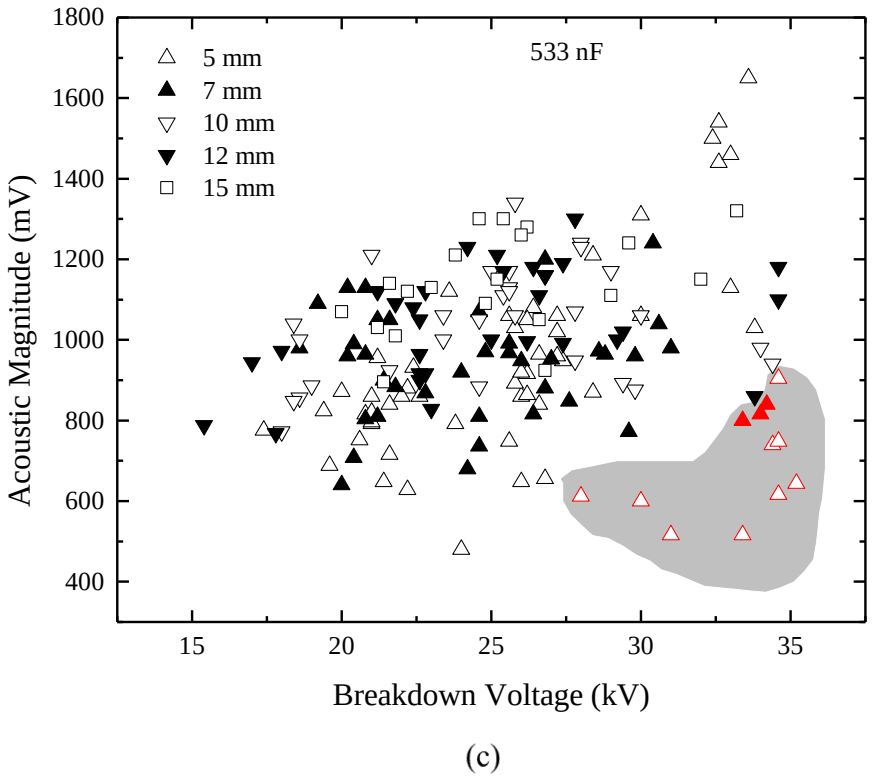

(c)

Figure 4-7. The acoustic magnitude as a function of the breakdown voltage for three values of capacitance: (a) 155 nF, (b) 266 nF, (c) 533 nF. The red data points in grey areas indicate obtained results where $R_{pl} < R_{circuit}$.

To establish an analytical link between the magnitude of the acoustic signals and the breakdown voltage, scaling relationship (4.14) is fitted to the experimental data in Fig. 4-8. The solid lines indicate the main trend fitted by (4.14) and dashed lines are upper and lower boundaries of the 95 % prediction intervals. The fitting procedure was also conducted in OriginLab Pro 9.0 software, k was used as a free parameter with known value of $\beta = 1.13$.

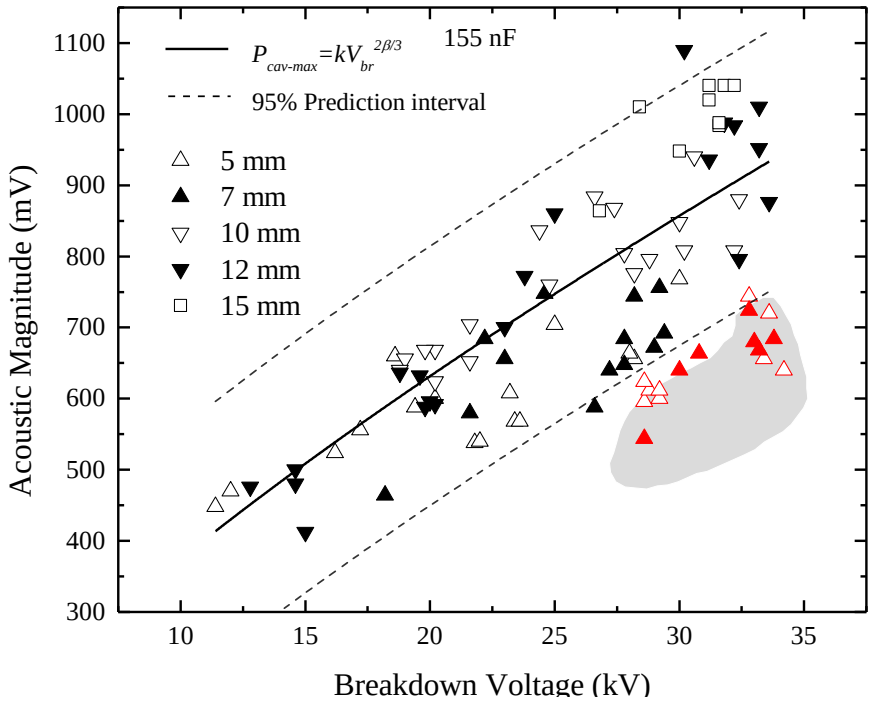
155 nF
$P_{cav\text{-}max}=kV_{br}^{2\beta/3}$
95% Prediction interval
5 mm
7 mm
10 mm
12 mm
15 mm
Acoustic Magnitude (mV)
Breakdown Voltage (kV)

(a)

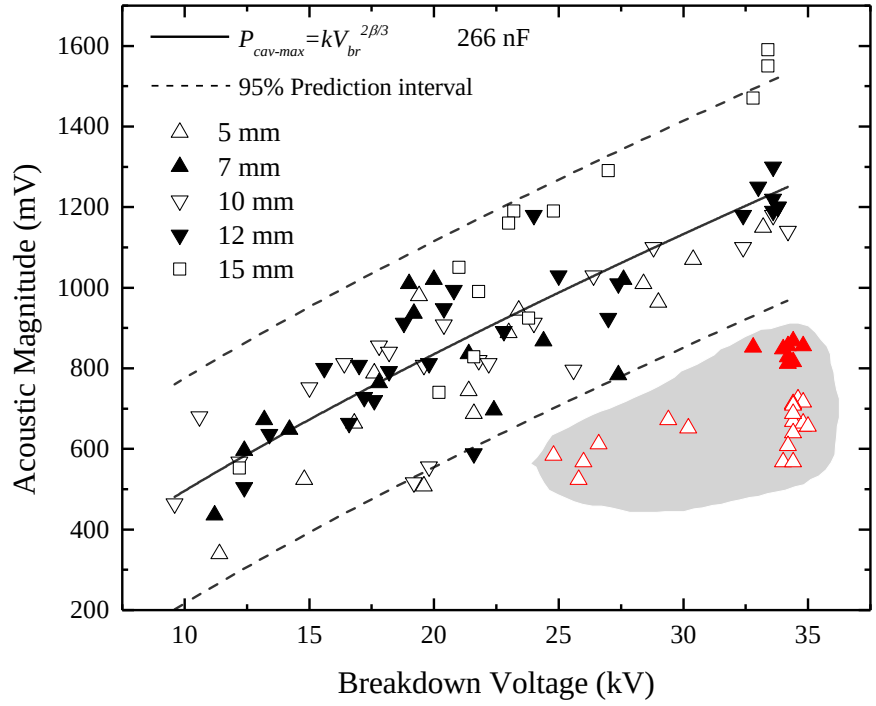
266 nF
$P_{cav\text{-}max}=kV_{br}^{2\beta/3}$
95% Prediction interval
5 mm
7 mm
10 mm
12 mm
15 mm
Acoustic Magnitude (mV)
Breakdown Voltage (kV)

(b)

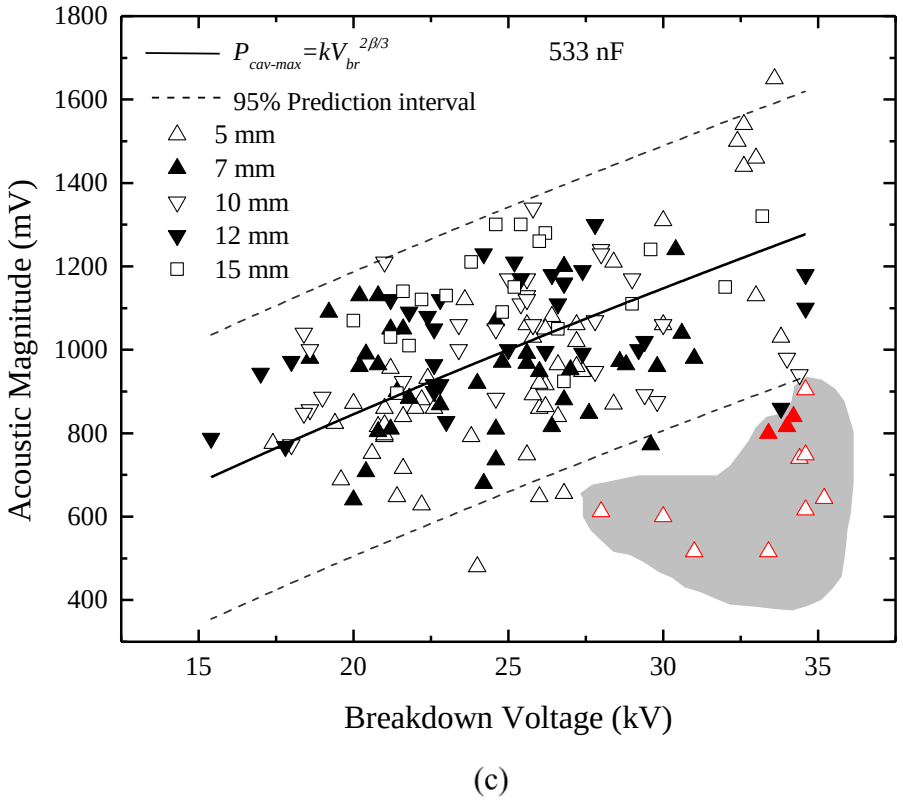

Figure 4-8. The fitting of (4.14) to the experimental data for all capacitance cases: (a) 155 nF, (b) 266 nF, (c) 533 nF, indicated by the solid lines. Dashed lines represent the upper and lower boundaries of the 95 % prediction intervals.

The obtained numerical values of k with their standard deviation for three different capacitances are given in Table. 4-2.

Table 4-2. Fitting parameters, k, of (4.14) to experimental results for three values of capacitance

C	155 nF	266 nF	533 nF
k	66.18 ± 1.39	87.44 ± 2.16	88.6 ± 2.12

As in the case of period of cavity oscillation, some data points have been found to be below the lower boundaries of the 95 % prediction intervals. These data points belong to the discharges with breakdown voltages > 20 kV and they are produced mainly in

short inter-electrode gaps (5 mm and 7 mm). Such clusters were also observed as the grey areas in Fig. 4-7, especially for the 155 nF and 266 nF cases. Similarly, these data points (T_{cavity}) were associated with the FD's whose plasma resistance was lower than the circuit resistance, $R_{pl} < R_{circuit}$. Their low values of energy conversion efficiency resulted in less energy delivered into the plasma channel and thereby weaker acoustic impulses even for high breakdown voltages.

The magnitudes of the acoustic impulses obtained in tests show significant sensitivity to variation in the inter-electrode gap. A clearly visible dispersion in the magnitude values and the wide prediction intervals can be found in Fig. 4-7 and Fig. 4-8. It was established that the acoustic magnitudes obtained in longer inter-electrode gaps are larger than those obtained in short inter-electrode gaps for the same values of breakdown voltage and capacitance. This proportionality relationship between the acoustic magnitude and the inter-electrode gap was also found in [35], [42], [126]. For example, in [126], with fixed capacitance of 5.22 μF and same breakdown voltage at ~14 kV, the peak pressure was ~10 MPa for 10 mm gap and it was only ~7 MPa for 5 mm gap. Such a dependency of acoustic magnitude on the inter-electrode gap was observed and confirmed in [35] under similar experimental conditions used in this work.

It is worthy of note that the increase in the acoustic magnitude by rising the capacitance from 266 nF to 533 nF was not as significant as that by rising capaictance from 155 nF to 266 nF. A possible explanation is that most of values of R_{pl} obtained for experimental data in the 533 nF case are either smaller than or close to $R_{circuit}$. In this case, their energy conversion efficiency is low and their energy delivered into the plasma channel will not be as high as it is expected. Therefore, less amount of data will be shown in the main trend in Fig. 4-7(c) and their acoustic magnitudes do not show significant increase with higher V_{br}.

Another suggestion is based on the investigation on the peak pressure generated by underwater spark discharge in [132]. In [132], a relationship between the peak acoustic pressure and the energy delivered into the spark channel from the breakdown moment to the moment when the channel expansion speed reaches its maximum, E^*, was established. It was found that the peak acoustic pressure is proportional to E^*. For example, in [132], similar values of peak pressure, ~ 11 MPa, were experimentally

obtained for underwater spark discharges with different energisation conditions (C = 5.22 uF and V_{br} = 13.11 kV; C = 1 μF and V_{br} = 16.18 kV) but with similar E^*~6 J. Therefore, in the 533 nF case presented in this work, similar acoustic magnitudes obtained for discharges with different breakdown voltages may result from negligible difference in their values of E^*. However, the study of the parameter $E^*$was out of scope of the present work and further investigation should be conducted to confirm this suggestion.

Despite the dispersion in acoustic magnitudes, the fitting of (4.14), together with the 95 % prediction intervals, provides a reasonable agreement with the experimental data for the 533 nF case in Fig. 4-8 (c). (4.14) can be used for estimation of acoustic magnitudes generated by underwater spark discharges with high energy levels.

4.4 Acoustic impulses: phenomenological link with the parameters of the pulsed driving circuit

In order to provide a more accurate calculation of the acoustic magnitude, an advanced analytical model has been developed based on (4.14) obtained in the 155 nF and 266 nF cases. As discussed above, the inter-electrode gap plays an important role in determining the acoustic magnitude. Therefore, the inter-electrode gap, l, is introduced in (4.14):

$$P_{cav-max} = k_{new} V_{br}^{2\beta/3} \tag{4.15}$$

$$k_{new} = A l^{f} C^{\beta/3} \tag{4.16}$$

where A and f are constant coefficients and k_{new} is the new proportionality coefficient between acoustic magnitude and the breakdown voltage.

The values of the coefficients, f and A for the 155 nF and 266 nF cases have been obtained by the fitting (4.16) to experimental data in Fig. 4-7 in OriginLab 9.0 software with known value of β = 1.13 (where $P_{cav\text{-}max}$ is in mV and V_{br} is in kV), which are shown in Table. 4-3.

Table 4-3. Fitting results of the coefficients, f and A, in (4.16) for 155 nF and 266 nF

Coefficients	155 nF	266 nF
f	0.255	0.189
A	6.00	6.54

The average values were calculated as $f = 0.22$ and $A = 6.27$ and the proportional relationship between $P_{cav\text{-}max}$ and V_{br}, C, and l is expressed as:

$$P_{cav-max} = Al^{0.22}C^{\beta/3}{V_{br}}^{2\beta/3} \quad (4.17)$$

Then, by adopting $A = 6.27$ in (4.17), a general scaling relationship (4.18) was obtained for FD's:

$$P_{cav-max} = 6.27l^{0.22}C^{\beta/3}{V_{br}}^{2\beta/3} \quad (4.18)$$

(4.18) allows the evaluation of $P_{cav\text{-}max}$ for given values of V_b, C, and l for the FD's corresponding to $R_{pl} > R_{circuit}$.

In order to verify the model (4.18) in describing the acoustic magnitude, the variation of the ratio, $P_{cav\text{-}max}/{V_{br}}^{2\beta/3}$, as a function of l was obtained for the 266nF and 533nF cases and is shown in Fig. 4-9. Solid lines correspond to a specific capacitance value in Fig. 4-9.

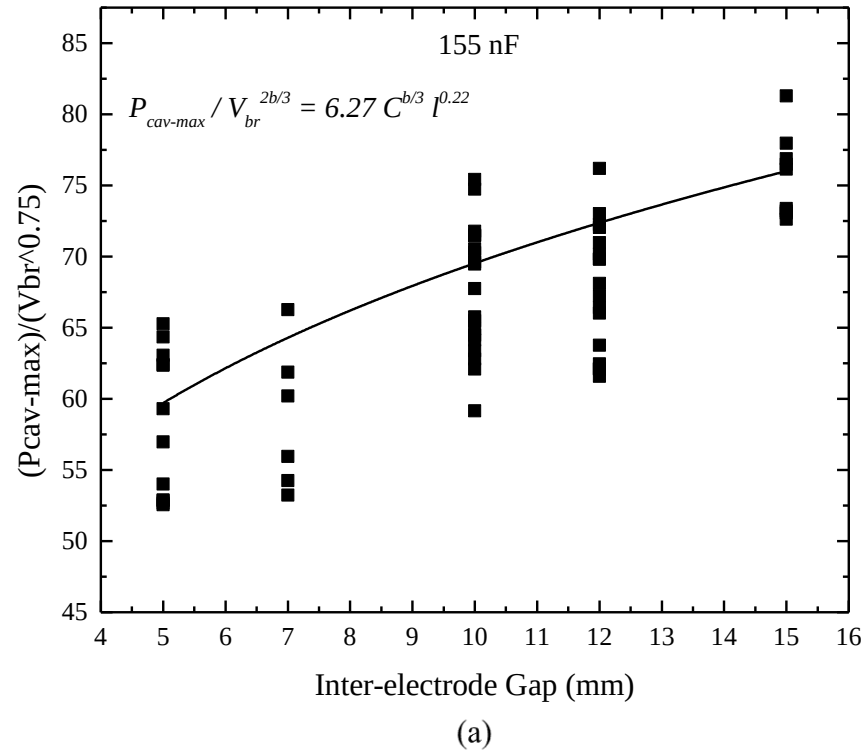

Figure 4-9. The ratio, $P_{cav\text{-}max}/V_{br}^{2\beta/3}$, as a function of l for (a) 155 nF and (b) 266 nF. Solid lines show the model: $P_{cav\text{-}max}/V_{br}^{2\beta/3} = 6.27C^{\beta/3}l^{0.22}$.

It can be seen that values of the ratio, $P_{cav\text{-}max}/V_{br}^{2\beta/3}$, for both 155 nF and 266 nF cases follow the general tendency with the variation of the inter-electrode gap, $l^{0.22}$, as indicated in (4.18), meaning the relationship (4.18) being suitable for acquisition of acoustic magnitude. The relationship between $P_{cav\text{-}max}$ and l, as described by (4.18), emphasises the important role of l in generating underwater acoustic impulses. It is worthy of note that (4.18) is an empirical relationship obtained with the purpose of establishment of more accurate link between $P_{cav\text{-}max}$ and V_{br} than it was done by (4.14). Model (4.18) is dedicated to the FD's case and its further applicability in other types of underwater spark discharges has to be verified. The data points ($P_{cav\text{-}max}$), which correspond to situation where $R_{pl} < R_{circuit}$, are excluded.

4.5 The hydrodynamic parameters: The role of the plasma resistance

4.5.1 Validation of the constant plasma resistance model

The plasma resistance is an important electrical parameter of the plasma channel. It defines energy partition between the plasma channel and the discharge circuit and thereby the hydrodynamic parameter of the plasma cavity and the characteristics of the acoustic impulses emitted by this cavity. This resistance helps to establish a link between these parameters. Therefore, the relationship between T_{cavity}, $P_{cav\text{-}max}$ and R_{pl} is one of the focusing points in present work.

This section presents the study of the constant plasma resistance for all conducted FD's tests. The impact of the plasma resistance on the electrical energy conversion efficiency is discussed in details. The relationships between the acoustic and hydrodynamic parameters, T_{cavity}, $P_{cav\text{-}max}$, and the plasma resistance are obtained and analysed.

As discussed in Section 2.5.3, once the plasma channel is established between the HV and ground electrodes, the resistance of the plasma channel drops to a relatively low value range (mΩ), compared to its initial high value (hundreds' of Ω) [110]. Thus, the conductive current starts to flow. The development of the plasma channel is a dynamic process during the post-breakdown stage, meaning that its resistance has a time-dependent dynamic behaviour. Such a varying plasma resistance ideally can be calculated as the ratio of the voltage and current signals. However, as pointed out in

[133], [134], the main obstacles in its direct measurement are the transient behaviour of the voltage and current in the circuit, and potential reactive components in the plasma-channel impedance. Therefore, this method of direct measurement of plasma resistance was not used in this work. Instead, an alternative method was applied which allows for calculation of the plasma resistance. This method is based on equations (2.22) - (2.23) which represent the transient current behaviour during the discharge period. This method is based on the assumption that the capacitive and inductive parts of the plasma impedance are not taken into account or they are treated as embedded within the circuit parameters, C and L. Thus, this model only focuses on the resistive component of the plasma channel impedance. A schematic diagram for the simplified discharge circuit is shown in Fig. 4-10.

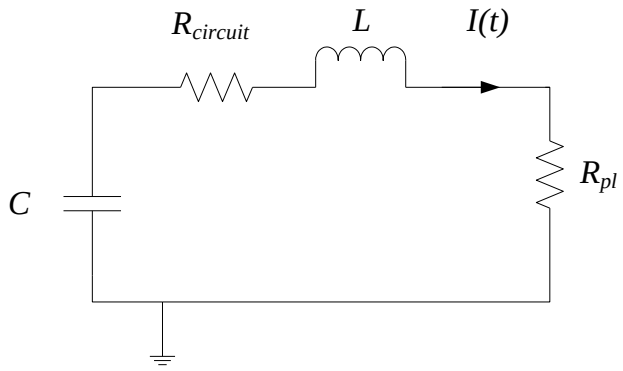

Figure 4-10. The schematic diagram of the simplified discharge circuit by focusing only on resistive impedance of the plasma channel.

To verify the constant plasma resistance model, an example of fitting of (2.22) to the current measurement waveform is shown in Fig. 4-11, as indicated by black solid line. The experimental data of current was obtained from Fig. 4-1(b). This fitting shows a good agreement with the experimental data, especially for the first few cycles of the current oscillation, accounting for the most part of the energy delivered into the plasma channel. The insignificant dispersion between the fitting line and the experimental data at the end of the waveform is due to the unstable extinction process of the plasma channel, which does not affect significantly the overall energy dissipating stage. Therefore, the resistance obtained from this current model can be used as an effective

value of the plasma resistance for describing its general behaviour during the discharge. This constant resistance will also be used in the analysis on the energy partition in Section 4.7 and 4.8. Similar validation process of the constant resistance model was conducted in [32], [70], [82], [118] by comparing the computed results and the experimental data (current waveforms). The analysis in the upcoming sections will be based on the constant plasma resistance model.

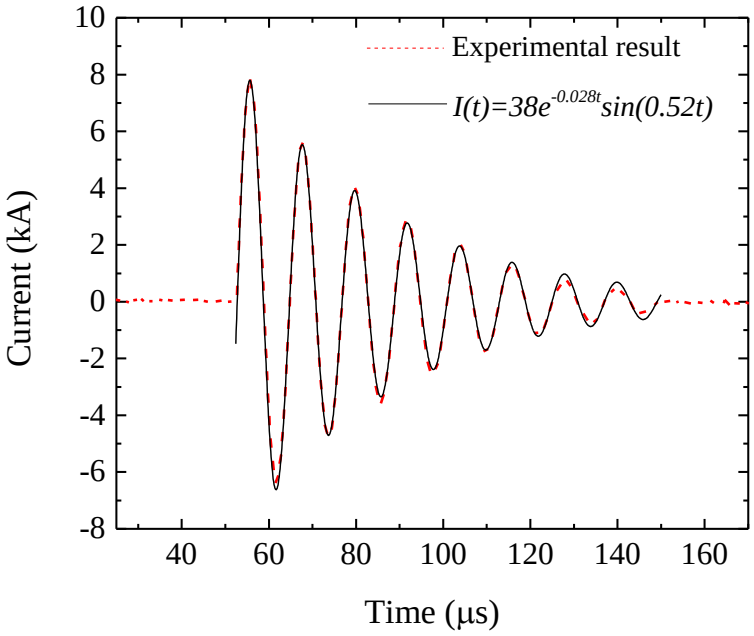

Figure 4-11. Comparison between the experimental current measurement and the analytical result obtained by (2.22) with constant plasma resistance. Red dashed line represents the experimental data obtained from Fig. 4-1(b) and black solid line shows the computed result of (2.22).

The resistance of the plasma channel was obtained for all tests conducted for FD's. This was achieved using the 'dumped sinusoidal' fitting function in OriginLab 9.0 software. The constant value of the plasma resistance, R_{pl}, cannot be directly calculated from (2.22)-(2.23) as the resistance term covers all resistive circuit elements. Therefore, the circuit resistance was calculated for each capacitance case by short-circuiting the discharge circuit. The results are shown in Table. 4-4. Then, the total discharge resistance for each FD's test was obtained from the experimental current waveform

and the plasma resistance was calculated as the difference between the total resistance and the circuit resistance, (2.21).

Table 4-4. The circuit resistance, $R_{circuit}$ obtained from short-circuit condition for different value of capacitance

C (nF)	$R_{circuit}$ (Ω)
155	0.534
266	0.401
533	0.273

4.5.2 Period of the cavity oscillation as a function of the plasma resistance

Fig. 4-12 shows the behaviour of the period of the cavity oscillation as a function of the calculated plasma resistance for all three capacitances. The resistance of the discharging circuit, obtained in short-circuit condition, is also indicated by vertical lines in these figures. It can be seen that the value of plasma resistance for different discharges varies in a wide range from ~ 35 mΩ up to ~ 5.9 Ω.

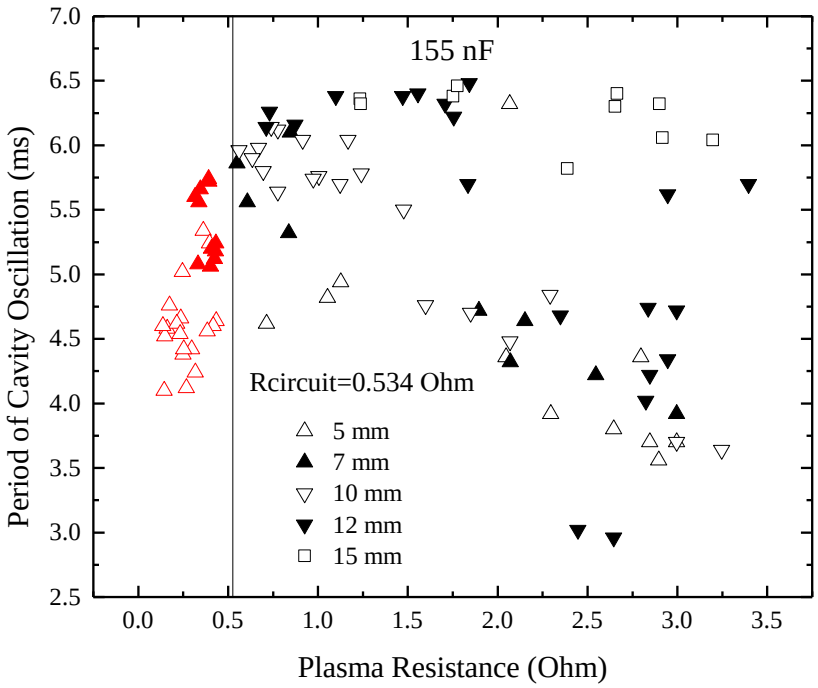

(a)

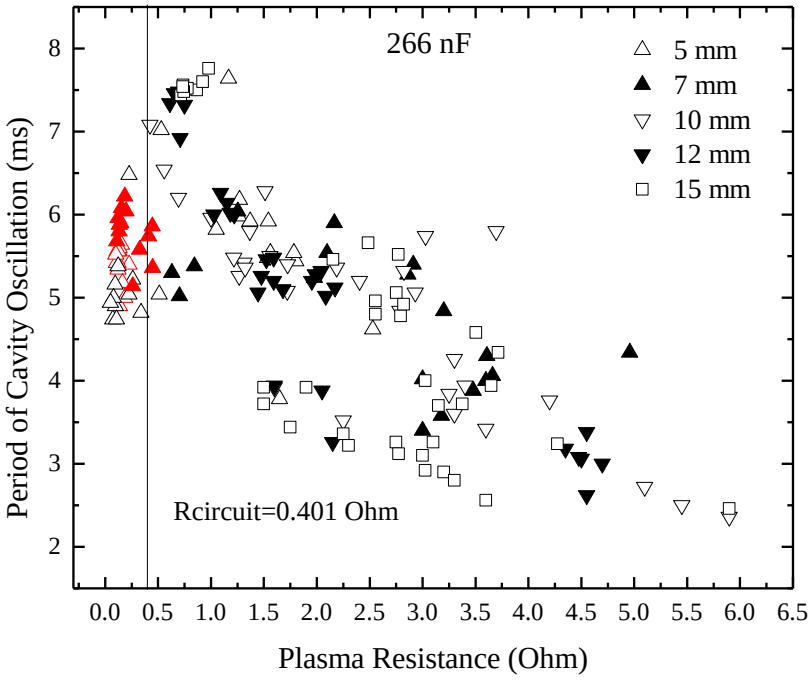

(b)

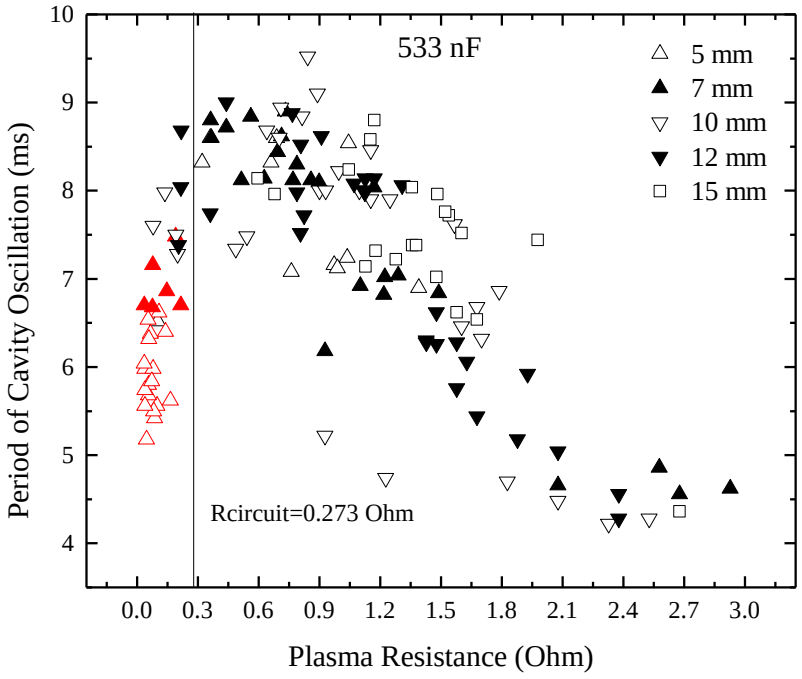

(c)

Figure 4-12. The period of cavity oscillation as a function of the plasma resistance for all three cases of capacitance: (a) 155 nF, (b) 266 nF, (c) 533 nF. Solid lines indicate the circuit resistance for each case and data points in red correspond to the outlying data shown in Fig. 4-3.

Two major pulsed driving circuit characteristics define the values of the plasma resistance: the energy available at breakdown ($CV_{br}^2/2$) and the inter-electrode gap, l. With the purpose of conducting straightforward analysis, the effective constant plasma resistance, R_{pl}, can be described by the following proportional relationship between R_{pl} and the physical parameters of the plasma channel:

$$R_{pl} \propto \rho_{re} \frac{l_{resistive}}{A_{resistive}} \tag{4.19}$$

where $l_{resistive}$ is the length of the resistive material, $A_{resistive}$ is the cross-sectional area of the specimen and ρ_{re} is the electrical resistivity.

In this work, the length of the resistive plasma channel is governed by the inter-electrode gap, l, and the electrical resistivity is related to the energisation (ionisation) level. Therefore, longer inter-electrode gap generally results in longer potential plasma channel path and thereby larger plasma resistance. On the other hand, the higher energy level (increase in either C or V_{br}) generally produces lower electrical resistivity. In conclusion, discharges achieved in long inter-electrode gaps but with low breakdown voltages will have higher values of R_{pl} than those obtained in short gaps with high breakdown voltages. Therefore, the outlying data points (T_{cavity} and $P_{cav\text{-}max}$) for 5 mm and 7 mm gaps observed with high breakdown voltages in Fig. 4-3 and Fig. 4-7 belong to discharges with plasma resistance smaller than the circuit resistance, as shown by red data points in Fig. 4-12. It is worthy of note that higher values of plasma resistance ($R_{pl} > 4.0\ \Omega$) have been registered in the 266 nF case, as compared with those in the 155 nF case. The reason is related to the minimum voltage level to initiate breakdown in different gaps. For long inter-electrode gaps (12 mm and 15 mm), breakdown could be successfully triggered using 25 kV and 266 nF capacitance. However, in the 155 nF case, 30 kV or 35 kV charging voltages were required to achieve breakdown in these gaps. Therefore, the largest plasma resistance value, which corresponds to 155 nF, 25 kV case, was not included in the experimental results as it was practically unable to achieve breakdown using these parameters.

For all three cases shown in Fig. 4-12, the variation of T_{cavity} as a function of R_{pl} followed a similar tendency: the values of T_{cavity} initially showed a significant

difference within a range of small R_{pl}; with an increase in R_{pl}, values of T_{cavity} reached their peak values and then started to decrease nonlinearly with further increase in R_p. The period for all three capacitance cases reach their peak values when R_{pl} and $R_{circuit}$ were comparable: ~ (0.5 - 1.0) Ω for 155 nF, ~ (0.50 - 0.75) Ω for 266 nF, ~(0.30 - 0.60) Ω for 533 nF. This peak performance can be explained by the optimal combination of the breakdown voltage and the energy conversion efficiency. For resistances smaller of higher than the peak values, the value of T_{cavity} (which directly related to the energy dissipated in plasma) decreases due to either the decrease in breakdown voltage (higher values of resistance) or sharp changing in the energy conversion efficiency (lower values of resistance).

4.5.3 Efficiency of energy conversion

In the discussion of the dependency of T_{cavity} and $P_{cav\text{-}max}$ on V_{br}, (Section 4.2 - 4.4) the concept of the efficiency of energy conversion has been introduced to explain the experimental discharges data outside from the main trend lines in Fig. 4-3 and Fig. 4-7 for short 5 mm and 7 mm gaps for high breakdown voltages. The key to this discussion was the relationship between the plasma resistance and circuit resistance. In order to conduct a detailed analysis of the energy disposition process, the resistance is isolated from the circuit as the active power is consumed only by the resistive components.

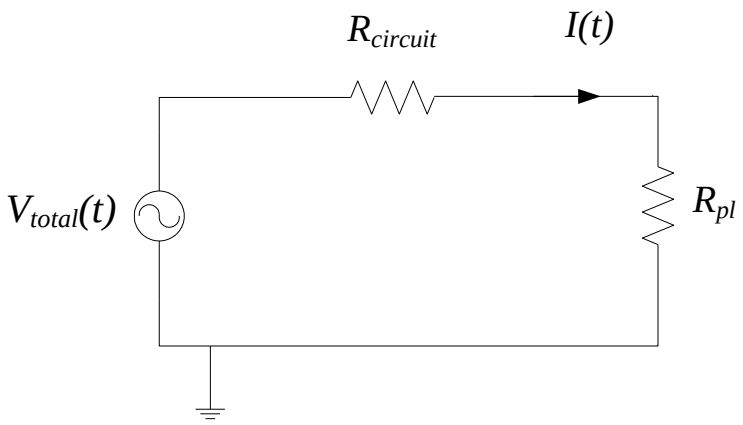

Figure 4-13. The simplified discharge circuit with only resistive elements included. $V_{total}(t)$ represents the total voltage occupied by $R_{circuit}$ and R_{pl}, $I(t)$ represents the circuit current.

Fig. 4-13 illustrates the energy-consuming components of the discharging circuit, which is simplified to a resistive network. $R_{circuit}$ represents the circuit resistance and R_{pl} is the effective plasma resistance. $V_{total}(t)$ is the total discharge voltage seen by $R_{circuit}$ and R_{pl} during the energy deposition stage. Based on this circuit, the efficiency of energy conversion, η_{pl}, is defined as a ratio of the energy delivered to the plasma channel E_{pl}, to the total energy dissipated in the circuit including the load (plasma channel), $E_{v(t)}$:

$$\eta_{pl} = \frac{E_{pl}}{E_{v(t)}} \tag{4.20}$$

For specific duration of discharge, from 0 s to T_d , both E_{pl} and $E_{v(t)}$ can be calculated as integrals of the transient power in the circuit, $P_{Ev(t)}$, and in the plasma channel, P_{pl}, therefore (4.20) can be rewritten as:

$$\eta_{pl} = \frac{E_{pl}}{E_{v(t)}} = \frac{R_{pl}\int_0^{T_d} I(t)^2 dt}{(R_{pl}+R_{circuit})\int_0^{T_d} I(t)^2 dt} \tag{4.21}$$

As the model circuit consists of a single loop, the overall energy conversion efficiency can be calculated by the ratio of the load resistance (the resistance of the plasma channel) and the total resistance of the circuit:

$$\eta_{pl} = \frac{R_{pl}}{R_{pl} + R_{circuit}} \tag{4.22}$$

For mathematical simplification, the ratio $x = \frac{R_{pl}}{R_{circuit}}$ can be introduced and (4.22) can be re-written as:

$$\eta_{pl} = \frac{x}{1+x}, x = \frac{R_{pl}}{R_{circuit}}, \quad x > 0 \tag{4.23}$$

Therefore, the energy conversion efficiency can be plotted as a function of x in Fig.4-14.

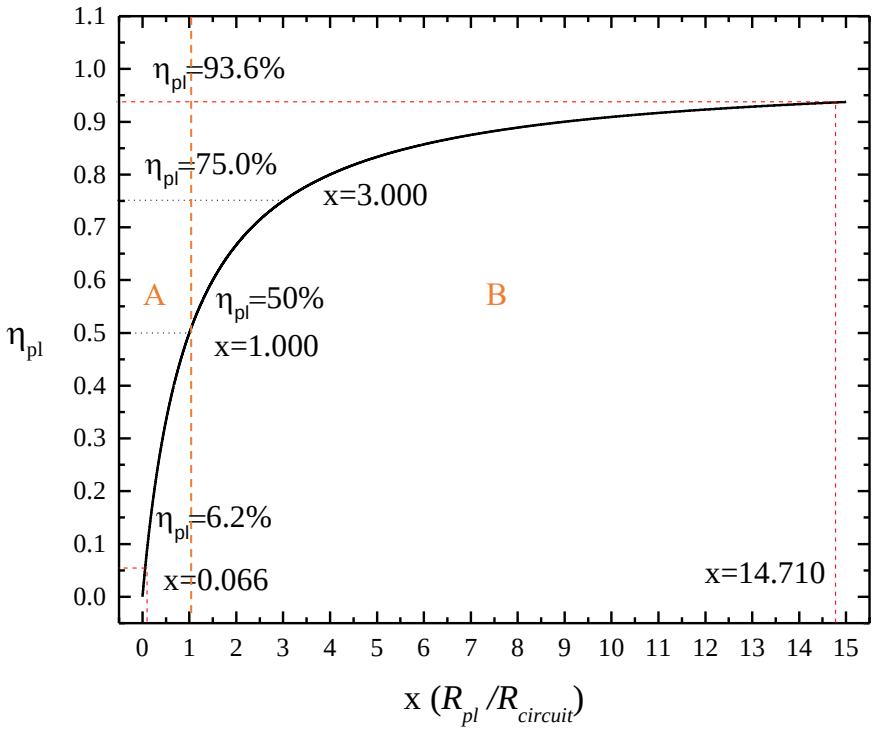

Figure 4-14. The electrical energy conversion efficiency as a function of the ratio of the plasma resistance and the circuit resistance. Several important moments with values of η_{pl} are marked as when $R_{pl} = R_{circuit}$, $R_{pl} = 3R_{circuit}$ and the smallest and largest values of x obtained in this work: 0.066, 14.710. A indicates the area in which $R_{pl} < R_{circuit}$ and B indicates the area in which $R_{pl} > R_{circuit}$.

Based on the values of the effective plasma resistance obtained for all discharge tests and the circuit resistance given in Table. 4-4, x was calculated in a range from 0.066 to 14.71 and the corresponding efficiency is in a range from 6.2% to 93.6%. It has to be mention that these values of the energy conversion efficiency given by (4.23) are obtained with some assumptions as made above. They cannot be used for accurate calculation of the energy partition for underwater spark discharges. However, they can

be used in engineering practice for analysis of the energy efficiency of the underwater spark discharges. Therefore, information given in Fig. 4.14 can be used as an effective reference material for further understanding and analysis of the relationships shown in Fig. 4-12.

The different variations in η_{pl} for different ranges of x values define the nonlinear behaviour of the variation of T_{cavity} with R_{pl}. Two critical points have been highlighted in Fig. 4-14 when x is equal to 1 and equal to 3 and the efficiency, η_{pl}, corresponds to 50% and 75% respectively. For x increasing in the range from 3.0 to 14.7, the energy conversion efficiency experiences a slow increasing trend from 75% to 93.6%. However, it shows a relatively faster increasing trend from 6.2% to 50% when x varies in a small range from 0.066 to 1.000.

As mentioned in previous section, the plasma resistance generally increases with the decreasing breakdown voltage and vice visa. Therefore, the value of x will follow a similar tendency with the variation in breakdown voltage. When the breakdown voltage increases from ~7.5 kV to ~20 kV, x decreases from ~ 14.7 to ~ 3.0 and η_{pl} decreases from ~ 93 % to ~ 75 %. The total energy increased by highr V_{br} dominate the slowly-dropping η_{pl}, still resulting in an increase in E_{pl} and thereby longer T_{cavity}. In other words, the dominant circuit parameter, which governs the energy delivered into the plasma channel in this particular x range, is V_{br} rather than η_{pl}. Such a relationship between V_{br} and η_{pl} corresponds to discharges with plasma resistances higher than circuit resistance in Fig. 4-12.

With further increase in the breakdown voltage from ~20 kV to ~25 kV, x enters the range from 1 to 3 and η_{pl} experiences a transition stage where its decreasing trend shifts from slow to fast. In this range of x, the increase in the total energy by higher V_{br} is compensated by the decrease of η_{pl}, resulting in no significant increase in E_{pl}. Therefore, T_{cavity} obtained in this range reaches their peak values as demonstrated by the peak value range in Fig. 4-12. This also explains why the R_{pl} obtained for peak values of T_{cavity} are equal to or slightly larger than the corresponding $R_{circuit}$ as observed in Fig. 4-12. Values of x for most of the experimental results obtained in 10 mm, 12 mm and 15 mm gaps and some in 5 mm and 7 mm gaps with relatively low breakdown voltages were in the range from 1 to 14.71, which correspond to the main trend described by (4.9) and (4.14).

As the breakdown voltage keeps increasing from ~25 kV to ~35 kV and the value of x finally drops below 1, thus, even a small decrease in R_{pl} (increase in V_{br}) will cause significant reduction in η_{pl}. Therefore, η_{pl}, instead of V_{br}, becomes the dominant parameter in determining the energy delivered into the plasma channel and in low values of η_{pl}. It puts a limitation on the potential increase in E_{pl}, resulting in no increase or even decrease in the final output of T_{cavity}. This particular relationship between V_{br} and η_{pl} explains the outlying data points (T_{cavity}) below the main trend for 5 mm and 7 mm gaps in Fig. 4-3 and the data points with plasma resistances smaller than the circuit resistance in Fig. 4-12.

In conclusion, the plasma resistance, together with the breakdown voltage, plays an important role in determining the energy delivered into the plasma channel for each individual discharge. The breakdown voltage (for a given value of the storage capacitance) defines amount of total energy available in the circuit after breakdown. The ratio of the plasma resistance to the circuit resistance, x, defines the energy partition between the circuit and the plasma channel and thereby the period of the cavity oscillation. The specific link between V_{br} and T_{cavity} through R_{pl}, η_{pl} and E_{pl} results in the relationship observed in Fig. 4-3. A similar observation has also been obtained for the relationship between the plasma resistance and acoustic magnitude, which will be shown in the next section.

4.6 The acoustic magnitude as a function of the plasma resistance

The relationships between the plasma resistance and the acoustic magnitude for all three values of capacitance are shown in Fig. 4-15. The values of the plasma resistance obtained for all tests vary from ~ 28 mΩ to ~ 4.27 Ω and the largest value was observed in the 266 nF case. Similar to the observation in Fig. 4-12, there was no breakdown event achievable with charging voltage level less than 30 kV for 155 nF and thereby no particularly large plasma resistance was seen in the 155 nF case. However, the acoustic magnitudes in Fig. 4-15 show clear spread between different inter-electrode gaps. This is due to the impact of the inter-electrode gap on the magnitude of the acoustic impulses as indicated by (4.18).

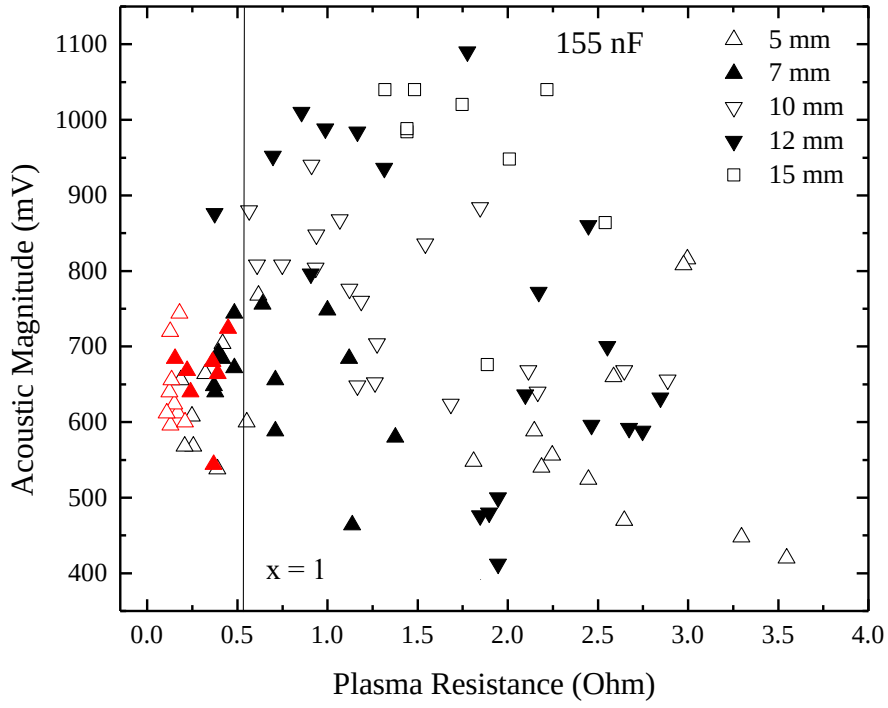
155 nF
5 mm
7 mm
10 mm
12 mm
15 mm
x = 1
Acoustic Magnitude (mV)
Plasma Resistance (Ohm)
1100
1000
900
800
700
600
500
400
0.0
0.5
1.0
1.5
2.0
2.5
3.0
3.5
4.0

(a)

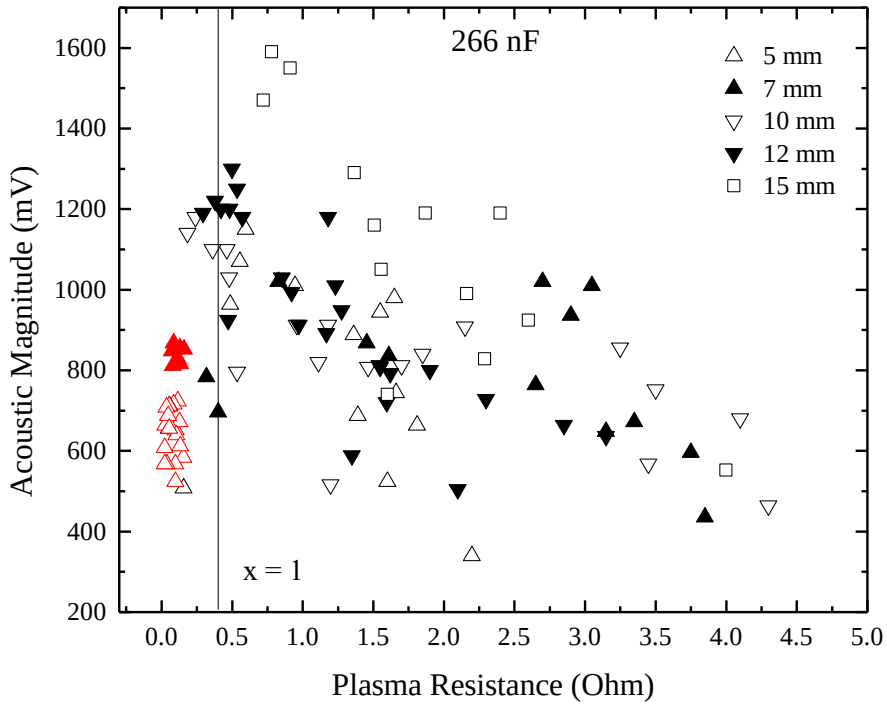
266 nF
5 mm
7 mm
10 mm
12 mm
15 mm
x = 1
Acoustic Magnitude (mV)
Plasma Resistance (Ohm)
1600
1400
1200
1000
800
600
400
200
0.0
0.5
1.0
1.5
2.0
2.5
3.0
3.5
4.0
4.5
5.0

(b)

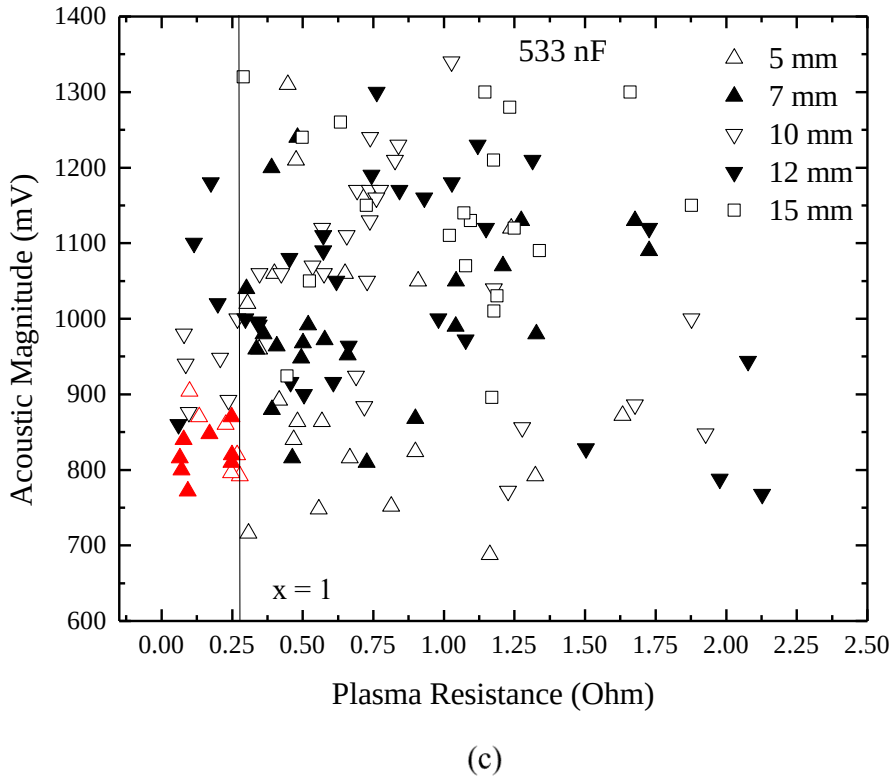

(c)

Figure 4-15. The acoustic magnitude as a function of the plasma resistance for all three cases of capacitance: (a) 155 nF, (b) 266 nF, (c) 533 nF. Solid lines indicate the circuit resistance for each case and data points in red correspond to the outlying data shown in Fig. 4-7.

The tendency obtained in Fig. 4-15 is similar to that for the period of cavity oscillation shown in Fig. 4-12. Initially, the acoustic magnitude shows a significant change with the variation in the plasma resistance when $R_{pl} < R_{circuit}$ and the value of the magnitude is increasing as R_{pl} is getting closer to $R_{circuit}$. Maximum values of the acoustic magnitude are observed when the plasma resistance is in the range from ~ $R_{circuit}$ to ~ $3R_{circuit}$ (circuit resistance), especially for the 155 nF and 266 nF cases. With further increase in the plasma resistance beyond this range, the acoustic magnitude decreases. This general relationship between the acoustic magnitude and the plasma resistance can be explained by the relationship between the energy conversion efficiency and the plasma resistance. Also, the link between the breakdown voltage and the acoustic magnitude, which is a function of the inter-electrode gap, l, (4.17) should be taken into consideration.

The values of resistances, which correspond to the peak acoustic magnitude in Fig. 4-15, are: ~ (0.60 - 1.30) Ω for 155 nF, ~ (0.50 - 0.85) Ω for 266 nF. However, it is difficult to define an accurate range for the 533 nF case. As discussed in Section 4.2.4, when x ($R_{pl}/R_{circuit}$) is lying in the range from 1 to 3, which is the case for almost all experimental results for C = 533 nF, the combination of the energy conversion efficiency and the breakdown voltage resulted in an (almost) constant E_{pl} and thereby there is no significant change in the acoustic magnitude.

In conclusion, similar to the period of cavity oscillation, the behaviour of the acoustic magnitude follows a specific tendency where the peak values occur when the plasma resistance is close to the circuit resistance, especially for the 155 nF and 266 nF cases. This tendency can be explained by the relationship between the energy conversion efficiency and the plasma resistance together with the dependency of the acoustic energy on energy dissipated into the plasma channel. The functional behaviour of acoustic magnitude in the 533 nF case is not well-defined due to the generally small values of plasma resistance for this capacitance.

4.7 The hydrodynamic parameters as functions of the energy delivered into the plasma channel

The energy delivered into the plasma channel through the Joule heating, E_{pl}, is a critical electrical parameter, which defines the strength of the acoustic impulse and the dynamic oscillation of the cavity. E_{pl} is parted into components associated with all post-breakdown processes, such as the development of the plasma channel, expansion of the gas cavity, emission of the acoustic pressure waves, emission of lights and heat transmission with surrounding water.

The energy delivered into the plasma spark channel can be calculated in the approximation of the lumped element RLC circuit:

$$E_{pl} = R_{pl} \int_{0}^{T_{current}} I(t)^2 dt \tag{4.24}$$

where $T_{current}$ refers to the moment of current disappearance; R_{pl} is the constant (effective) plasma resistance; $I(t)$ is the current obtained from the experimental measurements.

The integration in (4.24) was conducted in Microsoft Excel software. E_{pl} for all FD's tests conducted in this work have been calculated and its relationships with T_{cavity} and $P_{cav\text{-}max}$ will be discussed in detail in following sections.

Fig. 4-16 shows the relationship between the period of cavity oscillation and the energy delivered into the plasma channel for all three values of capacitance. It was found that for all three cases the period of the cavity oscillation increases with the increasing energy delivered into the plasma channel.

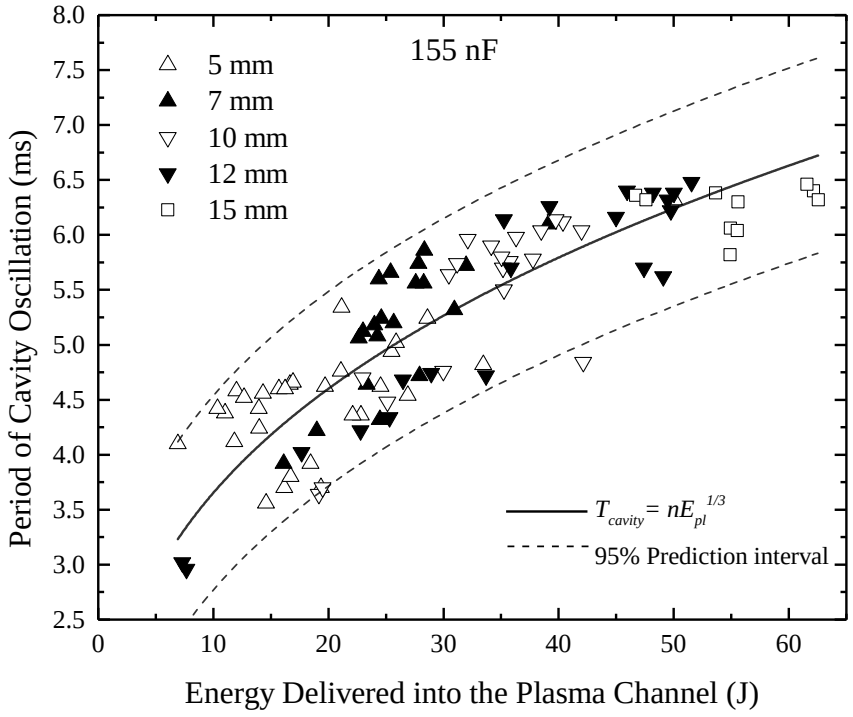

(a)

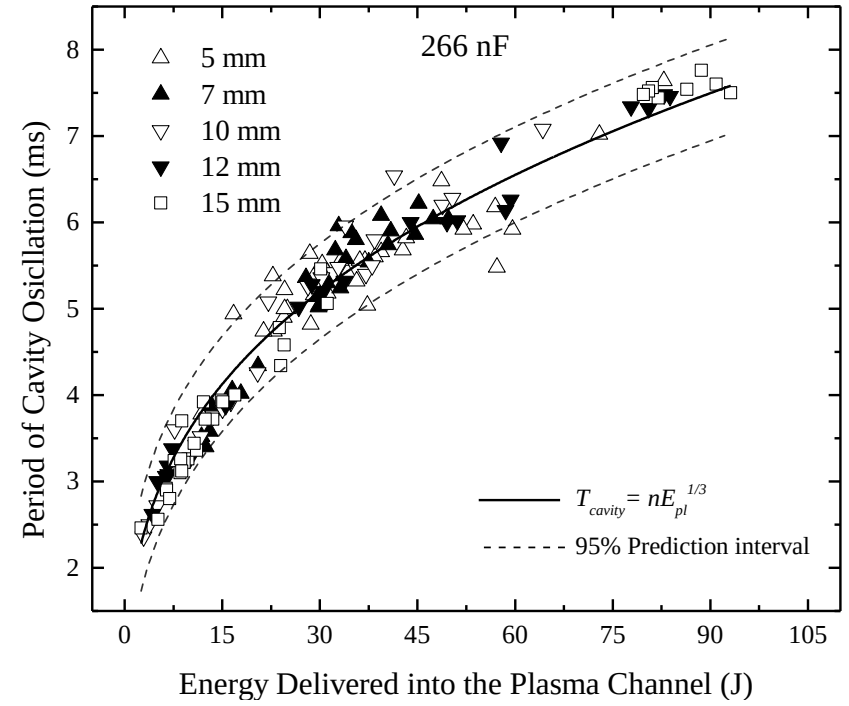

(b)

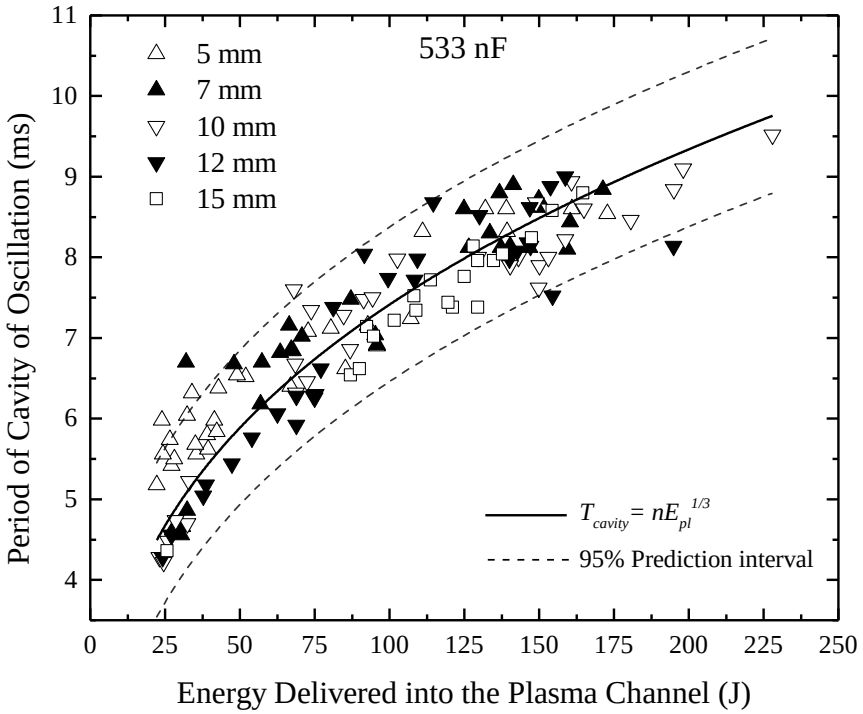

(c)

Figure 4-16. The relationship between T_{cavity} and E_{pl} for all three cases of capacitance: (a) 155 nF, (b) 266 nF, (c) 533 nF. Solid lines show the fitting results of (4.26) and dashed lines indicate the upper and lower boundaries of the 95 % prediction intervals.

The analytical link between the T_{cavity} and E_{pl} can be found by the combination of (4.3) and (4.7):

$$T_{cavity} = 1.14\delta^{1/3}{\rho_0}^{1/2}{E_{pl}}^{1/3}{P_\infty}^{-5/6} \quad (4.25)$$

For constant values of the parameters, ρ_o and p_∞, the relationship (4.25) can be simplified by introducing coefficient, *n,* as:

$$T_{cavity} = nE_{pl}^{1/3} \quad (4.26)$$

To verify scaling relationship (4.26) for the tendency shown in Fig. 4-16, fitting of (4.26) to the experimental data was conducted by using OriginLab 9.0 software. The fitting lines are plotted as the solid lines in Fig. 4-16 and the dashed lines indicate the corresponding upper and lower boundaries of the 95 % prediction intervals. The coefficient, *n*, was a free fitting parameter and its values obtained for different capacitances are shown in Table. 4-5.

Table 4-5. Values of coefficient, *n*, in (4.26) for 155 nF, 266 nF and 533 nF

Capacitance	155 nF	266 nF	553 nF
n	1.69 ± 0.02	1.68 ± 0.01	1.59 ± 0.02

It can be seen that the fitting curves show a satisfying agreement with the experimental results for all cases. Most of the data points (T_{cavity}) obtained from experimental measurements are included within the upper and lower boundaries of the 95 % prediction intervals. The values of the numerical coefficient, *n*, obtained for different capacitance cases are similar to each other, meaning the storage capacitance being no longer a variable as is in (4.10) since it has already included in the calculation of E_{pl}. Therefore, the combination of the three cases, as shown in Fig. 4-17, provides a better description of a general tendency.

A general value of the coefficient, n, can be obtained as the average of the values in Table. 4-5 and it gives:

$$T_{cavity} = 1.65 E_{pl}^{1/3} \tag{4.27}$$

Equation (4.27) has been plotted in Fig. 4-17. It can be seen that (4.27) describes the functional behaviour of the period of cavity oscillation reasonably and can be used for calculation of the expected value of T_{cavity} for a given value of E_{pl}. Also, (4.27) confirms that the inter-electrode gap makes no significant impact on the cavity oscillation dynamics.

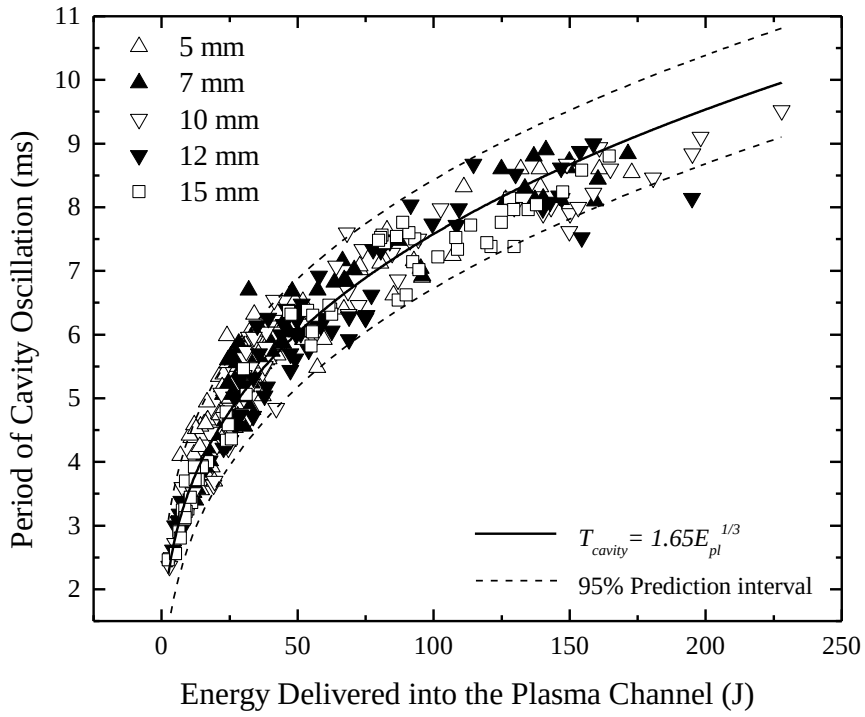

Figure 4-17. The combined results of T_{cavity} as a function of E_{pl} for the 155 nF, 266 nF and 533 nF cases, together with the fitting results of (4.26) (solid lines) and corresponding upper and lower boundaries of the 95 % prediction intervals (dashed lines).

It is worthy of note that there is no data cluster locating outside the main tendency in Fig. 4-16 as it has been observed for 5 mm and 7 mm gaps in Fig. 4-3. As discussed in Section 4.2, the main trend between the period of cavity oscillation and the breakdown voltage can be described by model (4.9) derived from (4.1)-(4.8). This procedure connects the energisation parameters and the acoustic output. This process contains several energy transfer stages, from energy stored in capacitance to E_{br}, and from E_{br} to E_{pl}. However, equation (4.26) takes only E_{pl} into consideration and other energy transfer stages are accounted for by the energy conversion efficiency.

4.8 The acoustic magnitude as a function of the energy delivered into the plasma channel

The acoustic magnitude as a function of the energy delivered into the plasma channel for all three values of capacitance and all inter-electrode gaps is shown in Fig. 4-17.

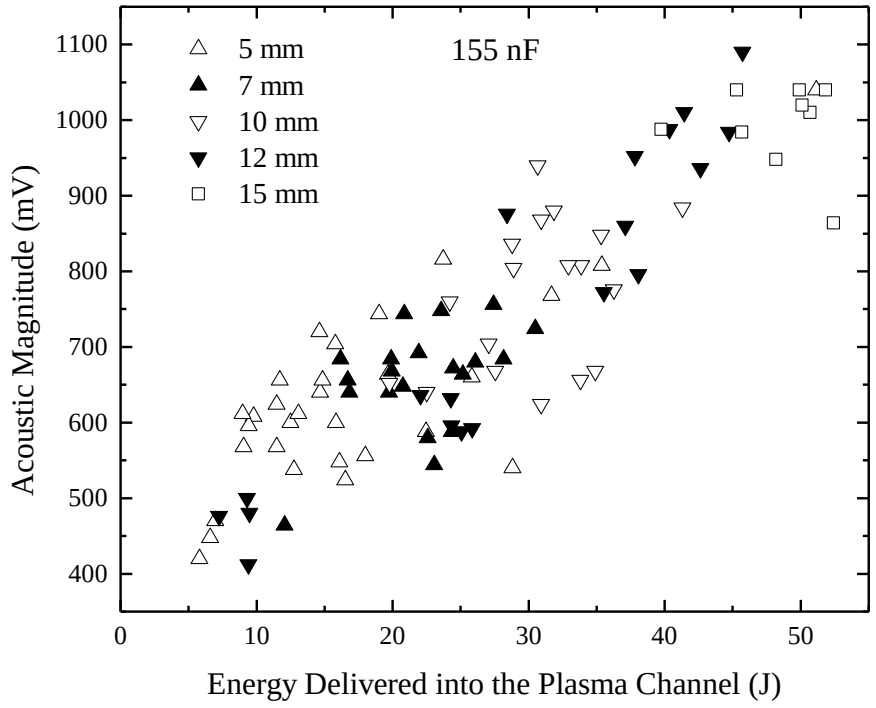

(a)

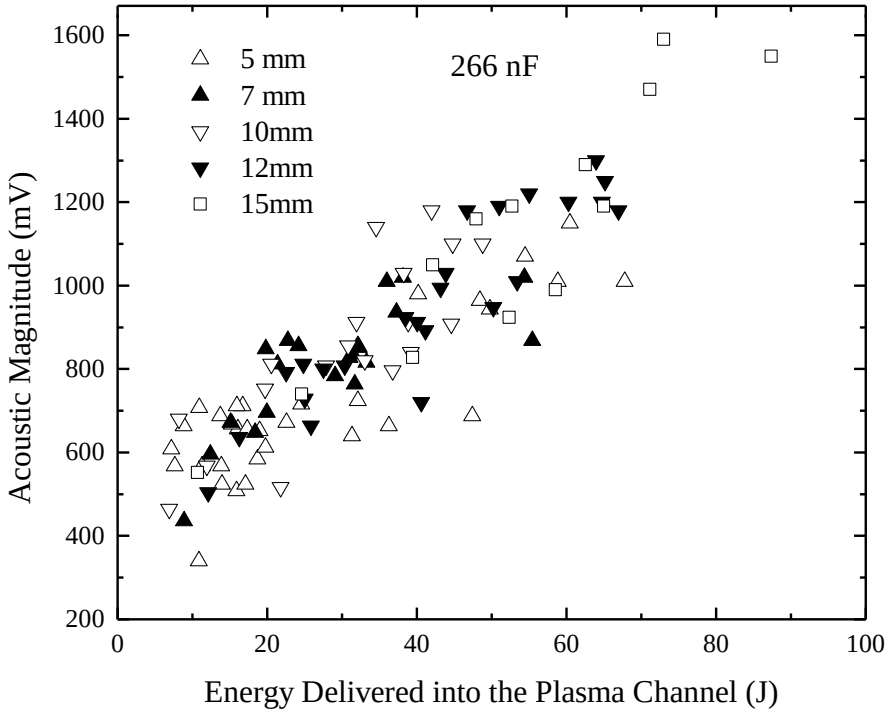
5 mm
7 mm
10mm
12mm
15mm
266 nF
Acoustic Magnitude (mV)
Energy Delivered into the Plasma Channel (J)
1600
1400
1200
1000
800
600
400
200
0
20
40
60
80
100

(b)

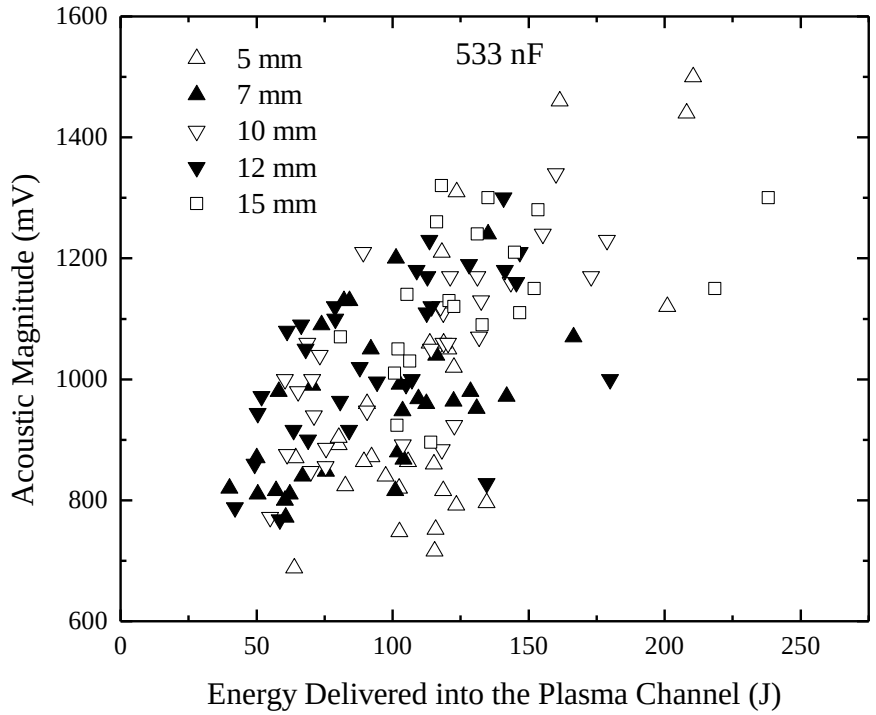
5 mm
7 mm
10 mm
12 mm
15 mm
533 nF
Acoustic Magnitude (mV)
Energy Delivered into the Plasma Channel (J)
1600
1400
1200
1000
800
600
0
50
100
150
200
250

(c)

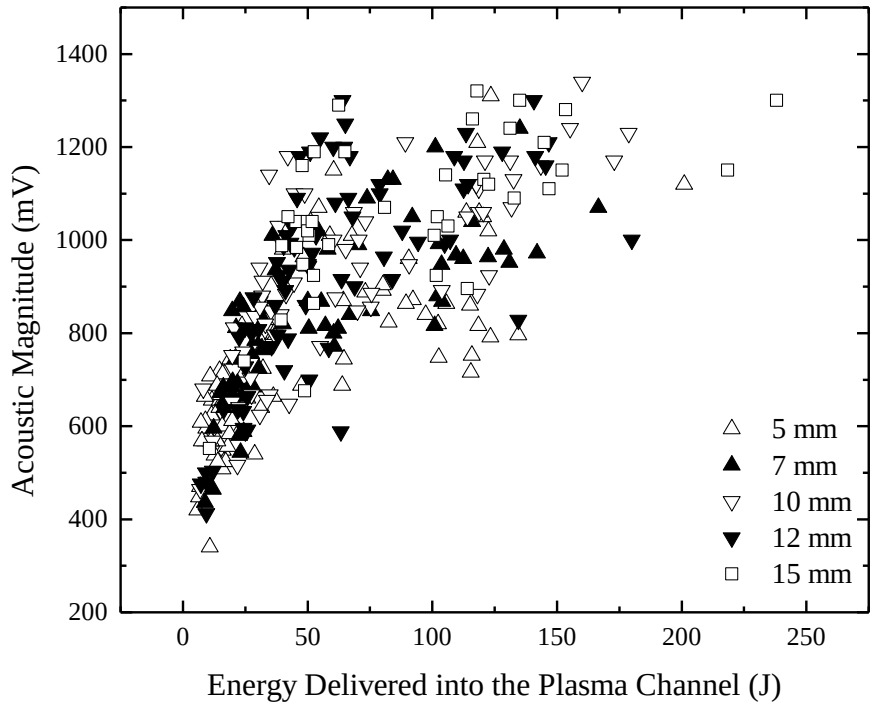

Figure 4-18. The relationship between $P_{cav\text{-}max}$ and E_{pl} for all three cases of capacitance: (a) 155 nF, (b) 266 nF, (c) 533 nF, (d) combined results for all values of capacitance.

It can be seen in the combined Fig. 4-18(d) that the $P_{cav\text{-}max}$ initially increases quickly with the increasing E_{pl} (up to < 60 J). For E_{pl} > 60 J, the increasing trend of $P_{cav\text{-}max}$ slows down and it becomes constant with further increase in E_{pl} up to ~ 250 J.

A scaling relationship can be derived to describe the dependency of $P_{cav\text{-}max}$ on E_{pl} based on (4.11). M in (4.11) represents the explosive mass (indicating potential energy used in conventional chemical explosion); therefore, it is reasonable to link M with the energy released into the plasma channel, E_{pl}, when this approach is applied to electrical discharges:

$$M \propto E_{pl} \tag{4.28}$$

Then a relationship between $P_{cav\text{-}max}$ and E_{pl} can be found based on (4.11) and (4.28):

$$P_{cav-max} \propto \left({E_{pl}}^{1/3}/\lambda\right)^{\beta} \tag{4.29}$$

With known values of λ and $\beta = 1.13$, (4.29) can be rewritten by introducing a proportion coefficient, q, as:

$$P_{cav-\max} = qE_{pl}^{\beta/3} \tag{4.30}$$

where $P_{cav\text{-}max}$ and E_{pl} are expressed in mV and J respectively.

The coefficient, $\beta/3$, of term E_{pl} derived in (4.30) is ~0.38, which is close to the empirical value 0.54 obtained for the relationship between the peak pressure and deposited energy into the plasma channel in [32].

For linearization of the fitting, (4.30) can be modified:

$$\ln(P_{cav-\max}) = \ln(q) + (\beta/3)\ln(E_{pl}) \tag{4.31}$$

The solid lines in Fig. 4-19 show the fitting by scaling relationship (4.31) to the experimental data points ($P_{cav\text{-}max}$). This fitting was conducted in OriginLab 9.0 software and the corresponding coefficient was found to be q = 194. The dashed lines in Fig. 4-19 indicate the upper and lower boundaries of the 95 % prediction intervals and most data points are located within this interval. In general, the fitting curve obtained by (4.31) shows a reasonable agreement with the experimental data. In [131] and [135], a similar analytical scaling relationship between them have been obtained for lower discharge energies: $P_{max} \sim (W_{ch}{}^{b}/p)$, where p is the external hydrostatic pressure, W_{ch} is the energy in the plasma channel and b is a free fitting parameter close to the value of $\beta/3$ used in (4.30). It has to be noted that scaling relationship (4.30) is not suitable for accurate calculation of the acoustic magnitude as it excludes the information on the inter-electrode gap. However, this straightforward scaling relationship provides a reasonable tool for analysis of the tendency of the variation of $P_{cav\text{-}max}$ along with E_{pl} and can be used for prediction and evaluation of the expected acoustic magnitude by a given value of E_{pl}.

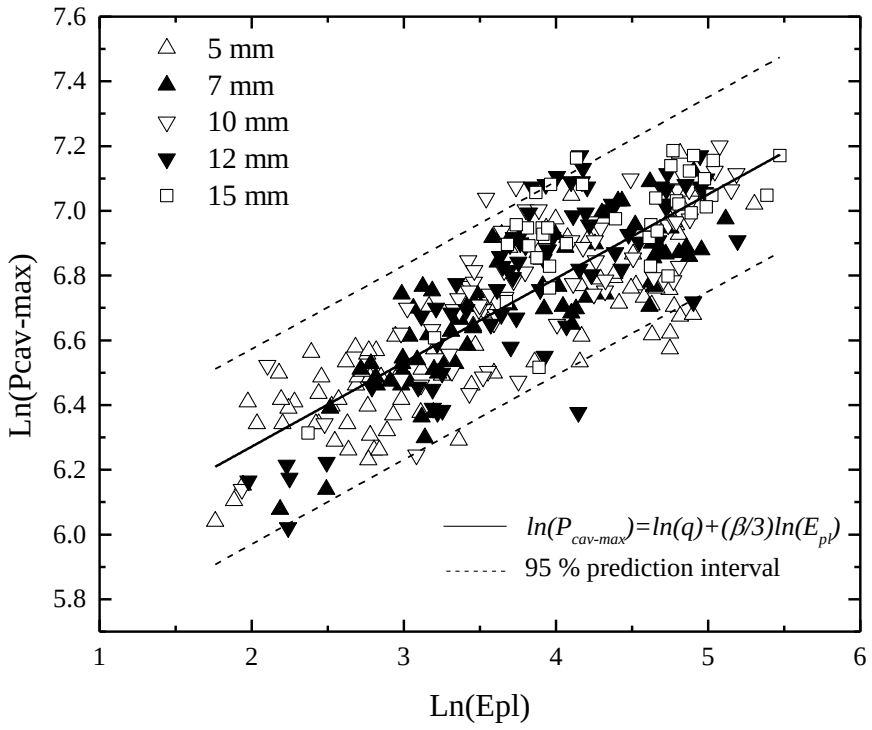

Figure 4-19. The logarithm form of the relationship between $P_{cav\text{-}max}$ and E_{pl} for all capacitance cases. Solid line represents the fitting (4.31) and dashed lines are upper and lower boundaries of the 95 % prediction intervals.

4.9 Relations between W_m and the energy delivered into the plasma channel

In (4.3), the coefficient, δ, was used to represent the portion of the energy delivered into the plasma channel transformed into the mechanical work done by the plasma channel against the surrounding water. After calculating W_m and E_{pl} by (2.24) and (4.1), values of δ for different capacitance cases can be obtained by plotting W_m as a function of E_{pl} and fitting (4.3) in OriginLab 9.0 software. The obtained δ are given in Table. 4-6. It can be seen that the proportion coefficient δ decreases with an increase in C. Similarly, in [136], the percentage of the mechanical work done by the cavity out of the total energy delivered into the plasma channel was found to be inversely proportional to the spark duration. However, the calculated percentage value in [136] was > 50 % while values of δ obtained in present work are close to 30 %.

Table 4-6. The proportion γ obtained for different values of capacitance

Capacitance (nF)	δ
155	0.35
266	0.32
533	0.25

4.10 Conclusions

In this chapter, the experimental results and the functional behaviour of the hydrodynamic, acoustic and electrical parameters have been investigated for the free self-triggering spark discharge mechanism. The period of the cavity oscillation and the acoustic magnitude were obtained from experimental measurements and their relationships with the breakdown voltage, the plasma resistance and the energy delivered into the plasma channel were obtained.

It was shown that the voltage and current waveforms demonstrated an under-damped oscillating behaviour, revealing the RLC circuit nature of the discharge circuit. The current waveform in the RLC circuit was used to obtain the constant plasma resistance, R_{pl}. The acoustic signal demonstrated a non-periodical impulsive profile and the first acoustic impulse emitted by the spark source demonstrated the highest peak magnitude, $P_{cav\text{-}max}$. The dynamic behaviour of the formed gas cavity was investigated by measuring the period between its formation and collapse, T_{cavity}.

It was found that the both T_{cavity} and $P_{cav\text{-}max}$ were functions of the breakdown voltage and the circuit capacitance. $P_{cav\text{-}max}$ was also sensitive to the inter-electrode gaps. Similar relationships between the hydrodynamic and acoustic parameters and the energy at breakdown were found in [35], [125], [132]. In the present work, clusters of data points (T_{cavity} and $P_{cav\text{-}max}$) were observed outside of the main trend lines shown in Fig. 4-3 and Fig. 4-7 for all three values of capacitance in short gaps (5 mm and 7 mm) with high breakdown voltages (> 20 kV). It was found that the effective plasma resistance of these discharges was smaller than the circuit resistance, resulting in the low potion of energy being transferred from the storage capacitance to the energy dissipated into the plasma channel at breakdown. A scaling relationship was developed

to link T_{cavity} and V_{br}: $T_{cavity} = 0.11C^{0.34}V_{br}^{0.67}$. Two analytical scaling relationships were also derived for $P_{cav\text{-}max}$: $P_{cav\text{-}max} = kV_{br}^{2\beta/3}$ was found for description of the main trend shown in Fig. 4-7, and $P_{cav\text{-}max} = 6.27l^{0.22}C^{\beta/3}V_{br}^{2\beta/3}$ was developed to accurately evaluate the acoustic magnitude in these conditions.

It was shown that T_{cavity} and $P_{cav\text{-}max}$ followed a non-linear tendency with the variation in the plasma resistance from ~0.028 Ω to ~5.9 Ω. For R_{pl} less than $R_{circuit}$, both T_{cavity} and $P_{cav\text{-}max}$ experienced significant change with a minor variation in R_{pl}. The maximum values of the period of cavity oscillation and the acoustic magnitude correspond to the plasma resistance, which was comparable to the circuit resistance ($1 < R_{pl}/R_{circuit} < 3$). For $R_{pl} > 3R_{circuit}$, T_{cavity} and $P_{cav\text{-}max}$ decreased with an increase in R_{pl}.

The energy delivered into the plasma channel through the Joule heating mechanism, E_{pl}, was calculated using the constant plasma resistance together with the experimental current waveforms. The period of the cavity oscillation was found to be in direct proportion to E_{pl} and no significant difference in T_{cavity} was observed for various capacitance cases, meaning E_{pl} being the deciding parameter in defining T_{cavity}. Similar tendency was also found for the relationship between $P_{cav\text{-}max}$ and E_{pl}. Phenomenological scaling relations (4.26) and (4.30) were developed to describe the functional behaviour of T_{cavity} and $P_{cav\text{-}max}$.

The investigation of free self-triggering discharges in this work allowed establishment of scaling relationships between the electrical, the hydrodynamic and the acoustic parameters. With the help of these scaling relations, it is possible to calculate corresponding acoustic magnitude, which is helpful in optimisation of plasma-acoustic sources by tailoring the pulse-power generation circuit parameters.

The next chapter will discuss the experimental results of the air-bubble triggered underwater spark discharges. An analysis on the discharge characteristics will be conducted to link the acoustic output paramters to the circuit parameters for this underwater spark discharge mechanism and to evaluate its performance in generating acoustic impulses.

5 Experimental results and analysis: Air-bubble stimulated discharges

In Chapter 4, free self-triggered underwater discharges have been comprehensively investigated, their efficiency in generating acoustic impulses have been obtained and analysed. It was established that this type of discharges can be achieved in relatively short inter-electrode gaps, up to 15 mm with pulsed with magnitude of 25 kV- 35 kV and energy varying from ~ 48 J to ~ 326 J. When the inter-electrode gap was increased, these energisation parameters resulted in low breakdown probability and unstable acoustic output.

As discussed in Section 2.2.2, the presence of gas bubbles in the vicinity of the HV electrode plays an important role in facilitating development of breakdown in liquid. It was shown in [39]-[41], [92], [95], [96], [137] that the pre-breakdown time can be reduced by injecting gas bubbles into the inter-electrode gap. For example, in [137] air and sulfur hexafluoride were injected into transformer oil to investigate their influence on DC breakdown characteristics of this insulting liquid. Experimental results showed that the average breakdown voltage was reduced by ~ 34 % if air as injected and ~ 19 % if SF_6 was injected into oil.

In the case of underwater breakdown, in [41] the statistical analysis of the breakdown time lag for breakdowns in water with and without bubbles under a pulsed electrical field with maximum magnitude of 800 kV/cm was conducted. Statistical analysis was conducted using the Laue statistical distribution. The Laue graph was plotted: $\ln(N_0/N_t)$ was presented as a function of time, t, where N_0 was the total number of the breakdowns and N_t was the number of breakdowns with the delay time longer than t. It was found that the value of $\ln(N_0/N_t)$ with the presence of gas bubbles was always larger than that with no gas bubbles. For example, $\ln(N_0/N_t) \sim 1.65$ for bubbled breakdown and $\ln(N_0/N_t) \sim 0.2$ for the original breakdown when $t = 2$ μs, confirming the efficiency of injected bubbles in reducing the pre-breakdown time.

It is worthy of note that [95] investigated the role of permittivity of liquid in streamer formation in injected gas bubbles. The result showed that the high permittivity of liquid increases the electrical field in the gas bubble. This high field results in the development of streamer in the gas bubble and thereby breakdown between electrodes in the liquid. Therefore, it is expected that injecting gas bubbles in water would be an

effective method to reduce the pre-breakdown time and breakdown voltage. In order to achieve stable breakdown repetition rate in long inter-electrode gap for stronger acoustic impulses, the underwater spark discharge system with injection of air bubbles was developed in this work.

In order to study the performance of the air-bubble stimulated discharges and to compare their properties with that of free self-triggering discharges, the same energisation conditions were used in the ABSD's tests and similar analysis of the breakdown characteristics was conducted. This chapter demonstrates the experimental waveforms of the electrical parameters and acoustic parameters. The functional behaviour of T_{cavity} and $P_{cav\text{-}max}$ for ABSD's are obtained and analytical models are used to describe their relationships with V_{br} and E_{pl}.

5.1 Experimental results

Preliminary tests were conducted to establish an upper limit of the inter-electrode gap (25 mm) at which impulses with low energy levels (based on 155 nF and 266 nF capacitance) did not result in complete breakdown between electrodes. Based on these tests, the lengths of the inter-electrode gap for the ABSD's were selected as 15 mm, 20 mm and 25 mm.

5.1.1 Voltage and current waveforms

By using the diagnostic system as described in Section 3.2, the electrical waveforms were obtained for the ABSD's and they are shown in Fig. 5-1. These examples of voltage and current waveforms correspond to a 15 mm inter-electrode gap with ~ 29.6 kV breakdown voltage and 533 nF capacitance. As the waveforms show, after applying the high voltage impulse to the electrodes, breakdown streamers develop in the pre-breakdown stage and then the breakdown occurs when a complete plasma channel is formed at breakdown moment, t_{br} = 38 μs. The reduction in the plasma resistance results in the drop of voltage and appearance of the conductive current.

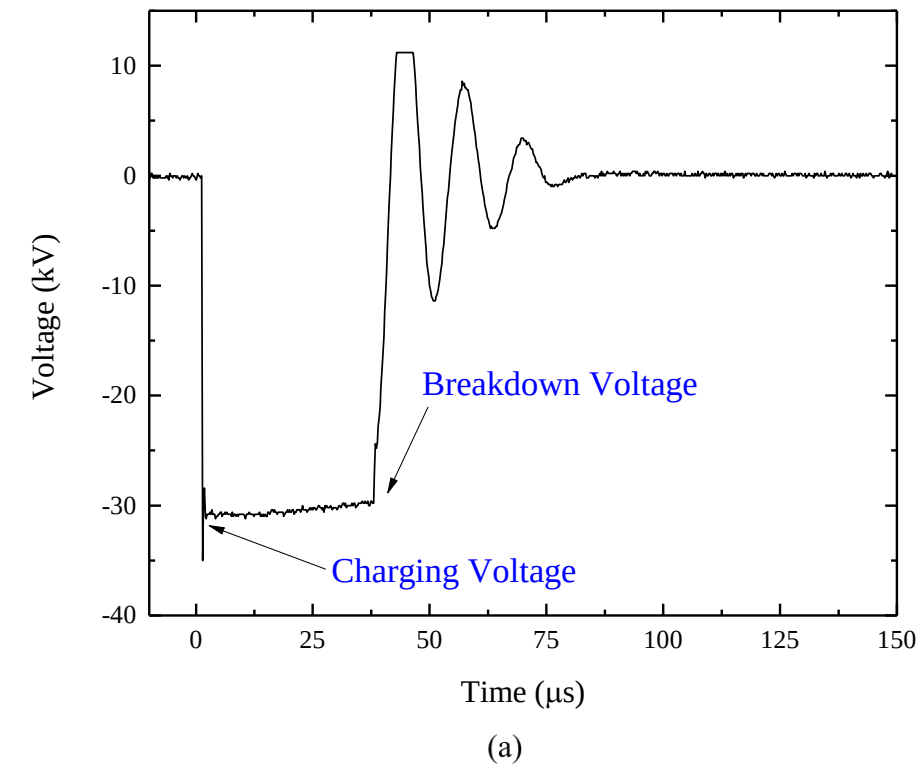

(a)

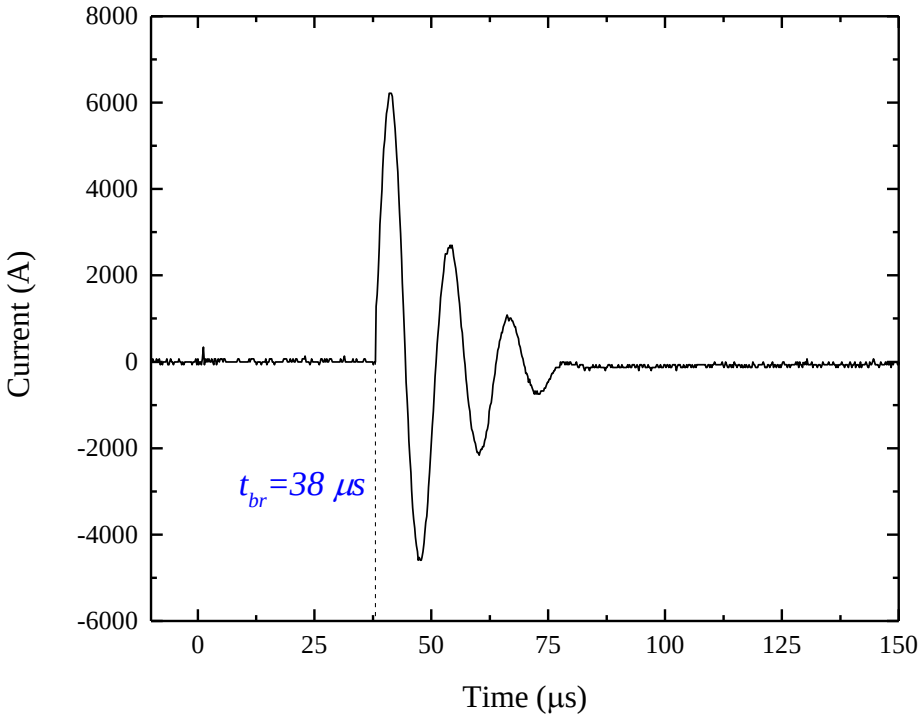

(b)

Figure 5-1. Example waveforms of the (a) voltage and (b) current obtained for ABSD's in a 15 mm gap with C = 533 nF and V_{br} = 29.6 kV. The pre-breakdown time is t_{br} = 38 μs.

It can be seen that these results shown in Fig. 5-1 are similar to the results obtained for FD's in Fig. 4-1, especially in the pre-breakdown stage. No significant difference is observed for waveforms for FD's and ABSD's during the post-breakdown stage. The pre-breakdown time for above example breakdown is 38 μs. The general range of pre-breakdown times obtained for ABSD's is from ~ 20 μs to ~ 500 μs, depending on the inter-electrode gap and energisation level used in the tests.

5.1.2 Hydrodynamic and acoustic signals

Fig. 5-2 shows the typical acoustic signals produced by ABSD's and captured by the Pinducer sensor in two different time scales. The profile of the acoustic pressure wave, shown in Fig. 5-2(a), is similar to that obtained for FD's, featuring major peaks present in the first positive half-cycle followed by a reduced negative half-cycle.

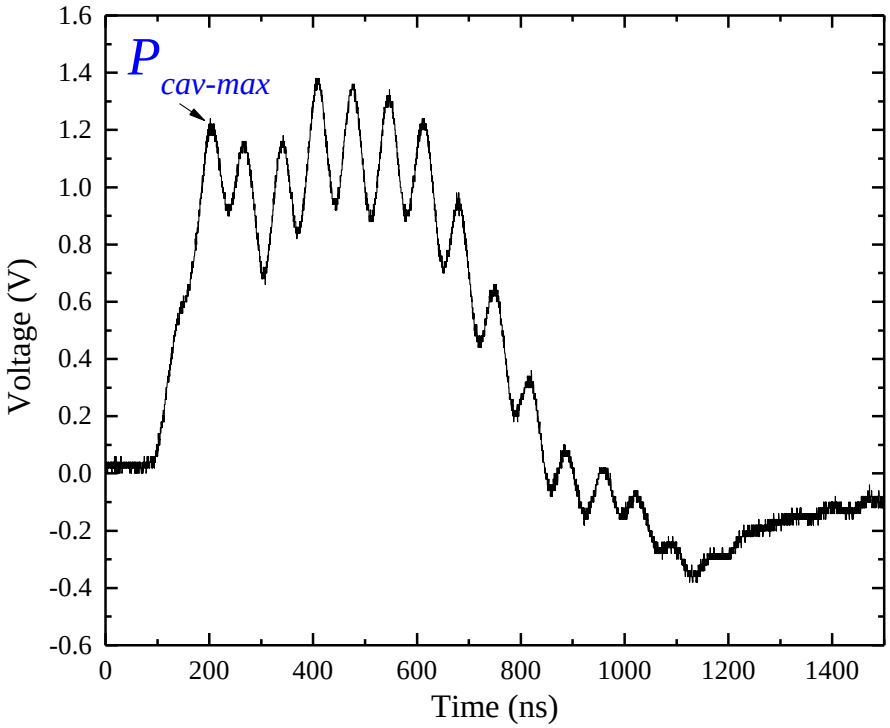

(a)

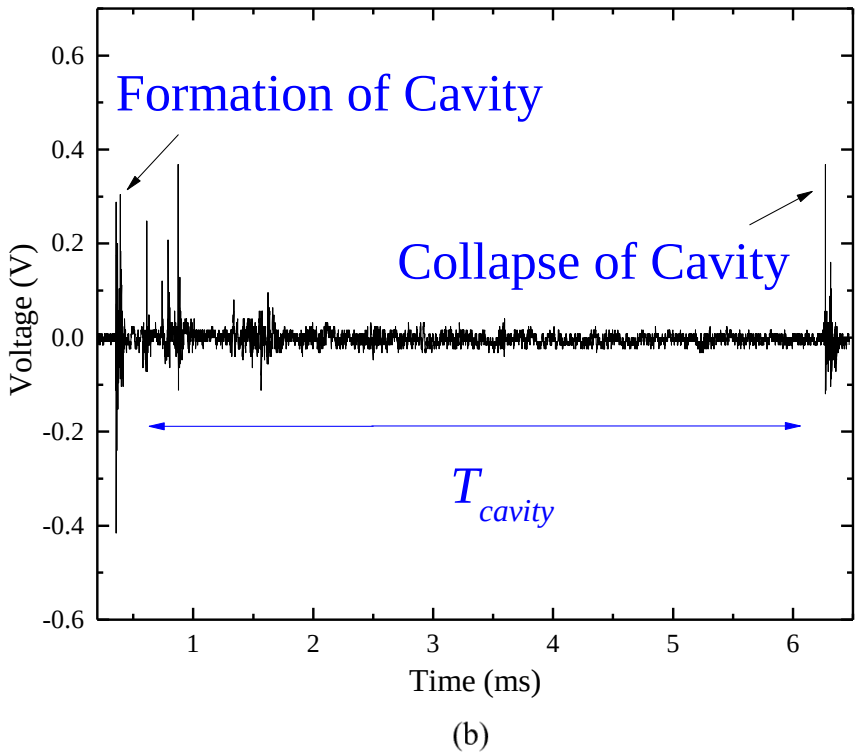

(b)

Figure 5-2. Acoustic signals generated by discharges: (a) the profile of the acoustic magnitude obtained in a 20 mm inter-electrode gap; (b) the primary and secondary acoustic impulses emitted at the formation and collapse of the cavity obtained in a 25 mm inter-electrode gap. $P_{cav\text{-}max}$ is the first peak of the impulse and T_{cavity} indicates the time duration of the primary oscillation of the cavity.

It can be concluded that, as expected, the initiation mechanism of the underwater spark discharge does not significantly influence the acoustic impulse profile. The magnitude of the acoustic impulse is represented by the value of its first sharp peak, and this peak is used in the following analysis as it was in the case of FD's. The period of the cavity oscillation can also be obtained by the time interval between two successive acoustic signals, shown in Fig. 5-2(b).

5.2 The pre-breakdown time comparison between free self-triggering discharges and air-bubble stimulated discharges

The main purpose of injection of gas bubbles into the inter-electrode gap is reduction of the breakdown voltage and the pre-breakdown time. Thus, the pre-breakdown

energy losses can be also reduced. The pre-breakdown time for ABSD's was obtained from the voltage waveforms and statistical analysis was conducted. For the purpose of comparison, the minimum, maximum, average value and the standard deviation of the pre-breakdown time were calculated for free self-triggering discharges and air-bubble stimulated discharges under the same experimental conditions (15 mm gap and 266 nF). The results of this analysis are shown in Table. 5-1.

Table 5-1. Average value, standard deviation, minimum and maximum values of the pre-breakdown time for FD's and ABSD's obtained in 15 mm gap with 266 nF

Charging voltage (kV)	Pre-breakdown time for FD's (μs)			Pre-breakdown time for ABSD's (μs)		
	Average ± Standard deviation	Minimum	Maximum	Average ± Standard deviation	Minimum	Maximum
25	N/A	N/A	N/A	134 ± 45	76	234
30	229 ± 88	140	336	77 ± 38	30	142
35	196 ± 118	38	328	46 ± 22	29	112

Fig. 5-3 illustrates the comparison between the pre-breakdown time obtained under the same experimental conditions for FD's and ABSD's. It was found that the average value and standard deviation of the pre-breakdown time for ABSD's were significantly smaller than those obtained for FD's. For different charging voltages (30 kV and 35 kV), the average pre-breakdown time was reduced by ~ 66 % for 30kV and ~ 77 % for 35kV in the case of ABSD's. These results have confirmed the effectiveness of injected air-bubbles in reduction of the pre-breakdown time, which potentially enlarges the achievable breakdown distance by using similar energisation conditions as compared with the FD's case. Smaller standard deviation obtained for ABSD's also indicates better breakdown stability as compared with FD's. No results were obtained for 25 kV in the FD's case as no breakdown events were registered under these conditions. In the ABSD's case, breakdown was successfully achieved with 25 kV by using injected bubbles and maximum breakdown gap was increased to 25 mm.

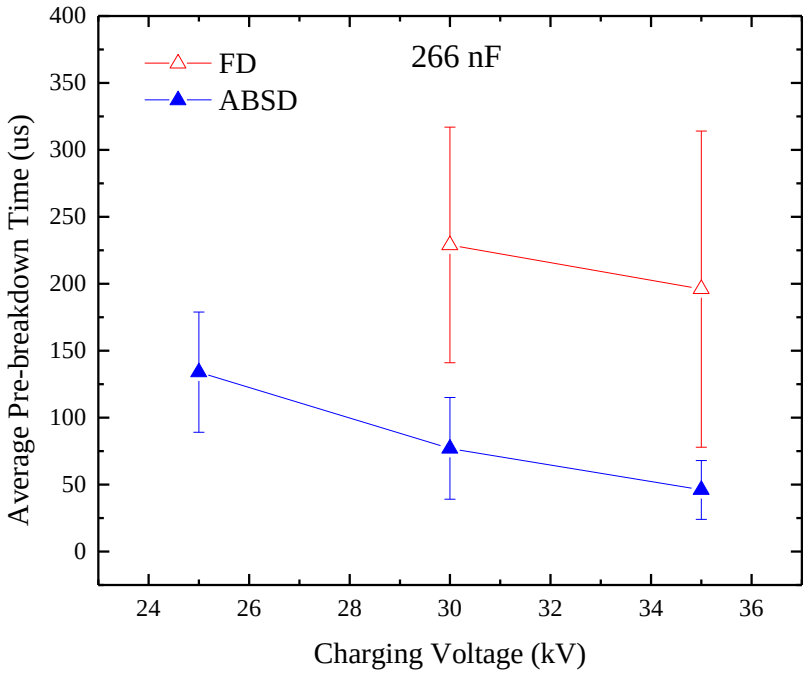

Figure 5-3. The comparison of the average value and standard deviation of the pre-breakdown time for FD's (red) and ABSD's (blue) in 15 mm and 266 nF capacitance.

In order to investigate the acoustic performance of the ABSD's, relationships between hydrodynamic and acoustic parameters, T_{cavity} and $P_{cav\text{-}max}$, and the electrical properties of the circuit, V_{br}, R_{pl} and E_{pl}, have been obtained. The functional dependencies of T_{cavity} and $P_{cav\text{-}max}$ on V_{br} will be presented and discussed. Phenomenological scaling relations will also be used to link the acoustic output and the electrical parameters.

5.3 The period of cavity oscillation as a function of the breakdown voltage

As discussed in Section 5.1.1, due to similarities in their electrical and acoustic waveforms, the ABSD's can be regarded as an extended version of the FD's in longer gaps in terms of the post-breakdown behaviour. The obtained results for ABSD's will be compared with the results obtained for FD's.

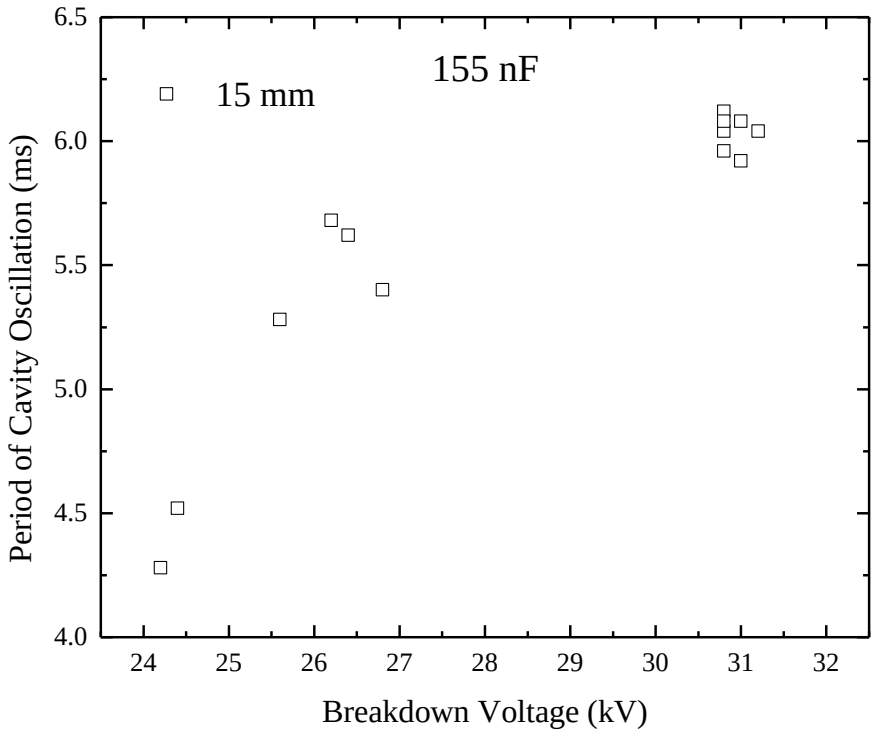
155 nF
15 mm
Period of Cavity Oscillation (ms)
Breakdown Voltage (kV)
6.5
6.0
5.5
5.0
4.5
4.0
24
25
26
27
28
29
30
31
32

(a)

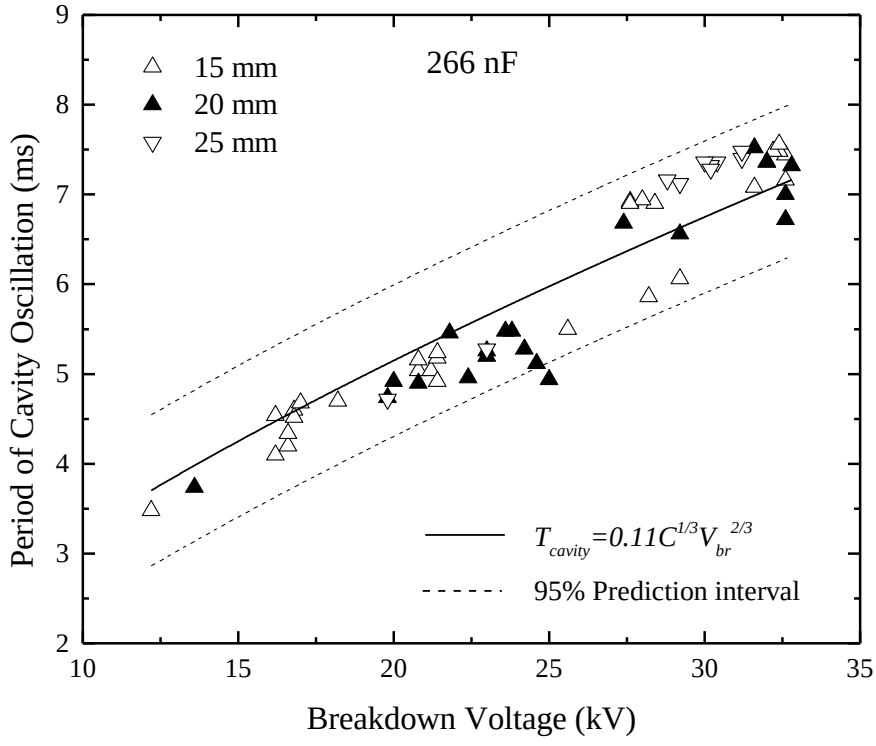
266 nF
15 mm
20 mm
25 mm
$T_{cavity}=0.11C^{1/3}V_{br}^{2/3}$
95% Prediction interval
Period of Cavity Oscillation (ms)
Breakdown Voltage (kV)
9
8
7
6
5
4
3
2
10
15
20
25
30
35

(b)

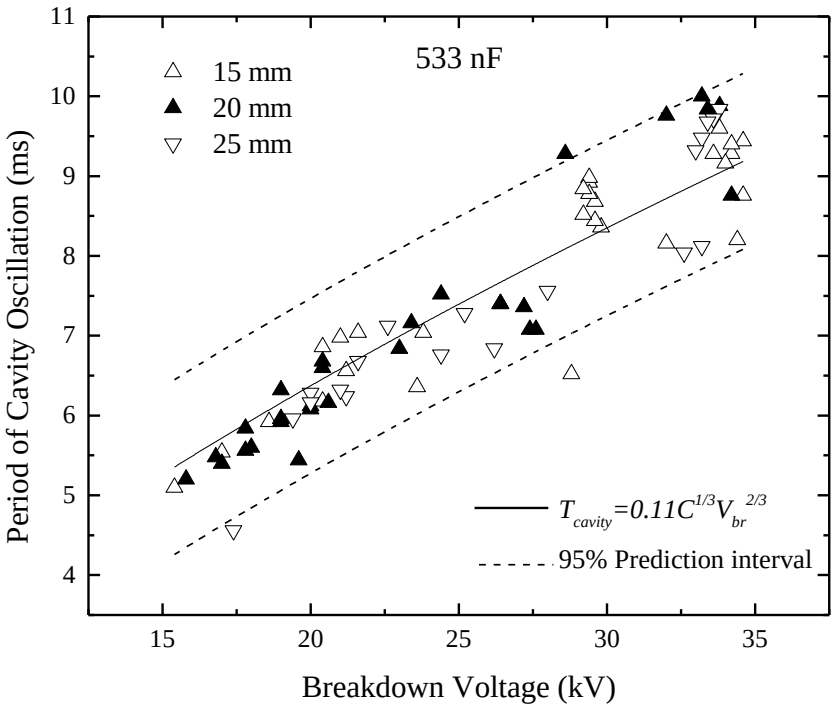

(c)

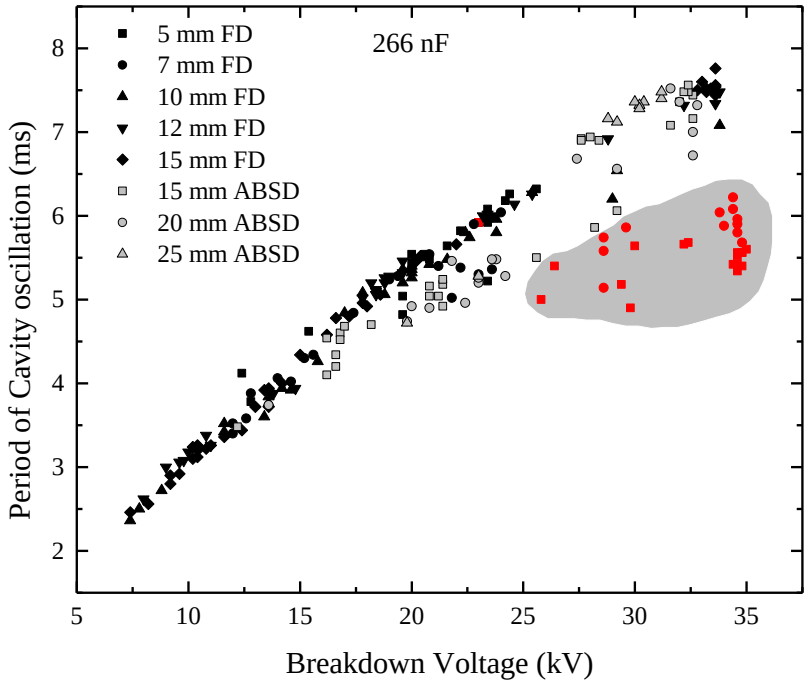

(d)

Figure 5-4. The T_{cavity} as a function of the V_{br} for (a) 155 nF, (b) 266 nF, (c) 533 nF, (d) comparison between FD's and ABSD's for 266 nF. Solid lines represent fitting results of (4.10) and dashed lines show the upper and lower boundaries of the 95 % prediction intervals. Red data points in grey area correspond to $R_{pl} < R_{circuit}$ for FD's.

Fig. 5-4 shows the variation in the period of cavity oscillation as a function of the breakdown voltage for three values of capacitance and comparison between the T_{cavity} obtained for FD's and ABSD's in the 266 nF case. It was found that T_{cavity} follows a non-linear increasing trend with the increasing breakdown voltage similar to the tendency observed in the FD's case. Using the same arguments as in the discussion of FD's. This tendency can be explained by the statement that the breakdown voltage is linked to the amount of electrical energy that can be transferred into the cavity. Thus, larger value of V_{br} indicates larger amount of energy delivered into the plasma-filled cavity and thereby larger size that the cavity can expand into.

Another important observation in Fig. 5-4(d) is that no significant difference in the value of T_{cavity} can be observed between FD's and ABSD's. The main difference in these two types of discharges is the triggering mechanism and the length of the inter-electrode gap. The inter-electrode gap does not affect T_{cavity} significantly, which was confirmed in the FD's case. As a result, the value of T_{cavity} only varies with the energisation level (breakdown voltage and storage capacitance), and does not depend on the plasma initiation mechanism.

Based on these findings, the phenomenological relationship (4.10), originally developed for FD's, can be used to describe the tendency observed for ABSD's. The solid and dashed lines in Fig. 5-4 (b) and Fig. 5-4 (c) shows the fitting of (4.10) to the experimental data and the upper and lower boundaries of the 95 % prediction intervals for 266 nF and 533 nF capacitances used in ABSD's. It was found that due to the lower number of tests conducted with 155 nF capacitance of ABSD's, (4.10) was not possible to fit the experimental data. The fitting lines show a good agreement with the experimental data and all data points are located within the upper and lower boundaries of the 95 % prediction intervals, confirming that scaling relationship (4.10) is suitable to be used to describe the relationship between T_{cavity} and V_{br} in the ABSD's case regardless of the length of the inter-electrode gap.

5.4 The acoustic magnitude as a function of the breakdown voltage

Similar to the analysis conducted for T_{cavity}, the phenomenological relationship (4.17), derived originally for FD's, is also used to describe the relationship between $P_{cav\text{-}max}$ and V_{br} in the case of ABSD's by assuming that the injected air bubbles only affect the pre-breakdown stage. The fitting results for different capacitances are shown as the solid lines in Fig. 5-5 and the values of coefficient, A, varying from 0.0063 to 0.0078, are given in Table. 5-2, where A_{15}, A_{20} and A_{25} indicated the coefficient A in (4.17) obtained for 15 mm, 20 mm and 25 mm inter-electrode gaps respectively.

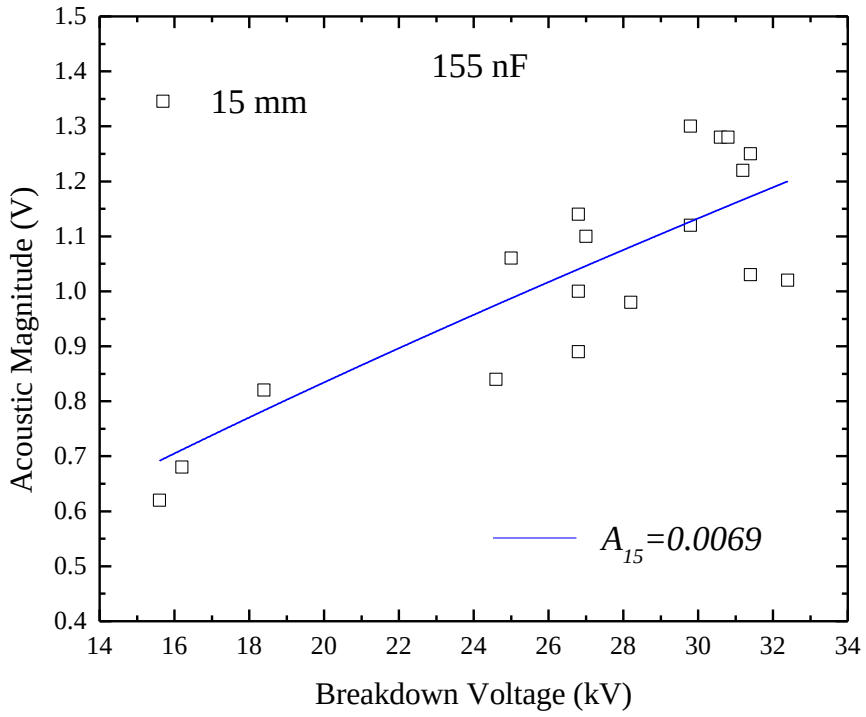

(a)

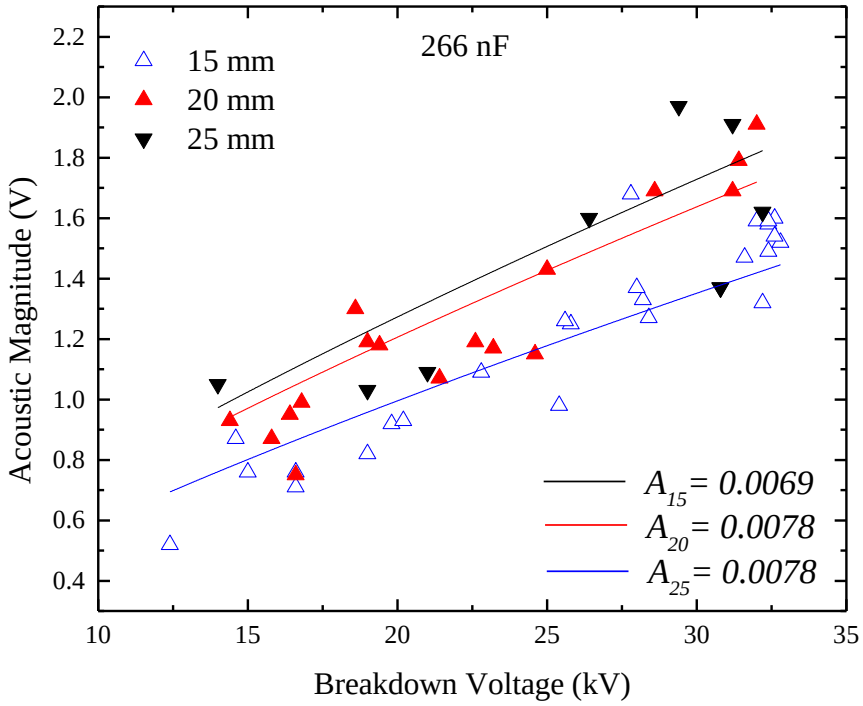
266 nF
15 mm
20 mm
25 mm
A_{15}= 0.0069
A_{20}= 0.0078
A_{25}= 0.0078
Acoustic Magnitude (V)
Breakdown Voltage (kV)

(b)

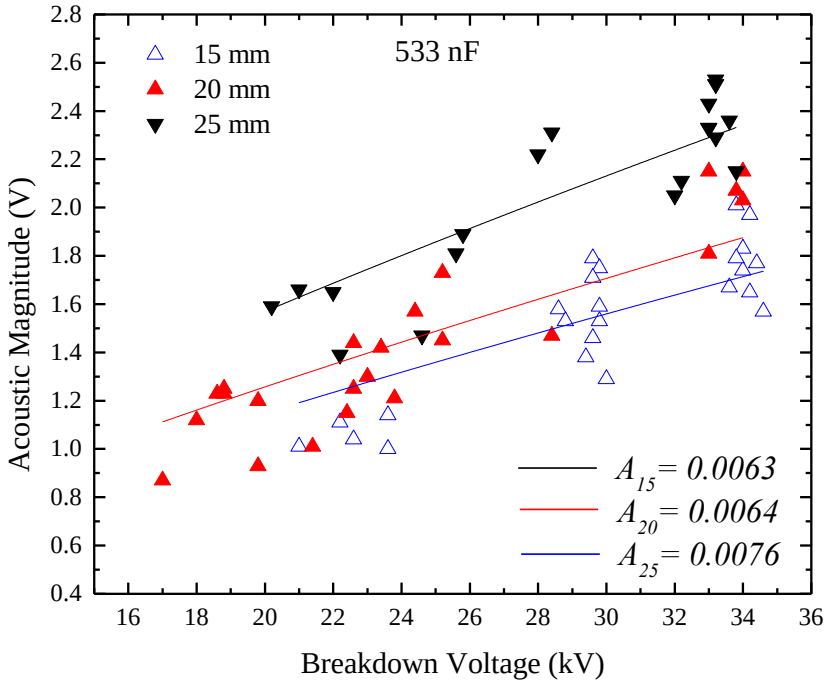
533 nF
15 mm
20 mm
25 mm
A_{15}= 0.0063
A_{20}= 0.0064
A_{25}= 0.0076
Acoustic Magnitude (V)
Breakdown Voltage (kV)

(c)

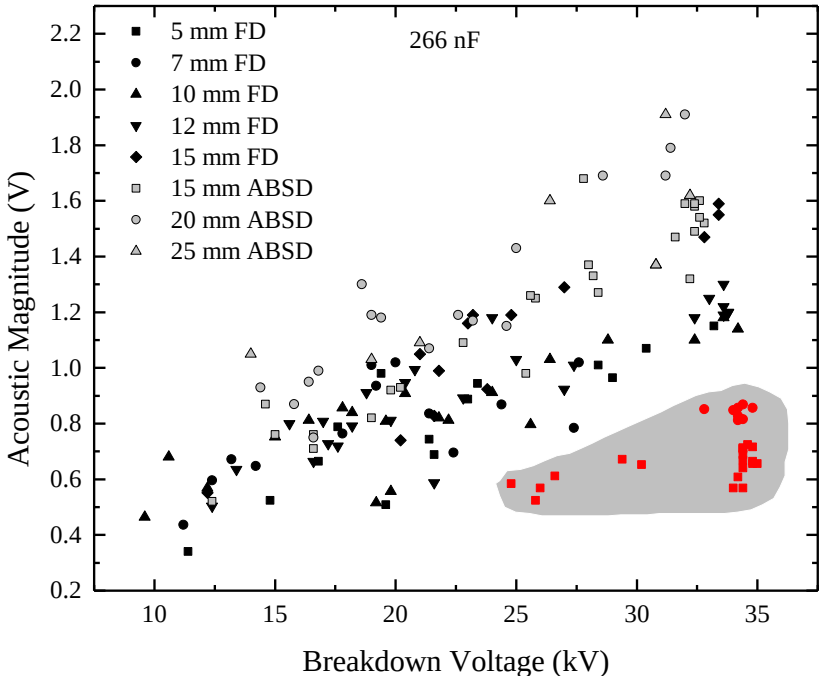

(d)

Figure 5-5. The $P_{cav\text{-}max}$ as a function of the V_{br} for (a) 155 nF, (b) 266 nF, (c) 533 nF, (d) combined experimental data for FD's and ABSD's with 266 nF. Solid colored lines (blue for 155 nF, red for 266 nF, black for 533 nF) represent fitting results of (4.17). Data points marked red in the grey area in (d) correspond to $R_{pl} < R_{circuit}$ for FD's.

Table 5-2. Values of proportionality coefficient, A, obtained for different combination of C and l

Coefficient A	155 nF	266 nF	533 nF
A_{15}	0.0069	0.0069	0.0063
A_{20}	N/A	0.0078	0.0064
A_{25}	N/A	0.0078	0.0076

It was shown that (4.17) fits the experimental data reasonably well for each combination of capacitance and inter-electrode gap, which allows (4.17) to be used for prediction of the acoustic output for specific experimental and circuit parameters. Based on the tendency shown in Fig. 5-5 and scaling relationship (4.17), it is worthy of note that an increase in the acoustic magnitude can be achieved by rising the breakdown voltage in a more effective way rather than by increasing the inter-

electrode gap, even though the length of the inter-electrode gap defines the upper limit of the achievable acoustic magnitude.

It was established that (4.10) is valid for the ABSD's case in the whole range of breakdown voltages. In other words, there is no 'saturation' in the values of T_{cavity} and $P_{cav\,-\,max}$ when V_{br} is larger than its critical value, which has been observed in the FD's case, as shown by red data points (T_{cavity} and $P_{cav\text{-}max}$) in Fig. 4-3(d) and Fig. 4-7(d). As explained in Section 4.5.3, in the case of FD's, these 'saturated' data points correspond to the free self-triggering discharges with values of the plasma resistance smaller than the value of circuit resistance. Thus, the energy transfer efficient is relatively low, resulting in the limited amount of energy delivered into the plasma channel even with larger amount of stored energy. Therefore, the absence of saturation in the ABSD's case indicates that the plasma resistance of obtained for ABSD's are higher than the circuit resistance. This will be investigated in detail in the next section.

5.5 The period of cavity oscillation as a function of the plasma resistance

Following the satisfactory fitting of (2.22) to the experimental current for FD's, the plasma resistance for ABSD's was also calculated using (2.22). Then, the energy delivered into the plasma channel was obtained by using (2.24). The relationships between T_{cavity}, $P_{cav\text{-}max}$ and R_{pl}, E_{pl} are investigated in the following sections.

The relationships between the period of cavity oscillation and the constant plasma resistance for all three values of capacitance are shown in Fig. 5-6. The calculated values of circuit resistance (obtained as average values of four independent closing-circuit tests) for all three values of capacitance are given in Table. 5-3 and are also shown as the vertical solid lines in Fig. 5-6.

Table 5-3. Values of circuit resistance, $R_{circuit}$ for three values of capacitance

C (nF)	$R_{circuit}$ (Ω)
155	0.56
266	0.41
533	0.29

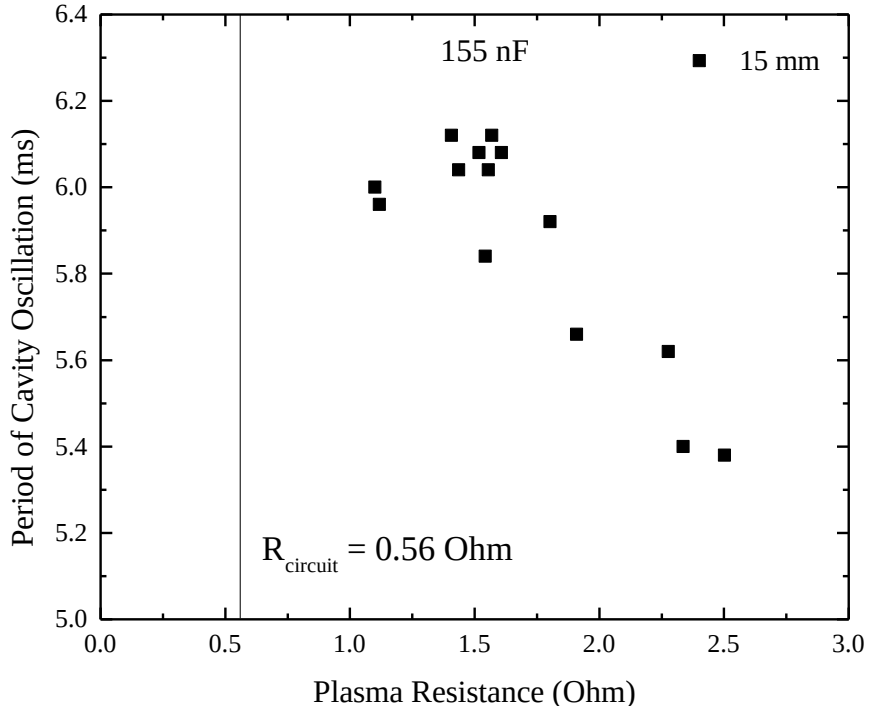
155 nF
15 mm
$R_{circuit}$ = 0.56 Ohm
Period of Cavity Oscillation (ms)
Plasma Resistance (Ohm)
6.4
6.2
6.0
5.8
5.6
5.4
5.2
5.0
0.0
0.5
1.0
1.5
2.0
2.5
3.0

(a)

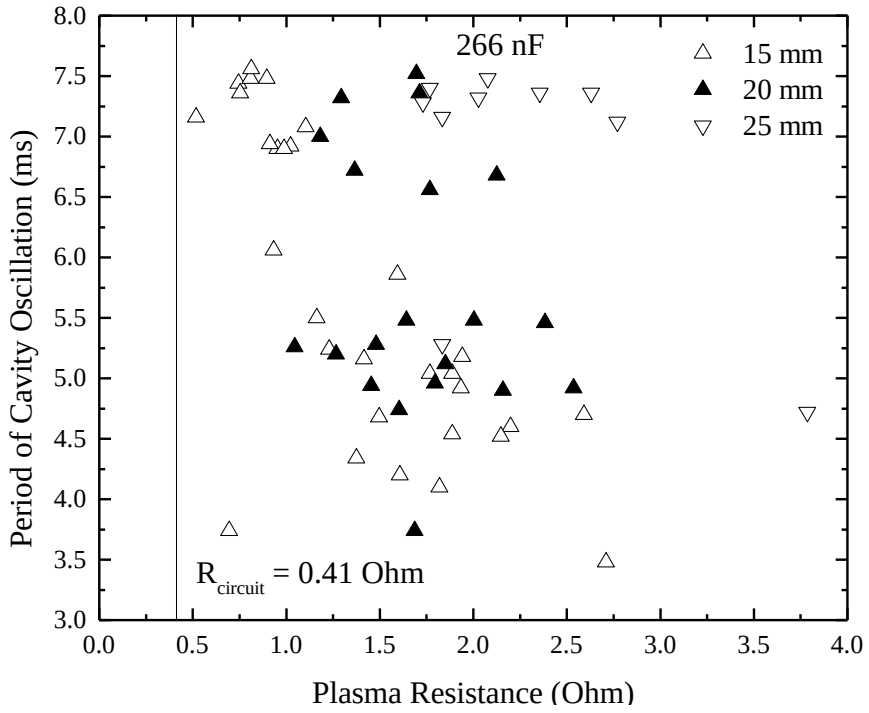
266 nF
15 mm
20 mm
25 mm
$R_{circuit}$ = 0.41 Ohm
Period of Cavity Oscillation (ms)
Plasma Resistance (Ohm)
8.0
7.5
7.0
6.5
6.0
5.5
5.0
4.5
4.0
3.5
3.0
0.0
0.5
1.0
1.5
2.0
2.5
3.0
3.5
4.0

(b)

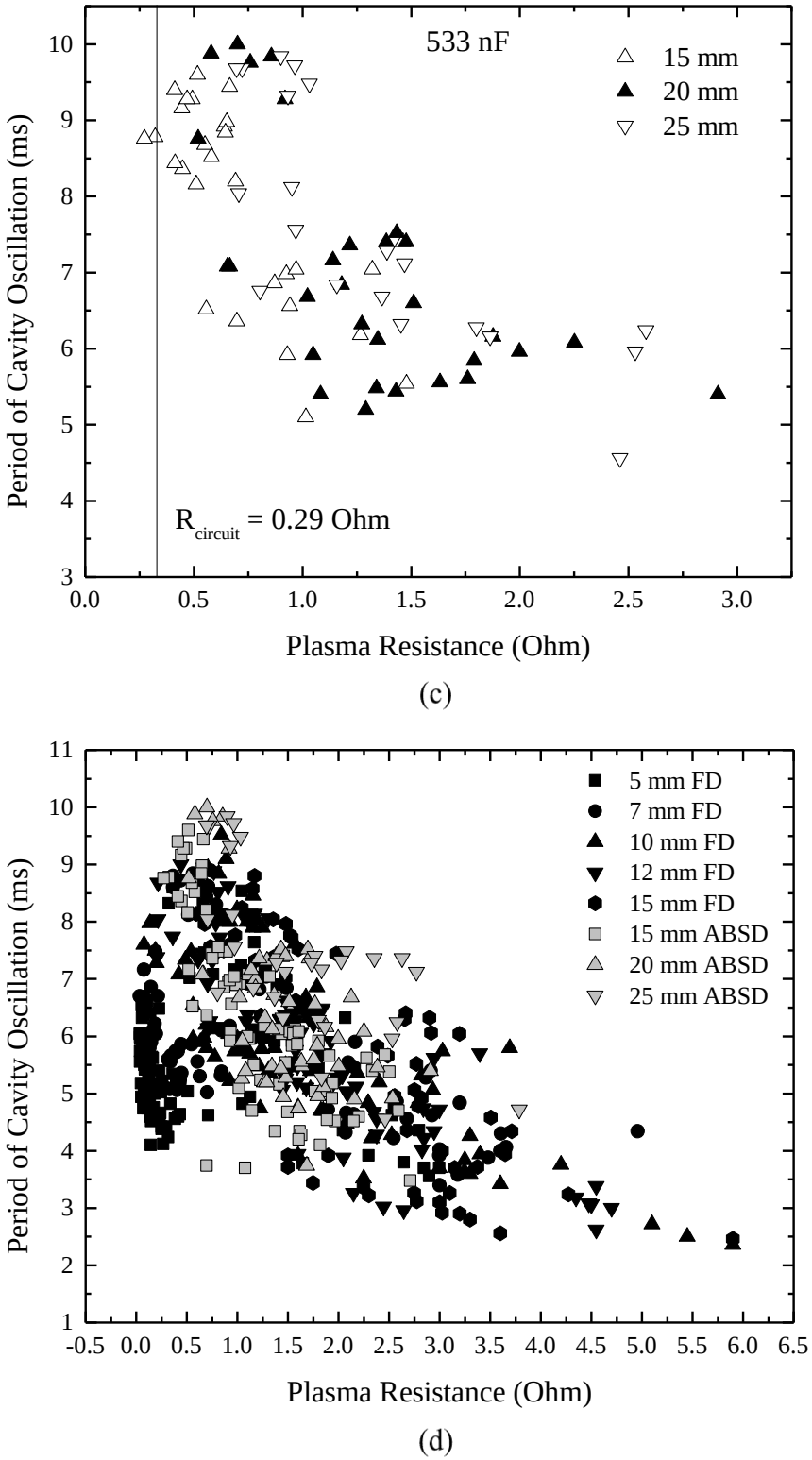

Figure 5-6. The T_{cavity} as a function of the R_{pl} for ABSD's for (a) 155 nF, (b) 266 nF, (c) 533 nF, (d) combined experimental data for FD's and ABSD's. Vertical solid lines show the circuit resistance for ABSD's discharge circuit.

As Fig. 5-6 shows, the relationship between T_{cavity} and R_{pl} demonstrates a decreasing trend for all values of capacitance and no discharges are found to have resistance lower than the circuit. This inverse proportionality between T_{cavity} and R_{pl} for ABSD's is similar to the tendency observed for discharges with $R_{pl} > R_{circuit}$, Fig. 4-12. Therefore, the higher value of R_{pl} indicates a lower electrical energy available at breakdown together with the relatively stable energy conversion efficiency, resulting in the reduction in T_{cavity}. This result is similar to a part of the tendency obtained for FD's. It also confirms that there is no saturation in the values of T_{cavity} and $P_{cav\text{-}max}$ as a function of V_{br} for any length of the inter-electrode gap.

The data points in Fig. 5-6(b) are dispersed and the data points (T_{cavity}) obtained in the same experimental conditions in Fig. 4-12(b) are more concentrated. This is due to the larger inter-electrode gap increment in the case of ABSD's (5 mm) than in the case of FD's (2/3 mm). Although l does not directly affect T_{cavity}, it defines the plasma resistance (by (4.19)) and the energy partition from the discharge circuit to the plasma channel and thereby the value of T_{cavity}.

Based on the previous conclusions on the relationships between R_{pl}, V_{br}, C and T_{cavity} for FD's, several findings can be obtained from Fig. 5-6 for ABSD's. First, for the same value of R_{pl} and C, ABSD's achieved in longer gaps typically have higher V_{br} and thereby longer T_{cavity}. Second, for the same value of l and C, discharges with higher R_{pl} produce lower T_{cavity} as V_{br} is lower in this case. Third, for the same values of l and R_{pl}, T_{cavity} is significantly longer for discharges with higher circuit capacitance. In other words, C is the major parameter, which affects T_{cavity}. These phenomena result in the dispersion of the data in Fig. 5-6(b).

The combined experimental data for all tests conducted for FD's and ABSD's are shown in Fig. 5-6(d). For FD's, the variation in T_{cavity} with R_{pl} was observed in the whole range of the plasma resistance values, ~ 35 mΩ to ~ 6 Ω. The peak value of T_{cavity} corresponds to the values of R_{pl}, which are comparable with $R_{circuit}$. For plasma resistance, which are greater than the circuit resistance, T_{cavity} decreased with an increase in R_{pl} (falling slope as seen in Fig. 5-6(d)). It was found that T_{cavity} measured for ABSD's only reduces with R_{pl}, which confirms that there are no ABSD's obtained for $R_{pl} < R_{circuit}$. It was also found that there is no significant difference in the values of

T_{caivty} for FD's and ABSD's, again indicating the strong dependence of T_{caivty} on energisation level rather than on the inter-electrode gap.

5.6 The acoustic magnitude as a function of the plasma resistance

The relationships between $P_{cav\text{-}max}$ and R_{pl} for all three values of capacitance and the combined results for FD's and ABSD's are shown in Fig. 5-7. It was found that the acoustic magnitude decreased with the increasing plasma resistance for all experimental results. Similar to the established relationship between T_{cavity} and R_{pl} (Fig. 5-6), the ratio $R_{pl}/R_{circuit}$ in Fig. 5-7 was found to be close to or larger than 1, thus, E_{pl} was mainly defined by the value of V_{br} (inversely proportional to R_{pl}). Therefore, together with the proportional relationship between $P_{cav\text{-}max}$ and V_{br} given by (4.17), the $P_{cav\text{-}max}$ is also expected to be inversely proportional to R_{pl}.

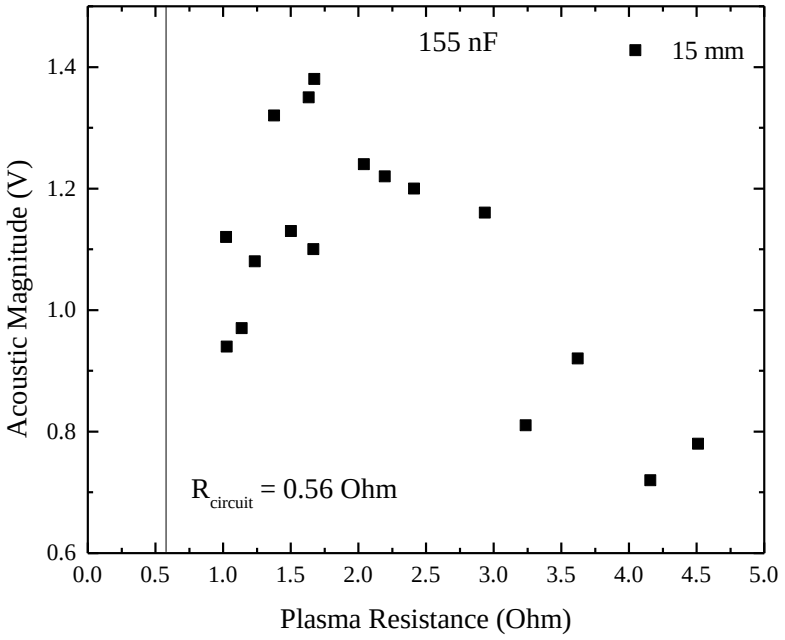

(a)

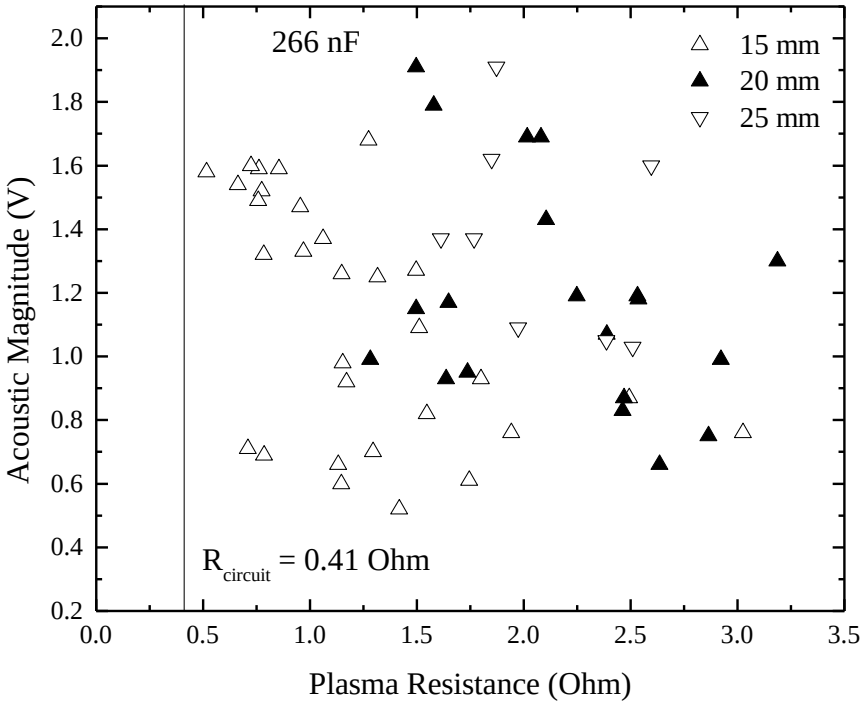
266 nF
15 mm
20 mm
25 mm
Acoustic Magnitude (V)
Plasma Resistance (Ohm)
R circuit = 0.41 Ohm

(b)

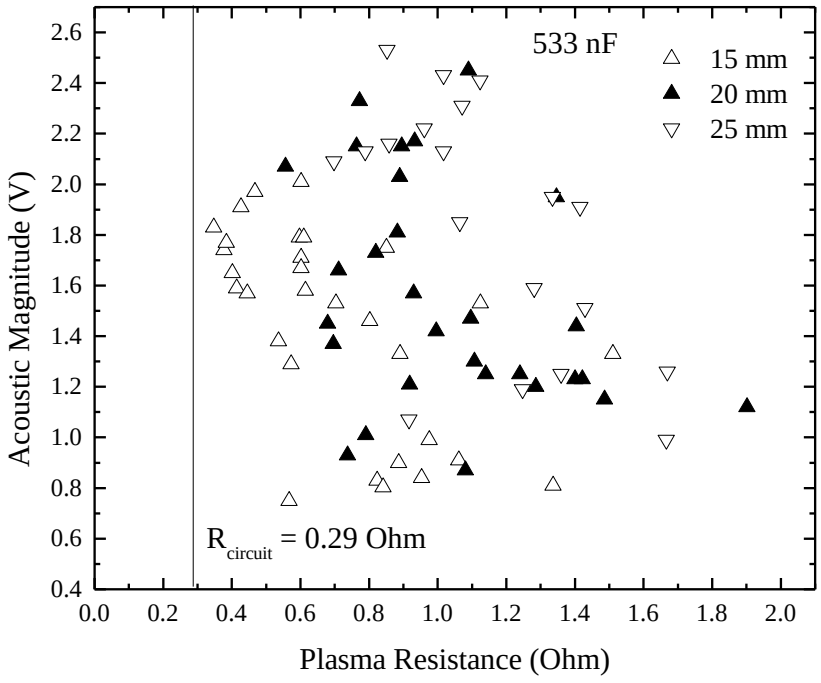
533 nF
15 mm
20 mm
25 mm
Acoustic Magnitude (V)
Plasma Resistance (Ohm)
R circuit = 0.29 Ohm

(c)

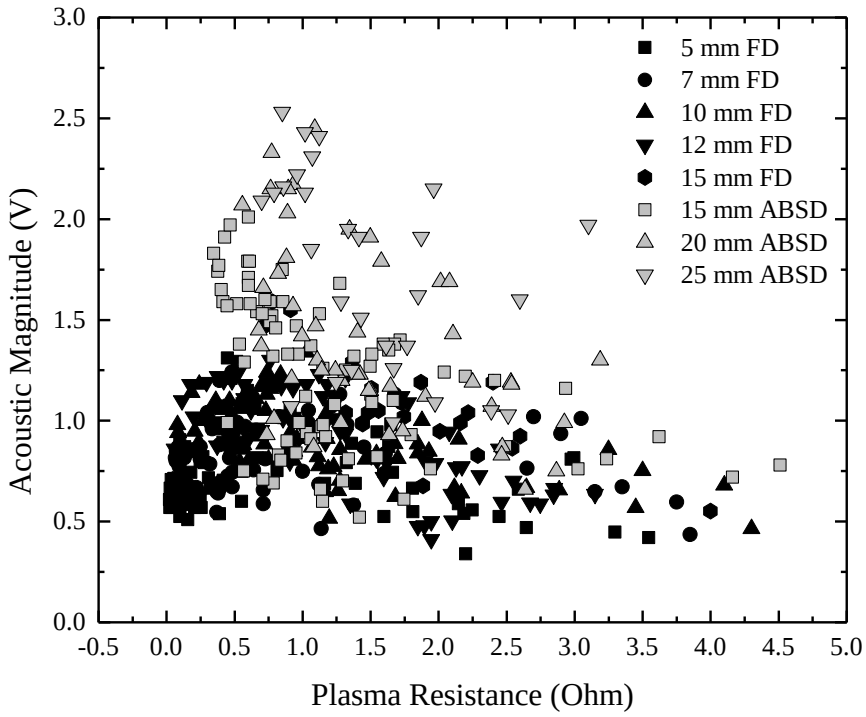

(d)

Figure 5-7. The $P_{cav\text{-}max}$ as a function of the R_{pl} for ABSD's for (a) 155 nF, (b) 266 nF, (c) 533 nF, (d) combined results for both FD's and ABSD's. Vertical solid lines show the circuit resistance for ABSD's discharge circuit.

It was found that the data points in Fig. 5-7 are more dispersed than those in Fig. 5-6. The major difference between the two parameters, T_{cavity} and $P_{cav\text{-}max}$, is their different sensitivity to the length of the gap. As discovered in the FD's, T_{cavity} was less sensitive to variation in the inter-electrode gap, l, and, $P_{cav\text{-}max}$ was dependent on l. Therefore, despite the influence of various combinations of V_{br} and R_{pl} on $P_{cav\text{-}max}$, the direct link between $P_{cav\text{-}max}$ and l increased the degree of dispersion in data points in Fig. 5-7.

The combined experimental results for FD's and ABSD's are shown in Fig. 5-7(d). A tendency, similar to the relationship between T_{cavity} and R_{pl} in Fig. 5-6(d), was observed: data points ($P_{cav\text{-}max}$) obtained for ABSD's demonstrate only the falling trend for $R_{pl} \geq R_{circuit}$. However, the values of $P_{cav\text{-}max}$ obtained for ABSD's were greater than those obtained for FD's with the same R_{pl} due to the significant influence of l on $P_{cav\text{-}}$

$_{max}$, indicating the effective improvement in the acoustic output by using longer inter-electrode gaps instead of ABSD's.

5.7 The period of cavity oscillation as a function of the energy delivered into the plasma channel

The dependency of the period of cavity oscillation on the energy delivered into the plasma channel for all three capacitance of ABSD's is shown in Fig.5-8. T_{cavity} showed an increasing trend with the increasing energy for all values of capacitance. Similar relationships were also found for FD's. This tendency is based on the proportionality between T_{cavity} and E_{pl} without any effect from the inter-electrode gap, l.

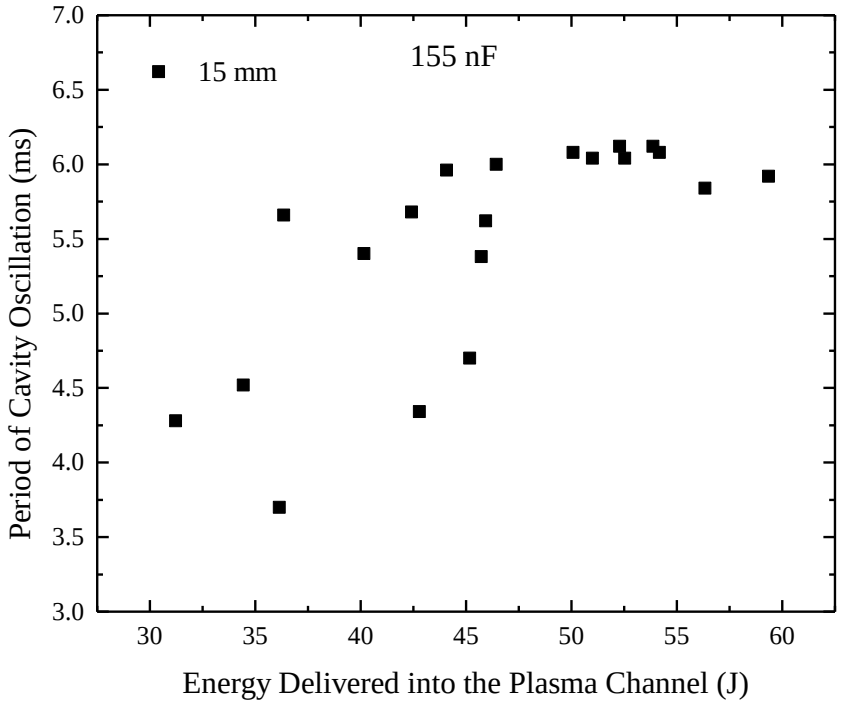

(a)

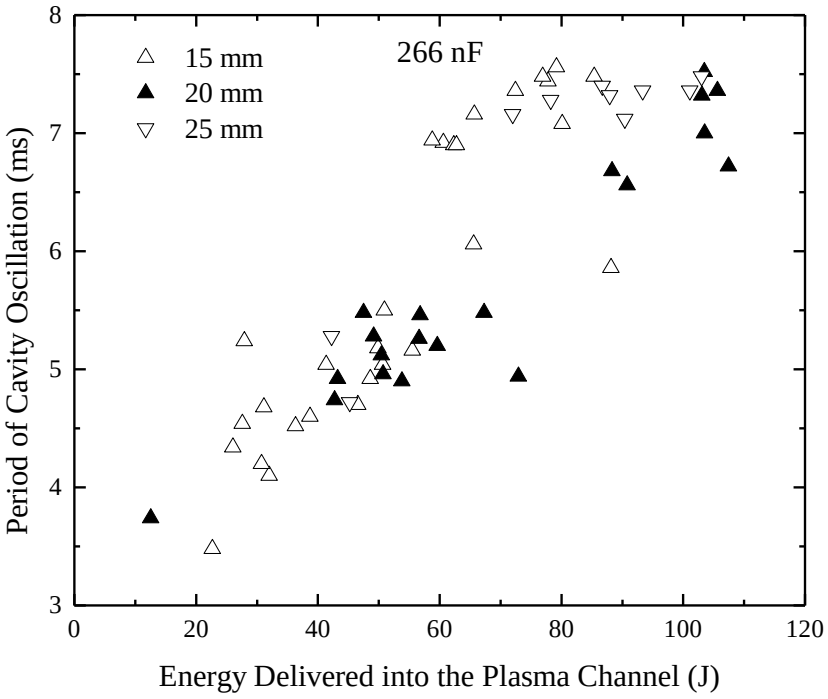
15 mm
20 mm
25 mm
266 nF
Period of Cavity Oscillation (ms)
Energy Delivered into the Plasma Channel (J)
0
20
40
60
80
100
120
3
4
5
6
7
8

(b)

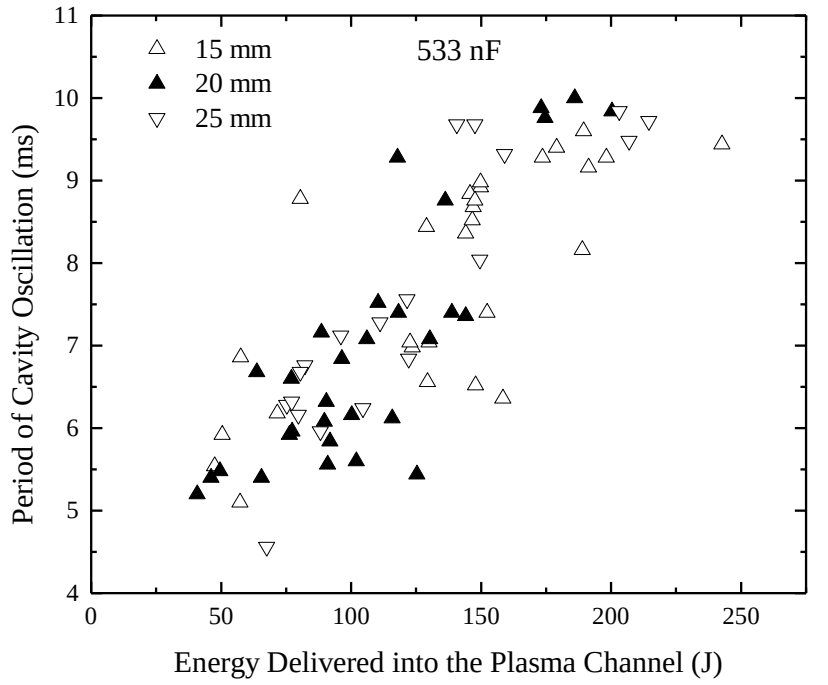
15 mm
20 mm
25 mm
533 nF
Period of Cavity Oscillation (ms)
Energy Delivered into the Plasma Channel (J)
0
50
100
150
200
250
4
5
6
7
8
9
10
11

(c)

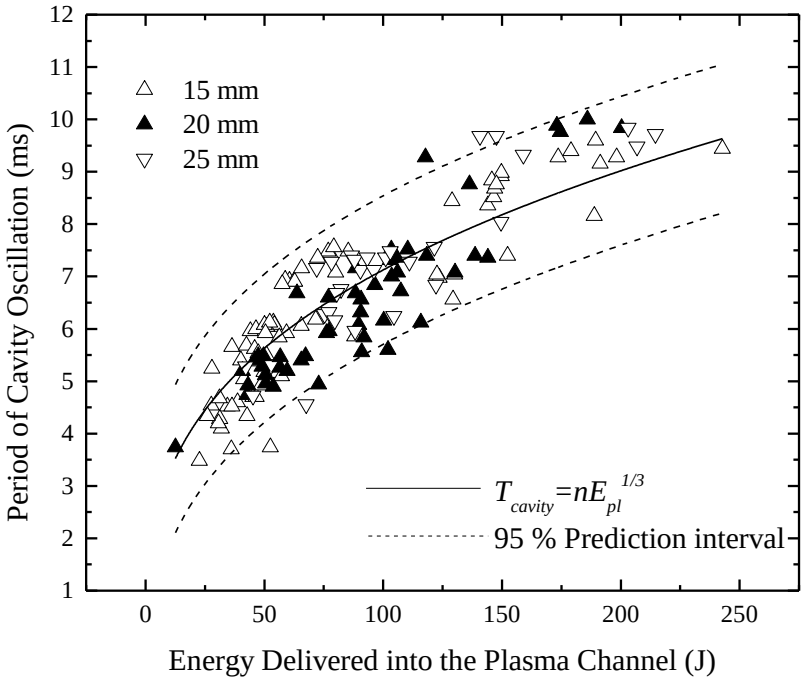

(d)

Figure 5-8. The relationship between the T_{cavity} and the E_{pl} for ABSD's for (a) 155 nF, (b) 266 nF, (c) 533 nF, (d) all three values of capacitance. Solid line shows the fitting result of (4.26) with n=1.49. Dashed line shows the upper and lower boundaries of the 95 % prediction intervals.

As it was established for the FD's, a part of the energy delivered into the plasma channel ($\delta \sim 0.3$) is expended on the cavity's work against water. Based on relationship between T_{cavity} and E_{pl} (4.26), it can be concluded that the expansion and collapse process of the cavity depends only on E_{pl}. Therefore, scaling relationship (4.26) was also used to fit the combined experimental results for all capacitance values for the ABSD's by using the software OriginLab 9.0.

The solid and dashed lines in Fig. 5-8(d) show the fitting of (4.26) to the experimental data and the upper and lower boundaries of the 95 % prediction intervals. A satisfactory agreement between (4.26) and the experimental data points can be seen in Fig. 5-8(d), verifying that (4.26) is suitable for describing the relationship between T_{cavity} and E_{pl} for the ABSD's. The proportionality coefficient, n, was found to be 1.49 ± 0.02, which was close to the value obtained for the FD's. The consistency of n for different types of discharges indicates similar dynamic behaviour of the cavity's

oscillation regardless of other parameters but the energy partition.

5.8 The acoustic magnitude as a function of the energy delivered into the plasma channel

Fig. 5-9 shows the functional behaviour of the magnitude of the acoustic impulse and the calculated energy delivered into the plasma channel for all three values of capacitance for ABSD's. In Fig. 5-9(a), experimental results for only 15 mm gap were registered with 155 nF capacitance due to the low probability of successful spark discharges in long inter-electrode gaps (20 mm and 25 mm). For all three values of capacitance, $P_{cav\text{-}max}$ increased with an increase in E_{pl}, which was similar to the FD's case. However, different from the FD's, the smooth slope-shifting stage at ~30 J was not clearly observed in the ABSD's case. This could be explained by the lack of experimental data in the range in which E_{pl} was less than ~ 30 J.

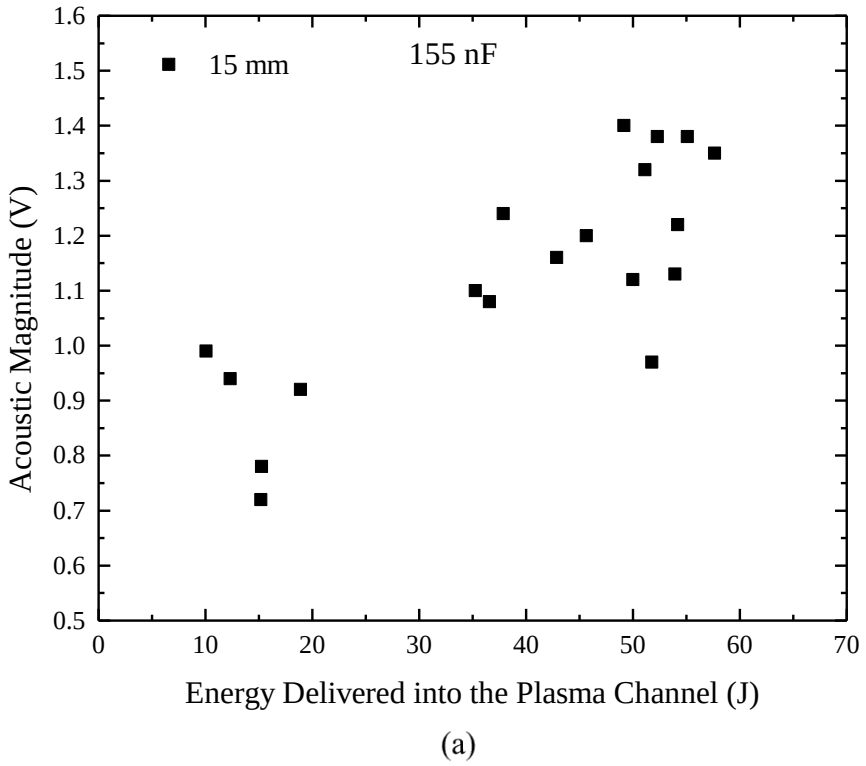

(a)

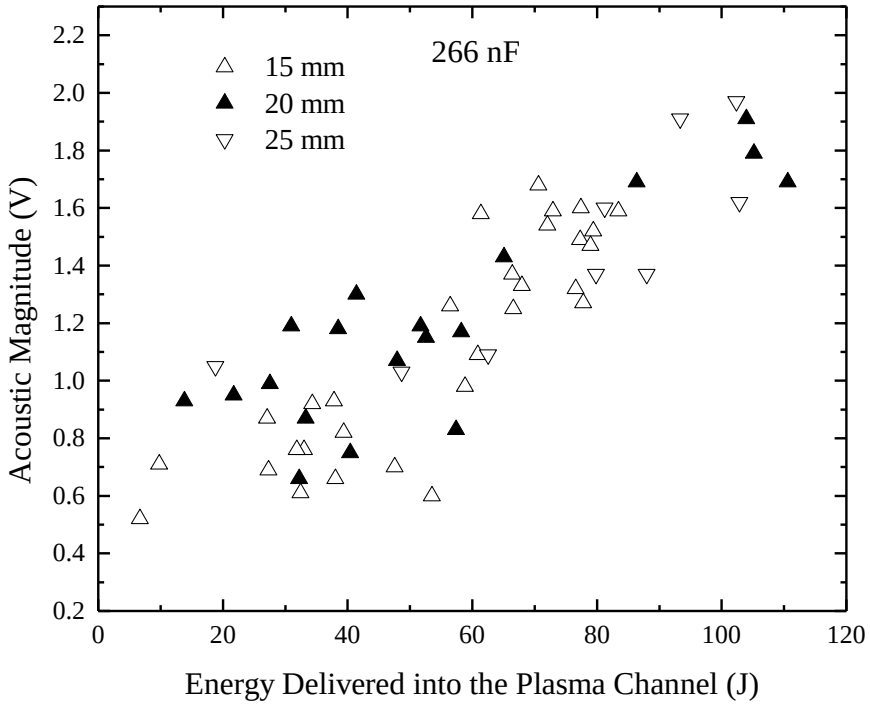
266 nF
15 mm
20 mm
25 mm
Acoustic Magnitude (V)
Energy Delivered into the Plasma Channel (J)

(b)

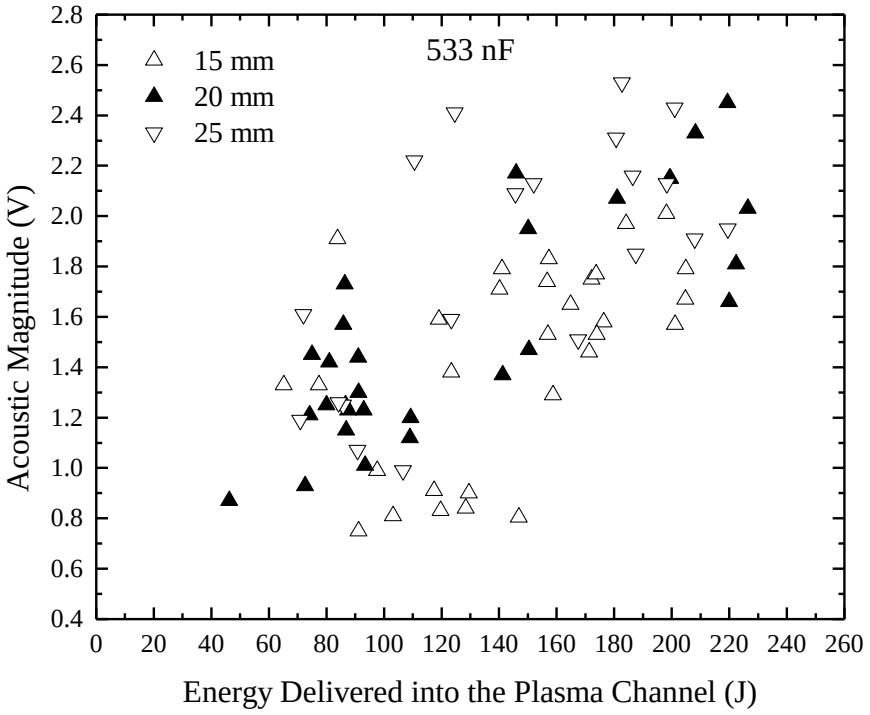
533 nF
15 mm
20 mm
25 mm
Acoustic Magnitude (V)
Energy Delivered into the Plasma Channel (J)

(c)

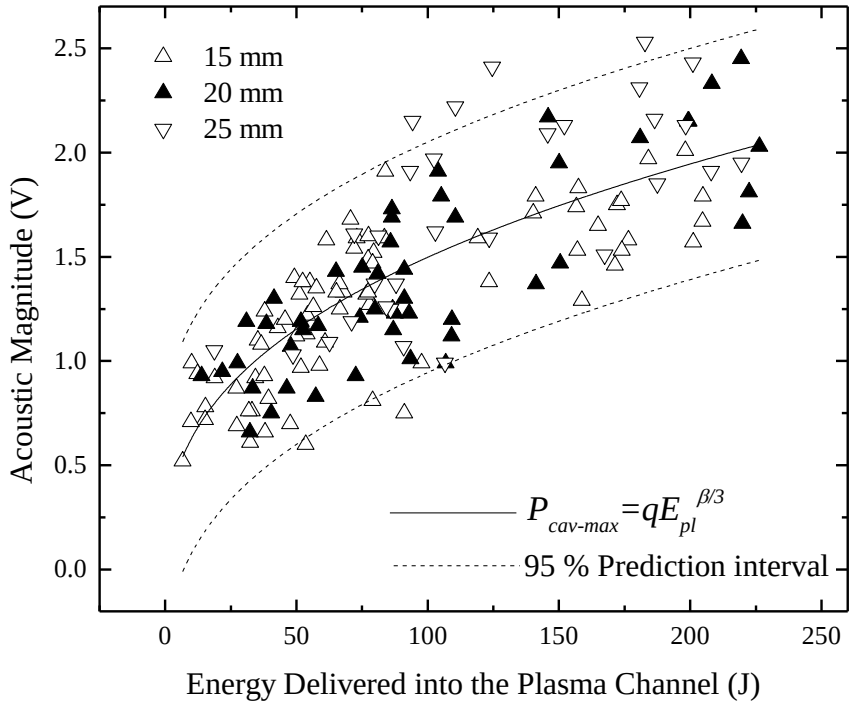

(d)

Figure 5-9. The relationship between the $P_{cav\text{-}max}$ and the E_{pl} for ABSD's for (a) 155 nF, (b) 266 nF, (c) 533 nF, (d) all three values of capacitance. Solid line shows the fitting result of (4.30) with q=0.26, $P_{cav\text{-}max}$ is in V and E_{pl} is in J. Dashed line shows the upper and lower boundaries of the 95 % prediction intervals.

To prove the link between $P_{cav\text{-}max}$ and E_{pl} for the FD's and ABSD's cases, scaling relationship (4.30), originally developed for FD's, was used to fit the combined experimental data points in Fig. 5-9(d). (4.30) with $q = 0.26$ provides a reasonable agreement with the experimental results, as shown in Fig. 5-9(d). Compared with the relationships between $P_{cav\text{-}max}$ and E_{pl} shown in Fig. 4-18(d), data points in Fig.5-9(d) showed a higher degree of dispersion, especially for $E_{pl} < 75$ J. This was due to greater increment in the inter-electrode gap in the ABSD's case as compared with the FD's case. The increment in the increase in the inter-electrode gap in the FD's tests was 2 or 3 mm while it was 5 mm in the ABSD's tests. Considering that the inter-electrode gap affects the acoustic output, the data points ($P_{cav\text{-}max}$) in Fig. 4-18(d) are more concentrated than those shown in Fig. 5-9(d), which demonstrate a higher degree of dispersion. Despite this, relationship (4.30) provides a reasonable tool for evaluation of the general behaviour of $P_{cav\text{-}max}$ with different E_{pl}. A detailed analytical model of

the link between $P_{cav\text{-}max}$ and E_{pl} in which l is included, will be developed in Chapter 6.

5.9 Conclusions

The comprehensive investigation of the ABSD's has been conducted in this chapter. The ABSD's were generated by injecting air bubbles into the inter-electrode gap to stimulate development of discharges as gas bubbles in the vicinity of the HV electrode facilitate the formation and propagation of the streamers. In order to investigate an efficiency of injected air bubbles in reducing the pre-breakdown time and in increasing magnitude of acoustic impulses, series of experimental tests have been conducted and the scaling phenomenological relationships between hydrodynamic, acoustic and electrical parameters were established.

In the case of ABSD's, the voltage during the pre-breakdown period monotonically decays until the breakdown occurs. The post-breakdown oscillation in the voltage and current waveforms for the ABSD's indicated that the pulsed power driving circuit and the plasma resistance can be modelled using the lumped RLC discharge circuit. Therefore, as in the case of the FD's, (2.21) and (2.22) were used together with the constant plasma resistance model to obtain the plasma resistance and the energy delivered into the plasma channel for the ABSD's.

Statistical analysis on the pre-breakdown time was conducted for the ABSD's in the case of discharges with 266 nF capacitance. It was found that the average pre-breakdown time obtained for the ABSD's was reduced by 66 % for 30 kV and 77 % for 35 kV, as compared with the FD's. This result shows the significant reduction in the breakdown formation time (time to complete breakdown) by injecting air bubbles into the inter-electrode gap. As a result, the maximum inter-electrode gap achieved by the ABSD's was increased to 25 mm by using the same energisation conditions as in the FD's.

It was found that both T_{cavity} and $P_{cav\text{-}max}$ increased with the increasing breakdown voltage. The T_{cavity} obtained for the ABSD's varied from ~ 3.5 ms to ~10 ms, which is similar to the results obtained for the FD's. The maximum magnitude $P_{cav\text{-}max}$ obtained in the ABSD's case was to ~2.45 V, which is ~ 53 % higher than in the case of the

FD's. The 'saturation' in T_{cavity} and $P_{cav\text{-}max}$ values was observed in short gaps with high breakdown voltages in the FD's. However, no such saturation was found in ABSD's, Fig. 5-4 and Fig. 5-5. Scaling relations, (4.10) and (4.17), were used to describe the dependency of T_{cavity} and $P_{cav\text{-}max}$ on V_{br}. The satisfactory agreement between analytical scaling and the experimental results confirmed similarities between FD's and the ABSD's in respect to the post-breakdown cavity formation and development.

No data points were found in the area in which the plasma resistance is smaller than the circuit resistance for the ABSD's. Both the T_{cavity} and the $P_{cav\text{-}max}$ followed a decreasing trend with an increase in R_{pl} when their values of plasma resistance were found to be larger than those of the circuit resistance, which explains the absence of the outlying data points (T_{cavity} and $P_{cav\text{-}max}$) in Fig. 5-4 and Fig. 5-5 corresponding to the condition $R_{pl} < R_{circuit}$.

The T_{cavity} and the $P_{cav\text{-}max}$ were found to be proportional to E_{pl}, similar to the the FD's case. Same scaling relations (4.26) and (4.30) were used in the ABSD's to link T_{cavity}, $P_{cav\text{-}max}$ and E_{pl}. The proportional coefficient, n, obtained for the ABSD's was 1.49, which was close to 1.65 obtained for the FD's, showing the similarity in the dynamic oscillation of the cavity produced by these two discharge mechanisms. The coefficient, q, obtained for the ABSD's case was 0.26 and was larger than 0.19 obtained for the FD's case, indicating the better performance of the ABSD's in generating stronger acoustic impulses.

The next chapter presents the experimental results obtained for the wire-guided discharges. The hydrodynamic and acoustic parameters and their relationships with the electrical parameters of the plasma channel will be investigated and different analytical models will be developed to link these parameters. The comparison between the acoustic generation capability of the FD's, ABSD's and WGD's was conducted and the advantages and disadvantages of each of these mechanisms are discussed.

6 Experimental results and analysis: Wire guided discharges

Free self-triggered underwater discharges can be developed using an electrode topology which allows repetitive breakdowns to be achieved without changing the electrodes. For example, in Chapter 4 in which the FD's have been discussed, the same electrode system was used to produce hundreds of discharges to investigate the relationships between their acoustic output paramters and energisation parameters. However, during the testing procedure, several obvious limitation factors attributed to the FD's technique were revealed: the probability of complete breakdown in longer inter-electrodes gaps became lower for low voltage/energy levels and the maximum magnitude of the acoustic impulse was thereby limited. In addition, even if the spark breakdown was successfully achieved, the acoustic performance (the acoustic magnitude) of the FD's was not stable. For example, in FD's tests with 15 mm gap and 533 nF storage capacitance, even the lowest charging voltage level (25 kV) would result in the discharge, which bridges the electrodes. However, after changing the capacitance to 266 nF (or 155 nF), and using higher charging voltage 30 kV (35 kV for 155 nF), the successful breakdown rate was less than ~ 30%.

The main reason for this low rate of successful breakdowns at lower energisation levels and/or longer inter-electrode distances is the longer propagation path of discharges and reduction in the pre-breakdown voltage due to Joule conduction throughout water (energy losses). One of the methods to address the issue is to use different triggering mechanism to facilitate the discharge formation and propagation, like the air-bubble stimulated discharge mechanism investigated in Chapter 5. It was confirmed that injection of air bubble into the inter-electrode gap is an effective method of increasing the maximum inter-electrode gap and of maintaining the repetitive breakdown operation rate.

Another method is to increase the energy available in discharge for longer gaps (by raising either the charging voltage or the storage capacitance). However, in many cases, it is not practical from dielectric coordination point of view in applications, such as the pre-treatment of oil extraction [25], the sea sonar system [26] and the rock fragmentation treatment [138], [139]. To increase the breakdown path without significant increase in the breakdown voltage, the wire-guided discharges can be used.

The fundamental principle of the wire-guided discharge is based on the establishment of a conductive straight path between the HV electrode and the ground electrode by a thin metallic wire. Using this approach, the ionic energy losses in water and the pre-breakdown time can be reduced and the inter-electrode distance (the discharge length) can be significantly increased. In [73], the comparison between the underwater spark discharges with and without the utilisation of metal wire was conducted for a 15 mm gap using the pulsed power driving circuit with 3 μF capacitance charged up to 30 kV. It was found that using the explosive wire approach result in significant reduction of the pre-breakdown time. The peak pressure of the shock wave generated by wire-guided discharges increased up to 6.31 MPa as compared with 3.3 MPa for free self-triggering discharges and the energy transfer efficiency was increased from 1.6 % (for free self-triggering discharges) to 7.7 % for wire guided discharges.

A number of investigations into the shock waves generated by wire-guided discharges have been conducted and presented in [64], [71], [73], [89], [99], [100], [102], [140], [141]. Different aspects of the wire-guided discharges have been studied including their mechanism and functional behaviour of the generated shock waves. For example, in [141], the time-dependent circuit parameters, and acoustic and light parameters were experimentally obtained. It was found that the heating and melting phases of the wire and its vaporization play an important role in the formation of the shock waves. In [64], it was found that the maximum pressure of the shock wave at the plasma-water interface was a linear function of the energy deposited per unit wire length and a function of the parameter, $\Pi = ((\rho_0/l_w)(\mathrm{d}P_{el}/\mathrm{d}t)_{\max})^{1/2}$, where ρ_0 is the initial density of the wire material and P_{el} is the electrical power of the discharge. In [140], it was shown that the energy deposited into the wire was ~4 kJ/mg and the peak pressure of the acoustic impulse was a non-linear increasing function of the applied voltage. Similar tendency was also obtained in [71]. Despite numerous publications on the underwater wire-guided discharges, there are significant gaps in understanding of their formation and development mechanism, and characteristics of the acoustic impulses generated by these types of discharges. Thus, a comprehensive study of WGD's is needed to establish relationships between the acoustic and hydrodynamic parameters and the electrical parameters of the circuit and the plasma channel. These characteristics will be important for optimisation of the acoustic output by tailoring the

circuit parameters in practical cases.

In the present work, electrical, hydrodynamic and acoustic parameters were obtained for the WGD's. It was shown that using the WGD's electrode topology described in Section 3.3.3, a significant improvement in the energy conversion efficiency and the strength of the acoustic impulses have been achieved for discharges in longer gaps with the same electrical parameters (charging voltage and storage capacitance) as in the case of the FD's. The relationships between the acoustic and electrical parameters have been established and analytical (phenomenological) scaling models have been developed.

6.1 Experimental results

As described in Chapter 3, with the purpose of comparisons between the different discharge initiation mechanisms, the energisation conditions for WGD's were kept the same as for FD's, including all combinations of charging voltages (25 kV, 30 kV and 35 kV) and three values of storage capacitance (155 nF, 266 nF and 533 nF). Three different lengths of thin copper wire were used in the tests: 15 mm, 45 mm and 75 mm, to investigate the effect of the inter-electrode gaps distance on the electrical and acoustic parameters of the WGD's.

6.1.1 Voltage and current waveforms

Voltage and current waveforms have been obtained for WGD's. An example of both *V(t)* and *I(t)* waveforms for a WGD with 45 mm gap and 266 nF capacitance, are shown in Fig. 6-1. The voltage and current waveform in Fig. 6-1 show the initial pre-breakdown process, which is different as compared with that of FD's.

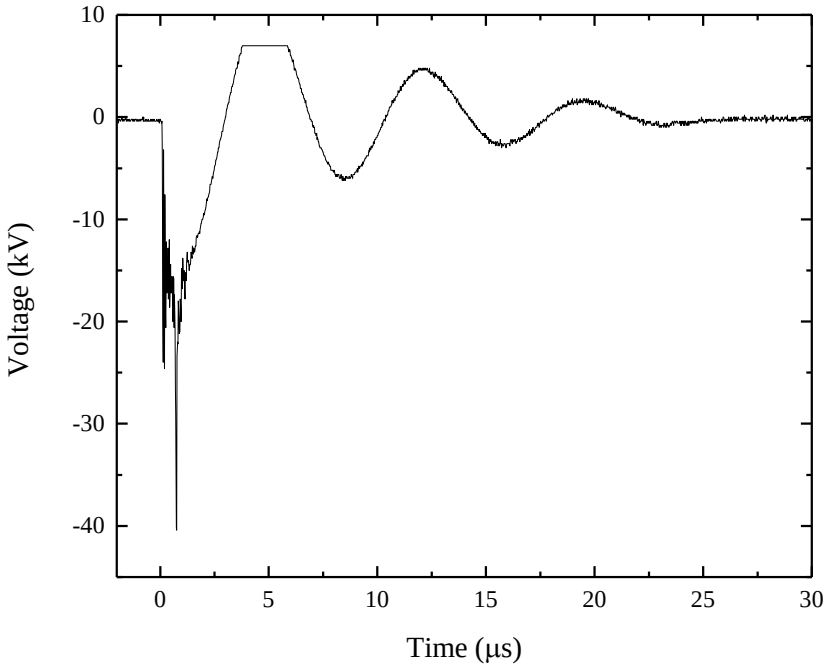
10
0
-10
-20
-30
-40
Voltage (kV)
0
5
10
15
20
25
30
Time (μs)

(a)

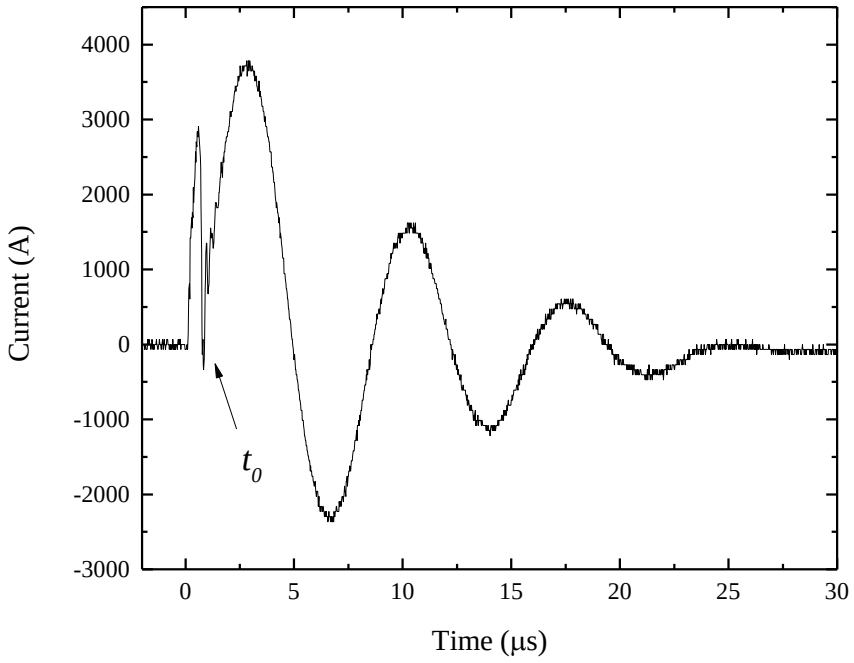
4000
3000
2000
1000
0
-1000
-2000
-3000
Current (A)
t_0
0
5
10
15
20
25
30
Time (μs)

(b)

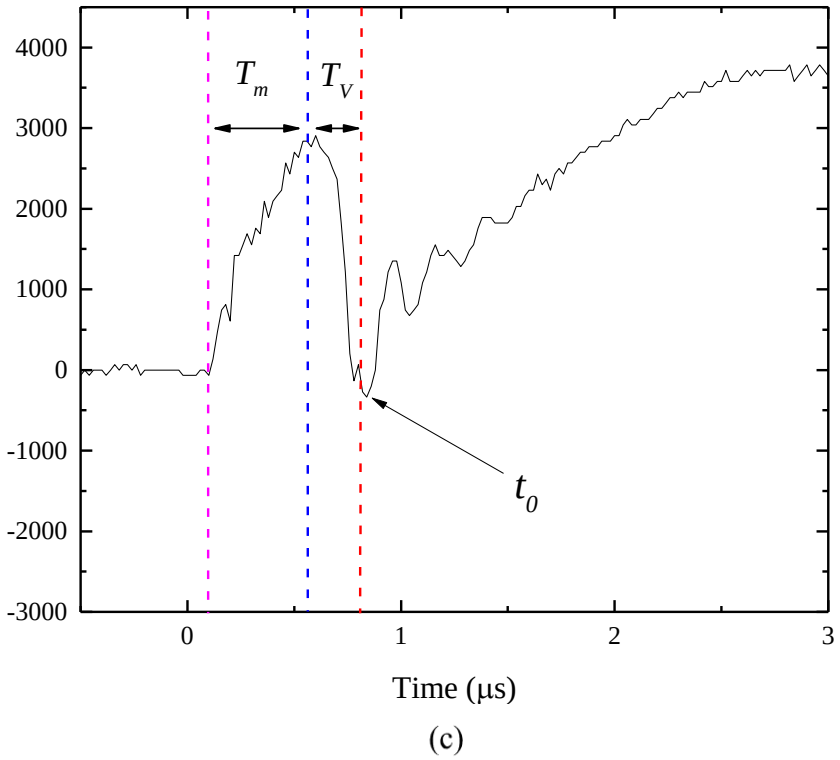

Figure 6-1. Example waveforms for the electrical parameters (a) voltage and (b) current during discharge period, t_0 showing roughly the breakdown moment when the current drops to zero. The variation of the current in the first ~ 3 μs after applying the voltage impulse is shown in (c). T_m indicates the wire heating, melting stage and T_v is the vaporization stage of the wire.

The relatively short pre-breakdown period with significant drop of voltage across the wire was observed for voltage from $t = 0$ μs to $t_0 = 1$ μs in Fig. 6-1 (a) for the breakdown above. A current pulse with magnitude of ~ 3 kA was observed during this period immediately after application of voltage to the HV electrode and before breakdown at moment t_0 in Fig. 6-1(b). During this period, a series of events took place in the system. Firstly, a voltage impulse appeared across the copper wire placed between the HV and ground electrodes. The wire resistance was relatively low (0.03 Ω - 0.16 Ω, obtained by (4.19) with $\rho_{cu} = 1.7 \times 10^{-8}$ Ω•m [142]), thus significant conductive current flows through the copper wire. This dynamic process resulted in the wire heating and melting stage and its disintegration stage, indicated by periods T_m

and T_v respectively in Fig. 6-1(c). Similar variation of the current as a function of time during the pre-breakdown period was also observed in [71], [140], [141]. After a complete plasma channel is formed between the HV and ground electrode at t_0, the underdamped oscillations in both voltage and current, similar to the FD's and ABSD's cases, were observed and the plasma resistance and the energy delivered into the plasma channel could be calculated using (2.21)-(2.24). However, the accurate "breakdown voltage" at the moment of the wire disintegration could not be obtained due to significant fluctuations in the voltage waveform, Fig. 6-1(a). Therefore, the analysis of the relationships between acoustic and hydrodynamic parameters and the breakdown voltage was not conducted for WGD's in this chapter.

6.1.2 Hydrodynamic parameters and acoustic signals

Fig.6-2 shows the acoustic signals (acoustic magnitude and period of cavity oscillation) obtained for a discharge in 15 mm gap with 155 nF. The basic profile of the acoustic impulse in Fig. 6-2(a) was similar to that in Fig. 4-2(a) obtained for FD's, which featured fluctuated multi-peaks and also a half cycle of negative pressure. It was found that the duration of the acoustic impulses emitted by either the FD's or the WGD's were same, which indicated that the initiation mechanisms of spark discharges have minimum impact on their acoustic emission. The magnitude of the acoustic impulse, $P_{cav\text{-}max}$ in Fig. 6-2(a) was again represented by the voltage signal from the Pinducer sensor and the period of cavity oscillation was defined as the time interval between the first and secondary acoustic impulses.

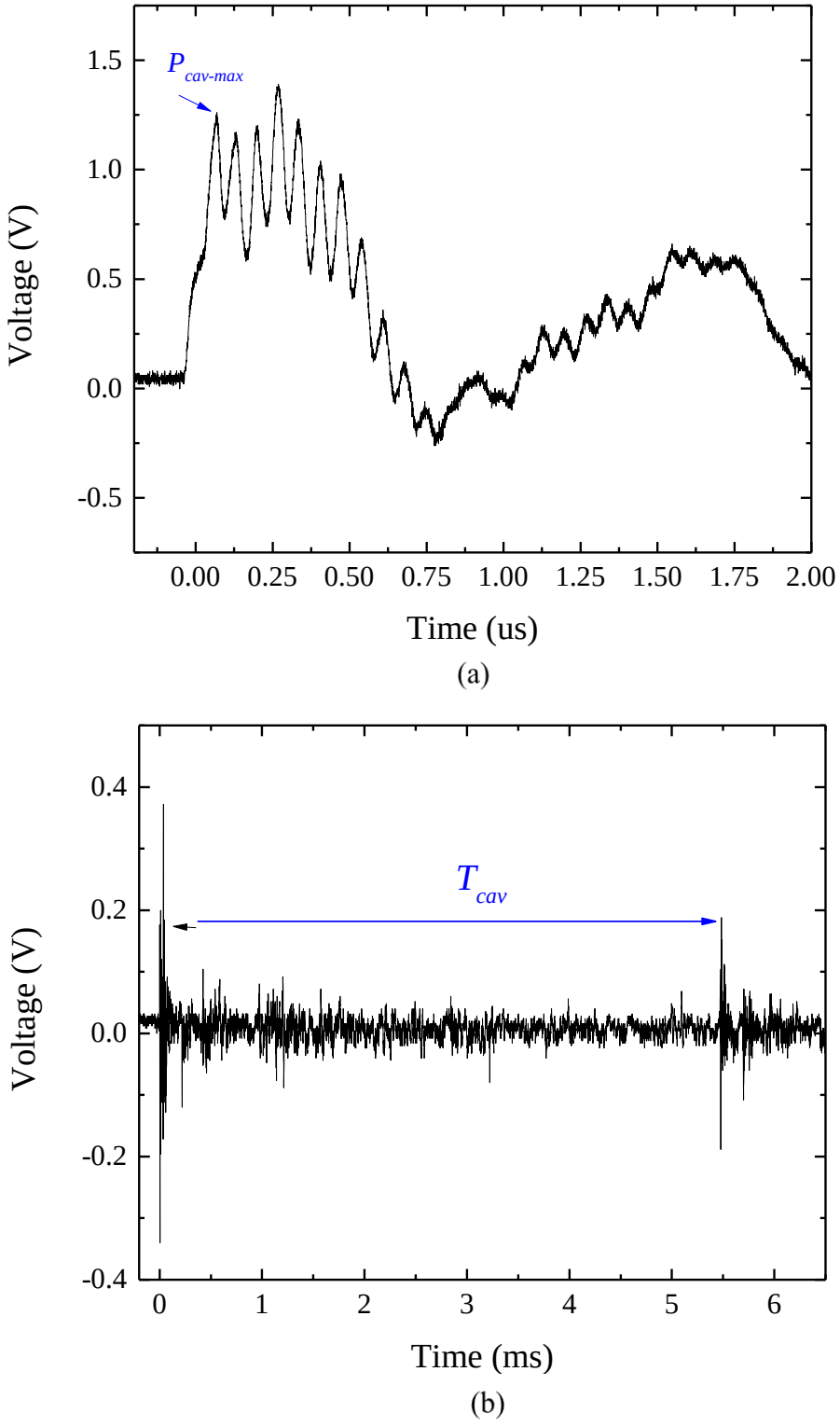

Figure 6-2. The acoustic signal obtained for a 15 mm gap: (a) the profile of the acoustic impulse with the maximum pressure $P_{cav\text{-}max}$, (b) the first and secondary acoustic impulses showing the period of cavity oscillation T_{cavity}.

6.2 The acoustic magnitude comparison between free self-triggering discharges and wire guided discharges

As discussed at the beginning of this chapter, the purpose of using copper wire was to 'optimise' the breakdown path and to create a straight plasma channel between electrodes in order to improve the acoustic magnitudes of the discharges and their stability. Therefore, the inter-electrode gap of 15 mm together with three values of capacitance have been used in both cases for the FD's and WGD's to investigate the impact of these two particular initiation mechanisms on their average acoustic output.

To conduct this comparison, statistical analysis of the acoustic magnitudes ($P_{cav\text{-}max}$), obtained in the 15 mm gap for both WGD's and FD's, was conducted for each energisation level i.e. for each combination of C and V_{br}. The average values of $P_{cav\text{-}max}$ and their standard deviation obtained for the FD's and WGD's in 15 mm gap are listed in Table. 6-1.

Table 6-1. Comparison of the acoustic magnitude between FD's and WGS cases for three values of capacitance

Capacitance (nF) and charging voltage (kV)		$P_{cav\text{-}max}$ for FD's (V)	$P_{cav\text{-}max}$ for WGD's (V)
		Average (± Standard deviation)	Average (± Standard deviation)
155	25	N/A	1.38 ± 0.01
	30	N/A	1.46 ± 0.06
	35	0.99 ± 0.05	1.50 ± 0.04
266	25	N/A	1.38 ± 0.03
	30	0.85 ± 0.21	1.51 ± 0.01
	35	1.29 ± 0.21	1.57 ± 0.03
533	25	N/A	1.43 ± 0.09
	30	1.05 ± 0.08	1.71 ± 0.07
	35	1.23 ± 0.08	1.77 ± 0.04

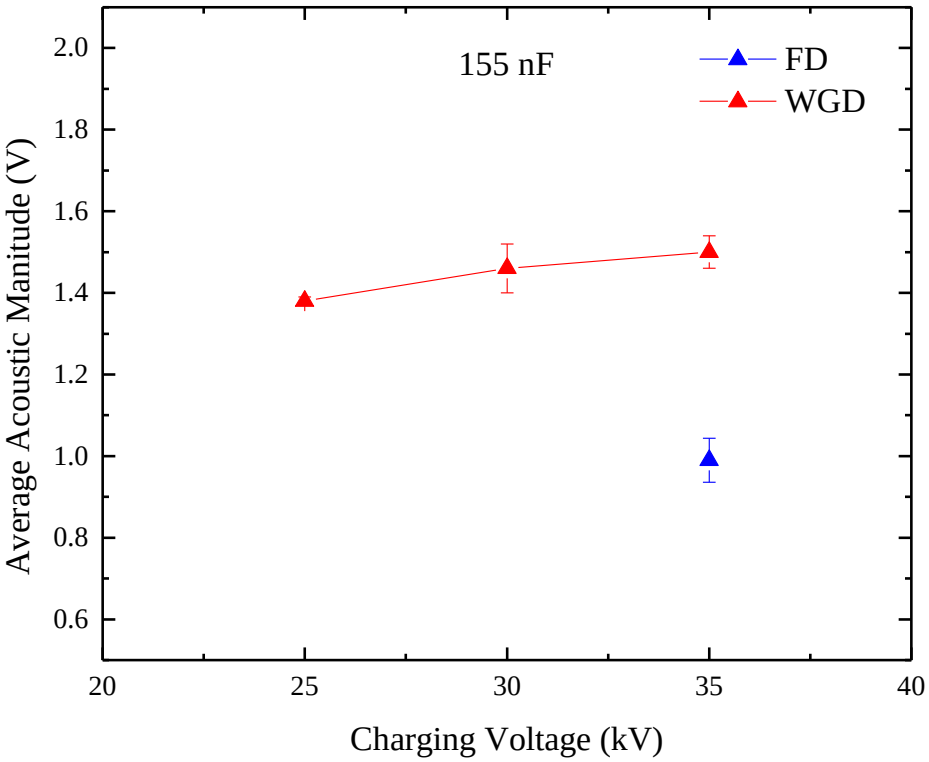
155 nF
FD
WGD
Average Acoustic Manitude (V)
2.0
1.8
1.6
1.4
1.2
1.0
0.8
0.6
20
25
30
35
40
Charging Voltage (kV)

(a)

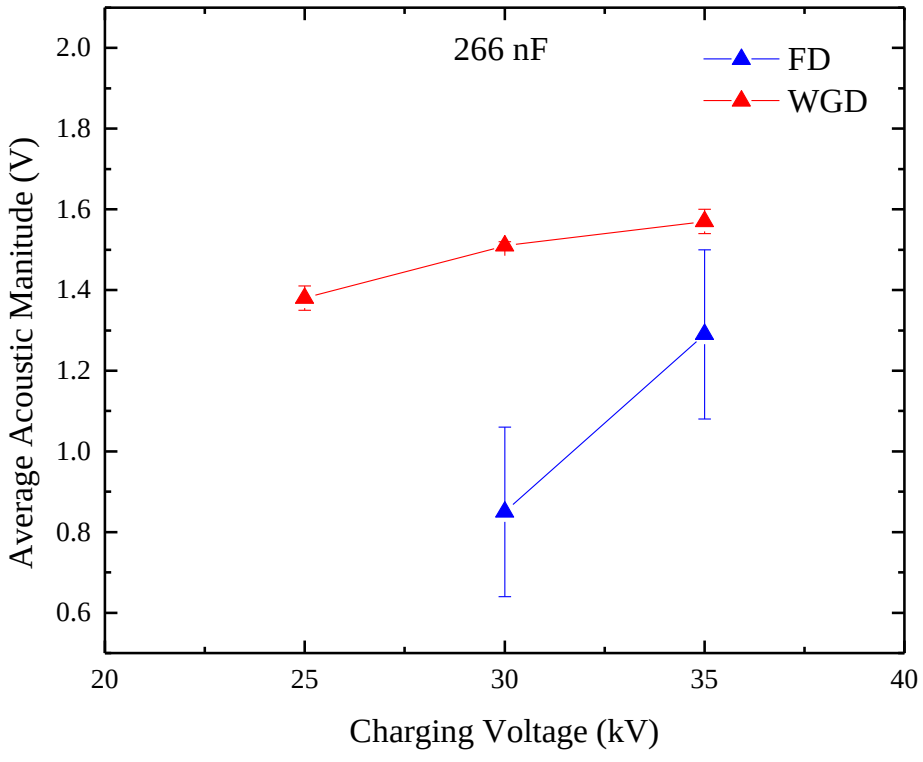
266 nF
FD
WGD
Average Acoustic Manitude (V)
2.0
1.8
1.6
1.4
1.2
1.0
0.8
0.6
20
25
30
35
40
Charging Voltage (kV)

(b)

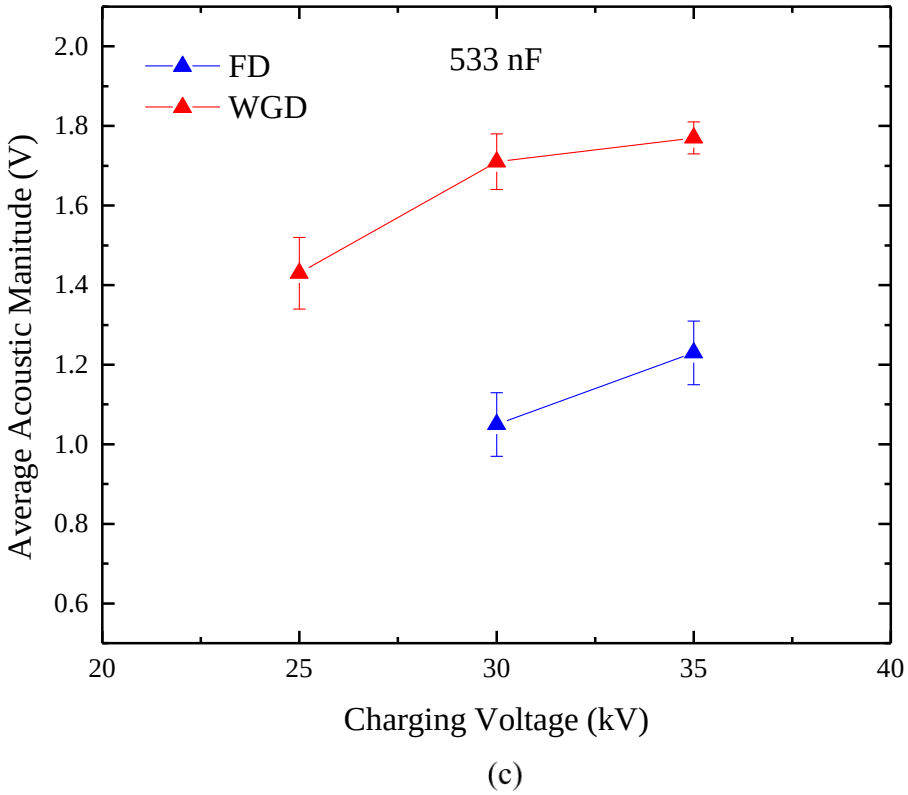

Figure 6-3. The average value of the acoustic magnitude together with standard deviation as a function of the charging voltage obtained for (a) 155 nF, (b) 266 nF and (c) 533 nF for both FD's (blue) and WGD's (red) cases. Solid lines are provided for visual guidance only.

Fig. 6-3 shows the comparison between the FD's and WGD's in terms of average values and the corresponding standard deviation of the acoustic magnitude as a function of the charging voltage. It is worthy of note that there are no experimental data ($P_{cav\text{-}max}$) for several combinations of the charging voltage and capacitance (25 kV and 30 kV for 155 nF and 266 nF, 25 kV for 533 nF), as no breakdown events were achieved. On the contrary, for all energisation levels, breakdowns in all inter-electrode gaps were successfully achieved with guidance wire, which confirmed the effective performance of the wire in reducing the pre-breakdown time and the conductive energy losses during this period. Using this wire initiation method, the breakdown was achieved in the 75 mm gap even at the lowest energisation level (25 kV changing voltage and 155 nF storage capacitance).

It was found that the average values of $P_{cav\text{-}max}$ for the WGD's were larger than those for the FD's and their corresponding standard deviation were also significantly smaller

for all charging voltage levels. The improvement in the average $P_{cav\text{-}max}$, $P_{cav\text{-}max\text{-}ave\text{-}WGD's}$/ $P_{cav\text{-}max\text{-}ave\text{-}FD's}$, varied from ~ 144 % to ~ 177 % and the reduction in the standard deviation of $P_{cav\text{-}max}$, varied from ~ 20 % to ~ 95 %. Small standard deviation for the peak pressure of the shock wave was also obtained in [140]. This finding indicates that the values of $P_{cav\text{-}max}$ obtained for WGD's under the same experimental conditions (C and $V_{charging}$) were close to each other, showing the stabilising effect of the wire in facilitating the spark breakdowns. The obtained results for FD's showed that although there were individual breakdowns with strong acoustic impulses (magnitude as high as ~1.6 V in Fig. 4-7), the relatively low average value and large standard deviation of $P_{cav\text{-}max}$ revealed the instable nature of the FD's in long inter-electrode gaps, especially when the energisation level was not too high, for example, 30 kV and 35 kV for 288 nF.

Despite a small amount of energy consumed by the electrically melted copper wire: ~ 3.3 to ~ 16.7 J (based on the data from [140], 4 kJ/mg, and the mass of the wires) for different wire lengths, the use of a thin conductor for initiation of discharges not only defines the 'ideal' breakdown path but also stabilises the discharge properties. Thus, the wire-guided initiation mechanism improves the general performance of the underwater spark discharge in terms of the generated acoustic impulses. This feature would be beneficial for the practical applications of such discharges when stable acoustic output is required.

6.3 The energy delivered into the plasma channel as a function of the plasma resistance

The values of the plasma resistance and the energy delivered into the plasma channel for all WGD's were obtained. The circuit resistance of the WGD's test was also calculated and the results are shown in Table. 6-2. Based on the normalized performance of the WGD's under the same experimental conditions, the relationship between R_{pl} and E_{pl} in this case is of great interest in order to investigate how R_{pl} determines E_{pl} and to find the link between them together with the information of the inter-electrode gap.

Table 6-2. The circuit resistance calculated for WGD's for three capacitances

C (nF)	$R_{circuit}$ (Ω)
155	0.49
266	0.37
533	0.29

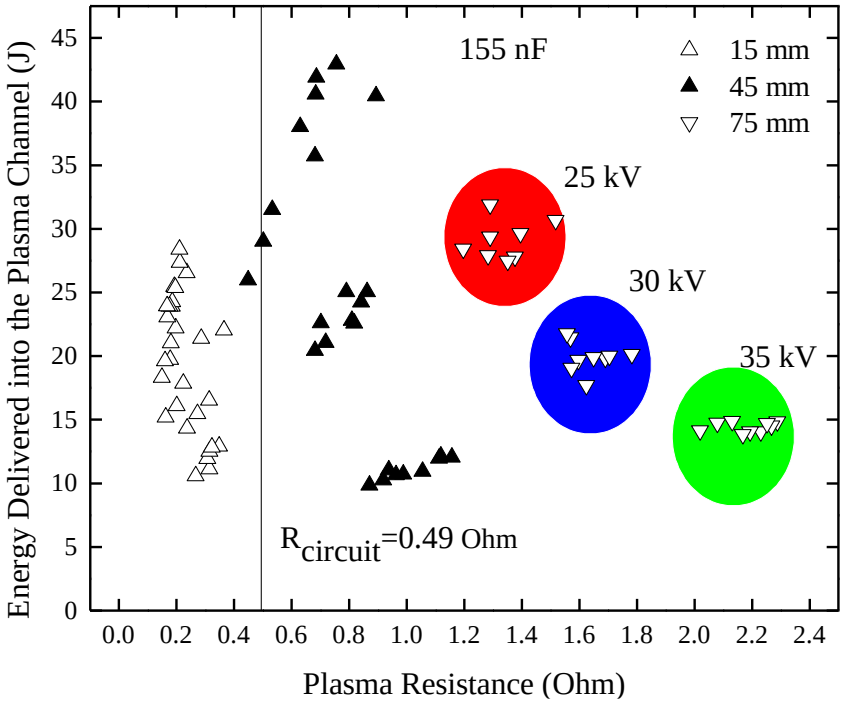

(a)

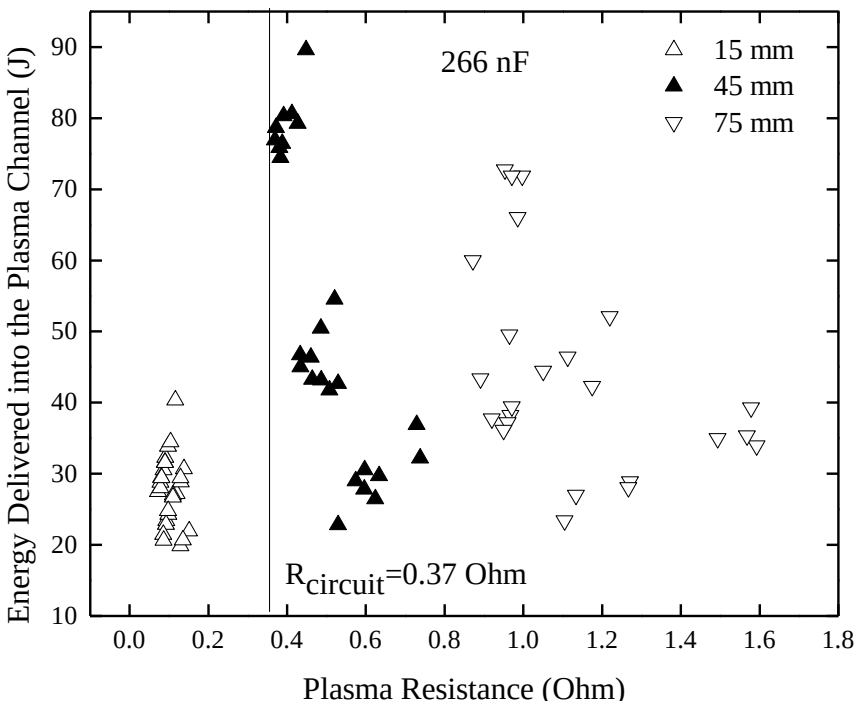
266 nF
15 mm
45 mm
75 mm
$R_{circuit}$=0.37 Ohm
Energy Delivered into the Plasma Channel (J)
Plasma Resistance (Ohm)

(b)

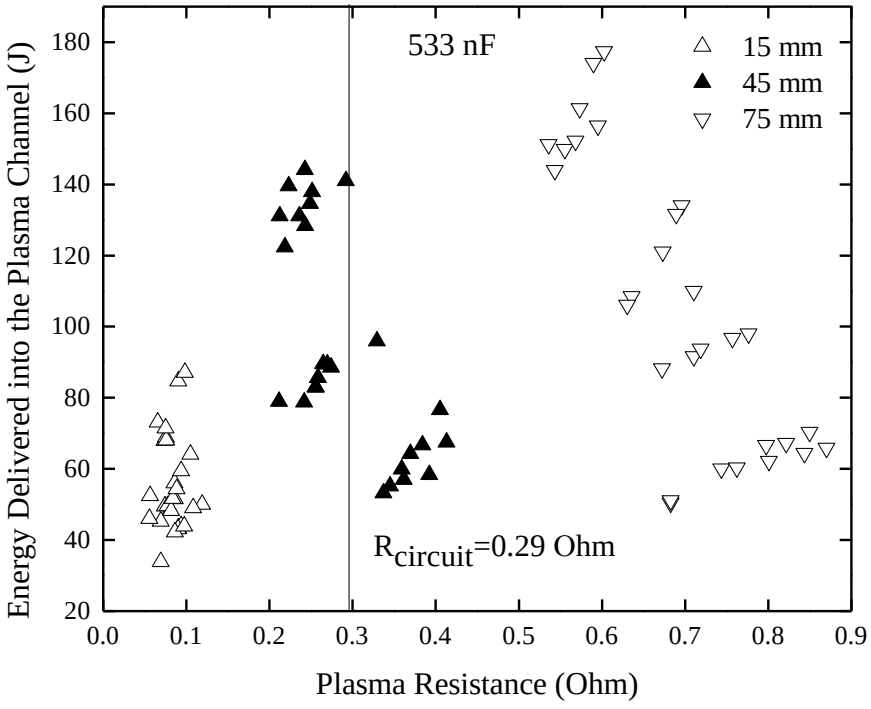
533 nF
15 mm
45 mm
75 mm
$R_{circuit}$=0.29 Ohm
Energy Delivered into the Plasma Channel (J)
Plasma Resistance (Ohm)

(c)

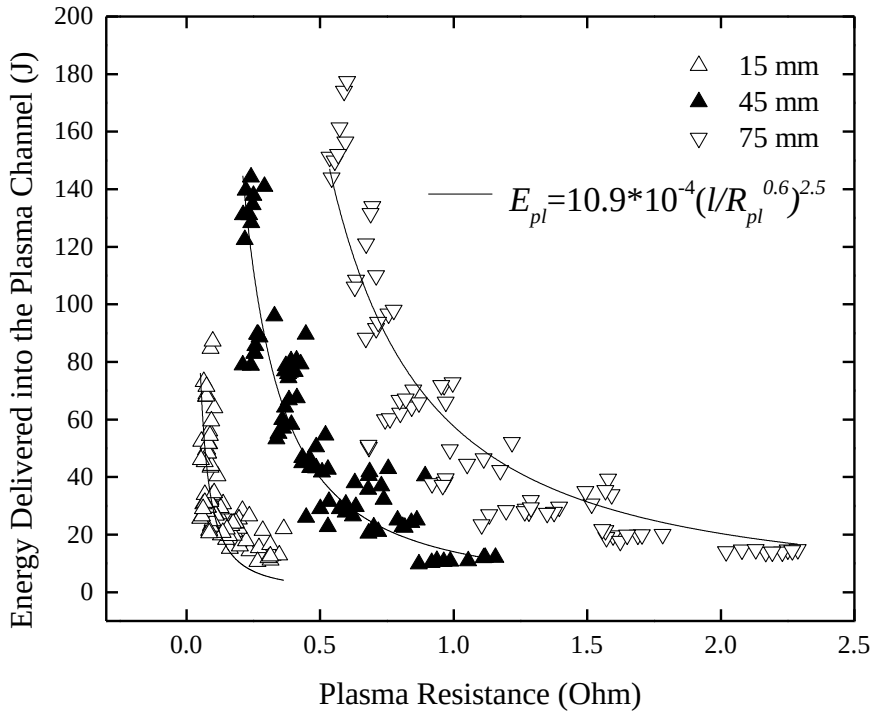

(d)

Figure 6-4. The energy delivered into the plasma channel as a function of the plasma resistance for (a) 155 nF, (b) 266 nF, (c) 533 nF, (d) all discharges for WGD's. Coloured areas indicate data points obtained in different charging voltage levels: 25 kV (red), 30 kV (blue) and 35 kV (green). Solid lines in (d) show the fitting lines of (6.4).

Fig. 6-4 shows the relationship between R_{pl} and E_{pl} for all three values of capacitance and for different lengths of wires. It was shown that values of R_{pl} obtained for 45 mm and 75 mm gaps were comparable with and greater than $R_{circuit}$ = 0.37 Ω and $R_{circuit}$ = 0.29 Ω and those for 15 mm gap were smaller than $R_{circuit}$ = 0.49 Ω. For all three cases, data points were gathered into different clusters. These clusters correspond to the three charging voltage levels used in the tests, indicated by the coloured areas for 75 mm gap in Fig. 6-4(a) as examples. For the same inter-electrode gap, discharges achieved by lower charging voltage had larger values of R_{pl}.

It was found that E_{pl} decreased with an increase in R_{pl}, especially for the 45 mm and 75 mm gaps. This tendency can be explained by the energy conversion efficiency shown in Fig. 4-14. For the results obtained for the15 mm gap, the value of the ratio, $x = R_{pl}/R_{circuit}$, was in the range from ~ 0.17 to ~ 0.76. The corresponding energy

conversion efficiency was low and it was sensitive to x. However, the discharges in this x range covered the charging voltage levels from 25 kV to 35 kV and resulted in large variation in the energy available in the circuit at breakdown. In this case, the amount of energy to be transferred into plasma was determined by the breakdown energy rather than the energy conversion efficiency as discussed in the case of FD's. Lower charging voltage produced higher value of R_{pl}. These observations explained the decreasing trend observed for 15 mm gap. For the discharges obtained for the 45 mm and 75 mm gaps, their values of x was in the range from ~ 0.9 to ~ 4.4 in which the energy conversion efficiency was in the shifting and slowly-increasing stages. Similar to the relationships between $T_{cavity,}$ $P_{cav\text{-}max}$ and R_{pl} observed for the FD's and ABSD's, the influence of the breakdown voltage in the final amount of energy delivered into the plasma channel was stronger than that of the relatively stable energy conversion efficiency. Therefore, E_{pl} decreased with an increase in R_{pl} in this range of x for the WGD's.

Considering the well-defined tendency (dependency of E_{pl} on R_{pl}) shown in Fig. 6-4, it is interesting and important to find a scaling relationship hip in order to describe the link between these two parameters. The plasma resistance was obtained as a constant value based on the (2.21)-(2.24). However, as discussed in Chapter 2, the development of the plasma channel is a dynamic process and the behaviour of the transient plasma resistance, $R_{pl}(t),$ is time-dependent. This behaviour of the plasma resistance as a function of time can be described using the model (2.19). This link between $R_{pl}(t)$ and $I(t)$ was derived for the breakdown channel in gas. However, in relationship to the post-breakdown process in water this model also can be used.

In the energy balance model developed by Rompe and Weizel [113], and discussed in [110], the coefficient n_1 is equal to 1/2. In Vlastos's model [105], $n_1 = 3/5$ and c_{co} is considered as a constant coefficient, depending on the radius of the arc channel and other plasma parameters. In [108], by assuming that n_1 was a phenomenological constant; it could be obtained by finding the best fit between experimental and calculated values of the plasma resistance. Also, it has been shown that (2.19) is applicable for description of the transient plasma channel resistance. For example, in [115], the value of $n_1 = 1/2$ was used to provide information of the transient plasma resistance in liquid hydrocarbons. In [110], [142], equation (2.19) together with

n_1 = 1/2 and n_1 = 3/5 showed a reasonable agreement with the experimental transient spark resistance in air. In [107], [144], equation (2.19) with n_1 = 1/2 and n_1 = 3/5 showed a good agreement with the initial phase of the resistance for a pulsed arc in air. In the case of WGD's in this work, (2.19) is used to establish a link between the plasma resistance and the inter-electrode gap. The phenomenological coefficient n_1 was obtained for all discharges for different inter-electrode gaps.

In Section 2.5.3, the difficulties of direct measurements of the transient plasma resistance have been discussed. As shown in [110], [143], after the rapid reduction, the plasma resistance stays almost constant for the next tens of microseconds. This period is long as compared with the fast decay phase (a few nanoseconds). Therefore, it is reasonable to use the effective (constant) plasma resistance, R_{pl}, obtained by (2.22) to represent the general behaviour of its time-dependent value, $R_{pl}(t)$, in (2.19). The feasibility of this approach has been confirmed in Chapter 4 and 5, which represented the analysis of FD's and ABSD's. Therefore, $R_{pl}(t)$ can be expressed as:

$$R_{pl}(t) = R_{pl} \tag{6.1}$$

By combining (2.19) and (6.1), the relationship between the constant plasma resistance, current waveform and the inter-electrode gap can be written as:

$$R_{pl} = \sqrt{2P_0 c_{co}} \cdot \frac{l}{\left(\int_{t_0}^{t} I(t)^2 dt\right)^{n_1}} \tag{6.2}$$

As shown in (6.2), the energy delivered into the plasma channel is directly related to the square value of the current oscillation. By substitute the current term by (2.24) in (6.2), a new model can be obtained to describe the relationship between E_{pl} and R_{pl} illustrated in Fig. 6-4:

$$E_{pl} = a\left(\frac{l}{R_{pl}^{1-n_1}}\right)^{1/n_1} \tag{6.3}$$

where a is phenomenological constant coefficient.

To find the value of coefficients a and n_1, (6.3) have been fitted to the experimental data for 45 mm and 75 mm gap (as data points for 15 mm gap did not show complete trend as the other two gaps) by using the nonlinear fitting function in OriginLab 9.0 software, where a and n_1 were set as free fitting parameters. E_{pl} is in J and R_{pl} is in **Ω** and l is in mm. The fitting results for all discharges are shown in Table. 6-3.

Table 6-3. The coefficient, a and n_1, obtained for 45 mm and 75 mm gaps

Inter-electrode gap (mm)	a	n_1
45	$(10.3 \pm 0.5) \times 10^{-4}$	0.45 ± 0.03
75	$(11.5 \pm 0.5) \times 10^{-4}$	0.34 ± 0.02

The average values of the coefficients a and n_1, were found to be 10.9×10^{-4} and 0.4 respectively and the value of n_1 was close to value 1/2 used in the RW model. Therefore, the analytical model for energy E_{pl} is:

$$E_{pl} = 10.9 \cdot 10^{-4} \left(\frac{l}{R_{pl}^{0.6}} \right)^{2.5} \tag{6.4}$$

The solid lines in Fig. 6-4(d) were obtained by fitting (6.4) to experimental data for all three inter-electrode gaps and showed a good agreement with the relationship between E_{pl} and R_{pl}, especially for 45 mm and 75 mm cases. Although an insignificant deviation of the fitting curve from the experimental data was observed at the tail of the 15 mm case, (6.4) provided a satisfactory description on the initial falling slope of E_{pl} (R_{pl}), where most of the data points for 15 mm gap fitted. Model (6.4) provides an analytical tool for investigation of the link between the electrical parameters of the plasma channel and for calculation of the amount of energy delivered into the plasma channel based on predictable value of the plasma resistance.

Fig. 6-5 and Fig. 6-6 showed a strong link obtained for the hydrodynamic and acoustic parameters and the plasma resistance. The peak values of T_{cavity} and $P_{cav\text{-}max}$ corresponded to the values of the plasma resistance close to the circuit resistance. There is a difference as compared with FD's and ABSD's. The values of the plasma resistance were classified by different energisation levels (combinations of capacitance

and charging voltage) for WGD's. Therefore, to conduct a detailed investigation on the dependency of T_{cavity} and $P_{cav\text{-}max}$ on R_{pl}, not only their relationships were plotted but also a series of scaling relations were established based on (6.4).

6.4 The period of cavity oscillation as a function of the plasma resistance

Fig. 6-5 showes the relationships between T_{cavity} and R_{pl} for all three values of capacitance. It was shown that T_{cavity} follows a well-defined decreasing tendency with an increase in R_{pl} for each inter-electrode gap and the value of T_{cavity} was greater for either larger capacitance or longer gap. It was found that E_{pl} is inversely proportional to R_{pl} as observed in Fig. 6-4 and confirmed by model (6.4). In the case of FD's and ABSD's, T_{caivty} is proportional to $E_{pl}^{1/3}$. The combination of these two models explains the functional behaviour of T_{cavity} in Fig. 6-5.

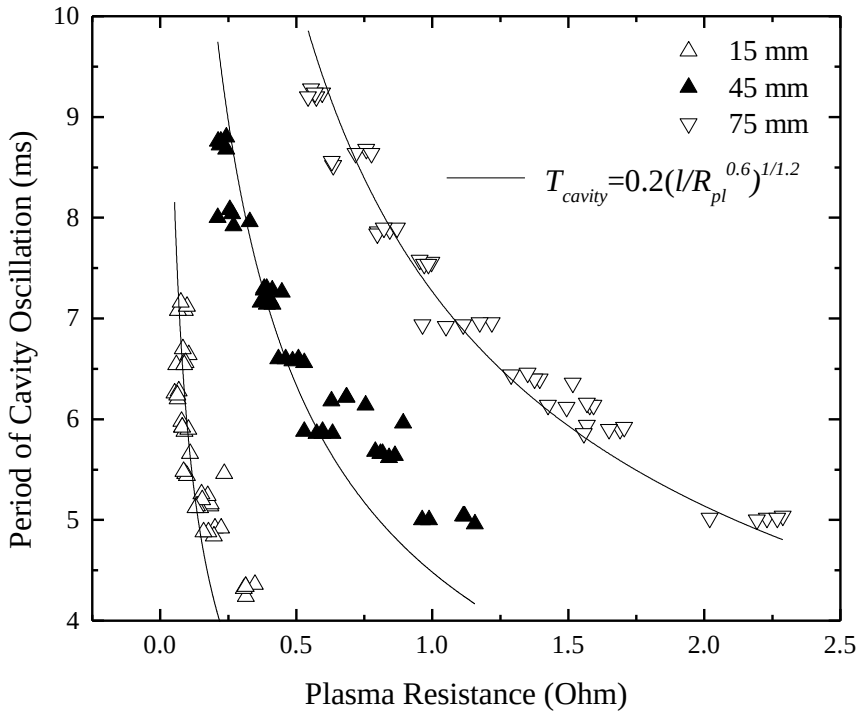

Figure 6-5. The period of cavity oscillation as a function of the plasma resistance for all WGD's. Solid lines in show the fitting results of (6.6).

Following the post-breakdown development of the cavity and acoustic emission in the case of FD's, it can be assumed that (4.26) is also applicable to the WGD's. Combination of (4.26) and (6.4) provides an analytical link between the period of cavity oscillation and the plasma resistance:

$$T_{cavity} = b\left(\frac{l}{R_{pl}^{1-n_1}}\right)^{1/3n_1} \tag{6.5}$$

where b is a phenomenological coefficient, which contains the information on proportionality coefficients in (4.26) and (6.4). T_{cavity} is in ms and R_{pl} is in Ω.

(6.5) has been fitted to the experimental data of each inter-electrode gap by setting b as a free parameters in OriginLab 9.0c software. The coefficient n_1 = 0.4, obtained for model (6.4), was used and the fitting results are shown in Table. 6-4.

Table 6-4. The coefficient, b, obtained as fitting parameter of (6.5) for different wire lengths

Inter-electrode gap (mm)	b
15	0.195 ± 0.007
45	0.187 ± 0.005
75	0.199 ± 0.003

Therefore, the average value of the coefficient, b, was found to be 0.194 and the phenomenological model (6.5) for WGD's is given as:

$$T_{cavity} = 0.194\left(\frac{l}{R_{pl}^{0.6}}\right)^{1/1.2} \tag{6.6}$$

Solid lines in Fig. 6-5(d) show the results obtained by fitting (6.6) to the experimental results for all inter-electrode gaps. A good agreement between the analytical lines and experimental data verified the effectiveness of (6.6) in describing the relationship between T_{cavity} and R_{pl}. This dependency can be used to calculate the value of R_{pl} from the hydrodynamic measurement and thereby E_{pl} can be obtained using (6.4).

6.5 The acoustic magnitude as a function of the plasma resistance

The acoustic magnitude as a function of the plasma resistance has been obtained for all three inter-electrode gaps and capacitance and it is shown in Fig. 6-6. It was found that $P_{cav\text{-}max}$ decreased with an increase in R_{pl} for each specific inter-electrode gap. For the same value of R_{pl}, $P_{cav\text{-}max}$ obtained with a longer wire length was larger than that generated with a shorter wire. This tendency is similar to the functional behaviour of $T_{cavity}(R_{pl})$ observed in Fig. 6-5.

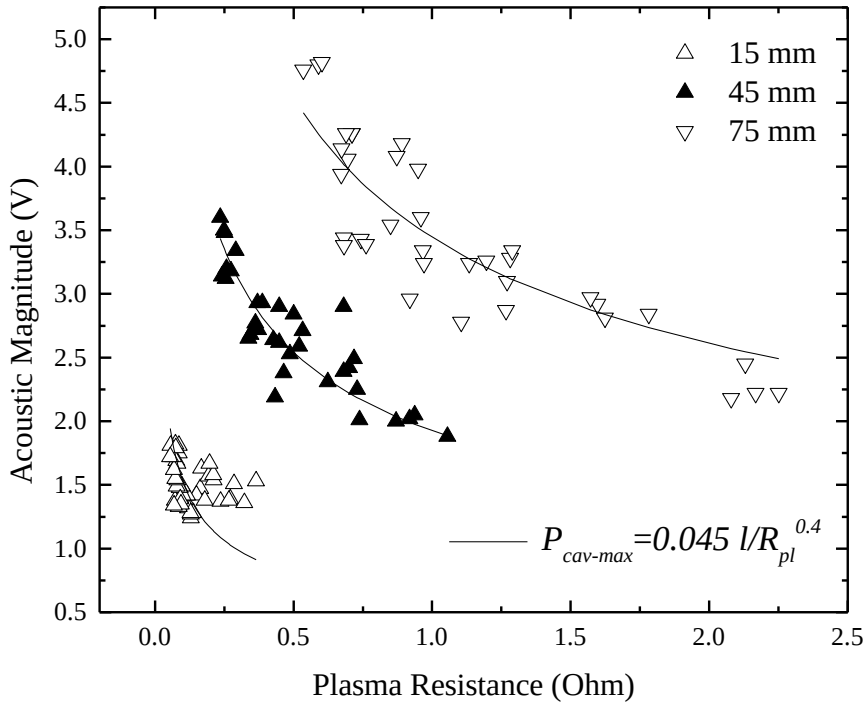

Figure 6-6. The acoustic magnitude as a function of the plasma resistance for all WGD's. Solid lines in (d) show the fitting results of (6.8).

Based on the above observation of similar dependency of $P_{cav\text{-}max}$ on R_{pl} for each inter-electrode gap, a phenomenological scaling relationship for $P_{cav\text{-}max}$ is obtained:

$$P_{cav-max} = c_1 \frac{l}{R_{pl}^{m_1}} \tag{6.7}$$

where c_1 and m_1 are phenomenological coefficients and l is the wire length. These coefficients were obtained by fitting (6.7) to the experimental data in Fig. 6-6, except the 15 mm case due to the compact location of the data points ($P_{cav\text{-}max}$) for this wire length. This procedure was implemented in OriginLab 9.0c by setting c_1 and m as free parameters. The results are shown in Table. 6-5.

Table 6-5. The coefficient, c_1 and m, obtained as fitting parameters of (6.7) for 45 mm and 75 mm gaps

Inter-electrode gap (mm)	c_1	m_1
45	0.043 ± 0.006	0.34 ± 0.05
75	0.047 ± 0.007	0.46 ± 0.07

Therefore, the average values of coefficients, c_1 and m_1, were calculated as 0.045 and 0.4 respectively and the analytical model (6.7) for WGD's is:

$$P_{cav-max} = 0.045 \frac{l}{R_{pl}^{0.4}} \tag{6.8}$$

The phenomenological scaling (6.8) has been applied to the experimental data as solid lines in Fig. 6-6(d). In 45 mm and 75 mm cases, good match between the fitting curves and experimental data was observed while a general trend was shown for only part of the data points ($P_{cav\text{-}max}$) in 15 mm gap due to the highly-centralised data distribution. This data-gathering phenomenon is due to the extremely short pre-breakdown time for breakdown tests conducted in 15 mm gap, resulting in the minor variation in the plasma resistance values for all applied energisation levels. Therefore, in order to see a further increase of plasma resistance for the 15 mm case, lower changing voltage (< 25 kV) or smaller capacitance (< 155 nF) will be needed.

6.6 The period of cavity oscillation as a function of the energy delivered into the plasma channel

The energy delivered into the plasma channel is the fundamental parameter, which defines the acoustic performance of the plasma system. It will be of great importance to establish the link between the acoustic magnitude and the energy delivered into the plasma channel to evaluate the hydrodynamic and acoustic performance of the system.

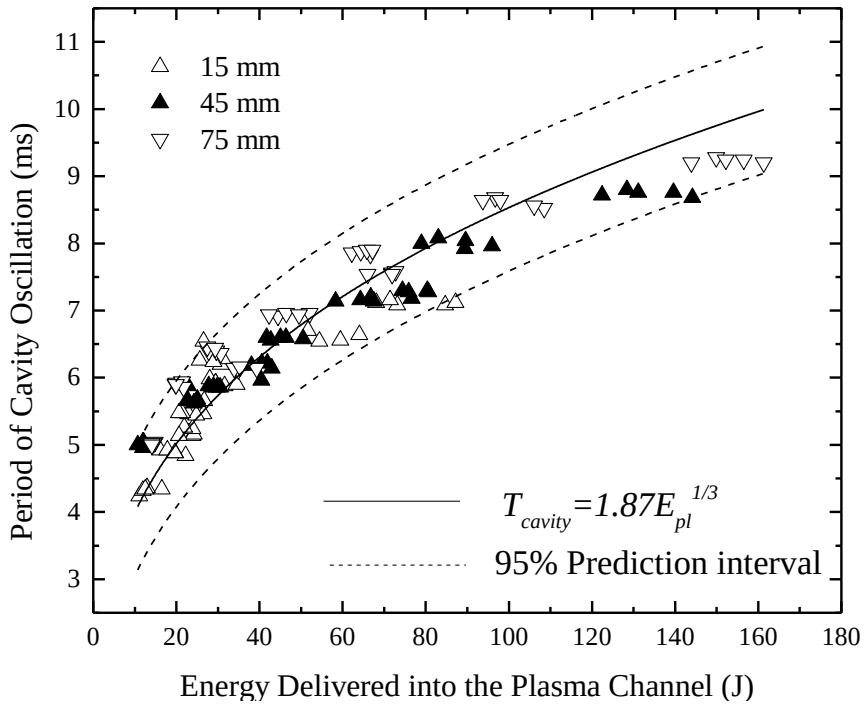

(a)

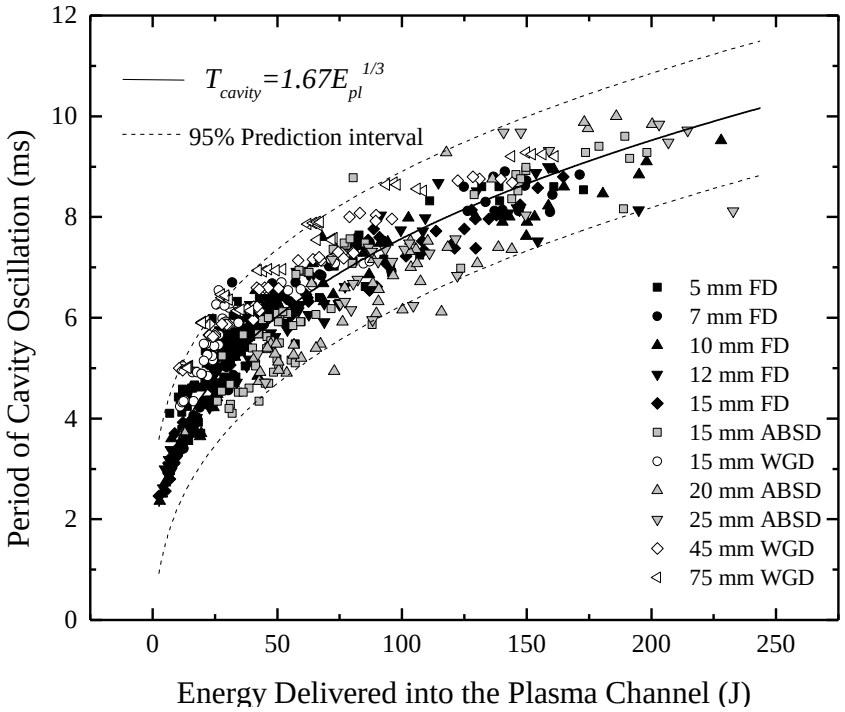

(b)

Figure 6-7. The period of cavity oscillation as a function of the energy delivered into the plasma channel for (a) all discharges for WGD's and (b) all discharges for FD's, ABSD's and WGD's. Solid lines and dashed lines show the fitting curves obtained by (4.26) and the upper and lower boundaries of the 95 % prediction intervals respectively.

The relationship between the period of cavity oscillation and the energy delivered into the plasma channel for all discharges, FD's, ABSD's and WGD's, are shown in Fig. 6-7. It is shown that T_{cavity} increases with an increase in E_{pl} for all three inter-electrode gaps for WGD's. The well-defined functional behaviour of $T_{cavity}(E_{pl})$ is similar to the results obtained in the case of FD's and ABSD's. Also, as shown in Fig. 6-7(a), there was no significant difference in the values of T_{cavity} for different wire lengths when the same E_{pl} was obtained for different discharges, indicating the minor influence of l on T_{cavity} in the case of WGD's. This finding confirms the conclusion made for the FD's and ABSD's: the development of the gas cavity after breakdown does not directly depend on the inter-electrode gap. Therefore, based on this observation, same scaling model (4.26), originally obtained for FD's, can be used to link T_{cavity} and E_{pl} for the WGD's.

Due to the monotonic tendencies for all wire lengths as shown in Fig. 6-7(a), it is reasonable to fit (4.26) directly to the combined experimental data in order to find n, which does not depend on l. By using fitting function in OriginLab 9.0c (T_{cavity} is in ms and E_{pl} is in J and n_1 is set as free parameter), the proportionality coefficient, n, was found to be 1.87 ± 0.02 for WGD's:

$$T_{cavity} = 1.87E_{pl}^{1/3} \tag{6.9}$$

The fitting leads to the fitting of phenomenological scale relationship (6.9) to the experimental data, which is shown as the solid line in Fig. 6-7(a), and upper and lower boundaries of the 95 % prediction intervals obtained and presented as dashed lines. It was shown that most of the experimental data points follow the main trend described by (6.9) whatever the wire length was and all points were within the upper and lower boundaries of the 95 % prediction intervals. The agreement observed between (6.9) and the experimental data is good enough to confirm the feasibility of (4.26) for wire-guided discharges. Therefore, it is possible to predict E_{pl} by knowing T_{cavity} without complex calculations of electrical parameters.

Table 6-6. The proportionality coefficient, n, obtained for the cases of FD's, ABSD's and WGD's

Discharge mechanism	n
FD's	1.65
ABSD's	1.49
WGD's	1.87

The values of the proportionality coefficients, n, obtained for FD's, ABSD's and WGD's are shown in Table. 6-6. It is shown that there is no significant difference between these values, thus, a same value of n can be obtained for all three discharge mechanisms. The average value of n = 1.67 was calculated and used in (6.10):

$$T_{cavity} = 1.67E_{pl}^{1/3} \tag{6.10}$$

Then, model (6.10) was fitted to the combined experimental data for all tests conducted for FD's, ABSD's and WGD's and was shown in Fig. 6-7(b) as solid line with upper and lower boundaries of the 95 % prediction intervals as dashed lines. A satisfactory agreement between (6.10) and the experimental data was found in Fig. 6-7(b).

Model (6.10) allows prediction of the development of the gas cavity after breakdown for all energy levels used for underwater spark discharge in this work. The relationship which states that T_{cavity} is proportional to E_{pl} to the power of *1/3* has been confirmed and can be used in different types of discharges, which is essential in the comprehensive study of the gas cavity (generated by the electrical discharge) and in the link between the hydrodynamic and electrical parameters.

6.7 The acoustic magnitude as a function of the energy delivered into the plasma channel

In the previous section, the relationship between T_{cavity} and E_{pl} has been obtained and phenomenological model (6.10) has been verified for all underwater spark discharge mechanisms. The acoustic magnitude, $P_{cav\text{-}max}$, is an important parameter and its relationship with E_{pl} will be established in this section.

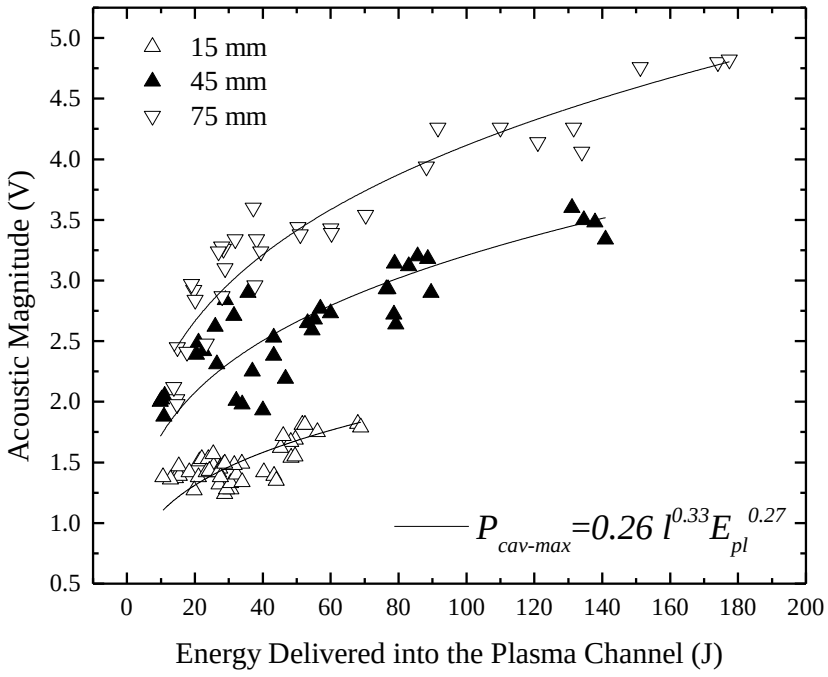

(a)

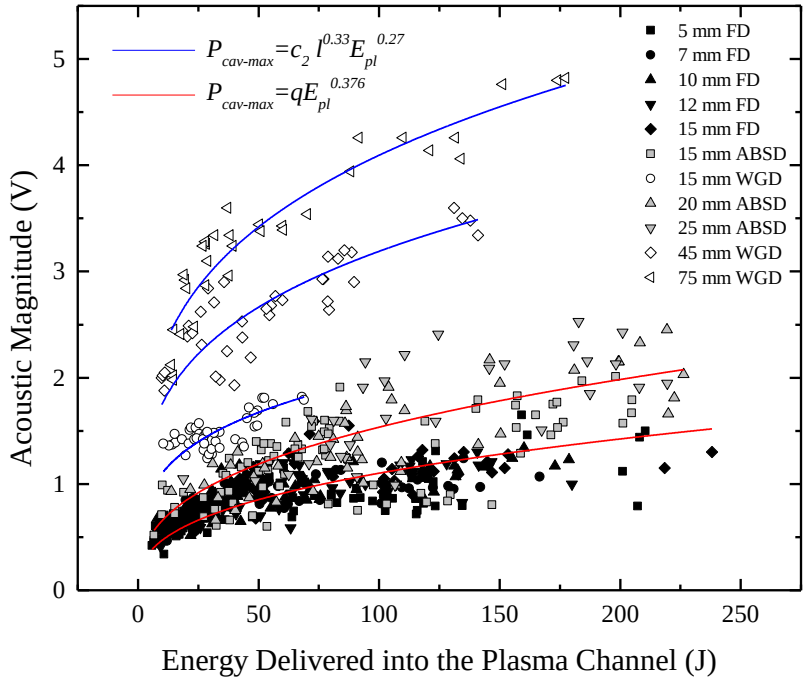

(b)

Figure 6-8. The acoustic magnitude as a function of the energy delivered into the plasma channel for (a) all discharges for WGD's and (b) all tests conducted for FD's, ABSD's and WGD's. Black lines in (a) show fitted lines obtained by (6.13). Blue and red lines in (b) show fitted lines obtained by (4.30) and (6.13) respectively.

Fig. 6-8 shows the behaviour of $P_{cav\text{-}max}$ as a function of E_{pl} for all wire lengths (inter - electrode gaps) in WGD's and for all tests conducted for FD's, ABSD's and WGD's. It is shown that $P_{cav\text{-}max}$ increases with an increase in E_{pl}. Similar to the tendency obtained for the case of FD's and ABSD's, the tdendency shown in Fig. 6-8(a) is nonlinear and the slope is smoother for E_{pl} in the range $E_{pl} > 80$ J. As compared with FD's and ABSD's, the experimental data obtained for each wire length are clearly separated from the other two lengths. This is due to the significant variation (30 mm) in the length of wire used in the WGD's tests, which shows sensitivity of $P_{cav\text{-}max}$ to l.

In Chapter 4 and 5, the link between $P_{cav\text{-}max}$ and E_{pl}, (4.30), was established from the relationship between the pressure impulse and the mass of high explosive used to generate underwater chemical explosion. For the WGD's, the relationship between $P_{cav\text{-}max}$ and R_{pl} is well-defined, Fig. 6-6(d), and a phenomenological scaling relationship, (6.8), which included the wire length, has been derived for these discharges. Also, it has been shown that E_{pl} is inversely proportional to the R_{pl} and this functional dependency was described by (6.4). Therefore, it is possible to establish a link between the acoustic magnitude and the total energy released into the plasma channel for wire-guided discharges by substituting (6.8) in (6.4), which provides a new scaling relationship:

$$P_{cav-max} = c_2\left(l^{(1-n_1-m_1)}E_{pl}^{n_1 m_1}\right)^{\frac{1}{1-n_1}} \tag{6.11}$$

where c_2 is the proportionality coefficient, which is also a function of c_1 and a in (6.4) and (6.8):

$$c_2 = c_1 a^{\frac{n_1 m_1}{n_1 - 1}} \tag{6.12}$$

With values of $n_1 = 0.4$ and $m_1 = 0.4$, (6.11) can be rewritten as:

$$P_{cav-max} = c_2 l^{0.33} E_{pl}^{0.27} \tag{6.13}$$

There are two ways to obtain the value of the coefficient, c_2. One method is to resolve (6.12) mathematically for known values of c_1, a, n_1 and m_1 in (6.12) to obtain c_2. The other method is to fit (6.13) to the experimental data in Fig. 6-9 (a) to obtain the value of c_2 matching the experimental data. In order to verify model (6.13), both methods were used and compared. If the resulting values of c_2 are close to each other, scaling relationship (6.13) can be confirmed as valid for the relationship between $P_{cav\text{-}max}$ and E_{pl} for the WGD's.

Coefficient, c_2: different approaches

- Coefficient c_2 can be calculated from (6.12). The value of c_2 obtained by this equation is $c_2 = 0.045 \times 0.00111^{(0.4 \times 0.4 / (0.4 - 1))} = 0.276$.
- Also, c_2 can be obtained by fitting model (6.13) to the experimental points in Fig. 6-8(a) using the fitting function in software OrignLab 9.0c. The results of this fitting procedure are shown in Table. 6-7. Then, the average value of c_2 is calculated as $c_2 = 0.26$.

Table 6-7. Values of coefficient, c_2, obtained for three wire lengths by fitting (6.13) to experimental data in Fig. 6-8(a)

Inter-electrode gap (mm)	c_2
15	0.24 ± 0.01
45	0.26 ± 0.01
75	0.29 ± 0.01

By comparing values of c_2 obtained by these two different methods, it is possible to conclude that they are close to each other. Thus, the procedure used to derive scaling relationship (6.13) is feasible and thus, this model can be used to describe the relationship between $P_{cav\text{-}max}$ and E_{pl}. The proportionality coefficient, $c_2 = 0.26$, will be used in (6.13) and this scaling model can be now rewritten as:

$$P_{cav-max} = 0.26\, l^{0.33} E_{pl}^{0.27} \quad (6.14)$$

The solid lines in Fig. 6-8(a) show the fitting curves obtained by (6.14) for three wire lengths. Again, a good agreement between the fitting lines and the experimental data confirms the effectiveness of (6.13) in linking $P_{cav\text{-}max}$ and E_{pl}.

The relationship between $P_{cav\text{-}max}$ and E_{pl} for all three types of underwater spark discharges is shown in Fig. 6-8(b). It was shown that an increase in l significantly improved $P_{cav\text{-}max}$ and it defined the upper limit of $P_{cav\text{-}max}$ by increasing E_{pl}. As compared with WGD's, FD's and ABSD's showed less effective in providing extremely large values of $P_{cav\text{-}max}$.

Scaling relations ((4.30) for FD's and ABSD's, (6.13) for WGD's) are also plotted in Fig. 6-8(b). It was found that for small variations (a few mms) in the inter-electrode gap, relationship (4.30) provided straightforward and reasonable calculation of the value of $P_{cav\text{-}max}$ with a specific value of E_{pl}. For large variations (tens of mms) in the length of gap, (6.13) is preferred to provide a reliable prediction of $P_{cav\text{-}max}$, as $P_{cav\text{-}max}$ is sensitive to the change in l.

6.8 Conclusions

Wire-guided discharges are initiated with a thin metal wire placed between electrodes, which facilitates the establishment of the plasma channel, minimises the pre-breakdown time and reduces the conductive energy losses before complete breakdown. The breakdown characteristics of WGD's and the relationships between hydrodynamic, acoustic and electrical parameters were investigated in this chapter.

The comparison between the values of $P_{cav\text{-}max}$ obtained for 15 mm gap in the case of FD's and WGD's was conducted. It was found that the reduction of the standard deviation in $P_{cav\text{-}max}$ values in the case of wire-guided discharges was at least 20 % and the average value of $P_{cav\text{-}max}$ obtained for WGD's was increased by at least ~ 44 %, as compared with FD's. This finding showed that the plasma-channel-stabilising function was achieved by using a thin metallic wire to establish the plasma channel path. This will be beneficial for the controllability and the predictability of the underwater spark discharges.

In this work, the inter-electrode gap was increased to 75 mm for the WGD's while

the maximum gap for FD's was 15 mm and for ABSD's it was 25 mm. A direct effect of this gap enhancement was the higher magnitude of the acoustic impulse. It was shown that the maximum value of $P_{cav\text{-}max}$ was ~4.5 V in the case of WGD's, as compared with ~1.6 V for FD's and ~2.3 V for ABSD's when the same amount of energy was available in these discharges. This is a significant improvement for practical applications [24], [79], [145], which requires strong magnitude of acoustic impulses.

The relationship between E_{pl} and R_{pl} was obtained. It was found that E_{pl} is inversely proportional to R_{pl} for all three wire lengths. A phenomenological scaling relationship (6.4) was derived from the time-dependent plasma resistance mode (2.19) with $n_1 = 0.4$ by assuming that the dynamic behaviour of the plasma resistance could be represented by a constant value. The importance of (6.4) is that it links analytically the electrical parameter (R_{pl}) and the acoustic parameters. With the help of (6.4), it is possible to derive the phenomenological model to link T_{cavity}, $P_{cav\text{-}max}$ and R_{pl} with l taken into account.

The relationships between T_{cavity}, $P_{cav\text{-}max}$ and R_{pl}, E_{pl} were also found for WGD's. It was shown that T_{cavity} and $P_{cav\text{-}max}$ decreases with an increase in R_{pl} and increases with an increase in E_{pl} for all wire lengths. These relationships show well-defend tendency and analytical models (6.5)-(6.13) were established to link these parameters. It was found that model (4.26) with $n = 1.66$ was suitable to describe the relationship between T_{cavity} and E_{pl} for all three types of discharge mechanisms in this work. Model (6.13) provides more accurate prediction of $P_{cav\text{-}max}$ with a known value of E_{pl} than model (4.30), especially for larger variation in the wire length. However, model (4.30) allows a straightforward calculation of $P_{cav\text{-}max}$ for a case when the inter-electrode gap is unknown. The phenomenological scaling relations established in this chapter will help in further optimisation and understanding of the usage of WGD's in practical applications, as it will help to adjust the circuit parameters of the discharge system to maximise the acoustic magnitude.

The next chapter presents the development of an analytical model to study the time-dependent behaviour of the hydrodynamic and acoustic parameters and the electrical parameters. Comparison is conducted between the analytical results and the experimental measurements to validate the model. The acoustic energy and efficiency

are calculated for all tests conducted in this work based on the results obtained from the analytical model. Their relationships with the electrical parameters of the plasma channel are also investigated.

7 Analytical model for underwater spark discharges

The comprehensive investigation on the acoustic and electrical properties of underwater spark discharges, including the period of the gas/plasma cavity oscillation, T_{cavity}, the peak acoustic pressure $P_{cav\text{-}max}$, the resistance of plasma, R_{pl} and the energy delivered into the plasma channel, E_{pl}, have been conducted for all three types of underwater spark discharges, FD's, ABSD's and WGD's. The results of this investigation were presented in Chapters 4 - 6.

Novel scaling relationships between the hydrodynamic, electrical and acoustic parameters have been established and analysed in Chapters 4-6. These relationships can be used in optimising the acoustic output by adjusting different circuit and topological parameters: charging voltage, storage capacitance and inter-electrode gap. However, this optimisation is based on the empirical scaling relationships obtained for the circuit parameters and topologies used in this work. Thus, it is important to develop a general model, which will be based on the fundamental characteristics of the pulse driving circuit, discharge plasma parameters, hydrodynamic and acoustic equations.

A complete underwater spark discharge progresses through a series of phases, including streamers' initiation and propagation, electrical energy injection into the formed plasma channel and the post-breakdown development of the plasma/gas cavity.

Apart from R_{pl} and E_{pl}, there are other properties which play important roles in the discharge and cavity's development process including internal pressure in the cavity, $P_i(t)$ and the radius of the gas/water interface, $r(t)$. Together with the hydrodynamic and electrical parameters investigated in the previous chapters, they will help to form a complete picture of the underwater spark discharge and the plasma-acoustic emission process.

Due to highly dynamic nature of the development of the gas/plasma filled cavity, the parameters mentioned above vary with time. Their transient behaviour is of great importance for understanding and modelling of the discharge process. However, the diagnostic system used in this work put some limitations on experimental measurements: i.e. some parameters can't be obtained directly from the experiments or there are limitations in terms of analysis of raw experimental data.

As discussed in Chapter 2, two different discharge stages follow the breakdown event, including the energy deposition stage (before the end of electrical energy injection)

and the cavity oscillation stage (after the energy injection). These two stages consist of several processes, including the electrical energy injection into the breakdown channel resulting in a fast expansion of this channel filled with hot plasma, hydrodynamic cavity expansion and collapse, emission of acoustic impulses during cavity expansion and collapse. Each of these individual processes has been studied thoroughly in the last few decades and many well-established models are available to describe these processes. For example, the energy deposition stage can be described by a simplified energy balance equation, which states that the energy deposited into the plasma channel accounts for the thermal energy of the gas/plasma cavity and mechanical work done on surrounding water. This equation has been used in [35], [70], [82], [126], [132], [146]. The cavity expansion and collapse can be described by Rayleigh model in non-compressible liquid ([75], [121], [147] - [151]) and Gilmore model [78] for compressible liquid with pressure-dependent speed of sound, which was used in studies of spark-generated cavity dynamics [35]. More detailed analysis of Gilmore model and comparison between these two models can be found in [75], [77], [81], [152]-[154]. The acoustic impulse from the spark source can be modelled by Braginskii's approximation [155] for shock wave (used in [126], [132]), which states that the acoustic pressure is proportional to the squared expansion velocity of the cavity, or by the acoustic approximation for calculation of pressure impulse generated by a gas-filled cavity at a observation point (studied in [70], [82], [156], [157]). Based on the developed models and the experimental conditions used in this work, the complete analytical description of the transient underwater cavity and acoustic impulses emitted by this cavity has been developed in this section.

The developed model has been implemented in MATLab R2016c software. This model allows the full transient analysis of the time-dependent parameters of the discharge cavity and help in further understanding of the acoustic emission by the underwater spark discharge. The value of the peak magnitude of the acoustic pressure waves can be obtained using the developed model, thus the acoustic energy and the acoustic efficiency, E_{ac} and η_{ac} can be obtained.

7.1 Development of the model

In this section, an analytic model was developed in order to study the evolution of the underwater spark discharge. The radially propagating acoustic pressure waves also can be obtained using this model. The primary pressure impulse is generated during the first quarter of circuit oscillation. Therefore, the study presented in this chapter will be focused on the first cavity's oscillation cycle. During the following cavity's oscillation cycles, the gas in the cavity behaves ideally and adiabatically.

7.1.1 Energy Deposition

After the first streamer bridges the inter-electrode gap, a plasma channel is formed and a conductive current starts to flow through the channel: this electrical energy is released in the plasma channel, resulting in the rapid Joule heating of the plasma. As plasma pressure increases, the plasma channel develops into a gas cavity. The high pressure inside the cavity results in its fast expansion, the expanding cavity emits a strong acoustic impulse. The cavity reaches its maximum radius and then starts to collapse due to the pressure difference at the cavity's interface (as the internal pressure inside the cavity is significantly lower than the external hydrostatic pressure at this moment). The development of the model is started with the analysis of the energy balance in the underwater spark discharges.

An energy balance equation is a key in modelling of the discharge process. It is related to the energy partition in the underwater spark discharge, which determines the dynamics of post-breakdown phenomena. Energy partition in underwater spark discharge has been studied in a number of papers [136], [158], [159]. In [158], UV light radiation for the underwater sparks with adjustable peak voltage and inter-electrode gap was investigated. It was found that although the energy of the UV radiation was affected by the electrode distance and inversely proportional to the peak voltage, the maximum energy associated with UV radiation was only 3.4 % of the total energy available in discharge. In [159] a series tests have been conducted to investigate the energy partition of an underwater spark. According to [159], the light emission measured accounted for only 4.9 % of the total energy delivered into the plasma channel. The thermal conduction losses were also negligible due to its small energy

contribution as compared with the mechanical work done by the cavity's expansion and the acoustic energy. In [136], a combination of models was used to calculate energy associated with the acoustic impulse and thermal energy in the cavity. It was found that the sum of the mechanical work done by the cavity against surrounding water and its internal energy accounted for the most part of the total energy transferred into the plasma, ~ (97 % - 99 %).

In this work, the measurements of the energy losses due to light emission and heat conduction were not conducted as it was beyond the scope of this work. A simplified energy balance equation for the energy deposition stage of the underwater spark discharge can be given as:

$$E_{pl}(t) = W(t) + E_{in}(t) \tag{7.1}$$

where $E_{pl}(t)$ is the electrical energy delivered into the plasma channel, $W(t)$ is the mechanical work done by the expanding cavity and $E_{in}(t)$ is the internal energy of the cavity. The term, $E_{in}(t)$, after breakdown covers the energy associated with the acoustic impulses as the intense internal pressure of the cavity achieve the emission of shockwaves. This energy balance equation was confirmed and used in [35], [70].

All three terms in (7.1) are time-dependent parameters, which will be taken into account in the following analysis. Energy relationship (7.1) links the electrical and the hydrodynamic parameters of the discharge and defines the energy partition during the energy deposition stage of the discharge. The energy delivered into the plasma channel, $E_{pl}(t)$, is defined as the electrical energy released through the Joule heating (2.24). The mechanical work done by the cavity and the thermal energy in the plasma in (7.1) are given by:

$$W(t) = P_{\infty}V_{ca}(t) + P_i(t)V_{ca}(t) \tag{7.2}$$

$$E_{in}(t) = \frac{P_i(t)V_{ca}(t)}{\gamma - 1} \tag{7.3}$$

where P_{∞} is the ambient undisturbed pressure in the water and it can be represented

by the hydrostatic pressure, P_0; $P_i(t)$ is the internal pressure of the gas mixture inside the expanding cavity and $V_{ca}(t)$ is the volume of the gas cavity in its oscillations; γ is the constant ratio of the specific heats of the gas mixture inside the cavity.

The first term in (7.2) refers to the potential energy stored in the surrounding water and the second term is the kinetic energy of the water in response to the expanding gas/water interface. The ratio of the specific heats (or the heat capacity ratio), γ, is the ratio of the heat capacity at constant pressure and the heat capacity at constant volume. This parameter, γ, is an important property of a gas content governing its thermodynamic behaviour. In this work, the gas content in the plasma-generated cavity is a mixture of water vapour, disassociated gas and ionised water components. The calculation of exact value of γ for this gas content is difficult and the procedure is beyond the study of this work.

Values of γ have been discussed in [35], [82], [160]-[163]. In [159], $\gamma = 1.4$ was found using the best fit between the experimental data of the cavity radius with the Rayleigh-Plesset cavity oscillation model. The same value of $\gamma = 1.4$ was also used in [35] in the energy balance equation to describe the plasma-generated cavity dynamics. In [162], $\gamma = 4/3$ was used in the internal energy of the plasma for spark discharges with low current (1 A – 10 A) with consideration that the energy in plasma was contributed by translational and rotational energy by particle collisions. For more examples, $\gamma = 1.3$ was used in [82], [132] for modelling the transient cavity in water. $\gamma = 1.25$ and $\gamma = 1.22$-1.30 were used in [161], [164] and [163] respectively for modelling of cavity generated by spark discharges. In this work, the mixture content in cavity was assumed to be adiabatic ideal gas mixture and to be constant during the cavity dynamics. Based on the literature data, the value of $\gamma = 1.3$ has been chosen.

The geometric shape of the cavity is assumed to be spherical. Then, the volume of the cavity during oscillation is governed by:

$$V_{ca}(t) = \frac{3}{4}\pi r(t)^3 \tag{7.4}$$

where $r(t)$ is the time-dependent radius of the cavity.

7.1.2 Hydrodynamic behaviour

The energy balance during the energy deposition stage was discussed in previous section, the internal pressure in the cavity, $P_i(t)$, was included in (7.3). To solve (7.3), the time-dependent volume of the cavity, $V_{ca}(t)$, has to be obtained, which refers to the hydrodynamic aspect of the energy deposition stage. As electrical energy is delivered into the plasma channel, the temperature inside the channel increases rapidly due to the Joule heating which results in vaporization of liquid water near the plasma channel. Then the plasma channel starts to develop into a cavity filled with a vapour-gases mixture. At the same time, the high pressure forces the cavity with radius $r(t)$ to expand at a considerable velocity. The cavity expansion after the energy deposition stage continues. The cavity expands adiabatically and it stops when the cavity reaches its maximum radius. The cavity then collapses to its minimum radius due to significantly higher hydrostatic pressure than the internal pressure in the cavity at its maximum radius.

The free (adiabatic) oscillation of the gas cavity in the liquid can be described by the Rayleigh-Plesset equation. The liquid considered in (2.8) is assumed to be incompressible, which means that the density of the liquid is constant and thereby the speed of sound is also constant during the oscillation. For the underwater spark discharges studied in this work, the compressibility of the water has to be taken into consideration as shock waves/acoustic impulses emitted from the spark-generated cavity and the gas/water interface of the cavity can significantly compress the liquid. Therefore, a model, which takes into account the equation of state of water, is required.

The velocity of the cavity expansion varies in a large range depending on the discharge circuit parameters. For example, as reported in [74] for the underwater spark discharges achieved with 720 J pulses, the average velocity of the cavity's interface was obtained, ~ 60 m/s. In [165], three different electrical power oscillation modes (charged by the same 600 J pulses but with different number of oscillation cycles) were used to generate sparks for the investigation of hydrodynamic process. It was found that the velocity dispersion in the middle of the discharge channel varied from ~ 170 m/s to ~ 250 m/s. In [132], spark discharges were achieved using capacitive high pulsed power system with different values of capacitance (1 μF, 5.22 μF and 10.37 μF).

For discharges with 5.22 μF and breakdown voltage of ~2 kV, the channel expansion speed reached its maximum value of ~340 m/s in ~1.5 μs after breakdown. For higher energy levels (> 1 kJ) used in [32], the velocity of cavity (or channel) expansion was found to be ~ 0.75 km/s for 20 mm and ~ 1.2 km/s for 28 mm inter-electrode gaps. Due to fast expansion of the plasma channel and strong shock wave, which is produced by the expanding plasma channel, the water density near the gas/water interface is no longer constant and the local speed of sound is now considered to be related to the density of the disturbed water. In the underwater spark discharge tests conducted in this work, no experimental techniques and systems were available for direct measurements of the expansion velocity of the underwater plasma channel and the velocity of the emitted shock wave. However, based on the similar experimental setup and conditions used in [35], the influence of the fast expanding cavity on the water content will be taken into account in the present work analytically.

In order to account for potential dependency of water density on pressure, the Gilmore approach is adopted in the present work. There are specific conditions, which have to be confirmed before the Gilmore model can be used and solved for the cases considered in the present work. As mentioned above, the water density is a pressure-dependent parameter, and Tait's equation of state can be used for description of this dependency of water density on disturbance pressure, [78]:

$$\rho\left(P_i(t)\right) = \rho_\infty \left(\frac{P_i(t)+B}{P_\infty+B}\right)^{1/n_2} \tag{7.5}$$

where B is 3×10^8 Pa and n_2 is 7 [78], [152], [153] and ρ_∞ is the density of undisturbed water.

Based on (7.5), the pressure-dependent speed of sound, c, can be expressed as [78]:

$$c = c_\infty \left(1 + \frac{n_2-1}{{c_\infty}^2} h\right)^{1/2} \tag{7.6}$$

where c_∞ is the speed of sound in undisturbed water, h is the enthalpy. By assuming the liquid is an isotropic medium, the specific enthalpy, h, can be defined as a function of the disturbing pressure, $P_i(t)$, [78]:

$$h(t) = \frac{n_2}{n_2-1}\frac{(P_\infty+B)^{\frac{1}{n_2}}}{\rho_\infty}\left((P_i(t)+B)^{\frac{n_2-1}{n_2}} - (P_\infty+B)^{\frac{n_2-1}{n_2}}\right) \qquad (7.7)$$

Taking into account all conditions described by (7.5)-(7.7), the Gilmore model for the cavity oscillation is given by, [78]:

$$r\ddot{r}\left(1-\frac{1}{c}\dot{r}\right)+\frac{3}{2}\dot{r}^2\left(1-\frac{1}{3c}\dot{r}\right)=h\left(1+\frac{1}{c}\dot{r}\right)+\frac{r}{c}\dot{h}\left(1-\frac{1}{c}\dot{r}\right) \qquad (7.8)$$

$$\ddot{r}=\frac{d^2r}{dt^2},\ \dot{r}=\frac{dr}{dt},\ \dot{h}=\frac{dh}{dt}$$

where r is short for $r(t)$, $\dot{r}$ and $\ddot{r}$ are the first order and second order derivatives of r respectively.

The full Gilmore's model includes the terms for the energy associated with the surface tension and also the effects of viscosity. These terms are significant in low energy discharges but it can be ignored in the higher energy levels considered in this work.

7.1.3 Acoustic emission

During the discharge, due to intense internal pressure inside the cavity, this cavity expands and generates a pressure impulse, which propagates into water. According to [166], this pressure impulse could be considered as a shock wave at its initial emission stage as the impulse propagation velocity, measured at 1 mm from the spark (an early stage of shock propagation), was ~ 1.86 km/s. After its propagation over a short distance (8 mm), the speed of this pressure impulse reduces to the ambient speed of sound (~ 1.5 km/s). In [72], velocities of pressure waves were measured from ~ 1.4 km/s to ~ 1.5 km/s, 50 μs after the electrical discharge. Therefore, at the observation point used in this work, 500 mm away from the spark electrodes, it is reasonable to assume that the propagation speed of the pressure wave is the speed of sound in water, ~ 1.45 km/s, so that the magnitude of the impulse can be calculated using the acoustic approximation.

Based on the assumption of acoustic approximation, the magnitude of the propagating acoustic impulse is a function of its observation position, *d*, and the time-dependent radius of the oscillating cavity, *r(t)*. The magnitude of the acoustic impulse, $P_{cav\text{-}max}(t)$, is expressed as below, [167]:

$$P_{cav-max}(\bar{t}) = P_{\infty} + \rho_{\infty}\left(\frac{1}{d}\left((r(\bar{t}))^2 r\ddot{(\bar{t})} + 2r(\bar{t})r\dot{(\bar{t})}^2\right) - \frac{r(\bar{t})^4}{2d^4} r\dot{(\bar{t})}^2\right) \quad (7.9)$$

$$\bar{t} = t - \frac{d}{c_{\infty}}$$

where $\bar{t}$ is the retarded time and it is defined zero when the first time that the acoustic impulse reaches the observation point, $r\dot{(\bar{t})}$ and $r\ddot{(\bar{t})}$ are first and second order derivatives of $r(\bar{t})$ respectively.

The acoustic energy can be obtained from the acoustic impulse waveform. In the case of underwater spark discharges where the acoustic impulses are emitted radically and the observation point is relatively far away from the spark source (and the observation distance is significantly longer than the inter-electrode gap), the acoustic impulse can be treated as a spherical wave. According to [168], the acoustic intensity of a spherical wave is governed by the same equation as the acoustic intensity of plane waves as an area element of a spherical wave can be approximated by an area element of a plane wave. Therefore, the acoustic intensity of the spherical wave is given by:

$$D_{ac} = \frac{P_{cav}(t)^2}{Z_{ac}} \quad (7.10)$$

$$Z_{ac} = \rho_{\infty} c_{\infty} \quad (7.11)$$

where Z_{ac} is the specific acoustic impendence of the water. In the acoustic approximation, water density and the speed of sound in water are equal to their values in undisturbed water at normal conditions.

By knowing the acoustic intensity, the acoustic power, $P_{cav\text{-}power}(t)$, of the emitted wave can be calculated as the product of the surface area at the observation point and (7.10), and this power is given by:

$$P_{cav-power}(t) = FD_{ac}(t), \quad F = 4\pi d^2 \tag{7.12}$$

where F is the surface area of the spherical acoustic impulse.

Then, the acoustic energy associated with the acoustic impulse is obtained as an integral of (7.12) with respect to time:

$$E_{ac} = \frac{F}{Z_{ac}} \int P_{cav}(t)^2 dt \tag{7.13}$$

7.2 Model development in MATLab

By combining (7.1)-(7.13), the hydrodynamic process (cavity dynamics) and the acoustic emission during the energy deposition stage can be described with the assumption that the cavity experiences adiabatic expansion after the disappearance of the current. The numerical solution of these equations has been implemented by building a model within the Simulink environment of the MATLab R2016c software.

Re-arrangements of equations (7.1)-(7.13) have been performed before developing a Simulink model and solving them in this programming environment. Different sub-models have been introduced and then united in a single global Simulink model. These sub-models follow one or several equations from (7.1)-(7.13), each containing several parameters as inputs and one parameter as an output. The inputs and outputs are inter-connected with each other in a manner that the output of a sub-model becomes an input of others, to form a closed-loop system. For example, the variation speed of the pressure in the cavity, $\dot{P_{i(t)}}$, can be obtained from (7.1) as an output and its integral form, $P_i(t)$, is an input to (7.7). Such parameters in this model include $P_{pl}(t)$, $c(t)$, $h(t)$ and the derivatives $\dot{h(t)}$ and $\ddot{r(t)}$. In total, six sub-models will be built to describe the electrical energy deposition and the cavity's oscillation processes and two extra sub-models will be built for representing the evolution of the acoustic impulse and its energy based on (7.9) and (7.13).

7.2.1 Sub-model for the electrical energy

The electrical energy deposited into the plasma channel is given by (2.24). It is worthy of note that the plasma resistance in (7.1) is a time-dependent resistance. However, the use of $R_{pl}(t)$ (time-dependent resistance) in the model may significantly increase the complexity of this model without bringing noticeable benefits in analysis of the complete cavity oscillation in this work. Moreover, a good match of (2.22) with the constant resistance to the experimental current waveform has been achieved for all three types of underwater spark discharges. Therefore, it was decided to implement the Simulink model using the constant plasma resistance approach. Thus, the resultant sub-model for the electrical power, $P_{pl}(t)$, is given by:

$$P_{pl}(t) = (I_0 e^{-\alpha/t} \sin(\omega t))^2 R_{pl} \tag{7.14}$$

where α is the damping factor, I_0 is the magnitude of the current oscillation, ω is the angular velocity and R_{pl} is the constant equivalent plasma resistance.

The sub-model structure is shown in Fig. 7-1. The inputs of this sub-model are R_{pl}, I_0, α, ω and time, t, the output of this sub-model is $P_{pl}(t)$.

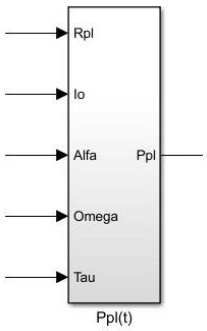

Figure 7-1. Sub-model for the electrical power delivered into the plasma channel with monitoring function.

7.2.2 Sub-model for the cavity oscillation model

The Gilmore model described by (7.9) is a second order non-linear differential equation. The output of this sub-model is the cavity's acceleration, $\ddot{r}(t)$. The cavity's

velocity of expansion, $r(\dot{t})$, and the cavity's radius, *r(t)*, are used as input parameters in this sub model. Therefore, (7.8) can be rewritten in the following form:

$$\ddot{r} = \frac{1}{\left(1-\frac{1}{c}\dot{r}\right)}\frac{1}{r}\left(h\left(1+\frac{1}{c}\dot{r}\right)+\frac{r}{c}\dot{h}\left(1-\frac{1}{c}\dot{r}\right)-\frac{3}{2}\dot{r}^2\left(1-\frac{1}{3c}\dot{r}\right)\right) \qquad (7.15)$$

The sub-model structure is shown in Fig. 7-2. The inputs in this sub-model are *r(t)*, *c(t)*, *h(t),* $h(\dot{t})$ and $r(\dot{t})$.

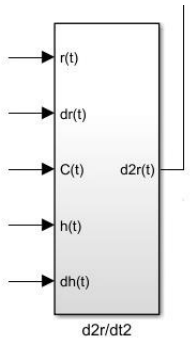

Figure 7-2. Sub-model for the acceleration of the gas/water interface.

7.2.3 Sub-models for the enthalpy

In order to solve (7.7), two sub-models were developed to obtain time-dependent enthalpy, *h(t)* and its time derivative, $h(\dot{t})$. The enthalpy is given by (7.7) and its derivative can be obtained as:

$$h(\dot{t}) = \frac{(P_\infty+B)^{1/n_2}}{\rho_\infty}(P_i(t)+B)^{-1/n_2}P_i(\dot{t}) \qquad (7.16)$$

The sub-models for *h(t)* and $h(\dot{t})$ are shown in Fig. 7-3. The inputs for *h(t)* and $h(\dot{t})$ sub-models include P_∞, B, ρ_0, $P_i(t)$ and $P_i(\dot{t})$.

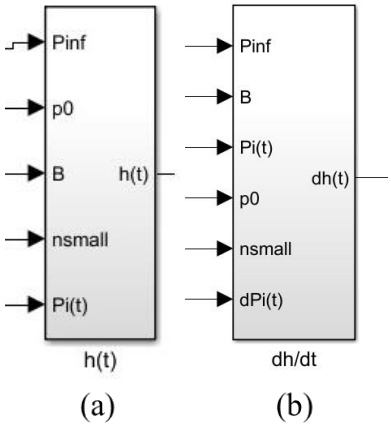

Figure 7-3. Sub models for (a) the enthalpy and (b) its derivative.

7.2.4 Sub-model for the pressure-dependent speed of sound

The pressure-dependent speed of sound is given by (7.6). The input parameter for this sub-model is c_∞ and $P_i(t)$. The sub-model structure is shown in Fig. 7-4.

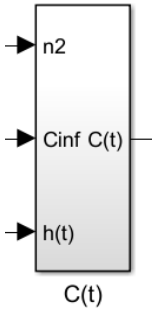

Figure 7-4. Sub-model for the pressure-dependent speed of sound in water.

7.2.5 Sub-model for the internal pressure in the cavity

Both the internal pressure in the cavity, $P_i(t)$, and its time derivative, $P_i\dot{(t)}$ are required for the analytical model. $P_i\dot{(t)}$ can be obtained from the energy balance equation (7.1) and $P_i(t)$ can be calculated as an integral of $P_i\dot{(t)}$.

In order to obtain the information on $P_i\dot{(t)}$, the energy balance equation (7.1) can be rewritten in its differential form:

$$(P_\infty + P_i(t))\frac{dV_{ca}(t)}{dt} + \frac{1}{\gamma - 1}\frac{d\left(P_i(t)V_{ca}(t)\right)}{dt} = P_{pl}(t) \qquad (7.17)$$

where $P_{pl}(t)$ is the transient electrical power given by (2.24), $V_{ac}(t)$ is the time-dependent volume of the cavity and $P_i(t)$ is the internal pressure in the cavity.

Thus, the time derivative of the gas pressure, $\dot{P_i}(t)$, can be represented by the following first order non-linear differential equation:

$$\dot{P_i}(t) = \frac{\gamma - 1}{V_{ca}(t)}\left(P_{pl}(t) - P_0\dot{V}_{ca}(t) - \frac{\gamma}{\gamma - 1}P_i(t)\dot{V}_{ca}(t)\right) \qquad (7.18)$$

where $\dot{V_{ca}}(t)$ is the time derivative of the transient cavity volume.

As discussed in Section 7.1.2, the cavity is assumed to be spherical with the volume given by (7.4). Therefore, by combining (7.4) and (7.18), the final form for equation used to build the sub-model for $\dot{P_i}(t)$ is given as:

$$\dot{P_i}(t) = \frac{3}{r(t)^3}\left(\frac{P_{pl}(t)(\gamma - 1)}{4\pi} - r(t)^2\dot{r}(t)\left((\gamma - 1)P_0 - \gamma P_i(t)\right)\right) \qquad (7.19)$$

This sub-model is shown in Fig. 7-5. The input parameters for this model are $P_{pl}(t)$, $P_i(t)$, γ, P_0, $r(t)$ and $\dot{r}(t)$.

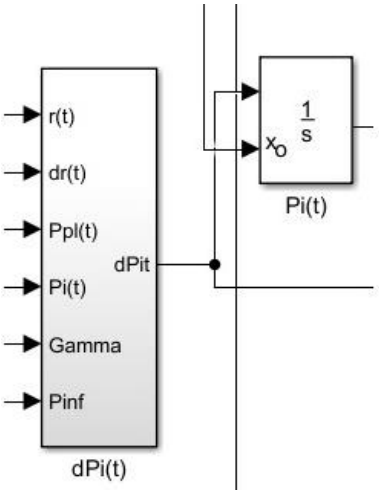

Figure 7-5. Sub-model for the time derivative of the internal pressure in the cavity.

7.2.6 Sub-models for acoustic impulse

The sub-models for the magnitude of the acoustic impulse and its energy was developed based on (7.9) and (7.13) and shown in Fig. 7-6. The input parameters for $P_{cav}(t)$ sub-model are P_0, ρ_0, a, $r(t)$, $\dot{r(t)}$ and $\ddot{r(t)}$. The inputs parameters for $E_{ac}(t)$ sub-model are d, $P_{cav}(t)$, P_0 and c_∞.

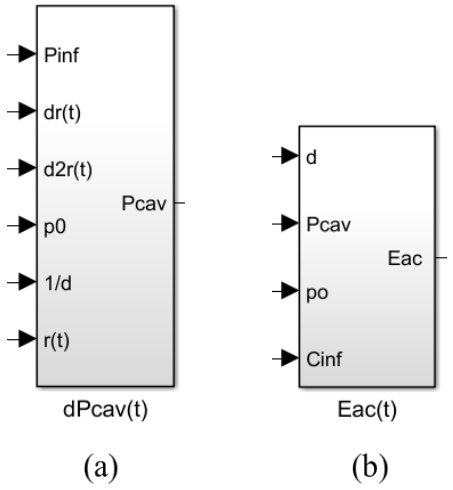

Figure 7-6. Sub-models for (a) the acoustic magnitude and (b) the acoustic energy.

There is a time delay ~ 300 ms, which is the propagation time from the spark source to the observation point for the acoustic impulse in the test setup. This time delay is also taken into consideration in the diagnostic system by using the delay triggering function of the digitizing oscilloscope. The acoustic impulse is emitted at the same time when the electrical energy is released in the plasma channel. Therefore, the time delay, which existed in the practical situation, is ignored in this simulation model as there is no restriction for synchronisation of the acoustic signal and the electrical energy in this analytical model. The distance, a, used in this model is 500 mm.

7.2.7 Initial conditions for the model

With the sub-models developed and described in previous sections, the simulation of the discharge process can be conducted. To run this model and to model hydrodynamic

properties of the spark discharge cavity, four initial parameters obtained from the experiment current waveform are required: the constant plasma resistance, R_{pl}, the initial current magnitude, I_0, the damping factor of the current oscillation, α, and the angular frequency of the current oscillation, ω. These parameters determine the amount of the energy injected into the plasma channel. Each set of these four parameters corresponds to a specific individual discharge. Apart from these four input parameters, which describe the energy released into the plasma channel, the model also requires several initial conditions, which are listed in Table. 7-1.

Table 7-1. Initial condition parameters required for the analytical model

Initial conditions	Symbols
Specific heats of the water content	γ
Constant	n_2
Constant	B
Hydrostatic pressure	P_∞
Undisturbed water density	ρ_0
Undisturbed speed of sound	c_0
Initial internal pressure in the cavity	$P_i(0)$
Initial acceleration of the cavity expansion	$\ddot{r}(0)$
Initial radius of the cavity	$r(0)$

These initial conditions describe the conditions of the hydrodynamic environment for the post-breakdown discharge. P_∞, ρ_0, and c_0, are related to the physical properties of the liquid water. As mentioned before, the water used in the tests was tap water. The values of ρ_0 and c_0 correspond to normal conditions: room temperature 20 ^oC and atmosphere pressure. These parameters are $\rho_0 = 0.998$ kg/m^3 and $c_0 = 1483$ m/s [169], [170].

In the model, the pressure in water is assumed to be the superposition of the atmosphere pressure, P_{atm}, and the hydrostatic pressure, $\rho_o g h_{depth}$, and is given by:

$$P_\infty = P_{atm} + \rho_0 g h_{depth} \tag{7.20}$$

where g is the free fall acceleration, 9.8 m/s^2, and h_{depth} is the distance from water surface to the observation point.

According to the experimental topology used in this work, the electrodes were located 0.5 m below water surface. In this case, the hydrostatic component of pressure P_∞ at this point is 4900 Pa. Compared to the normal atmosphere pressure of 10^5 Pa at room temperature, the second term in (7.20) can be neglected and thus $P_\infty = 10^5$ Pa is used in this analysis. The value of the initial internal pressure in the cavity, $P_i(0)$, is assumed to be equal to the pressure at the moment of its formation, $P_i(0) \approx P_\infty$. Initial values of the cavity radius and its velocity, $r(0)$ and $\dot{r}(0)$, should be selected based on the sensitivity of the model to these parameters, which will be established in this chapter.

7.2.8 Model's sensitivity to initial cavity's radius and its velocity

The investigation of the model's sensitivity to the initial values $r(0)$ and $\dot{r}(0)$ was investigated by comparing the model output parameters (T_{cavity}, $P_{cav\text{-}max}$, and E_{ac}) for different values of these parameters . The values of $r(0)$ and $\dot{r}(0)$ provide the initial radius of the cavity and its initial velocity when the cavity starts to expand and their values should not be significant. Values of $r(0)$ and $\dot{r}(0)$ for the control set were chosen based on the literature data and close to the practical cases of breakdown in water considered in this work [31], [39], [40], [54]. Then, the values of $r(0)$ and $\dot{r}(0)$ for the comparison set were chosen ten times greater than those in the control set. The values of $r(0)$ and $\dot{r}(0)$ for the control set and for the comparison set are shown in Table. 7-2.

Table 7-2. The control and comparison sets of values of initial condition $r(0)$ and $\dot{r}(0)$

Initial conditions	Control set	Comparison set
$r(0)$	0.0001 m	0.001 m
$\dot{r}(0)$	0.001 m/s^2	0.01 m/s^2

Different simulation settings have been used in the model. As can be seen from the experimental measurements in Chapters 4 – 6, T_{cavity} is few to tens of milliseconds: 3-4 ms for the lowest energy level and 10-11 ms for the highest energy level. Therefore, the simulation time in the model was set to >10 ms with a time step of 100 ns to obtain the evolution of the cavity's oscillation for at least one complete cycle.

Duration of a typical acoustic impulse is tens of microseconds, which is relatively short as compared with that of T_{cavity}. As a result, to model the acoustic waveform, $P_{cav}(t)$, simulation time of 10 μs (with the fixed time step of 1 ns) was used. Using these two specific simulation configuration settings, $r(t)$, $P_i(t)$ and $P_{cav}(t)$ can be obtained with satisfying resolution and details.

The comparison between the simulation results (T_{cavity}, $P_{cav\text{-}max}$ and E_{ac}) obtained for different sets of initial conditions ($r(0)$ and $\dot{r}(0)$ as shown in Table. 7-3) has been conducted. An example discharge obtained in a 75 mm gap with 533 nF capacitance was modelled. The energy-related input parameters of this example were R_{pl} = 0.7975 Ω, I_0 = 6122 A, α = 95491 Ω/L and ω = 565034 rad/s.

Table 7-3. Computed results of T_{cavity}, $P_{cav\text{-}max}$ and E_{ac} obtained for different values of $r(0)$ and $\dot{r}(0)$

Parameters	$r(0)$		$\dot{r}(0)$	
	0.0001 m	0.001 m	0.001 m/s^2	0.01 m/s^2
T_{cavity} (ms)	7.91	7.92	7.91	7.91
$P_{cav\text{-}max}$ (MPa)	1.67	1.74	1.67	1.67
E_{ac} (J)	10.67	10.86	10.67	10.67

It was found that the values of T_{cavity} calculated by different values of $r(0)$ were virtually the same, which verifies that the initial radius of the cavity and its initial velocity do not affect the hydrodynamic parameters of the developed gas/plasma cavity significantly. Also, no significant difference in the values of $P_{cav\text{-}max}$ and E_{ac} for different cases of $r(0)$ and $\dot{r}(0)$ was observed. Thus, selection of $r(0)$ and $\dot{r}(0)$ will not affect significantly the acoustic output from the discharge. The relative differences in the output parameters, T_{cavity}, $P_{cav\text{-}max}$ and E_{ac} for the control and the comparison sets

of initial parameters were calculated and shown in Table. 7-4. It is shown that 900 % increase in *r(0)* only resulted in few percent change (up to ~ 4.2 % in $P_{cav\text{-}max}$) in the model output parameters. The variation of the cavity's velocity, $r(\dot{t})$, and the cavity's radius, *r(t)*, as a function of time were shown in Fig. 7-7 for the first 20 ns and 25 µs after breakdown respectively. It is shown that the difference in the initial values of these two initial parameters were rapidly compensated with the intense expansion of the cavity and will not significantly impact the model outputs. It can be concluded that the developed model is not sensitive to the selection of the initial conditions, *r(0)* and $r(\dot{0})$. The values of *r(0)* and $r(\dot{0})$ in the control set (0.0001 m and 0.001 m/s^2 respectively) were used in the modelling procedure.

Table 7-4. Relative change in T_{cavity}, $P_{cav\text{-}max}$ and E_{ac} for different values of *r(0)* and $r(\dot{0})$

Initial condition	T_{cavity}%	$P_{cav\text{-}max}$%	E_{ac}%
r(0): 900% higher	0.12%	4.19%	1.78%
$\boldsymbol{r(\dot{0})}$: 900% higher	0%	0%	0%

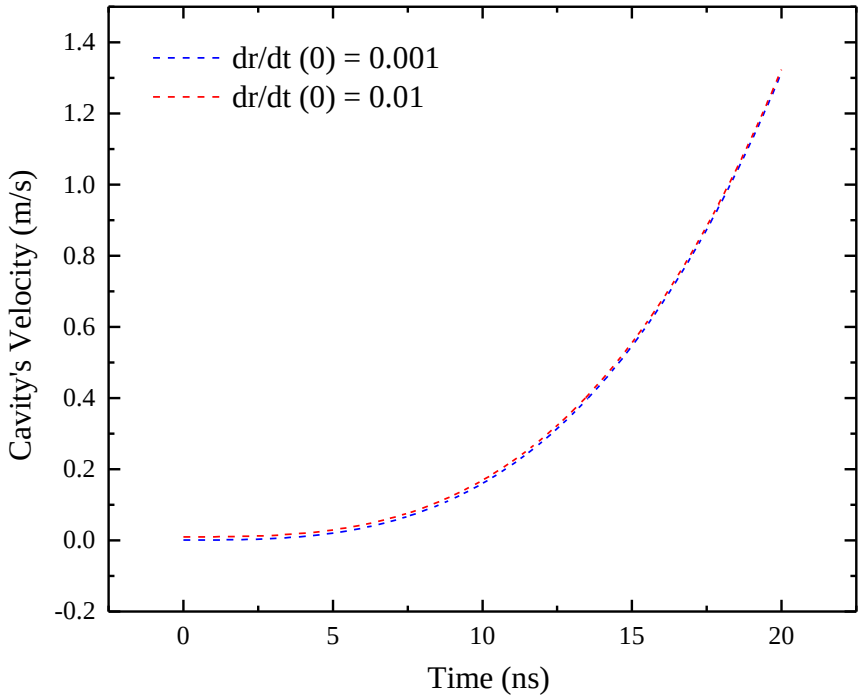

(a)

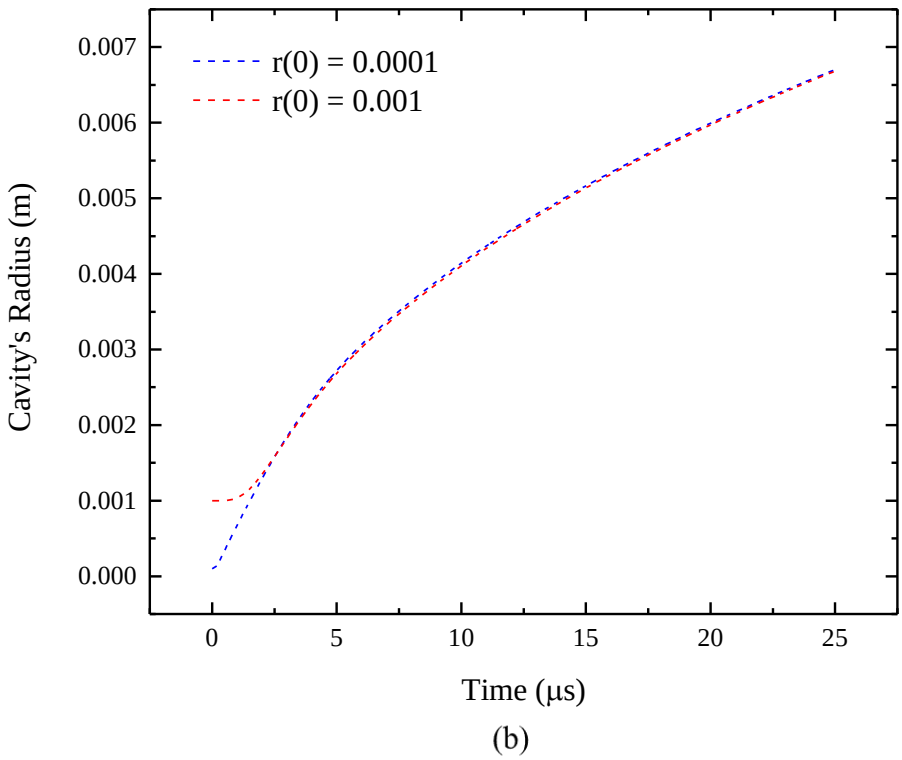

Figure 7-7. The variation of (a) the cavity's velocity, $\dot{r(t)}$, and (b) the cavity's radius, *r(t)*, as a function of time for the first 20 ns and 25 μs after breakdown respectively.

7.2.9 Model's sensitivity to electrical parameters

Apart from the initial conditions for the plasma channel, it is also important to investigate the model's sensitivity to the input parameters (R_{pl}, I_0, α and ω). By using the same procedure, the relative change in three output parameters (T_{cavity}, $P_{cav\text{-}max}$ and E_{ac}) due to variation in the input parameters are listed in Table. 7-5. It was found that an increase in R_{pl}, I_0, and ω causes the model output parameters to increase. On the other hand, an increase in α resulted in a decrease in these parameters. Among all four inputs, the current magnitude, I_0, produces the most significant impact on the output parameters while the angular velocity, ω, makes the least impact.

Table 7-5. Relative change in T_{cavity}, $P_{cav\text{-}max}$ and E_{ac} for different values of R_{pl}, I_0, α and ω

Input parameter	T_{cavity}	$P_{cav\text{-}max}$	E_{ac}
ω: 10% higher	0.13 % longer	4.19 % larger	1.4 % larger
α: 10% higher	3.54 % shorter	2.39 % lower	7.49 % lower
I_0: 10% higher	6.19 % longer	11.37 % larger	24.65 % larger
R_{pl}: 10% higher	3.03 % longer	5.39 % larger	11.71 % larger

In the next section, the experimental data will be used in the model and comparison between the simulation results and the experimental measurements will be conducted to verify the model. Further calculations and analysis of the acoustic energy and acoustic efficiency based on the simulated acoustic impulses will also be conducted.

7.3 Simulation results

After selecting the initial conditions, the model is used to obtain the time-dependent behaviour of the discharge parameters, $P_{pl}(t)$, $r(t)$, $P_i(t)$, $P_{cav\text{-}max}(t)$ and $E_{ac}(t)$. Example waveforms of these parameters will be shown in the following section, which are all obtained for an individual discharge with input parameters: $R_{pl} = 0.7975\ \Omega$, $I_0 = 6122$ A, $\alpha = 95491\ s^{-1}$ and $\omega = 565034$ rad/s. The acoustic energy obtained from this model is used to obtain the acoustic efficiency, η_{ac}, for all underwater spark discharges conducted for FD's, ABSD's and WGD's in Chapters 4 – 6. Its relationships with R_{pl} and E_{pl} have also been investigated, which is important for optimising the efficiency of the acoustic impulse generated by underwater spark discharges.

7.3.1 Electrical power

The time-dependent electrical power governs the dynamics of the initial expansion stage of the plasma cavity. The energy released into the plasma channel leads to change in the temperature and content of the expanding gas/plasma cavity.

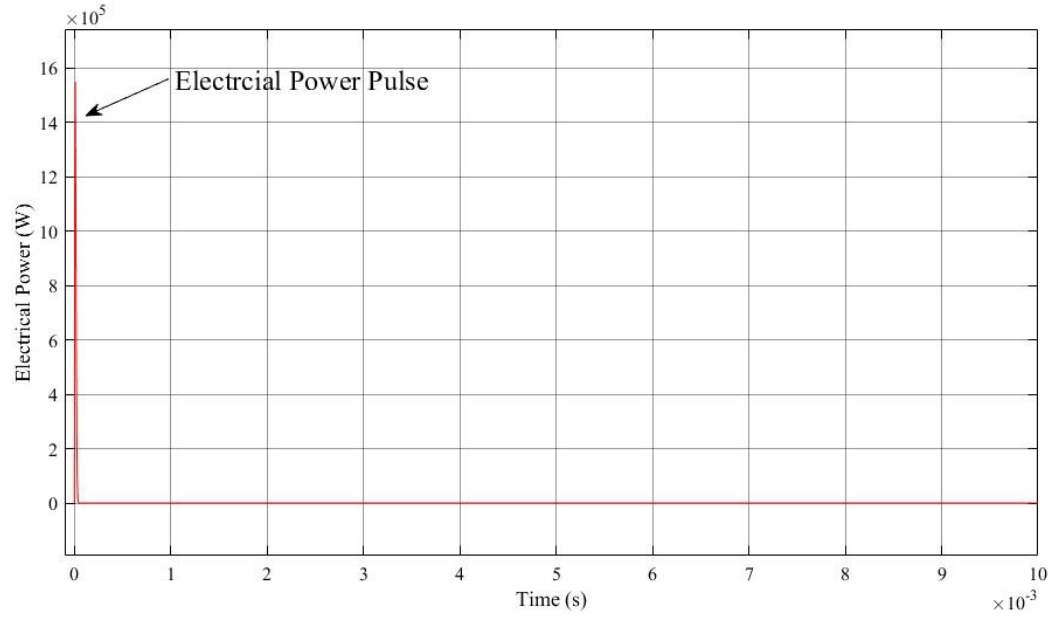

(a)

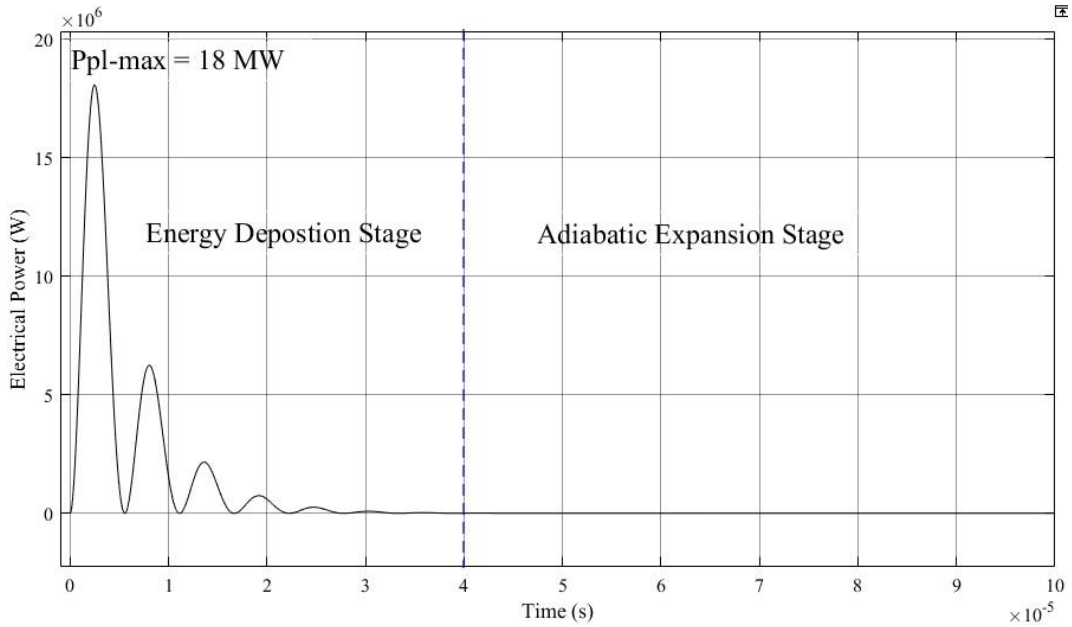

(b)

Figure 7-8. The time-dependent behaviour of the electrical power in the plasma channel for (a) 10 ms after breakdown and (b) 100 μs after breakdown with a maximum electrical power peak of 18 MW. Dashed line indicates the change between the energy deposition stage and the adiabatic expansion stage.

An example of the evolution of electrical power in the breakdown channel is illustrated in Fig. 7-8. The electrical power shown in Fig. 7-8(b) is given for the first 100 μs from the breakdown moment and corresponds to the oscillating character of electric current in the plasma channel. This profile is similar to the electrical power obtained for underwater discharges in 20 and 25 mm inter-electrode gaps in [32]. It was shown that although cavity's oscillation cycle might last several milliseconds, the electrical energy dissipates in the plasma channel only in the first tens of microseconds during the energy deposition stage as indicated in Fig. 7-8. For the rest of the post-breakdown phase in Fig. 7-8(a), the adiabatic cavity oscillation takes place.

7.3.2 Internal pressure in the cavity

An example of the dynamic behaviour of the cavity's internal pressure is shown in Fig. 7-9. Fig. 7-9(a) shows variation of $P_i(t)$ over the first cavity's oscillation cycle while Fig. 7-9(b) shows its detailed profile within the first 100 μs of the discharge, corresponding to the first impulse in Fig. 7-9(a).

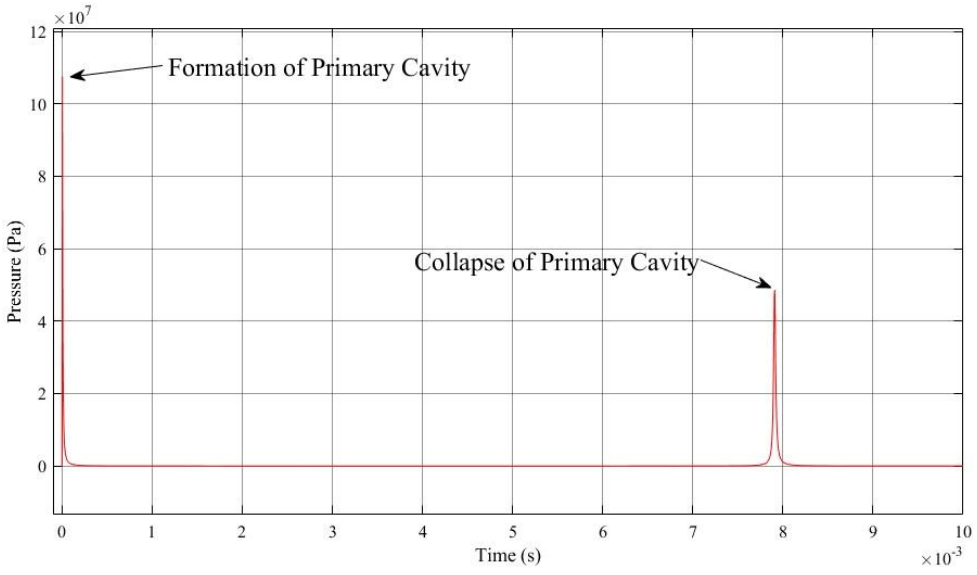

(a)

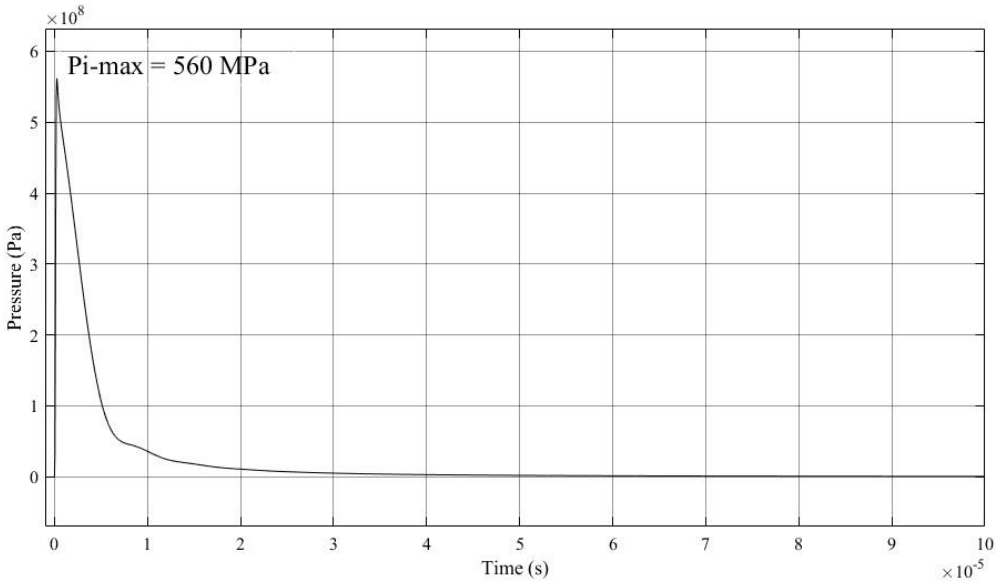

(b)

Figure 7-9. The internal pressure in the cavity as a function of time for (a) 10 ms and (b) 100 μs after breakdown. The peak pressure of $P_i(t)$ is found to be ~ 560 MPa. The minimum value of $P_i(t)$ (flat waveform in (a)) is slightly below 10^5 Pa, which is not able to be shown in (a) and (b), as compared with large magnitude of $P_i(t)$.

It is shown that the cavity's internal pressure demonstrates two peak values at the beginning and the end of the first cavity's oscillation cycle. The profile of the first internal pressure impulse is illustrated in Fig. 7-9(b). This profile has a sharp rising edge and a fluctuating falling edge. Compared with the waveform in Fig. 7-8(b), it can be seen that oscillations in $P_i(t)$ correspond to the oscillating electrical power. This finding can be explained by the energy balance equation (7.1) since $P_i(t)$ is obtained from the transient electrical power.

The peak magnitude of $P_i(t)$ in Fig. 7-9(b) is ~ 560 MPa, which is significantly higher than the hydrostatic pressure present in the vicinity of the formed cavity. The net force on the cavity's interface is the superposition of the outward $P_i(t)$ and the inward P_∞, if the viscous force and surface tension are not taken into account in this work. Such high magnitude of $P_i(t)$ resulted in an intense net force acting outwards on the cavity's interface, forcing the interface to expand with a considerable initial speed.

At the end of energy deposition stage, $P_i(t)$ reduced to its minimum level, which was lower than P_∞, resulting in the deceleration of the cavity's interface. $P_i(t)$ remains low

during the afterward adiabatic expansion stage. In the last tens or hundreds of μs of the oscillation cycle, with the decrease in the cavity's radius, the cavity's internal pressure becomes high again as shown by the second internal pressure impulse in Fig. 7-9(a).

7.3.3 Radius of the cavity

Fig. 7-10 illustrates the variation of the cavity's radius and the cavity's velocity in first 10 ms after breakdown.

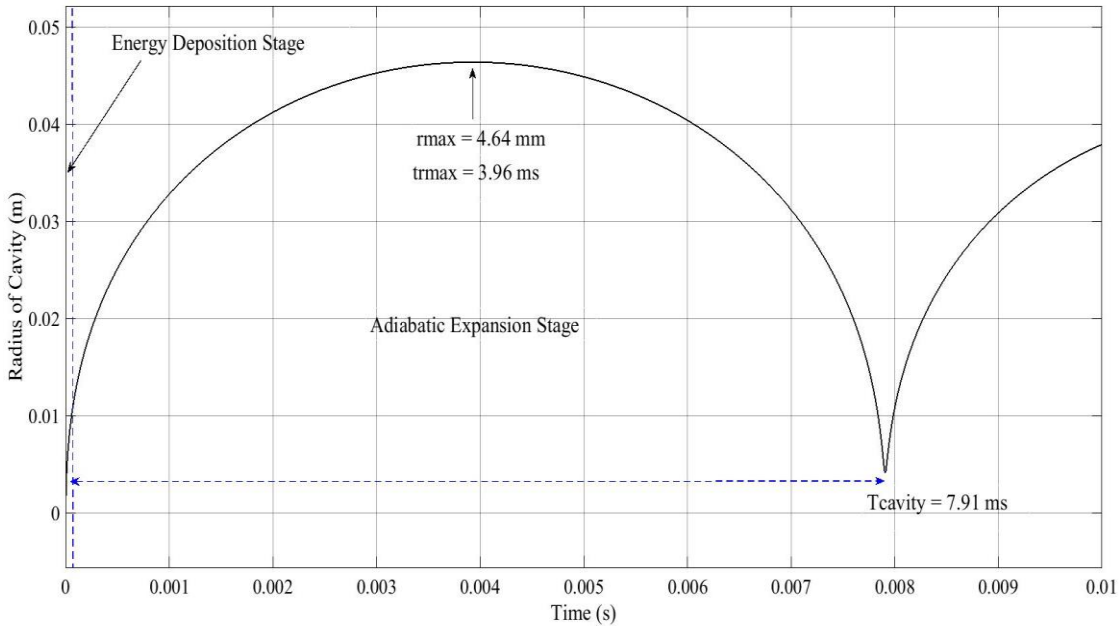

(a)

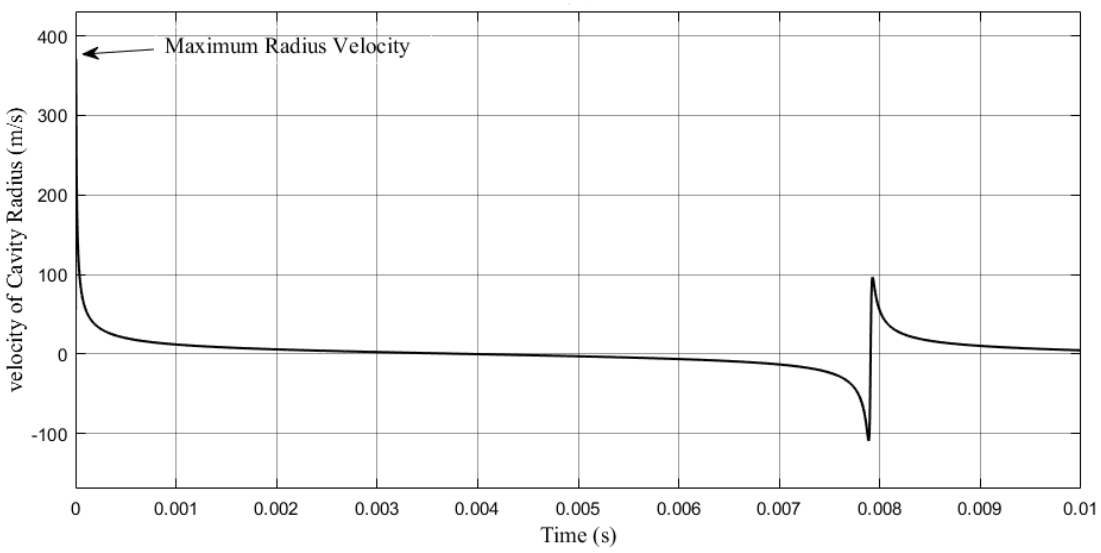

(b)

Figure 7-10. The variation of the (a) cavity's radius, (b) velocity of cavity's radius as a function of time in first 10 ms. The maximum radius for the cavity is r_{max} = 4.64 cm at t_{rmax} = 3.96 ms. T_{cavity} is found to be ~ 7.91 ms. Dashed line indicates the stage change from the energy deposition stage to the adiabatic expansion stage.

It was found that the radius of the cavity expands initially with a small value. As discussed above, the internal pressure, $P_i(t)$ produces significant force on the cavity's interface in the early stage of discharge, resulting in fast acceleration on the interface and large velocity of the cavity's radius (fast rising in the beginning of Fig. 7-10(b)). Then, the cavity's acceleration drops due to the decrease in $P_i(t)$. At some point, the internal pressure in the cavity reduces below the hydrostatic pressure, which results in the deceleration of the cavity's interface and the reduction of the cavity's velocity. The velocity of the cavity's radius becomes zero when the maximum radius is achieved, r_{max} = 4.64 cm, at the half cycle of the oscillation, t_{rmax} = 3.96 ms. Then, the cavity starts to collapse as a result of the hydrostatic pressure, which is higher than the cavity's internal pressure. The inward velocity of the cavity radius (negative value in Fig. 7-10(b)) increases during the collapse process. When the cavity reaches its minimum size, r_{min} = 0.42 cm, at T_{cavity} = 7.91 ms, the internal pressure in the cavity becomes high again as shown in Fig. 7-9(a). A secondary expansion of the cavity starts due to this high pressure. Similar dynamics of the cavity's radius were obtained by

analytical models established in [35], [81], [82].

7.3.4 Acoustic impulse

The acoustic impulse registered at the observation point, 500 mm away from the discharge centre, is shown in Fig. 7-11. Fig. 7-11(a) shows the detailed variation of the acoustic pressure in 100 μs period after breakdown. Similar to the waveform of $P_i(t)$ obtained in Fig. 7-9(b), a rapid rising slope is observed for $P_{cav}(t)$, which is followed by a oscillating falling edge. Such profile of the acoustic impulses was also experimentally obtained in [32], [73].

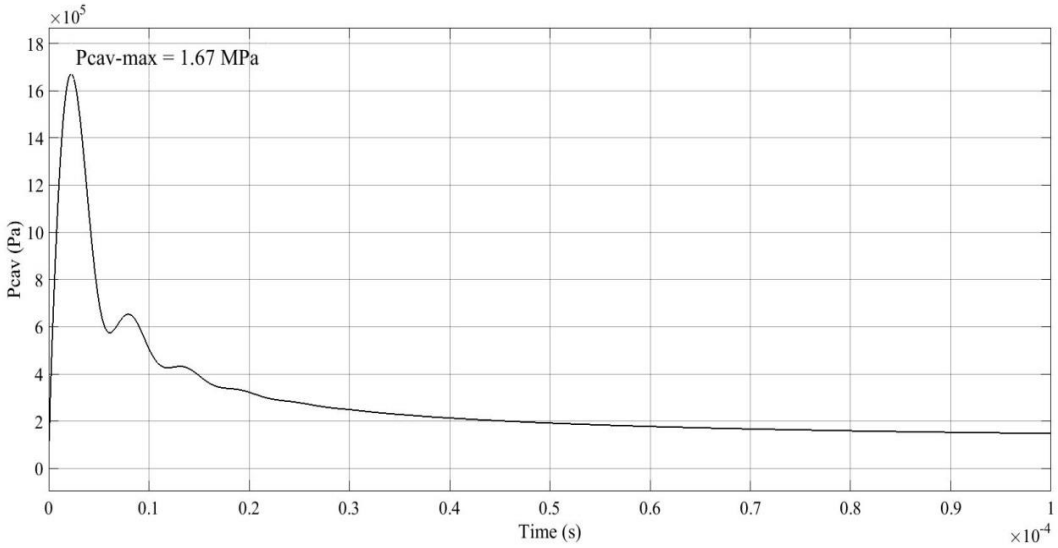

(a)

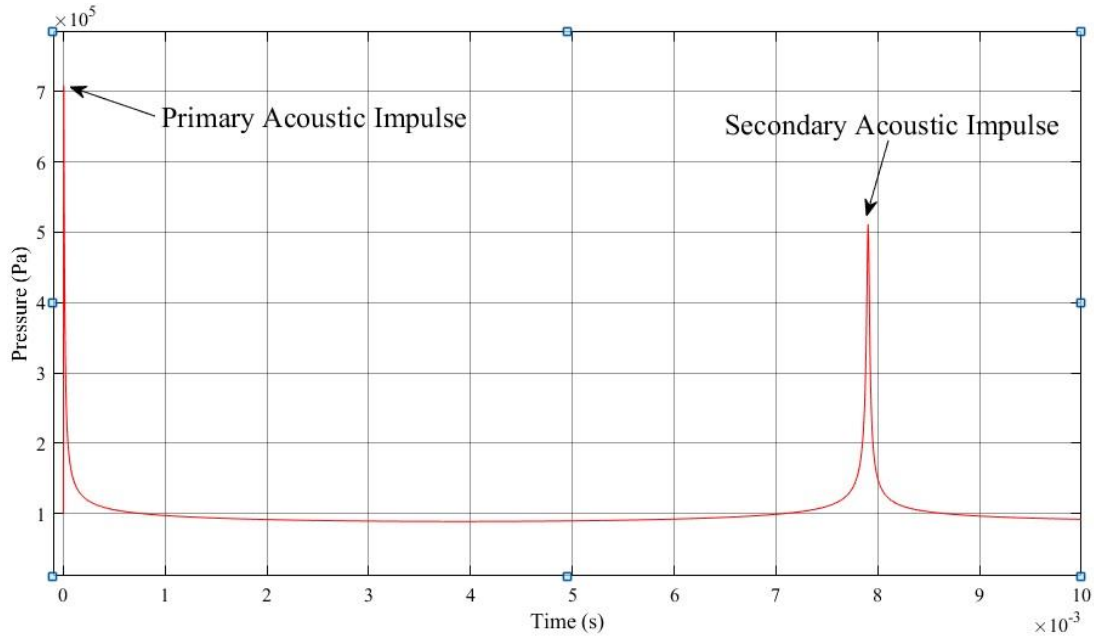

(b)

Figure 7-11. The acoustic pressure registered at the observation point, 500 mm from the discharge, with no retarded time reference for (a) 100 μs and (b) 10 ms after breakdown. $P_{cav\text{-}max}$ is obtained to be ~ 1.67 MPa.

The maximum value of the acoustic pressure was found to be ~ 1.67 MPa. With consideration of the attenuation effect of the acoustic magnitude with an increase in the observation distance, *d*, [73], [126], [171], the peak pressure of the acoustic impulse produced by this particular example discharge might reach at least tens of MPa in the vicinity of the discharge source.

Fig. 7-11(b) shows the computed result of acoustic impulses generated at the formation and collapse stages of the cavity. This waveform corresponds to the experimental measurement of the acoustic signal obtained in the longer time scale (2 ms/dev) in Fig. 4-2(b), Fig. 5-2(b) and Fig. 6-2(b). A good agreement was found between these computed and experimental waveforms.

7.3.5 Acoustic energy

The variation of the acoustic energy over time is shown in Fig. 7-12. According to (7.13), $E_{ac}(t)$ is an integral of $P_{cav}(t)$ over time. As shown in Fig. 7-11(b), the acoustic

pressure experienced impulsive change at the beginning of cavity's expansion and remains constant until the end of the cavity's collapse. As a result, the cumulative acoustic energy for the primary acoustic impulse increases to its maximum value in first tens of microseconds after breakdown as shown in Fig. 7-12. The generation of a secondary acoustic impulse at the collapse stage resulted in the stepwise increase in the cumulative E_{ac}. The first maximum value of E_{ac} is used in the following analysis as it represents the energy associated with the primary acoustic impulse. It is worthy of note that the propagation losses are neglected in this model.

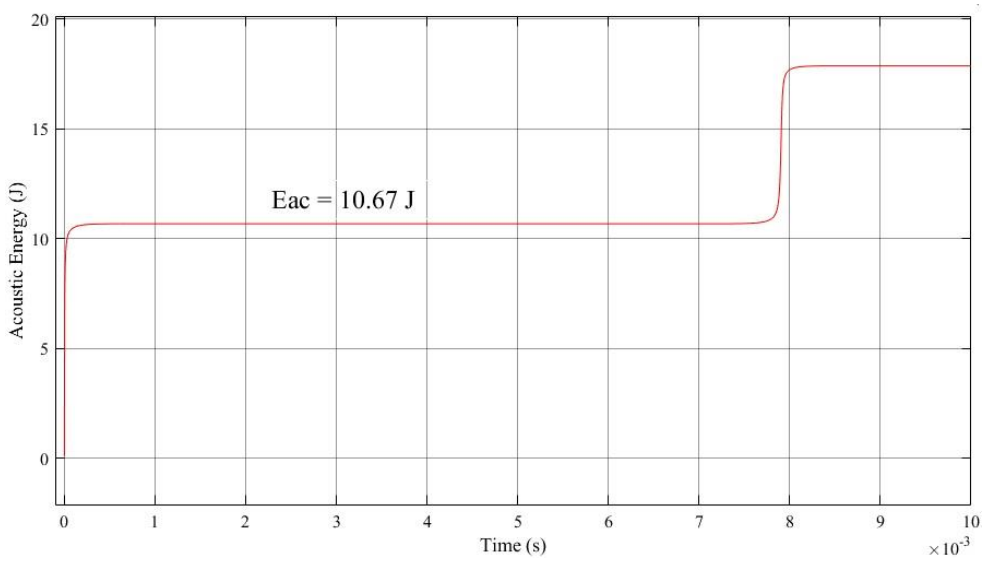

Figure 7-12. The variation in the acoustic energy in 10 ms after breakdown. The energy cumulated in the primary acoustic impulse is E_{ac} = 10.67 J.

7.4 Verification of the model

To validate the developed model and its suitability for the practical discharges studied in this work, it is necessary to check its compatibility with the practical experimental data. A straightforward method is to compare the values of the parameter, T_{cavity}, obtained by experiment and by modelling of a specific discharge, which will be studied in this section.

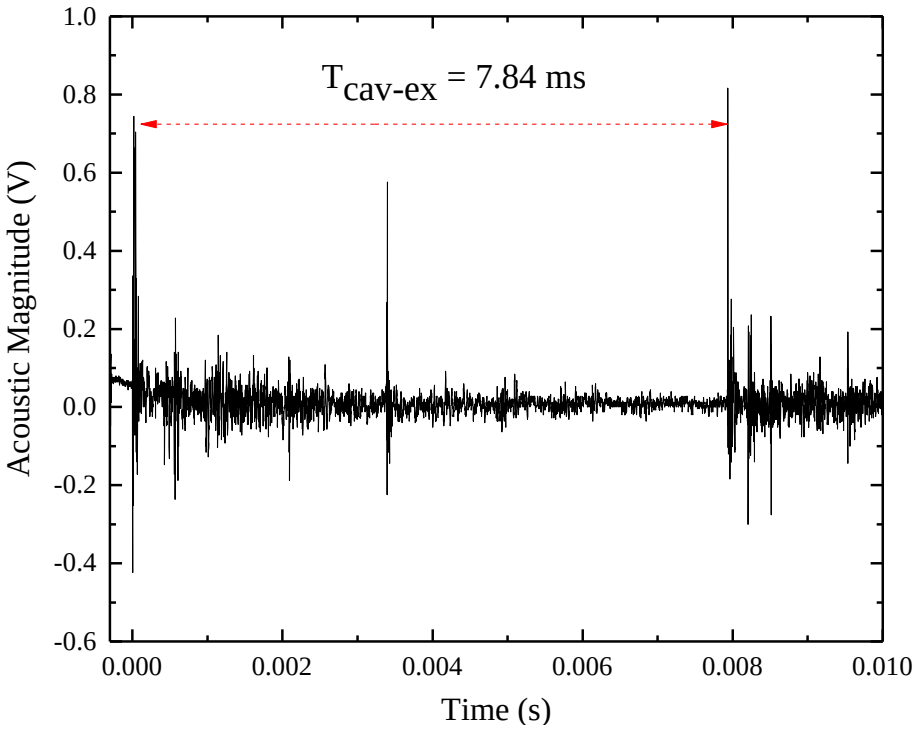

(a)

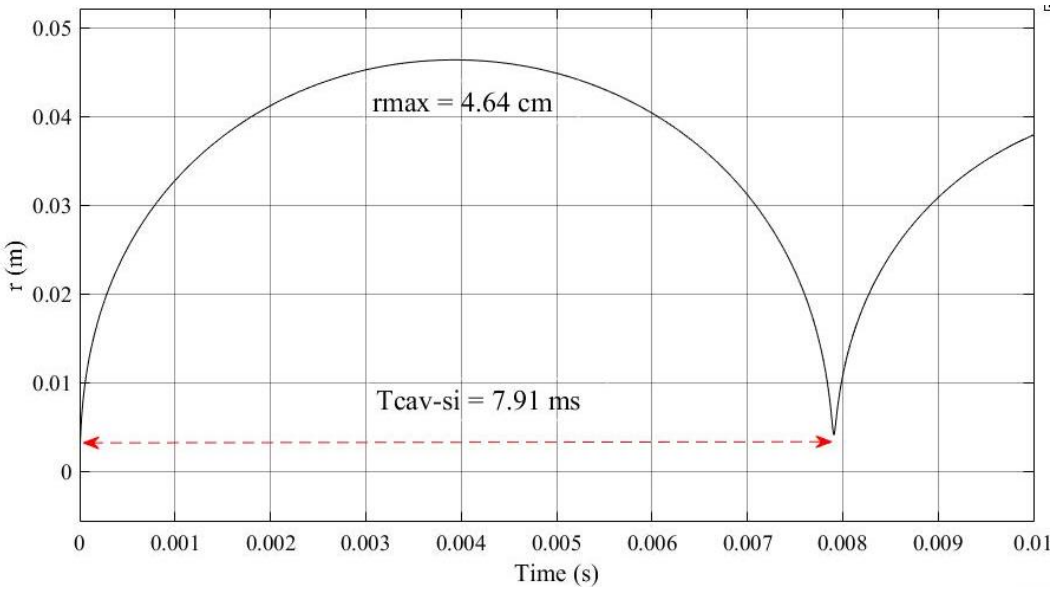

(b)

Figure 7-13. A comparison between (a) experimental acoustic signals and (b) simulated cavity expansion-collapse cycle for a spark discharge with input parameters: R_{pl} = 0.7975 Ω, I_0 = 6122 A, α = 95491 Ω/L and ω = 565034 rad/s. The experimental $T_{cav\text{-}ex}$ is ~ 7.84 ms and the simulated $T_{cav\text{-}si}$ is ~ 7.91 ms.

An example of the comparison between the experimental value, $T_{cav\text{-}ex}$, and the simulated value of the period, $T_{cav\text{-}si}$, is shown in Fig.7-13. In this example, a wire-guided discharge in 75 mm gap with C = 533 nF was considered. Fig. 7-13(a) shows the experimental acoustic waveform with two successive acoustic impulses generated during the primary cavity's oscillation cycle, with the experimental value, $T_{cav\text{-}ex}$, ~ 7.84 ms. Fig. 7-13(b) illustrates the simulated evolution of the cavity's radius in the primary oscillation cycle for the same discharge. The simulated $T_{cav\text{-}si}$ is ~ 7.91 ms, as shown in Fig. 7-13(b). It can be seen that the calculated period, 7.91 ms, is close to the experimental value, 7.84 ms, for this specific example discharge, indicating a good match between the modelled and experimental results for discharges. In order to establish the model reliability, such comparison between $T_{cav\text{-}si}$ and $T_{cav\text{-}ex}$ was conducted for all individual discharges and their acoustic waveforms studied in the previous chapters.

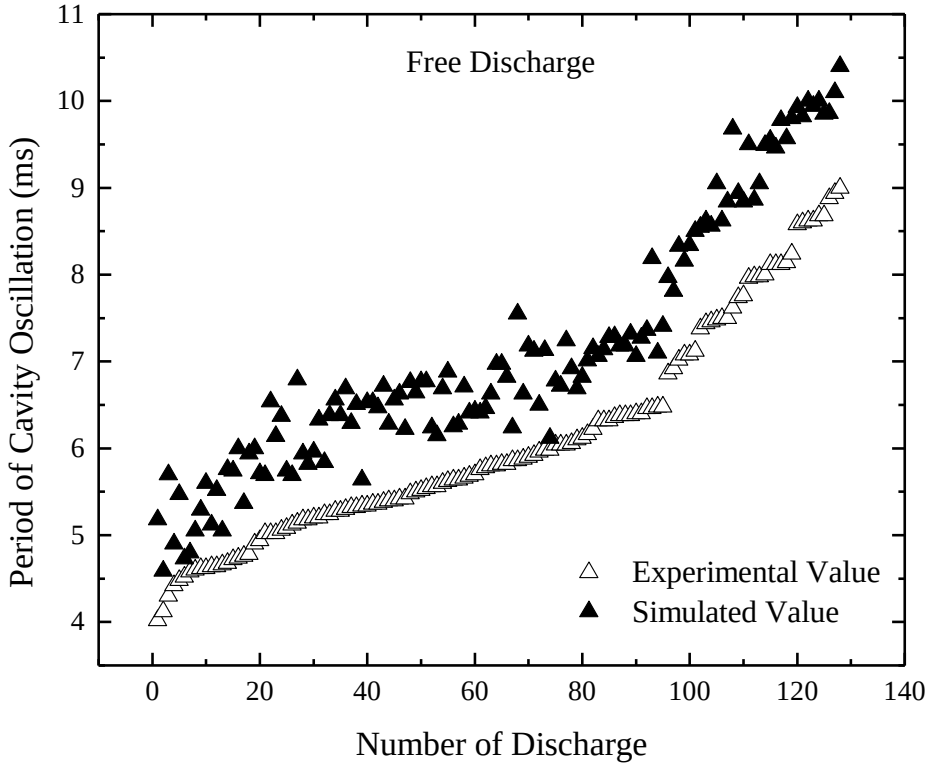

(a)

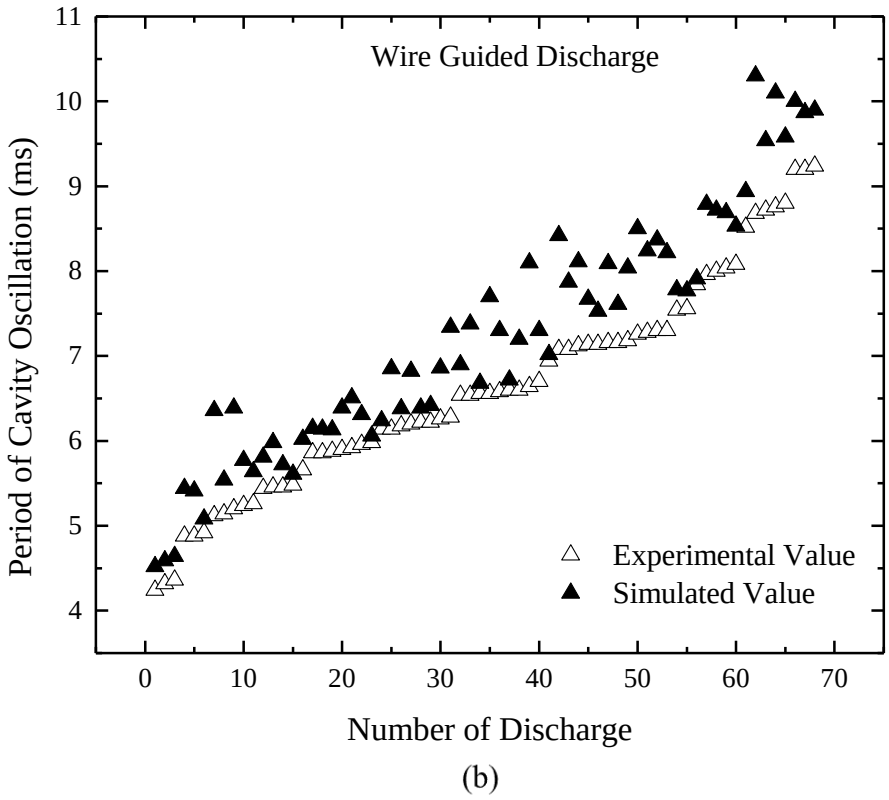

(b)

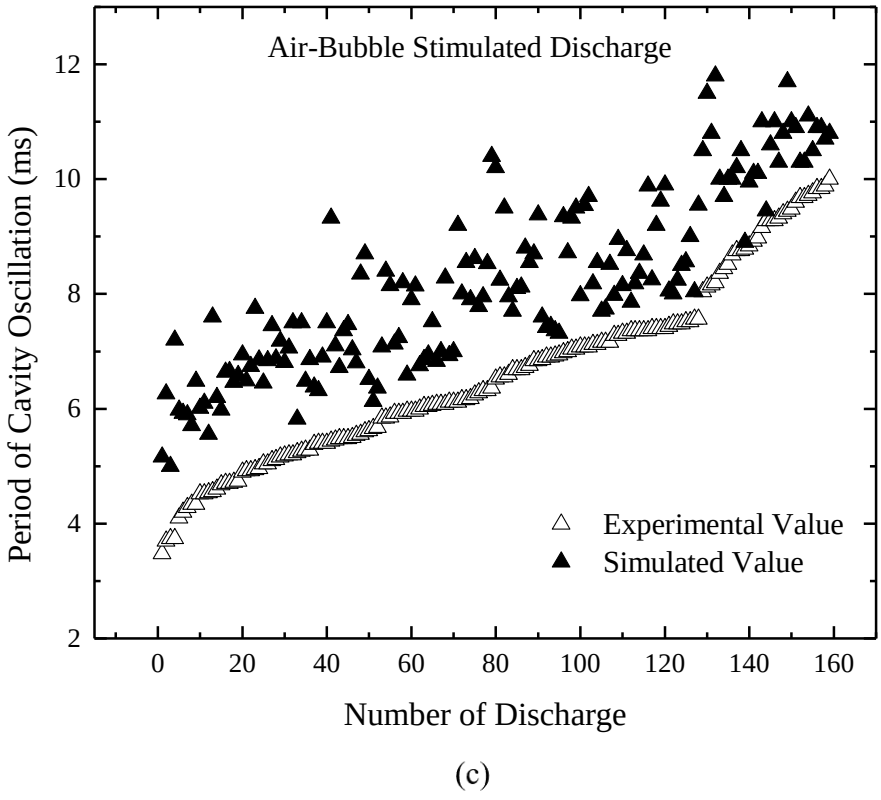

(c)

Figure 7-14. The comparison between the experimental and simulated values of T_{cavity} for (a) FD's, (b) ABSD's and (c) WGD's.

Fig. 7-14 shows the results of the comparison between $T_{cav\text{-}si}$ and $T_{cav\text{-}ex}$ for all three types of underwater spark discharges. The open triangles represent the experimentally obtained values of the period, $T_{cav\text{-}ex}$, and the black triangles represent the simulated values, $T_{cav\,-\,si}$, obtained by using the current-associated input parameters in the model. The horizontal axis refers to the number of the discharge tests. The discharge points in these three figures are sorted by the values of $T_{cav\text{-}ex}$, from smallest to largest.

It was found that the variation in $T_{cav\text{-}si}$ follows the increasing tendency of $T_{cav\text{-}ex}$. This indicates their similar functional behaviour. Thus, further analysis on relationships between different discharge parameters can be made based on the proposed model. It can be seen in Fig. 7-14 that the simulated values of T_{cavity} are marginally larger than corresponding experimental values. This difference can be explained by energy losses, which are not taken into account in the model. Also, a spherical topology of the cavity and its adiabatic expansion was assumed in the model. However, the practical evolution of the cavity could be complicated. For example, the cavity during its expansion stage could experience severe deformation or distortion due to the dynamic process of the energy injection. For discharges initiated in long inter-electrode gaps, the plasma channel may not follow the straight path between the HV and ground electrodes and could be bended.

All these possibilities will potentially alter the ideal oscillation process of the cavity described by the model. Therefore, by considering energy losses and potential complications in the cavity development, the difference between $T_{cav\text{-}si}$ and $T_{cav\text{-}ex}$ in Fig. 7-14 can be expected.

Additional information can be obtained from Fig. 7-14(c). It can be seen that $T_{cav\text{-}si}$ for the wire-guided discharges are closer to $T_{cav\text{-}ex}$ than $T_{cav\text{-}si}$ for other types of discharges. Thus, it can be stated that for discharges achieved in longer gaps, when energy conversion efficiency is higher, the model produces better results.

7.5 Acoustic efficiency

As discussed in Chapter 3, it was not possible to obtain direct pressure reading in Pa from the Pinducer's sensor as the calibration of the sensor is not provided. However, the acoustic wave-shapes with magnitude, obtained from the developed model, is

related to the pressure in Pa. Thus, an investigation on the acoustic efficiency for the underwater spark discharges can be conducted.

The acoustic efficiency is a critical parameter used to evaluate the performance of a spark generation system in producing intense acoustic impulses. It describes the ability of the system to convert the energy delivered into the plasma channel into the acoustic energy. Using (2.24) and (7.13), the acoustic efficiency, η_{ac} can be obtained by:

$$\eta_{ac} = \frac{E_{ac}}{E_{pl}} \tag{7.21}$$

The acoustic energy used in this work refers to the energy associated with the primary acoustic impulse, as shown in Fig. 7-12. As described by (2.24) and (7.13), the acoustic efficiency is related to the combination of the acoustic signature, the circuit parameters and the electrode topology.

The acoustic efficiency in underwater spark discharges has been investigated in a number of papers [73], [81], [99], [128], [172]. The obtained values of η_{ac} vary in a range from ~ 2.5 % to ~ 56 %. For example, in [81], the acoustic efficiency obtained in sea water (with energy of ~ (10 - 70) kJ) was from ~ 2.5 % to ~ 3.5 %. In [172], higher values of the acoustic efficiency were obtained, ~ (5 % - 10 %) for ~ 1 kJ spark discharges in sea water and it was found that η_{ac} is inversely proportional to the value of capacitance. For spark discharges in tap water [32], [73], the acoustic efficiency was in a range from ~ 23 % to ~ 30 % for different combinations of the energy delivered into the plasma channel and the inter-electrode gap. Similar effect of the inter-electrode gap on the acoustic efficiency was observed in [99]. In [128], the calculated acoustic efficiency ranged from ~ 14 % to ~ 40% and it varied inversely with the squared value of the energy input, which was accounted for ~ 85 % of the initial energy stored in the capacitor bank considering energy losses during the discharge.

Based on these papers, it can be stated that the acoustic efficiency is related to different circuit parameters, such as the capacitance of the energy source system, the inter-electrode gap of the electrode topology and the energy delivered into the plasma channel. The dependency of η_{ac} on these parameters needs to be established for optimisation in practical applications. The plasma resistance, R_{pl}, is also an important parameter, which defines the partition of the storage energy and defines the amount of

energy, which is transferred into the plasma channel as described in chapter 4. Therefore, the investigation of the relationships between η_{ac} for all types of discharges FD's, WGD's and ABSD's and the circuit and plasma parameters, l, C, R_{pl} and E_{pl} is present in the next section and an empirical model is established to link η_{ac} and R_{pl}.

7.5.1 Acoustic efficiency as a function of the plasma resistance

Fig. 7-15 shows the variation of the acoustic efficiency with the constant plasma resistance for all three types of underwater spark discharges. The acoustic efficiency, η_{ac}, covers a range from ~ 5 % up to ~ 52.5 %. However, the higher values of η_{ac} were observed for FD's and lower η_{ac}'s were obtained for WGD's. For the relationships between $P_{cav\text{-}max}$ and other parameters, including V_{br}, R_{pl} and E_{pl}, discussed in Chapters 4 - 6, a general conclusion, which can be derived from this study, is that discharges in longer gaps generate acoustic impulses with higher magnitude when other discharges parameters are the same. It means that higher E_{ac} and thereby higher η_{ac} can be expected for the discharges with longer l, especially for WGD's. However, in the developed model, $P_{cav}(t)$ was obtained in the acoustic approximation and its dependency on l was not directly included in the model. Therefore, the acoustic efficiency obtained for long inter-electrode gaps, for example 45 mm and 75 mm gaps, is considered to be underestimated. The accurate value of η_{ac} for these cases are expected to be higher than the modelled values as shown in Fig. 7-15(e) and (f). Despite above analysis on the value of η_{ac}, the relationships shown in Fig. 7-15 provide important functional dependencies of the acoustic efficiency in underwater spark discharges.

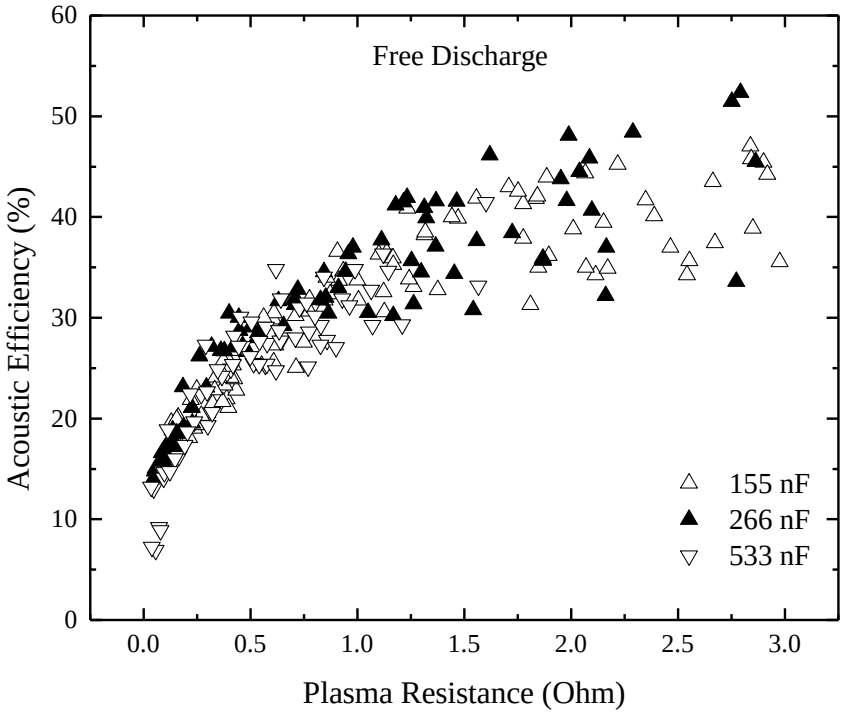
Free Discharge
Acoustic Efficiency (%)
Plasma Resistance (Ohm)
155 nF
266 nF
533 nF
0
10
20
30
40
50
60
0.0
0.5
1.0
1.5
2.0
2.5
3.0

(a)

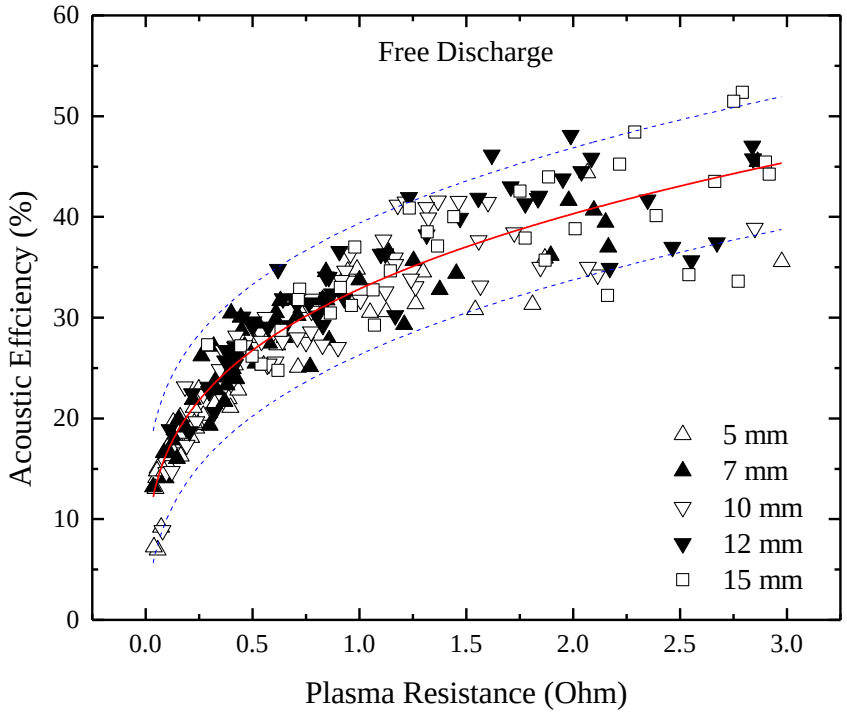
Free Discharge
Acoustic Effciency (%)
Plasma Resistance (Ohm)
5 mm
7 mm
10 mm
12 mm
15 mm
0
10
20
30
40
50
60
0.0
0.5
1.0
1.5
2.0
2.5
3.0

(b)

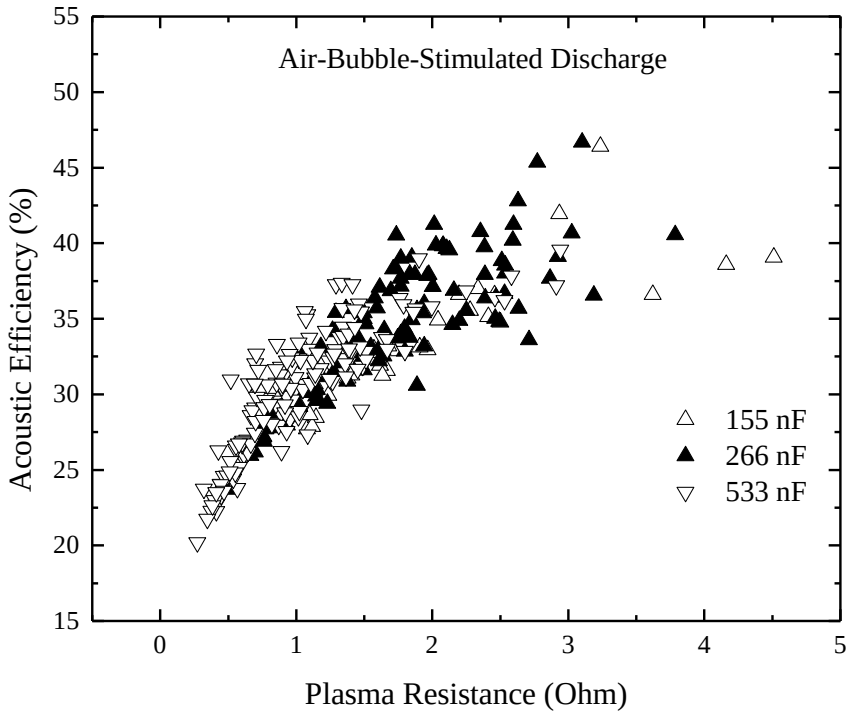
Air-Bubble-Stimulated Discharge
Acoustic Efficiency (%)
Plasma Resistance (Ohm)
155 nF
266 nF
533 nF

(c)

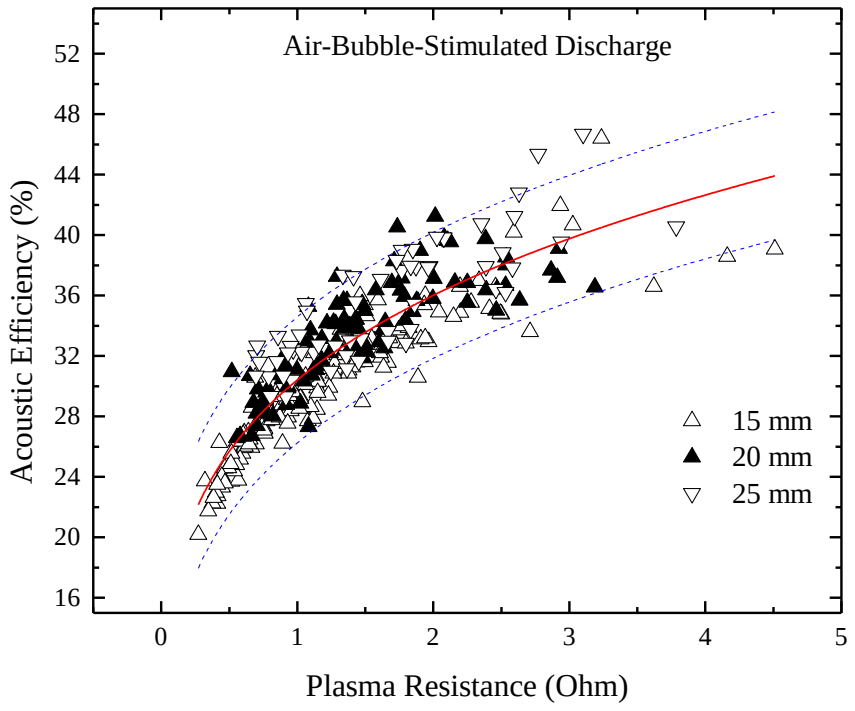
Air-Bubble-Stimulated Discharge
Acoustic Efficiency (%)
Plasma Resistance (Ohm)
15 mm
20 mm
25 mm

(d)

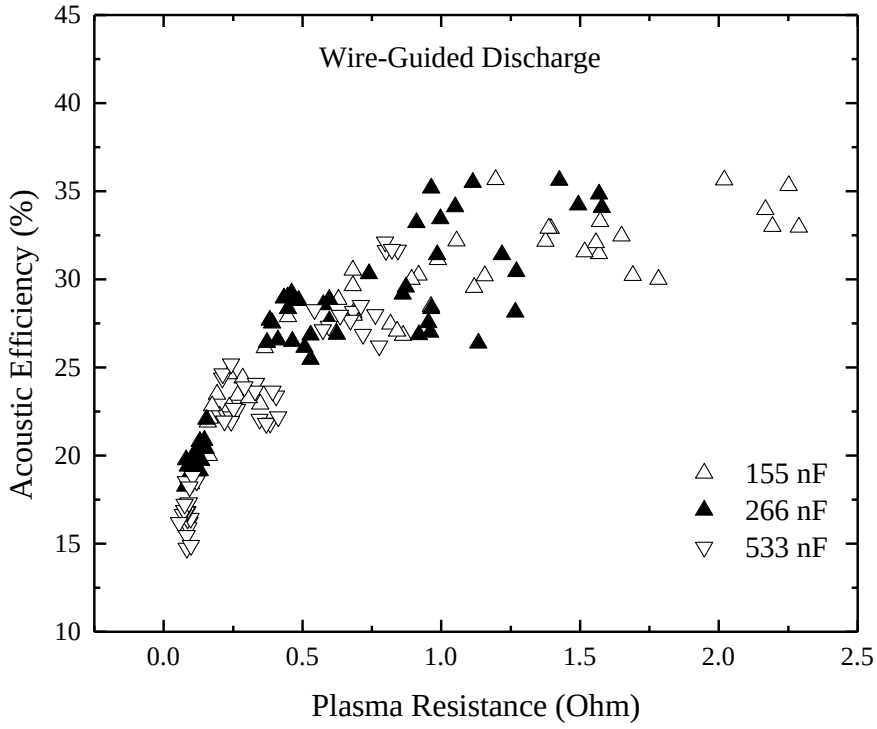
Wire-Guided Discharge
Acoustic Efficiency (%)
Plasma Resistance (Ohm)
155 nF
266 nF
533 nF

(e)

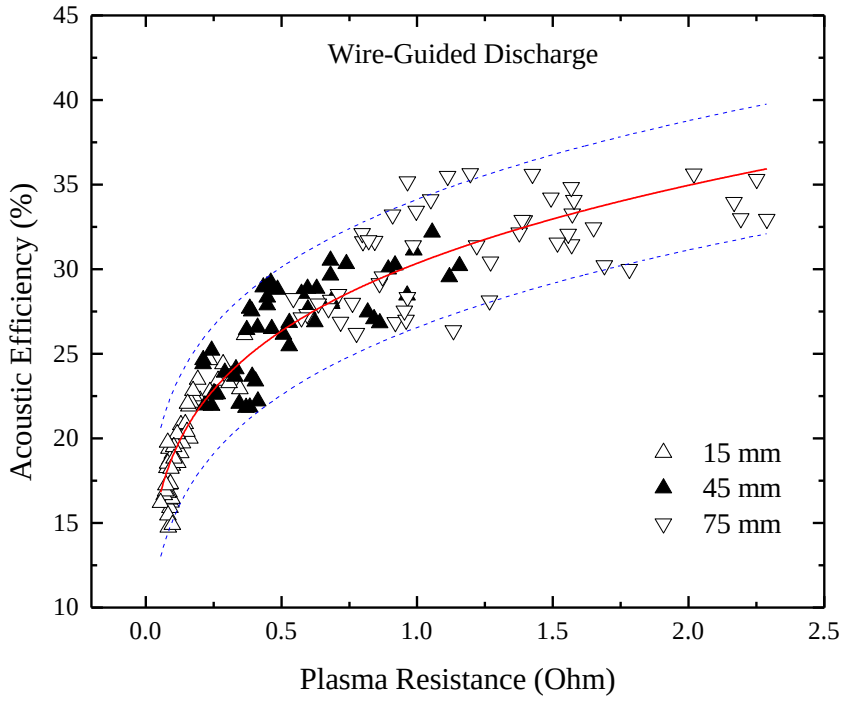
Wire-Guided Discharge
Acoustic Efficiency (%)
Plasma Resistance (Ohm)
15 mm
45 mm
75 mm

(f)

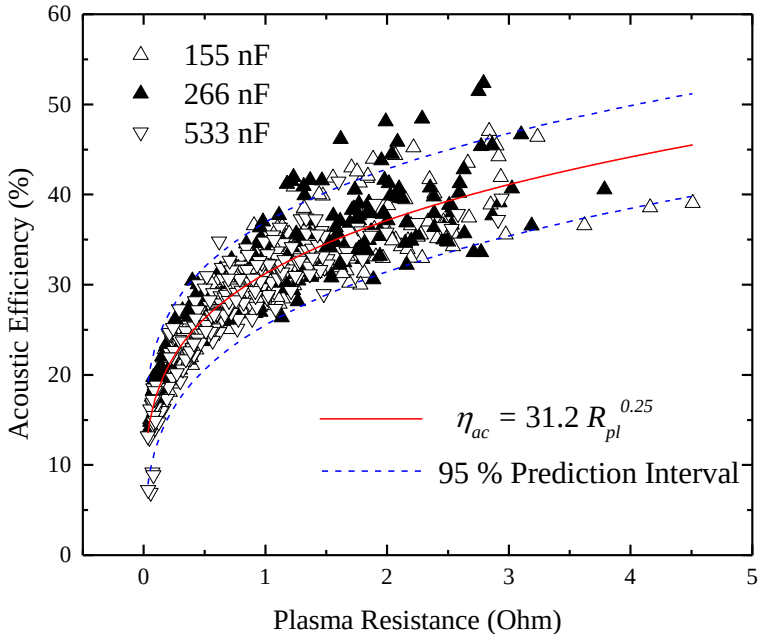

(g)

Figure 7-15. The acoustic efficiency as a function of the plasma resistance, classified by either capacitance or inter-electrode gap, for tests conducted for: (a) - (b) FD's; (c) – (d) ABSD's; (e) – (f) WGD's; (g) all three types of underwater spark discharge. Red solid line shows trend line obtained by (7.23) and blue dashed lines show the upper and lower boundaries of the 95 % prediction intervals.

From the general perspective, it can be seen from Fig. 7-15 that the acoustic efficiency increases non-linearly with an increase in the plasma resistance. This tendency is opposite to the relationship between $P_{cav\text{-}max}$ (equivalent to E_{ac}) and R_{pl} obtained in Chapters 4 – 6: $P_{cav\text{-}max}$ decreases with an increase in R_{pl} for most discharges with plasma resistance greater than the circuit resistance, $R_{pl} > R_{circuit}$. Therefore, based on these relationships between η_{ac}, $P_{cav\text{-}max}$ and R_{pl}, the following conclusion can be drawn: an increase in $P_{cav\text{-}max}$ may result in decrease in η_{ac}. Does this mean that the optimisation of either $P_{cav\text{-}max}$ or η_{ac} has to be based on the sacrifice of the other one? The answer to this question is no or it is only partially correct.

To verify this statement, the dependency of η_{ac} on C and l was investigated. According to (4.18) and (6.13), an increase in either C or l generates larger $P_{cav\text{-}max}$ and thereby larger E_{ac}. An increase in C also results in larger E_{pl}. However, an increase in l results in undefined variation in E_{pl}. Therefore, to separate the combined effect of C and l on E_{pl} and to investigate their individual influence on η_{ac} in Fig. 7-15, two scenarios have

to be considered. One scenario is to change C with constant l. The other is to change l with constant C. In the first scenario, for discharges with the same l in Fig. 7-15(e), it was found that η_{ac} varies inversely with C (equivalent to $P_{cav\text{-}max}$). This observation verifies the conclusion made above: an increase in $P_{cav\text{-}max}$ will reduce η_{ac}. However, this conclusion is only valid for discharges with constant l. In the second scenario, for data points (η_{ac}) with constant C in Fig. 7-15(f), it was found that η_{ac}'s obtained for longer gaps have larger values, indicating the proportional relationship between η_{ac} and l for constant C. By combining analysis of these cases, a conclusion can be made on the effect of C and I on η_{ac}: an increase in both C and l will increase the acoustic magnitude and the acoustic energy. However, the acoustic efficiency will be negatively affected by larger capacitances but will be enhanced by longer inter-electrode gaps. Therefore, in order to optimise $P_{cav\text{-}max}$ while keeping high η_{ac}, the underwater spark discharges in longer inter-electrode gaps achieved by using lower capacitances are preferred.

Regarding the well-defined relationship between η_{ac} and R_{pl} in Fig. 7-15(g), it is important and beneficial to develop an analytical model in order to establish functional behaviour of η_{ac} with R_{pl}. Due to a complex nature of the link between $r(t)$ and R_{pl}, a simplified empirical model is proposed to describe the link between η_{ac} and R_{pl} :

$$\eta_{ac} = z_1 R_{pl}^{\ z_2} \tag{7.22}$$

where z_1 and z_2 are constant coefficients.

The coefficients, z_1 and z_2, were obtained by fitting (7.22) to the computed results in Fig. 7-15(b), (d) and (f) using software OriginLab 9.0c and these coefficients are given in Table 7-6.

Table 7-6. Values of coefficients, z_1 and z_2, for (7.22) obtained for FD's, ABSD's and WGD's

Discharge mechanism	z_1	z_2
FD's	32.84 ± 0.36	0.30 ± 0.01
WGD's	30.35 ± 0.36	0.21 ± 0.01
ABSD's	30.41 ± 0.21	0.24 ± 0.01

The trend lines obtained from (7.22) for three types of underwater spark discharges are shown as the red solid lines in Fig. 7-15(b), (d) and (f). It can be seen that most of the data points (η_{ac}) fit within the upper and lower boundaries of the 95 % prediction intervals as shown by blue dashed lines. It was found that coefficients z_1 and z_2 obtained for different types of discharges were close to each other. Therefore, a general form for the relationship (7.22) can be obtained. By calculating the average values of $z_1 = 31.2$ and $z_2 = 0.25$, (7.22) then can be rewritten as:

$$\eta_{ac} = 31.2 R_{pl}^{\,0.25} \tag{7.23}$$

The empirical relationship (7.23) has been fitted to the data points in Fig. 4-14(g) and a good agreement was observed between the trend line and computed results. This result confirms that (7.23) is suitable for all types of underwater spark discharges proposed in this work. The relationship between η_{ac} with R_{pl} obtained in this section not only provides a novel view on understanding of the acoustic performance of underwater spark discharges but also allows the link between the acoustic efficiency and the plasma resistance to be established. Observations made for the dependency of η_{ac} on C and l provide important guidance in optimising the acoustic efficiency by adjusting C and l in the circuit.

7.5.2 Acoustic efficiency as a function of the energy delivered into the plasma channel

Apart from the plasma resistance, the energy delivered into the plasma channel also plays an important role in determining the characteristics of the acoustic impulses produced by discharges and it is directly related to the acoustic efficiency as indicated by (7.21). The variation of η_{ac} as a function of E_{pl} for all three types of discharge is shown in Fig. 7-16. The data points included in Fig. 7-16 have also been classified by the capacitance, C, and the length of the inter-electrode gap, l. It was found that η_{ac} decreases with an increase in E_{pl}, although a dispersion in data points (η_{ac}) was observed for different types of underwater spark discharges.

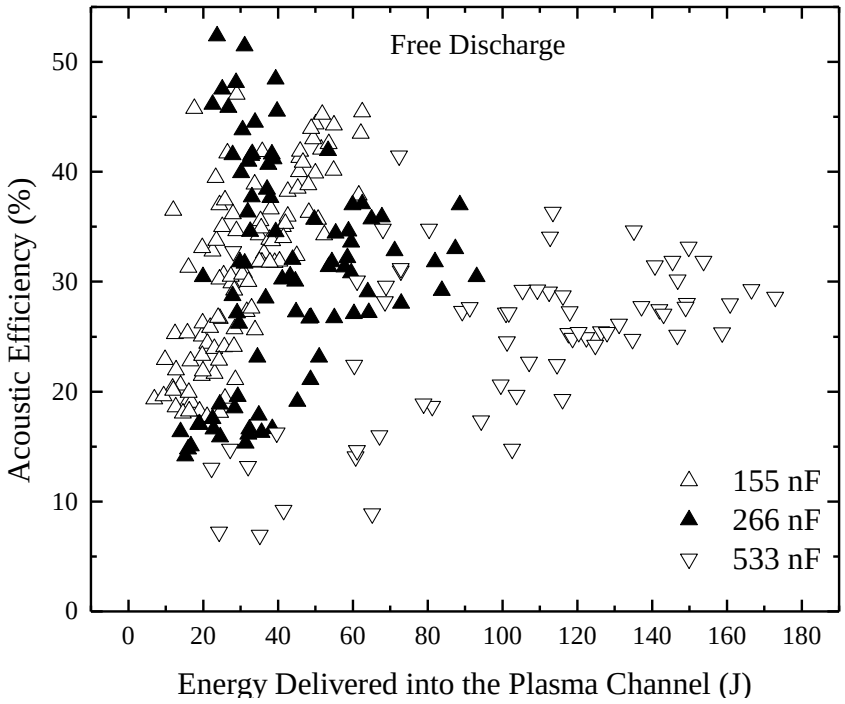
Free Discharge
Acoustic Efficiency (%)
Energy Delivered into the Plasma Channel (J)
155 nF
266 nF
533 nF
0
10
20
30
40
50
0
20
40
60
80
100
120
140
160
180

(a)

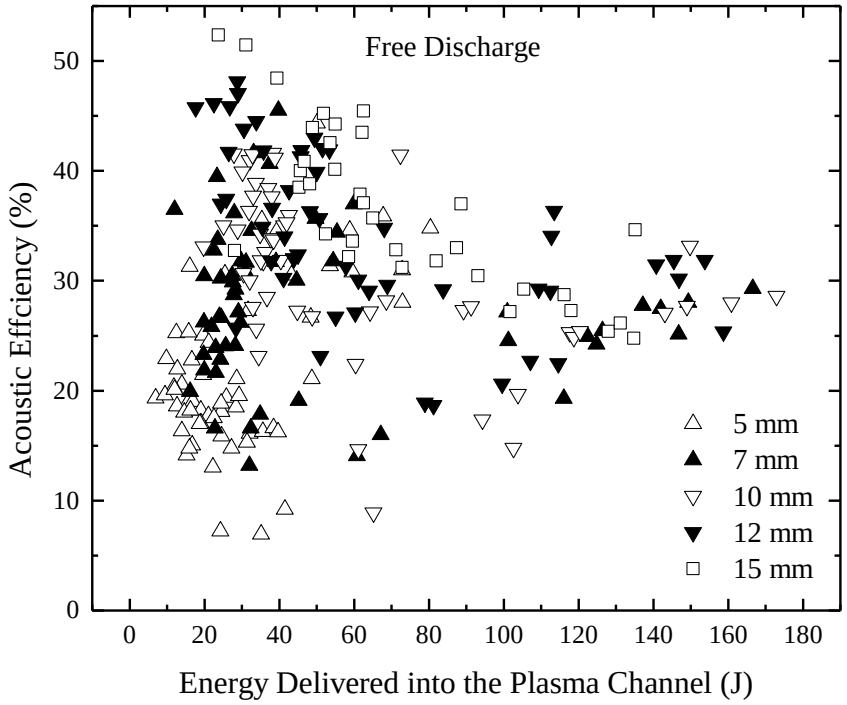
Free Discharge
Acoustic Effciency (%)
Energy Delivered into the Plasma Channel (J)
5 mm
7 mm
10 mm
12 mm
15 mm
0
10
20
30
40
50
0
20
40
60
80
100
120
140
160
180

(b)

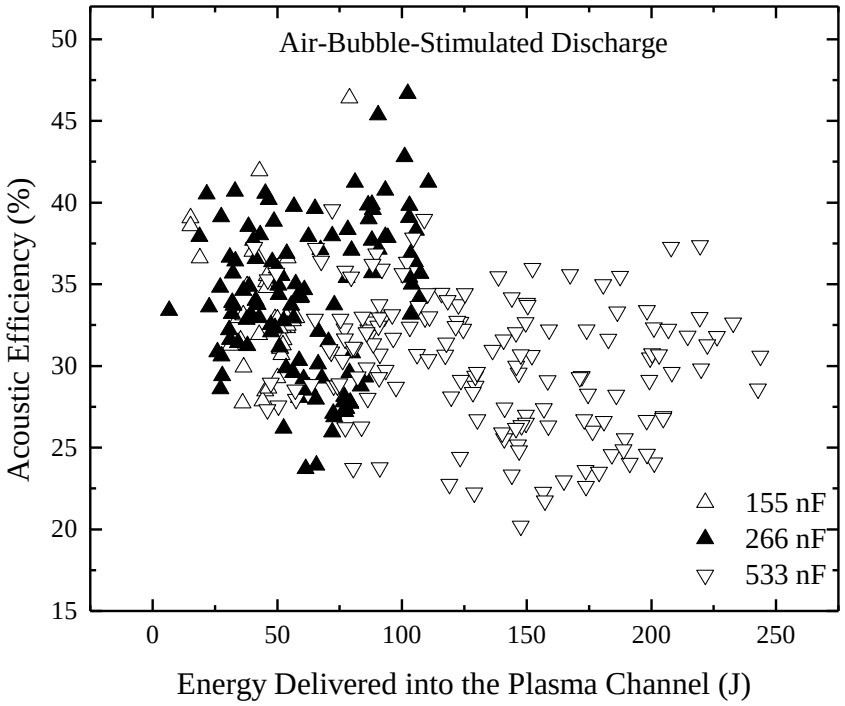
Air-Bubble-Stimulated Discharge
Acoustic Efficiency (%)
Energy Delivered into the Plasma Channel (J)
155 nF
266 nF
533 nF

(c)

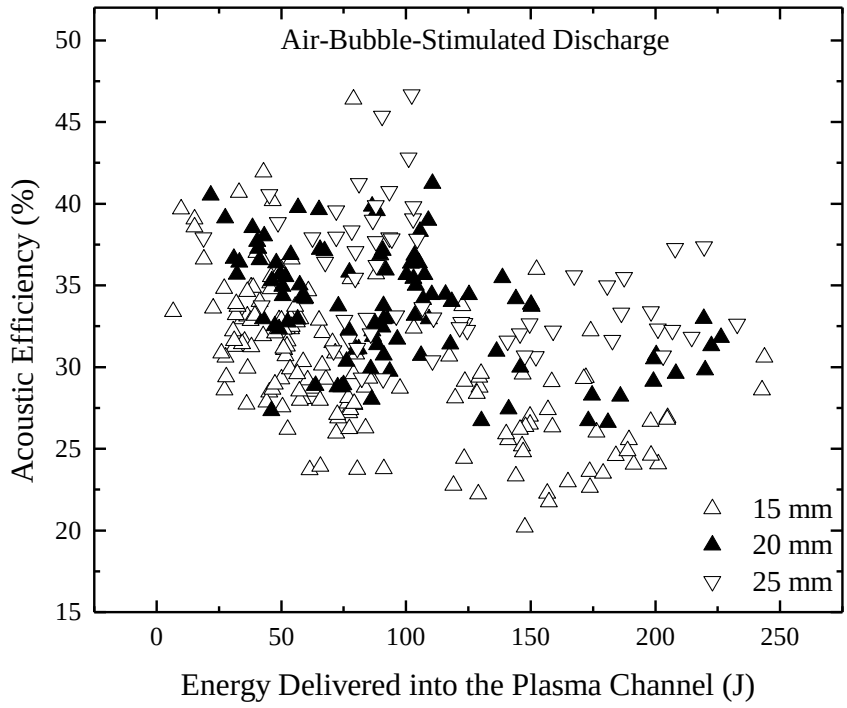
Air-Bubble-Stimulated Discharge
Acoustic Efficiency (%)
Energy Delivered into the Plasma Channel (J)
15 mm
20 mm
25 mm

(d)

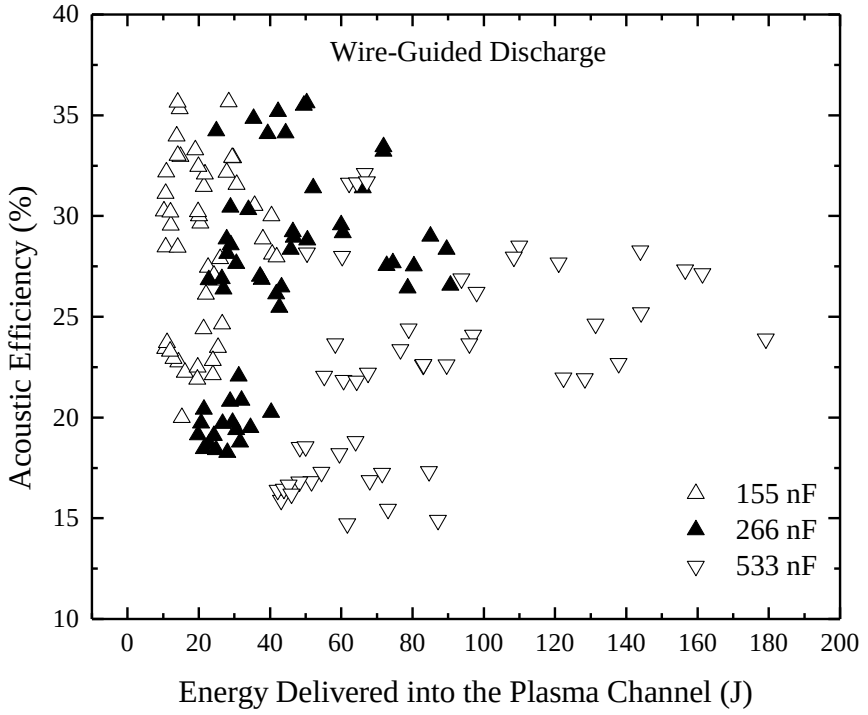

(e)

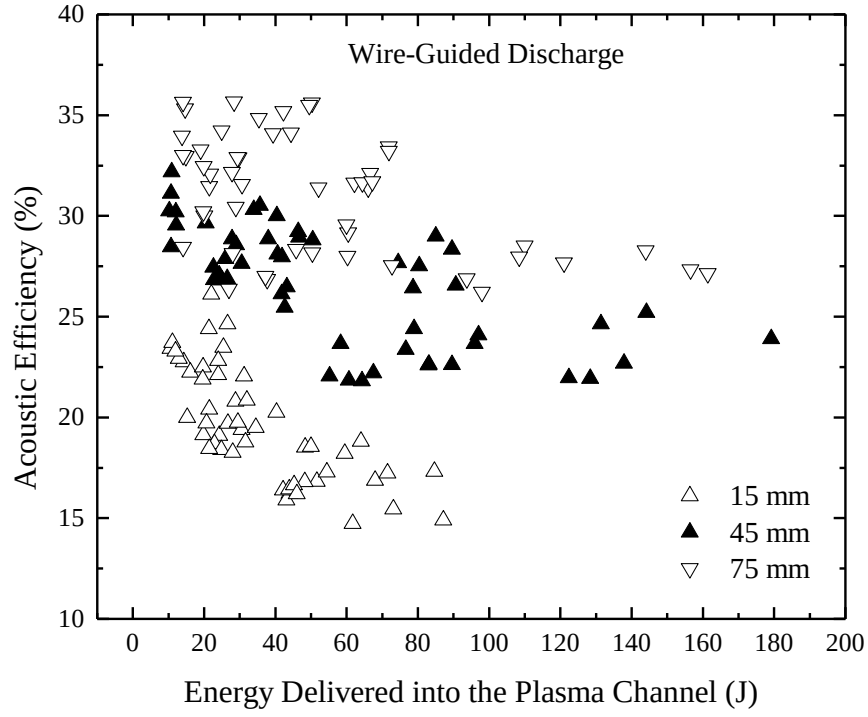

(f)

Figure 7-16. The acoustic efficiency as a function of the energy delivered into the plasma channel, classified by capacitance and inter-electrode gap, for tests conducted for: (a) - (b) FD's; (c) – (d) ABSD's; (e) – (f) WGD's.

It can be seen in Fig. 7-16 (e) and (f) that discharges with longer l provide higher values of η_{ac} for the same amount of E_{pl}. However, discharges with larger C produce lower values of η_{ac}. This observation not only confirms the conclusion made previously for Fig. 7-15 that the discharges in longer gaps have higher values of η_{ac} under the same energisation levels, but also emphasises the major role played by l in defining η_{ac}. A similar statement can be made here: by using long gaps and relatively low capacitances, both high values of $P_{cav\text{-}max}$ and η_{ac} can be achieved.

7.6 Conclusions

In this chapter, an analytical model has been developed to analyse and investigate the time-dependent post-breakdown behaviour of the hydrodynamic and acoustic parameters of all types of underwater spark discharges. The analysis on the acoustic efficiency and its relationships with discharge parameters, C, l, R_{pl} and E_{pl} was conducted.

The model describes two stages of the underwater discharges: the energy deposition stage and the adiabatic expansion stage. During the energy deposition stage, the major dynamic of the plasma channel is governed by energy injection into the discharge channel. The adiabatic expansion stage is related to the adiabatic oscillation of the cavity. Several sub-models (7.1)-(7.19) have been built to describe all discharge processes during these two stages. The energy deposition in the discharge channel and the energy partition in the plasma channel were described using the energy balance equation which stated that the energy delivered into the plasma channel is divided into the thermal energy and the mechanical work done by the cavity against water. An acoustic approximation approach was used to model the acoustic impulse propagation in water. The Gilmore model with the pressure-dependent speed of sound was used to describe the post-breakdown oscillation of the spark-generated cavity. The complete model was implemented in MatLab R2016b software package.

The sensitivity of the model to different initial conditions and input parameters was investigated. It was found that $r(0)$ and $\dot{r}(0)$ produces a minor effect on the output parameters, T_{cavity}, $P_{cav\text{-}max}$ and E_{ac}. This is due to fast expansion of the plasma channel during the energy deposition stage. It was shown that the input parameters, ω, α, I_0 and

R_{pl}, produce different effects on the output parameters.

It has been assumed that the plasma resistance is constant in this model, however as the shockwave is generated during the first quarter of cycle when the resistance is changing rapidly this may impact the accuracy of the model. However, there is no suitable model for the behaviour of $R_{pl}(t)$.

The time-dependent waveforms of different discharge parameters, including the electrical power, $P_{pl}(t)$, the internal pressure in cavity, $P_i(t)$, the radius of cavity, $r(t)$, the acoustic impulse, $P_{cav}(t)$ and the primary acoustic energy E_{ac} have been obtained. It was found that high pressure (up to ~ 560 MPa) is developed in the spark channel during the energy deposition stage. This high internal pressure results in significant acceleration of the cavity/water interface. At the same time, an acoustic impulse is emitted by the cavity into water. With expansion of the cavity, the pressure inside becomes lower than the hydrodynamic pressure. When radius of the cavity reaches its maximum value, the cavity starts to collapse. After the cavity reaches its minimum size, a secondary acoustic impulse is emitted.

Comparison between the simulated and experimentally obtained values of T_{cavity} was conducted to validate the model. It was found that the simulated values of T_{cavity} are greater than their experimental values. This difference can be explained by energy losses in the discharge process which were not taken into account in the developed model.

With known values of $P_{cav}(t)$, the acoustic energy, E_{ac}, and the acoustic efficiency, η_{ac}, were calculated using (7.13) and (7.21) for all types of discharges studied in this work. Their relationships with R_{pl} and E_{pl} are obtained. It was found η_{ac} increases with an increase in R_{pl} but it is not strongly dependent on the E_{pl}. This phenomenon reveals that increasing $P_{cav\text{-}max}$ by injecting more energy into the plasma channel does not necessarily lead to an increase in η_{ac}. It was also established that either longer l or smaller C will help achieve higher η_{ac} in underwater spark discharges. Therefore, in practical applications, discharges with longer l and lower C are preferable as they result in a higher acoustic efficiency for the same $P_{cav\text{-}max}$.

An empirical model, $\eta_{ac} = z_1 R_{pl}^{Z2}$, was developed for describing the relationship between η_{ac} and R_{pl}. A general form of the model with $z_1 = 31.2$ and $z_2 = 0.25$ was obtained for all discharge types studied in this work. This model provides a reasonable

agreement between the experimental measurements and the analytical results. Thus, (7.22) can be used in practical cases for evaluation of the acoustic efficiency for underwater spark discharges. This model also allows to analyse the influence of different factors on the hydrodynamic and acoustic parameters of the underwater spark discharges, which is important for development of practical underwater plasma-acoustic sources and for optimisation of pulsed power driving circuits to desired acoustic impulses.

8 Conclusions and future work

8.1 Conclusions

The main objectives of this work were to investigate the breakdown characteristics of the underwater spark discharges with different initiation mechanisms and to comprehensively study the acoustic performance of these discharges. These aims have been achieved by producing underwater spark discharges with different energisation levels and by establishing phenomenological scaling relationships between the circuit and discharges parameters.

A review of literature on various aspects of the underwater spark discharge was conducted. The underwater spark discharges are used in practical applications due to their ability to generate intense acoustic impulses. It was shown that gas bubbles present in water play an important role in initiation and propagation of streamers in water and may result in reducing the pre-breakdown delay and losses. An effective approach to increase the inter-electrode gap for stronger acoustic impulses generated by underwater discharges is to artificially inject air bubbles in the inter-electrode gap. Another approach to increase the inter-electrode gap is to place a thin metallic wire between the HV and ground electrodes. Together with free self-triggering discharges, air-bubble stimulated discharges and wire-guided discharges are the main focus of the present work.

An experimental set-up consisting of the pulsed power generation system, diagnostic devices and electrode topologies was designed and constructed in this work. With the purpose of comparison between acoustic performance of different types of discharges, similar energisation levels were used in all underwater spark discharge tests in this work. Three levels of capacitances and charging voltages were used: 155 nF, 266 nF, 533 nF and 25 kV, 30 kV, 35 kV. A point-to-point electrode topology was used for FD's. For ABSD's and WGD's, novel electrode topologies have been designed in this research project. A point-to-plane electrode with embedded air-bubble injection system was designed for ABSD's. An electrode topology with copper wire holders was constructed for WGD's. Different lengths of the inter-electrode gaps, from 5 mm to 75 mm, were used. For all tests conducted in this work, voltage, current, and acoustic waveforms were obtained. These waveforms were used to obtain different

parameters: the breakdown voltage, V_{br}, the constant plasma resistance, R_{pl}, the energy delivered into the plasma channel, E_{pl}, the acoustic magnitude, $P_{cav\text{-}max}$ and the period of the cavity oscillation, T_{cavity}.

The investigation into the relationships between these parameters for all three types of underwater spark discharges has been conducted. The novelty of this work is the establishment of the phenomenological scaling relationships between these parameters based on the experimental results. The statistical and analytical analysis on these experimental results provided a new level of understanding of the effect of different circuit and topological parameters on the acoustic output from the underwater discharges. This analysis also allowed calculation and prediction of the acoustic impulse for different combinations of circuit parameters (C, l, V_{br}, R_{pl}, and E_{pl}).

Investigation into the breakdown characteristics and their relationships with acoustic impulses generated by free self-triggering discharges was conducted. It was found that the period of the cavity oscillation and the acoustic magnitude generally increase with an increase in the breakdown voltage as the energy available at breakdown increase. However, for short inter-electrode gaps (5 mm and 7 mm), there were outlying data points (T_{cavity} and $P_{cav\text{-}max}$) observed below the main trend for high breakdown voltages (> 20kV). It was established that the plasma resistance of these discharge was smaller than the pulsed driving circuit resistance. Two phenomenological scaling relations were developed to describe the link between T_{cavity}, $P_{cav\text{-}max}$ and V_{br}: $T_{cavity} \propto V_{br}^{2/3}$ and $P_{cav\text{-}max} \propto V_{br}^{2\beta/3}$. Also, an empirical link was obtained for describing a functional dependency of $P_{cav\text{-}max}$ on the inter-electrode, $l^{0.22}$. Based on the discussion of the relationships between the plasma resistance and circuit resistance, it was found that the energy conversion efficiency, η_{pl}, was proportional to the ratio between R_{pl} and $R_{circuit}$. For discharges obtained in the main trend, the values of their energy conversion efficiency were in a range from ~ 60 % to ~ 93 %.

It was found that values of the plasma resistance varied in a range from ~ 0.028 Ω to ~ 6.0 Ω for free self-triggering discharges. In general, lower breakdown voltage and longer inter-electrode gaps resulted in a larger plasma resistance. Non-linear relationships between T_{cavity}, $P_{cav\text{-}max}$ and R_{pl} were established and it was found that the peak values of T_{cavity} and $P_{cav\text{-}max}$ corresponded to: $1 < R_{pl}/R_{circuit} < 3$. It was also shown that T_{cavity} and $P_{cav\text{-}max}$ increase with an increase in E_{pl}: T_{cavity} is proportional to $E_{pl}^{1/3}$,

while $P_{cav\text{-}max}$ is proportional to $E_{pl}^{\beta/3}$.

The comprehensive investigation of ABSD's was conducted using analytical approaches similar to the approaches used for FD's. By analysing the pre-breakdown time obtained for FD's and ABSD's under the same experimental conditions, it was found that the values of pre-breakdown time for ABSD's were reduced by at least 60 %, as compared with FD's. This confirms the effect of the injected air-bubbles in reducing the pre-breakdown time and in reducing the pre-breakdown conductive losses. The relationships between T_{cavity}, $P_{cav\text{-}max}$ and V_{br} for ABSD's were established and found to be similar to those for FD's. Both T_{cavity} and $P_{cav\text{-}max}$ increase with increasing V_{br}. Due to the longer gap achieved in ABSD's, the saturation in T_{cavity} and $P_{cav\text{-}max}$, for FD's observed in short gaps 5 mm and 7 mm with $V_{br} > 20$ kV, did not appear in the case of ABSD's. Scaling relations, $T_{cavity} \propto V_{br}^{2/3}$ and $P_{cav\text{-}max} \propto V_{br}^{2\beta/3}$, were used to describe the dependency of T_{cavity} and $P_{cav\text{-}max}$ on V_{br}.

The general relationships between T_{cavity}, $P_{cav\text{-}max}$ and R_{pl} have been established for ABSD's. The obtained dependencies of T_{cavity}, $P_{cav\text{-}max}$ on R_{pl} for ABSD's show a decreasing trend with an increase in R_{pl} as R_{pl} defines the portion of energy delivered into the plasma channel. It is critical to control the value range of ratio $R_{pl}/R_{circuit}$ and keep it in the range from 1 to 3 in optimising $P_{cav\text{-}max}$. It was shown that the relationships between T_{cavity}, $P_{cav\text{-}max}$ and E_{pl} for ABSD's have similar tendencies as observed in the case of FD's.

The wire-guided discharges were initiated with a thin metallic wire placed between inter-electrode gap to facilitate the establishment of the plasma channel. The maximum gap used for WGD's has been increased to 75 mm. As a result, it was found that the maximum value of $P_{cav\text{-}max}$ obtained for WGD's was increased by ~ 153 %, as compared with that obtained for FD's, for the same energisation level.

The relationship between E_{pl} and R_{pl} has been obtained for WGD's. It was shown that E_{pl} is inversely proportional to R_{pl} for all gaps. Scaling relations, which link the electrical parameters (R_{pl} and E_{pl}) of the plasma channel with the acoustic and hydrodynamic parameters (T_{cavity} and $P_{cav\text{-}max}$) have been established for WGD's. It was shown that T_{cavity} and $P_{cav\text{-}max}$ decrease monotonously with R_{pl}.

A novel analytical model has been developed to investigate the dynamic behaviour of the post-breakdown hydrodynamic and acoustic parameters for all types of

underwater discharges studied in this work. The analysis of the acoustic efficiency and its relationships with other discharge properties was conducted. This study provides an important information for optimisation of the acoustic output from the underwater discharge system.

An energy balance equation has been used to describe the energy partition in the plasma channel. The Gilmore model was used to obtain the evolution of the cavity radius. An acoustic approximation was used for modelling of propagation of acoustic impulses. It was shown that this model was not particularly sensitive to initial values of *r(0)* and $r(\dot{t})$. Based on the simulated results, it was found that the internal pressure in the cavity demonstrates a rapid rise in response to the energy released in the plasma channel after breakdown. At this stage, a primary acoustic impulse is generated with a magnitude of a few MPa. The pressure inside the cavity decreases as the radius of the cavity increases and after reaching its maximum value, the cavity collapses with emitting a secondary acoustic impulse.

Comparison between the experimental and computed periods of cavity's oscillation, T_{cavity}, demonstrated that the computed values of T_{cavity} are in reasonable agreement with the experimental data. Thus, it was confirmed that this model can be used in analysis of the underwater spark discharge processes.

The acoustic efficiency was calculated as the ratio between the acoustic energy and the energy delivered into the plasma channel. It was found that η_{ac} increases with an increase in R_{pl}. The dependency of η_{ac} on C and l was also established and it was found that longer l and smaller C help to improve η_{ac}. Therefore, in order to achieve a high acoustic efficiency, it is recommended that discharges should be implemented in longer gaps and with lower capacitances.

Based on all experimental results obtained for three types of discharges, it can be concluded that the WGD's can be considered as the most effective underwater spark discharges for generation of acoustic pressure waves. However, the limitation of the WGD's is the low repetition rate, which may narrow their use in practical applications. As compared with WGD's, the FD's are less effective in generating acoustic impulses. However, their simple electrode topology and flexible set-up with high breakdown operation frequency have made them the most common discharge type in underwater plasma-acoustic applications. The ABSD's can be considered as a trade-off between

FD's and WGD's as they provide higher acoustic magnitude, as compared with FD's, and have benefits of a high repetition rate. Therefore, depending on operational and acoustic requirements in specific practical applications, any of these three types of underwater spark discharges will have their own advantages and disadvantages.

The experimentally obtained results and their analytical analysis, together with the developed analytical model, provide effective approaches to predict and to evaluate the acoustic output from the underwater spark discharges. The scaling relationships between different electrical and hydrodynamic properties of the plasma channel have been established. The results obtained in this work will provide new opportunities in further development of practical applications of underwater plasma-acoustic sources and in optimisation of the acoustic output from underwater spark discharges.

8.2 Future work

The investigation on the underwater spark discharges as acoustic sources was conducted for three different types of discharges. The main focus of this work was on the generated acoustic impulses and analysis of the dynamics of cavity oscillation.

As presented in Chapter 3, a dedicated electrode topology has been designed for FD's, ABSD's and WGD's. Based on the achieved results, a few potential future tasks have been identified and presented in this section.

A future work could be focused on using different metallic wires, for example Al, as the wire material can change the dynamics of the pre-breakdown process.

For better understanding of physical properties of the plasma channel, plasma emission spectroscopy can be used in future work, which would allow measurements of the temperature and spectrum of the plasma, electrical conductivity of the plasma and chemical species developed in the plasma channel.

Together with the plasma optical diagnostic system, it could be beneficial to use a high-speed camera (with ns shutter time) to record the discharge process and the post-breakdown development of the cavity.

From the acoustic point of view, the use of larger test water tanks would allow further investigation into acoustic signal propagation especially over longer distances, which can be useful for different practical applications. Development of discharges and generation of acoustic impulses in water with different salinities, for example sea water, also would be of interest for practical applications of underwater plasma-acoustic sources.

Further development of the analytical model would include taking into account different processes such as thermal radiation, mass transfer between gas mixture in the cavity and water, and light emission. This would allow achievement of a higher accuracy of the proposed model.

9 References

[1] R. Tachikawa, A. Tsukamoto, K. Nakagawa, T. Arafune, H. Liao, E. Kobayashi, T. Ushada and I. Sakuma, "Development of an expansion wave generator for shock wave therapy," *Adv. Biomed. Eng*., vol. 1, pp. 68-73, 2012.

[2] B. R. Locke, M. Sato, P. Sunka, M. R. Hoffmann and J. S. Chang, "Electrohydraulic discharge and nonthermal plasma for water treatment," *Ind. Eng. Chem. Res.*, vol. 45, no. 3, pp 882–905, 2006.

[3] J. Eguchi, S. H. R. Hosseini, Y. Miyamoto, D. K. Kang, D. Oshita, K. Mawatari and H. Akiyama, "Effects of underwater shock waves generated by pulse electric discharge on embryonic development of medaka," in *19th IEEE PPC.*, San Francisco, CA, USA, June 16 – 21, 2013, pp. 1-4.

[4] G. Bonizzoni and E. Vassallo, "Plasma physics and technology; industrial applications," *Vacuum*, vol. 64, pp. 327-336, Jan. 2002.

[5] I. B. Napotnik, M. Rebersek, P. T. Vernier, B. Mali and D. Miklavcic, "Effects of high voltage nanosecond electric pulses on eukaryotic cells (in vitro): A systematic review," *Bioelectrochemistry*, vol. 110, pp 1-12, Aug. 2016.

[6] J. O. Pouzo and M. M. Milanese, "Applications of the dense plasma focus to nuclear fusion and plasma astrophysics," *IEEE T. Plasma Sci.*, vol. 31, no. 6, pp. 1237-1242, Dec. 2003.

[7] J. Thornblom and K. J. Roihjert, "Utilizing plasma technology for chemical reactions in controlled atmosphere," *Pure & Appl. Chem.*, vol. 64, no. 5, pp. 671-676, 1992.

[8] K. Okazaki, S. Hirai, T. Nozaki, K. Ogawa and K. Hijikata, "Plasma chemical reactions at atmospheric pressure for high efficiency use of hydrocarbon fuels," *Energy*, vol. 22, no. 2/3, pp. 369-374, 1997.

[9] L. Barillas, “Design of a prototype of water purification by plasma technology as the foundation for an industrial wastewater plant,” *J. Phys.: Conf. Ser.*, vol. 591, 012057, pp. 1-12, 2015.

[10] J. E. Foster, “Plasma-based water purification: challenges and prospects for the future,” *Phys. Plasmas*, vol. 24, 055501, pp. 1-16, Mar. 2017.

[11] G. R. Stratton, C. L. Bellona, F. Dai, T. M. Holsen and S. M. Thagard, “Plasma-based water treatment: Conception and application of a new general principle for reactor design,” *Chem. Eng. J.*, vol. 273, pp. 543-550, Aug. 2015.

[12] G. R. Stratton, C. L. Bellona, F. Dai, T. M. Holsen and S. M. Thagard, “Plasma-based water treatment: efficient transformation of perfluoroalkyl substances in prepared solutions and contaminated groundwater,” *Environ. Sci. Technol.*, vol. 51, no. 3, pp. 1643-1648, 2017.

[13] J. Kitayama and M. Kuzumoto, “Theoretical and experimental study on ozone generation characteristics of an oxygen-fed ozone generator in silent discharge,” *J. Phys. D: Appl. Phys.*, vol. 30, no. 17, pp. 2453-2461, 1997.

[14] M. Nur, M. Restiwijaya, Z. Muchlisin, I. A. Susan, F. Arianto and S. A. Widyanto, “Power consumption analysis DBD plasma ozone generator,” *J. Phys.: Conf. Ser.*, vol. 776, 012101, no. 1, pp. 1-6, 2016.

[15] U. Andres, I. Timoshkin, J. Jirestig and H. Stallknecht, “Liberation of valuable inclusions in ores and slags by electrical pulses,” *Powder Technol.*, vol. 114, pp. 40-50, Jan. 2001.

[16] H. Bluhm, W. Frey, H. Giese, P. Hoppe, C. Schultheiss and R. Strassner, “Application of pulsed HV discharges to material fragmentation and recycling,” *IEEE T. Dielect. El. In.*, vol. 7, no. 5, pp. 625-636, Oct. 2000.

[17] T. Parker, F. Shi, C. Evans and M. Powell, “The effects of electrical comminution on the mineral liberation and surface chemistry of a porphyry copper ore,” *Miner. Eng.*, vol. 82, pp. 101-106, Oct. 2015.

[18] P. T. Mativenga, N. A. Shuaib, J. Howarth, F. Pestalozzi and J. Woidasky, “High voltage fragmentation and mechanical recycling of glass fibre thermoset composite,” *CIRP Ann.*, vol. 65, pp. 45-48, 2016.

[19] N. S. Kuznetsova, V. V. Lopatin and A. S. Yudin, “Effect of electro-discharge circuit parameters on the destructive action of plasma channel in solid media,” *J. Phys.: Conf. Ser.*, vol. 552, 012029, pp. 1-7, 2014.

[20] I. V. Lisitsyn, T. Muraki and H. Akiyama, “Mechanism of shock waves generation and material destruction in a wire induced surface flashover,” *Physica B.*, vol. 239, pp. 6-8, Aug. 1997.

[21] V. N. Safronov, “Electric pulse technology for aggregate and aggregate-based concrete production,” (translated by M.V Vorob’eva), *Vestnik TSUAB*, pp. 89-98, 2013.

[22] I. V. Timoshkin, J. W. Mackersie and S. J. MacGregor, “Plasma channel miniature hole drilling technology,” *IEEE T. Plasma Sci.*, vol. 32, no. 5, pp. 2055-2061, Oct. 2004.

[23] H. S. Kim, K. Wright, D. J. Cho and Y. I. Cho, “Self-cleaning filtration with spark discharge in produced water,” *Int. J. Heat Mass Tran.*, vol. 88, pp. 527-537, Sept. 2015.

[24] K. J. Chung, S. Lee, Y. S. Hwang and C. Y. Kim, “Modeling of pulsed spark discharge in water and its application to well cleaning,” *Curr. Appl. Phys.*, vol. 15, pp. 977-986, Sept. 2015.

[25] Y. M. Zhang, A. C. Qiu, H. B. Zhou, Q. Y. Liu, J. P. Tang and M. J. Liu, "Research progress in electrical explosion shockwave technology for developing fossil energy," *Chin. Phys. Lett.*, vol. 42, 01009, pp. 1009-1017, 2016.

[26] USGS, "WHSC seismic profiling systems," [Online]. Available: https://woodshole.er.usgs.gov/operations/sfmapping/sparker.htm.

[27] C. Chaussy and E. Schmiedt, "Extracorporeal shock wave lithotripsy (ESWL) for kidney stones. An alternative to surgery?," *Urol. Radiol.*, vol. 6, pp. 80-87, 1984.

[28] USGS, "WHSC seismic profiling systems," [Online]. Available: https://woodshole.er.usgs.gov/operations/sfmapping/seismic.htm.

[29] M. Grasso, L. J. Paik, D. A. Green and B. S. Alexander, "Extracorporeal shockwave lithotripsy," 2018. [Online]. Available: https://emedicine.medscape.com/article/444554-overview#a5.

[30] M. G. Hogg, I. V. Timoshkin, M. J. Given, M. P. Wilson, S. J. Macgregor, T. Wang, R. A. Fouracre and J. M. Lehr, "Impulse breakdown of water with different conductivities," *IEEE T. Dielect. El. In.*, vol. 19, no. 5, pp. 1559-1568, Oct. 2012.

[31] I. Marinov, O. Guaitella, A. Rousseau and S. M. Starikovskaia, "Modes of underwater discharge propagation in a series of nanosecond successive pulses," *J. Phys. D: Appl. Phys.*, vol. 46, 464013, pp. 1-9, Oct. 2013.

[32] Y. Liu, Z. Y. Li, X. D. Li, S. W. Liu, G. Y. Zhou and F. C. Lin, "Intensity improvement of shock waves induced by liquid electrical discharges," *Phys. Plasmas*, vol. 24, 043510, pp. 1-10, Apr. 2017.

[33] W. J. Guman and B. G. Humphrey Jr., “Studies on an electric discharge underwater sound source,” Fairchild Hiller Corp., Farmingdale, New York, USA, Rep. AD 681862, 1968.

[34] A. Claverie, J. Deroy, M. Boustie, G. Avrillaud, A. Chuvatin, E. Mazanchenko, G. Demol, and B. Dramane, “Experimental characterization of plasma formation and shockwave propagation induced by high power pulsed underwater electrical discharge,” *Rev. Sci. Instrum.*, vol. 85, 063701, pp. 1-8, 2014.

[35] J. W. Mackersie, I. V. Timoshkin and S. J. MacGregor, “Generation of high-power ultrasound by spark discharges in water,” *IEEE T. Plasma Sci.*, vol. 33, no. 5, pp. 1715-1724, Oct. 2005.

[36] A. Grinenko, S. Efimov, A. Fedotov, and Y. E. Krasika, “Efficiency of the shock wave generation caused by underwater electrical wire explosion,” *J. Appl. Phys.*, vol. 100, 113509, pp. 1-8, Dec. 2006.

[37] A. Grinenko, V. T. Gurovich, A. Saypin, S. Efimov, Y. E. Krasik, and V. I. Oreshkin, “Strongly coupled copper plasma generated by underwater electrical wire explosion,” *Phys. Rev. E*, vol. 72, 066401, pp. 1-6, Dec. 2006.

[38] A. Grinenkoa, A. Sayapin, V. T. Gurovich, S. Efimov, J. Felsteiner and Y. E. Krasik, “Underwater electrical explosion of a Cu wire,” *J. Appl. Phys.*, vol. 97, 023303, pp. 1-6, 2005.

[39] S. M. Korobeinikov, A. V. Melekhov, V. G. Posukh, V. M. Antonov and M. E. Royak, “Experimental investigation of the behaviour of bubbles in water under the effect of strong electric fields,” *High Temp+.*, vol. 39, no. 2, pp. 163-168, Mar. 2001.

[40] S. M. Korobeinikov, A. V. Melekhov, Y. N. Sinikh and Y. G. Soloveichik, "Effect of strong electric fields on the behaviour of bubbles in water," *High Temp+.*, vol. 39, no. 3, pp. 368-372, May 2001.

[41] S. M. Korobeinikov, A. V. Melekhov and A. S. Besov, "Breakdown initiation in water with the aid of bubbles," *High Temp+.,* vol. 40, no. 5, pp. 652-659, Sept. 2002.

[42] D. Q. Posin, "The Townsend coefficients and spark discharge," *Phys. Rev.*, vol. 50, pp. 650-658, Oct. 1936.

[43] D. Xiao, "Fundamental theory of Townsend discharge," in *Gas Discharge and Gas Insulation*, Berlin, Heidelberg, Germany: Springer, 2016, Ch 3, pp. 47-88.

[44] Hgih Voltage Connection, "Paschen Curve," [Online]. Available: http://www.highvoltageconnection.com/articles/paschen-curve.html.

[45] H. Fujita, S. Kanazawa, K. Ohtani, A. Komiya, T. Kaneko and T. Sato, "Initiation process and propagation mechanism of positive streamer discharge in water," *J. Appl. Phys.*, vol. 116, 213301, pp. 1-12, Dec. 2014.

[46] V. D. Tarasov, V. A. Balakin and O. P. Pecherskii, "Electrical breakdown in water by 0.5-1.7-MV pulses 0.5-5 μsec long," *Sov. Phys. Tech. Phys.*, vol. 16, p.1379, Feb. 1972.

[47] H. M. Jones and E. E. Kunhardt, "The influence of pressure and conductivity on the pulsed breakdown in water," *IEEE T. Dielect. El. In.*, vol. 1, no. 6, pp. 1016-1025, Dec. 1994.

[48] R. P. Joshi, J. Quian and K. H. Shoenbach, "Electrical network based time dependent model of electrical breakdown in water," *J. Appl. Phys.*, vol. 92, no.

10, pp. 6245-6251, Nov. 2002.

[49] V. Ushakov, “Statistical investigations of the electrical breakdown,” in *Impulse breakdown of liquids*, Berlin, Heidelberg, Germany: Springer-Verleg, 2007, pp. 239-262.

[50] H. Bluhm, W. Frey, H. Giese, P. Hoppe, C. Schultheiss and R. Strassner, “Application of pulsed HV discharges to material fragmentation and recycling,” *IEEE T. Dielect. El. In.*, vol. 7, no. 5, pp. 625-636, Oct. 2000.

[51] P. Vaclav, K. Karel, S Jiri, S. Jaroslav, F. Oleksandr and M. Martinkova, “Apparatus for converging cylindrical shock wave In water generated by pulsed multi‐streamer discharge at one cylindrical electrode,” *AIP Conf. Proc.*, vol. 812, 435, Jan. 2006.

[52] Y. Seepersad, M. Pekker, M. N. Shneider, A. Fridman and D. Dobrynin, “Investigation of positive and negative modes of nanosecond pulsed discharge in water and electrostriction model of initiation,” *J. Phys. D: Appl. Phys.*, Vol. 46, 355201, pp. 1-12, Aug. 2013.

[53] A. Starikovskiy, Y. Yang, Y. I. Cho and A. Fridman, “Non-equilibrium plasma in liquid water: dynamics of generation and quenching,” *Plasma Sources Sci. Technol.*, vol. 20, no. 2, pp. 1-7, Apr. 2011.

[54] P. Ceccato, O. Guaitella, L. Shaper, B. Graham and A. Rousseau, “Time resolved imaging of a pulsed plasma discharge in water,” in *IEEE PPC*, Washington, DC, USA, Jun. 28 – Jul. 2, 2009, pp. 866-871.

[55] J. N. Salazar, O. Lesaint and A. Denat, “Transient current and light emission associated to the propagation of pre-breakdown phenomena in water,” in *C. Elect. Insul. Diel. P.*, Albuquerque, NM, USA, Oct. 19-22, 2003, pp. 542-545.

[56] J. N. Salazar, N. Bonifaci, A. Denat, O. Lesaint, “Characterization and spectroscopic study of positive streamers in water,” in *IEEE ICDL*, Coimbra, Portugal, Jun. 26 – Jul. 1, 2005, pp. 1-4.

[57] M. N. Shneider1 and M. Pekker, “Dielectric fluid in inhomogeneous pulsed electric field,” *Phys. Rev. E*, vol. 87, 043004, pp. 1-13, Jan. 2013.

[58] D. Dobrynin, Y. Seepersad, M. Pekker, M. Shneider, G. Friedman and A. Fridman, “Non-equilibrium nanosecond-pulsed plasma generation in the liquid phase (water, PDMS) without bubbles: fast imaging, spectroscopy and leader-type model,” *J. Phys. D: Appl. Phys.*, vol. 46, no. 10, pp. 1-9, Feb. 2013.

[59] A. Starikovskiy, “Pulsed nanosecond discharge development in liquids with various dielectric permittivity constants,” *Plasma Sources Sci. Technol.*, vol. 22, no. 1, pp. 1-5, Jan. 2013.

[60] B. H. Lee, D. S. Kim and J. H. Choi, “Underwater discharge phenomena in inhomogeneous electric fields caused by impulse voltages,” *J. Electrical Eng. Technol.*, vol. 5, no. 2, pp. 329-336, Jun. 2010.

[61] R. Kumagai, S. Kanazawa, K Ohtani, A. Komiya, T. Kaneko, T. Nakajima and T. Sato, “Propagation analysis of negative streamer channel in water,” in *23rd ISPC*, Montreal, Canada, Jul. 30 – Aug. 4, 2017, pp. 1-4.

[62] F. D. Bennett, “High-temperature cores in exploding wires,” *Phys. Fluids*, vol. 8, no. 6, pp. 1106-1108, Jun. 1965.

[63] F. D. Bennett, “Shock-producing mechanisms for exploding wires,” *Phys. Fluids*, vol. 5, pp. 891-898, Aug. 1962.

[64] Y. E. Krasik, A. Fedotov, D. Sheftman, S. Efimov, A. Sayapin, V. T. Gurovich, D. Veksler, G. Bazalitski, S. Gleizer, A. Grinenko and V. I. Oreshkin,

"Underwater electrical wire explosion," *Plasma Sources Sci. Technol.*, vol. 19, no. 3, pp. 1-8, May 2010.

[65] S. V. Lebedev and A. I. Savvatimskiĭ, "Metals during rapid heating by dense currents," *Sov. Phys. Uspekhi*, vol. 27, no. 10, pp.749-771, Oct. 1984.

[66] L. Li, D. Qian, X. Zou and X. Wang, "Underwater electrical wire explosion: Shock wave from melting being overtaken by shock wave from vaporization," *Phys. Plasmas*, vol. 25, 053502, pp. 1-5, May 2018.

[67] Y. E. Krasik, A. Grinenko, A. Sayapin, S. Efimov, A. Fedotov, V. Z. Gurovich and V. I. Oreshkin, "Underwater electrical wire explosion and its applications," *IEEE T. Plasma Sci.*, vol. 36, no. 2, pp. 423-434, Apr. 2008.

[68] D. Veksler, A. Sayapin, S. Efimov and Y. E. Krasik, "Characterization of different wire configurations in underwater electrical explosion," *IEEE T. Plasma Sci.*, vol. 37, no. 1, pp. 88-98, Jan. 2009.

[69] T. Izdebski, M. Dors and J. Mizeraczyk, "Energy emissions of spark discharges under water," *Eur. Chem. Bull.*, vol. 3, no. 8, pp. 811-814, 2014.

[70] I. V. Timoshkin, R. A. Fouracre, M. J. Given and S. J. MacGregor, "Analysis of the transient process in underwater spark discharges," in 27th *Int. Conf. Power Modulator Symposium*, Arlington, VA, USA, May 14-18, 2006, pp. 310-313.

[71] I. V. Timoshkin, S. J. MacGregor, M. J. Given and R. A. Fouracre, "High power ultrasound impulses induced by wire-guided spark discharges in water," in *16th Int. Conf. Pulsed Power*, Albuquerque, NM, USA, Jun. 17-22, 2007, pp. 33- 36.

[72] O. Higa, R. Matsubara, K. Higa, Y. Miyafuji, T. Gushi, Y. Omine, K. Naha, K.

Shimojima, H. Fukuoka, H. Maehara, S. Tanaka, T Matsui and S. Itoh, "Mechanism of the shock wave eneration and energy efficiency by underwater discharge," *Int. Jnl. of Multiphysics*, vol. 6, no. 2, pp. 89-87, Jun. 2012.

[73] Y. Liu, Z. Li, X. Li, G. Zhou, H. Li, Q. Zhang and F. Lin, "Energy transfer efficiency improvement of liquid pulsed current discharge by plasma channel length regulation method," *IEEE T. Plasma Sci.*, vol. 45, no. 12, pp. 3231-3239, Apr. 2017.

[74] S. Buogo and G. B. Cannelli, "Implosion of an underwater spark-generated bubble and acoustic energy evaluation using the Rayleigh model," *J. Acoust. Soc. Am.*, vol. 111, no. 6, pp. 2594-2600, Jun. 2002.

[75] D. A. Sutherland, "Models of ultrasound contrast agents," Ph.D. dissertation, Appl. Mathematics, Sydney Univ., Sydney, Australia, 2008.

[76] H. Medwin and C. S. Clay, "Sound propagation," in *Fundamentals of Acoustical Oceanography*, 1st ed., London, UK: Academic Press, 1997, Chap. 2, pp. 35-66.

[77] A. Ziolkowski, "Measurement of air-gun bubble oscillations," *Geophysics*, vol. 63, no. 6, pp. 2009-2024, 1998.

[78] F. R. Gilmore, "The growth or collapse of a spherical bubble in a viscous compressible liquid," California Institute Technol., Pasadena, CA, USA, Rep. No. 26-4, 1952.

[79] M. P. Wilson, L. Balmer, M. J. Given, S. J. MacGregor and I. V. Timoshkin, "An investigation of spark discharge parameters for material processing with high power ultrasound," *Miner. Eng.*, vol. 20, no. 12, pp. 1159-1169, Jun. 2007.

[80] Y. Okuda, S. H. R. Hosseini, D. Oshita, S. Iwasaki, T. Sakugawa and H.

Akiyama, “Production of uniform underwater shock waves by pulsed electric discharge,” in *IEEE PPC.*, Chicago, IL, USA, Jun. 19-23, 2011, pp. 1-5.

[81] J. A. Cook, A. M. Gleeson and R. M. Roberts, “A spark-generated bubble model with semi-empirical mass transport,” *J. Acoust. Soc. Am.*, vol. 101, no. 4, pp. 1908-1920, 1997.

[82] I. V. Timoshkin, R. A. Fouracre, M. J. Given and S. J. MacGregor, “Hydrodynamic modelling of transient cavities in fluids generated by high voltage spark discharges,” *J. Phys. D: Appl. Phys.*, vol. 39, no. 22, pp. 4808-4817, Nov. 2006.

[83] G. Massala and O. Lesaint, “A comparison of negative and positive streamers in mineral oil at large gaps,” *J. Phys. D: Appl. Phys.*, vol. 34, no. 10, pp. 1525-1532, 2001.

[84] A. Venkattraman, “Electric field enhancement due to a saw-tooth asperity in a channel and implications on microscale gas breakdown,” *J. Phys. D: Appl. Phys.*, vol. 47, no. 42, pp. 1-11, Sept. 2014.

[85] J. Qian, R. P. Joshi, K. H. Schoenbach, J. R. Woodworth and G. S. Sarkisov, “Model analysis of self- and laser-triggered electrical breakdown of liquid water for pulsed-power applications,” *IEEE T. Plasma Sci.*, vol. 34, no. 5, pp. 1680-1691, Oct. 2006.

[86] S. Xiao, Y. Sun, J. Kolb, U. Pliquett, T. Heeren, H. Akiyama and K. H. Schoenbach, “Electrically triggered water switches,” in *27th Int. Conf. Power Modulator Symposium*, Arlington, VA, USA, May 14-18, 2006, pp. 449-452.

[87] A. Hamdan and M. S. Cha, “The effects of gas bubble composition and gap distance on the characteristics of nanosecond discharges in distilled water,” *J. Phys. D: Appl. Phys.*, vol. 49, no. 24, pp. 1-13, May 2016.

[88] V. Stelmashuk, “Microsecond electrical discharge in water in plate-to-plate configuration with nitrogen bubble injection,” *IEEE T. Plasma Sci.*, vol. 44, no. 4, pp. 702-707, Feb. 2016.

[89] L. S. Nelson, S. R. Hogeland and T. C. Roth, “Aluminum-enhanced underwater electrical discharges for steam explosion triggering,” Sandia National Lab., New Mexico, USA, Jul. 1999.

[90] W. An, K. Baumung and H. Bluhm, “Underwater streamer propagation analyzed from detailed measurements of pressure release,” *J. Appl. Phys.*, vol. 101, 053302, pp. 1-10, Mar. 2007.

[91] B. S. Sommers and J. E. Foster, “Plasma formation in underwater gas bubbles,” *Plasma Sources Sci. Technol.*, vol. 23, no. 1, pp. 1-10, Feb. 2014.

[92] A. S. Tyuftyaev, M. K. Gadzhiev, M. A. Sargsyan, P. L. Akimov and N. A. Demirov, “The effect of gas bubbles on electrical breakdown in transformer oil,” *J. Phys.: Conf. Ser.*, vol. 774, no. 1, pp. 1-6, 2016.

[93] Y. Hayashi, N. Takada, H. Kanda and M. Goto, “Effect of fine bubbles on electric discharge in water,” *Plasma Sources Sci. Technol.*, vol. 24, no. 5, pp. 1-6, Sept. 2015.

[94] A. Hamdan and M. S. Cha, “Ignition modes of nanosecond discharge with bubbles in distilled water,” *J. Phys. D: Appl. Phys.*, vol. 48, 405206, pp. 1-12, Sept. 2015.

[95] N. Y. Babaeva, D. V. Tereshonok and G. V. Naidis, “Initiation of breakdown in bubbles immersed in liquids: pre-existed charges versus bubble size,” *J. Phys. D: Appl. Phys.*, vol. 48, no. 35, pp. 1-8, Aug. 2015.

[96] N. Y. Babaeva and M. J. Kushner, “Structure of positive streamers inside gas bubbles immersed in liquids,” *J. Phys. D: Appl. Phys.*, vol. 42, 132003, pp. 1-5, Jun. 2009.

[97] C. Peng, J. Wang, N. Zhou and G. Sun, “Fabrication of nanopowders by electrical explosion of a copper wire in water,” *Curr. Appl. Phys.*, vol. 16, no. 3, pp. 284-287, Mar. 2016.

[98] Y. E. Krasik, S. Efimov, D. Sheftman, A. F. Gefen, O. Antonov, D. Shafer, D. Yanuka, M. Nitishinskiy, M. Kozlov, L. Gilburd, G. Toker, S. Gleizer, E. Zvulun, V. T. Gurovich, D. Varentsov and M. Rodionova, “Underwater electrical explosion of wires and wire arrays and generation of converging shock waves,” *IEEE T. Plasma Sci.*, vol. 44, no. 4, pp. 412-431, Jan. 2016.

[99] T. Sasaki, Y. Yano, M. Nakajima, T Kawamura and K. Horioka, “Warm-dense-matter studies using pulse-powered wire discharges in water,” *Laser Part. Beams*, vol. 24, pp. 371-380, Sept. 2006.

[100] K. Kolacek, V. Prukner, J. Schmidt, O. Frolov and J. Straus, “A potential environment for lasing below 15 nm initiated by exploding wire in water,” *Laser Part. Beams*, vol. 28, no. 1, pp. 61-67. Jan. 2010.

[101] A. F. Gefen, S. Efimov, L. Gilburd, G. Bazalitski, V. T. Gurovich, and Y. E. Krasik, “Generation of a 400 GPa pressure in water using converging strong shock waves,” *Phys. Plasmas*, vol. 18, 062701, pp. 1-8, Jun. 2011.

[102] I. V. Lisitsyn, T. Muraki and H. Akiyama, “Wire induced flashover as a source of shock waves for destruction of solid materials,” *Jpn. J. Appl. Phys.*, vol. 36, no. 3A, pp. 1258-1263, 1997.

[103] V. T. Gurovich, A. Grinenko, Y. E. Krasik and J. Felsteiner, “Simplified model of underwater electrical discharge,” *Phys. Rev. E*, vol. 69, 036042, pp. 1-6, Mar. 2004.

[104] M. J. Given, I. V. Timoshkin, M. P. Wilson, S. J. MacGregor and J. M. Lehr, "Analysis of the current waveforms observed in underwater spark discharges," in *16th IEEE PPC*, Albuquerque, NM, USA, Jun. 17-22, 2007, pp. 37- 40.

[105] A. E. Vlastós, "The resistance of sparks," *J. Appl. Phys.*, vol. 43, pp. 1987-1989, 1972.

[106] H. Akiyama, M. Kristiansen, H. Krompholz and B. Maas, "Current-voltage characteristics of a high-current pulsed discharge in air," *IEEE T. Plasma Sci.*, vol. 16, no. 2, pp. 312-316, Apr. 1988.

[107] T. G. Engel, A .L. Donaldson and M. Kristiansen, "The pulsed discharge arc resistance and its functional behaviour," *IEEE T. Plasma Sci.*, vol. 17, no. 2, pp. 323-329, Apr. 1989.

[108] S. P. Bugaev, N. N. Koval, N. S. Sochugov and A. N. Zakharov, "Investigation of a high-current pulsed magnetron discharge initiated in the low-pressure diffuse arc plasma," in *Proc. ISDEIV*, Berkeley, CA, USA, Jul. 21-26, 1996, pp. 1074-1076.

[109] M. J. Kushner, W. D. Kimura and S. R. Byron, "Arc resistance of laser triggered spark gaps," *J. Appl. Phys.*, vol. 58, pp. 1744-1751, 1985.

[110] R. Montanomontano, M. Becerra, V. Cooray, M. Rahman and P. Liyanage, "Resistance of spark channels," *IEEE T. Plasma Sci.*, vol. 34, no. 5, pp. 1610-1619, Oct. 2006.

[111] S. I. Barannik, S. B. Vasserman and A. N. Lukin, "Resistance and inductance of a gas arc," *Sov. Phys. Tech. Phys.*, vol. 19, pp. 1449-1453, May 1975.

[112] J. V. Demenik, "Resistance of a xenon plasma in a large flash lamp," *Sov. Phys.*

Tech. Phys., vol. 13, pp. 829-832, 1968.

[113] R. Rompe and W. Weizel, "Uber das toeplersche funkengesetz," *Z. Physik*, vol. 122, pp. 636–639, 1944.

[114] M. Toepler, "Zur kenntnis der gesetze der gleitfunkenbildung," *Ann. Phys.* D, vol. 326, no. 12, pp. 193-222, 1906.

[115] J. Fuhr, and W. F. Schmidt, "Spark breakdown of liquid hydrocarbons. II. temporal development of the electric spark resistance in n-pentane, n-hexane, 2,2 dimethylbutane, and n-decane," *J. Appl. Phys.*, vol. 59, no. 11, pp. 3702-3708, 1986.

[116] Scottish Water, 'Water Register,' [Online]. Avaliable: http://www.scottishwater.co.uk/~/media/water%20quality/Data/707/201803/Water%20201704%20Milngavie%20C3%20Last%2012%20Months.pdf.

[117] D. Yan, D. Bian, J. Zhao, Z. Yin, S. Jia and J. Feng, "Efficiency analysis of bubble pulsation formed by high-voltage discharge in nonfree field water," *Adv. Mech. Eng.*, vol. 8, no. 8, pp. 1-11, Aug. 2016.

[118] S. Buogo, J. Plocek and K. Vokurka, "Efficiency of energy conversion in underwater spark discharges and associated bubble oscillations: experimental results," *Acta Acust. united Ac.*, vol. 95, no. 1, pp. 46-59, Jan. 2009.

[119] C. E. Brennen, "Bubble growth and collapse," in *Fundamentals of Multiphase Flows*, Pasadena, California, USA: Cambridge University Pre., 2005, Ch. 4, pp. 100-126.

[120] E. A. Neppiras, "Acoustic cavitation," North-Holland Publishing Co., Amsterdam, Holland, Phys. Reports (Review of Physics Letters) 61, no. 3, pp. 159-251, 1980.

[121] C. E. Brennen, “Spherical bubble dynamics,” in *Cavitation and bubble dynamics*, New York, USA: Oxford University Pre., 1995, Chap. 2, pp. 47-75.

[122] J. P. Franc, “The Rayleigh-Plesset equation: a simple and powerful tool to understand various aspects of cavitation,” in *Fluid Dynamics of Cavitation and Cavitating Turbopumps*, Vienna: Springer, 2007, pp. 1-41.

[123] P. Sunka, V. Babicky, M. Clupek, M. Fuciman, P. Lukes, M. Simek, J. Benes, B. Locke and Z. Majcherova, “Potential applications of pulse electrical discharges in water,” *Acta Phys. Slovaca*, vol. 54, no. 2, pp. 135-145, Jan, 2003.

[124] H. Tsuchiya, T. Inoue, Y. Mori and N. Taniguchi, “Generation and propagation of pressure wave by spark discharge in liquid,” *CIRP Ann.*, vol. 31, no. 1, pp. 107-110, 1982.

[125] D. Yan, D. Bian, J. Zhao and S. Niu, “Study of the electrical characteristics, shock-wave pressure characteristics, and attenuation law based on pulse discharge in water,” *Shock Vib.*, vol. 2016, pp. 1-11, May 2016.

[126] S. G. Lee, “Efficient generation of strong shock waves in underwater pulsed spark discharge,” Ph. D Thesis, Energy System Eng. Dept., Seoul National Univ., South Korea, 2015.

[127] D. L. Jones, G. G. Goyer and M. N. Plooster, “Shock wave from a lightning discharge,” *J. Geophys. Res.*, vol. 73, no. 10, pp. 3121-3127, May 1968.

[128] N. W. Page and P. I. Mckelvie, “Shock waves generated by spark discharge,” in *6th Australasian Hydraulics and Fluid Mech. Conf.*, Adelaide, Australia, Dec 5-9, 1966, pp. 221-224.

[129] J. R. McGrath, “Scaling underwater exploding wires,” *J. Appl. Physs*, vol. 37,

no. 12, pp. 4439-4443, Nov. 1966.

[130] D. C. Bian, D. Yan, J. C. Zhao, and S. Q. Niu, “Experimental study of pulsed discharge underwater shock-related properties in pressurized liquid water,” *Adv.Mater. Sci. Eng.*, vol. 2018, pp. 1-12, Jan. 2018.

[131] G. Touya, T. Reess, L. Pecastaing, A. Gibert and P. Domens, “Development of subsonic electrical discharges in water and measurements of the associated pressure waves,” *J. Phys. D: Appl. Phys.*, vol. 39, no. 24, pp. 5236-5244, Dec. 2006.

[132] S. G. Lee, K. J. Chung and Y. S. Hwang, “Correlation of the peak pressure generated by an underwater spark discharge with energy absorption in a spark channel,” *J. Korean Phys. Soc.*, vol. 66, no. 12, pp. 1845-1851, Jun. 2015.

[133] J. P. VanDevender, “The resistive phase of a high voltage water spark,” *J. Appl. Phys.*, vol. 49, no. 5, pp. 2616-2620, May 1978.

[134] J. M. Lehr, J. P. Corley, J. E. Elizondo, P. Corcoran, D. L. Johnson, J. M. Maenchen, M. Mazarakis, D. H. McDaniel, I. D. Smith, M. Kincy, D. L. Kittennan, P. Wakefield and K. Struve, “Multi-megavolt switching in water: considerations for the Z-R machine,” in *C. Elect. Insul. Diel. P.*, Cancun, Mexico, Oct. 20-24, 2002, pp. 554-557.

[135] J. Martin, “Etude et caractérisation d’onde de pression générée par une décharge électrique dans l’eau,” Ph.D. thèse, à l'Université de Pau et des Pays de l'Adour, La faculté des sciences et techniques, Pyrénées-Atlantiques, France, 2013.

[136] R. M. Roberts, J. A. Cook, R. L. Rogers, A. M. Gleeson and T. A. Griffy, “The energy partition of underwater sparks,” *J. Acoust. Soc. Am.*, vol. 99, no. 6, pp. 3465-3475, Jun. 1996.

[137] V. A. Panov, Y. M. Kulikov, E. E. Son, A. S. Tyuftyaev, M. K. Gadzhiev and P. L. Akimov, “Electrical breakdown voltage of transformer oil with gas bubbles,” *High Temp+.*, vol. 52, no. 5, pp. 770-773, Oct. 2014.

[138] B. M. Kovalchuk, A. V. Kharlova, V. A. Vizir, V. V. Kumpyak, V. B. Zorin and V. N. Kiselev, “High-voltage impulsed generator for dynamic fragmentation of rocks,” *Rev. Sci. Instrum.*, vol. 81, 103506, pp. 1-7, Oct. 2010.

[139] K. P. Wielen, R. Pascoe, A. Weh, F. Wall and G. Rollinson, “The influence of equipment settings and rock properties on high voltage breakage,” *Miner. Eng.*, vol. 46-47, pp. 100-111, Jun. 2013.

[140] R. Han, H. Zhou, J. Wu, A. Qiu, W. Ding and Y. Zhang, “Relationship between energy deposition and shock wave phenomenon in an underwater electrical wire explosion,” *Phys. Plasmas*, vol. 24, 093506, pp. 1-8, Aug. 2017.

[141] R. Han, H. Zhou, J. W. Wu, T. Clayson, H, Ren, J. Wu, Y. Zhang and A. Qiu, “Experimental verification of the vaporization's contribution to the shock waves generated by underwater electrical wire explosion under micro-second timescale pulsed discharge,” *Phys. Plasmas*, vol. 24, 063511, pp. 1-8, Jun. 2017.

[142] Copper Development Association, “Bulk properties of copper: density and resistivity,” [Online]. Available: http://copperalliance.org.uk/education-and-careers/education-resources/bulk-properties-of-copper-density-and-resistivity.

[143] P. Castera and P. Q. Elias, “Resistance models applied to the return stroke phase of negative pulsed surface discharges in air,” *IEEE T. Plasma Sci.*, vol. 42, no. 7, pp. 1922-1931, Jul. 2014.

[144] H. Akiyama, M. Kristiansen, H. Krompholz and B. Maas, “Current-voltage characteristics of a high-current pulsed discharge in air,” *IEEE T. Plasma Sci.*, vol. 16, no. 2, pp. 312-316, Apr. 1988.

[145] K. Lee, K. J. Chung, Y. S. Hwang and C. Y. Kim, “Underwater spark discharge with long transmission line for cleaning horizontal wells,” *J. Appl. Phys.*, vol. 121, 243302, pp. 1-9, Jun. 2017.

[146] A. I. Ioffe, “Theory of the initial stage of an electrical discharge in water,” *Zhurnal Prikladnoi Mekhaniki i Tekhnicheskoi Fiziki*, vol. 7, no. 6, pp. 69-72, 1966.

[147] Lord Rayleigh, “On the pressure developed in a liquid during the collapse of a spherical cavity,” *Philos. Mag.*, vol. 34, no. 200, pp. 94-98, 1917.

[148] K. Vokurka, “On Rayleigh's model of a freely oscillating bubble. I. basic relations,” *Czech. J. Phys. Sect. B*, vol. 35, no. 1, pp. 28-40, Jan. 1985.

[149] N. Schwartz, “On the collapse of a spherical cavity in water,” California Univ., California, USA, ASTIA AD 263778, Jul. 1961.

[150] L. V. Wijngaarden, “Mechanics of collapsing cavitation bubbles,” *Ultrason. Sonochem.*, vol. 29, pp. 524-527, Mar. 2016.

[151] R. A. V. Gorder, “Dynamics of the Rayleigh–Plesset equation modelling a gas-filled bubble immersed in an incompressible fluid,” *J. Fluid Mech.*, vol. 807, pp. 478-508, Nov. 2016.

[152] K. Vokurka, “Comparison of Rayleigh’s, Herring’s, and Gilmore’s models of gas bubbles,” *Acta Acust. united Ac.*, vol. 59, no. 3, pp. 214-219, Jan. 1986.

[153] K. L. de Graaf, I. Penesis and P. A. Brandner, “Comparison of the Rayleigh–

Plesset and Gilmore equations and additional aspects for the modelling of seismic airgun bubble dynamics," in *18th Australasian Fluid Mech. Conf.*, Launceston, Australia, Dec 3-7, 2012, pp. 1-4.

[154] W. Lauterborn and T. Kurz, "Physics of bubble oscillations," *Rep. Prog. Phys.*, vol. 73, 106501, pp. 1-13. Sept. 2010.

[155] S. I. Braginskii, "Theory of the development of a spark channel," *Sov. Phys. Jetp.*, vol. 34, no. 6, pp. 1068-1074, Dec. 1958.

[156] C. A. MacDonald, V. Sboros, J. Gomatama, S. D. Pye, C. M. Moran and W. N. McDicken, "A numerical investigation of the resonance of gas-filled microbubbles: resonance dependence on acoustic pressure amplitude," *Ultrasonics*, vol. 43, no. 2, pp. 113-122, Dec. 2004.

[157] A. A. Doinikov, B. Dollet and P. Marmottant, "Model for the growth and the oscillation of a cavitation bubble in a spherical liquid-filled cavity enclosed in an elastic medium," *Phys. Rev. E*, vol. 97, 013108, pp. 1-12, Jan. 2018.

[158] B. Sun, S. Kunitomo and C. Igarashi, "Characteristics of ultraviolet light and radicals formed by pulsed discharge in water," *J. Phys. D: Appl. Phys.*, vol. 39, no. 17, pp. 3814-3820, Aug. 2006.

[159] E. A. Martin, "Experimental investigation of a high‐energy density, high‐pressure arc plasma," *J. Appl. Phys.*, vol. 31, no. 2, pp. 255-267, Feb. 1960.

[160] G. L. Chahine, G. S. Frederick, C. J. Lambrecht, G. S. Harris and H. U. Mair, "Spark-generated bubbles as laboratory-scale models of underwater explosions and their use for validation of simulation tools," in *SAVIAC Proc. 66th Shock and Vibrations Symposium*, Biloxi, MS, USA, Nov. 1995, pp. 265-276.

[161] K. Vokurka, “A model of spark and laser generated bubbles,” *Czech. J. Phys. B*, vol. 38, no. 1, pp. 27-34, Jan. 1988.

[162] E. Gidalevich, R. L. Boxman and S. Goldsmith, “Hydrodynamic effects in liquids subjected to pulsed low current arc discharges,” *J. Phys. D: Appl. Phys.*, vol. 37, no. 10, pp. 1509-1514, Apr. 2004.

[163] G. A. Shneerson, “Estimation of the pressure in a ‘slow’ spark discharge in a cylindrical water-filled chamber,” *Tech. Phys.*, vol. 48, no. 3, pp. 374-375, Mar. 2003.

[164] K. Vokurka, “Free oscillations of a cavitation bubble,” *J. Sound Vib.*, vol. 135, no. 3, pp. 399-410, Dec. 1989.

[165] G. A. Barbashova and V. V. Shomko, “The discharge mode influence on the hydrodynamic processes of underwater electric explosions,” *Surf. Eng. Appl. Elect.*, vol. 43, no. 6, pp. 465-469, Dec. 2007.

[166] D. Oshita, S. H. R. Hosseini, Y. Miyamoto, K. Mawatari and H. Akiyama, “Study of underwater shock waves and cavitation bubbles generated by pulsed electric discharges,” *IEEE T. Dielect. El. In.*, vol. 20, no. 4, pp. 1273-1278, Aug. 2013.

[167] K. A. Naugol’nykh and N. A. Roi, “Spark discharges in water, a hydrodynamic description,” Foreign Tech. Div., Wright-Patterson Air Force Base, Ohio, USA, Rep. AD/A-006 728, Dec. 1974.

[168] T. Leighton, “The sound field,” in *The acoustic bubble*, 1st ed., London, UK: Academic Press Inc., 1994, Ch. 1, pp. 16-19.

[169] *Handbook of Chemistry & Physics,* 53rd ed., CRC Press, Boca Raton, FL, USA, 1971. [Online]. Available:

http://jupiter.plymouth.edu/~jsduncan/courses/2012_Spring/Techniques/Exams/DensityOfWater-vs-Temp.pdf

[170] M. Greenspan and C. E. Tschiegg, “Speed of sound in water by a direct method,” *J. Res. Nat. Bur. Stand.*, vol. 59, no. 4, pp. 249-254, Oct. 1957.

[171] I. P. Hoffer, “Shock waves generated by corona-like discharges in water,” Ph.D. dissertation, Physics Dept., Czech Technical Univ., Prague, Czech, 2014.

[172] G. B. Cannelli, E. D'Ottavi and A. Prosperetti, “Bubble activity induced by high-power marine sources,” in *Conf. Proc. Eng. Ocean Environ.*, Washington, DC, USA, Sept. 24-26, 1990, pp. 533-537.

Appendix 1 Published journal paper on wire-guided discharges

Y. Sun, I. V. Timoshkin, M. J. Given, M. P. Wilson, T. Wang, S. J. MacGregor and N. Bonifaci, "Electrical and acoustic parameters of wire-Guided discharges in water: experimental determination and phenomenological scaling," *IEEE T. Plasma Sci*, vol. 45, no. 10, pp. 2648-2655, Jun. 2017.

Impulsive Discharges in Water: Acoustic and Hydrodynamic Parameters

Ying Sun, Igor Timoshkin, *Senior Member, IEEE*, Martin Given, *Member, IEEE*, Mark P. Wilson, *Member, IEEE*, Tao Wang, Scott MacGregor, *Senior Member, IEEE*, Nelly Bonifaci

***Abstract*—Underwater spark discharges are used in multiple practical applications including plasma closing switches, water treatment, plasma channel drilling and mineral processing, waste recycling, treatment of metals, and medical lithotripsy. Spark discharges in water have been studied for several decades, however, despite significant research efforts and progress in this area, further investigation into the efficiency of plasma-acoustic sources and their optimisation is required in order to expand their practical application. This paper is aimed at investigation of the electrical and hydrodynamic parameters of underwater plasma-generated cavities, including plasma resistance, energy delivered into the plasma cavity, period of cavity oscillations and characteristics of pressure impulses. Different energy levels, breakdown voltages and gap distances were used in the present study to allow systematic analysis of these electrical and hydrodynamic parameters. Empirical scaling relations which link the maximum acoustic pressure and the period of cavity oscillations with the energisation parameters and the resistance of plasma have been obtained. These empirical functions can be used for optimisation of the plasma-acoustic sources and for tailoring their parameters for specific practical applications.**

***Index Terms*—Underwater spark discharges, plasma resistance, hydrodynamic parameters of period of cavity, acoustic impulses**

I. Introduction

In recent years, significant research efforts have been focused on investigation of high-voltage spark discharges in water. Such discharges have found practical application in different technological areas, including water-filled plasma closing switches used in high-voltage, pulsed-power systems [1], medical lithotripters [2], minerals engineering [3], recycling of solid materials [4, 5, 6], in water cleaning and remediation operations, and water-well cleaning operations [7]. An important area of potential practical applications of underwater spark discharges is generation of wide-band ultrasound impulses [8, 9]. Underwater, high-voltage spark discharges have advantages over traditional methods of generation of pressure impulses, as they provide better controllability and higher reproducibility. The spark-discharge method is also environmentally friendly, as no chemical explosives are used in the plasma-acoustic process. In order to optimise the process of generating acoustic impulses via spark plasma discharges in water, and to tailor their parameters to satisfy specific practical applications, it is important to investigate the characteristics of the acoustic impulses produced under various energisation conditions.

By applying high-voltage impulses with a suitable magnitude, duration and rise-time to a pair of water-immersed electrodes, at least one of which is a point electrode, a highly non-uniform electrical field facilitates electrical breakdown. The breakdown is initiated by the formation of gaseous, pre-breakdown bubble(s)/cavity(ies), generated by a combination of different processes, including Joule heating of the water [10], electron emission, and electro-mechanical rupture of water in the vicinity of the high-potential electrode [11]. The electric field inside this cavity becomes higher than the field in the surrounding water, due to the low permittivity of the gas within the cavity. Once the critical threshold field is exceeded, ionization processes are triggered inside the cavity, resulting in the development of the initial discharge, primarily across the gas/water interface [12]. Plasma streamers then continue to form, progressing through the bulk of the water towards the opposite electrode. The pre-breakdown processes in water stressed with short-duration, high-voltage impulses, including the formation of pre-breakdown gas bubbles and the development of streamers, have been studied in [13 - 17] and other works.

When one of the plasma streamers bridges the inter-electrode gap, the conductive plasma channel closes the circuit, leading to a rapid deposition of energy into the plasma channel (post-breakdown stage). Initially, the plasma resistance is high, due to the relatively-low temperature of the plasma in the channel and its small initial diameter. However, with the establishment of the conductive plasma path and injection of energy into the conductive channel, the plasma inside this channel becomes thermalised and the channel becomes filled with a hot, pressurised, and highly-conductive ionized gas. As the temperature inside the channel rises, the plasma resistance drops rapidly to its minimum value, which is usually in the range between hundreds of mΩ and a few Ω [18]. The post-breakdown cavity rapidly expands into the surrounding water, generating a primary acoustic pressure impulse. The velocity of this pressure impulse rapidly becomes equal to the speed of sound in water. The cavity continues to expand until it

This manuscript was submitted on 21 December 2015, in final form on 20 June 2016. Financial support to Dr Bonifaci was provided by The Royal Academy of Engineering, Dr Bonifaci was visiting the University of Strathclyde as the RAEng Distinguished Fellow

Y. Sun I. Timoshkin, M. Given, M.P. Wilson, T. Wang, S. MacGregor are with the High Voltage Technologies Group, Department of Electronic and Electrical Engineering, University of Straclyde, Glasgow, G1 1XW, UK (E-mail: ying.sun.2013@uni.strath.ac.uk; igor.timoshkin@strath.ac.uk; m.given@strath.ac.uk; mark.p.wilson@strath.ac.uk; tao.wang@strath.ac.uk; barbara.stewart@strath.ac.uk).

N. Bonifaci is with CNRS, G2E Laboratory, Grenoble, France. (E-mail: nelly.bonifaci@g2elab.grenoble-inp.fr)

Digital Object Identifier 10.1109/TPS.2016.2583066

reaches its maximum size (the gas pressure inside the cavity is minimum at this moment) and then collapses - due to the external hydrostatic pressure - to its minimum size, emitting a secondary acoustic pressure impulse. Several expansion/collapse cycles can potentially be observed [19]. A detailed analysis of the dynamics of the type of post-breakdown plasma/gas cavities formed by spark discharges in water is presented in [20, 21]. A hydrodynamic model of the post-breakdown cavity which takes into account the equation of state of water is described in [20]. The development of spark-driven acoustic impulses in water is discussed in [21], considering different electrode topologies: a spherical topology, which is appropriate to shorter inter-electrode gaps; and a cylindrical topology, which can be used for analysis of the acoustic emission from longer, wire-guided discharges.

However, despite a substantial number of publications in the field of plasma discharges in water, the functional behaviour of the acoustic impulses generated by plasma cavities and its link with the hydrodynamic parameters of the cavity and electrical parameters of the circuit are not fully understood, and require further experimental investigation. This paper details an experimental study of the development of plasma-generated, post-breakdown, gaseous cavities in tap water, and analysis of the acoustic impulses produced by such cavities: the dependency of the peak acoustic pressure and the period of cavity oscillations on the electrical energy available in the discharge, the energy-storage capacitance, the breakdown voltage, and the inter-electrode distance. This investigation will help in furthering the understanding of the hydrodynamic behaviour of spark-generated, underwater plasma cavities: the efficiency of production of acoustic impulses and its dependency on the parameters of the pulsed-power driving circuit. The obtained results can be used in the design and development of different plasma-acoustic systems, with parameters tailored for a wide range of practical applications.

II. Experimental Setup

The test system developed for the present study consists of a water tank with dimensions of 2 m (length) × 1 m (width) × 1 m (depth), where spark discharges were generated; a high-voltage, pulsed-power driving circuit, generating negative high-voltage impulses with peak magnitude up to 60 kV; and diagnostic devices (high-voltage, high-current and acoustic probes, and digitising oscilloscopes). The pulsed-power system is based on capacitive energy storage: a high-voltage capacitor, or capacitors (Maxwell Laboratories Ltd, USA) connected in parallel when higher energy was required. Three different capacitor combinations were used: two 80 nF capacitors in parallel; one 280 nF capacitor; and two 280 nF capacitors in parallel (these are the nominal capacitance values provided by the manufacturer). Accurate measurements of the capacitances were conducted using a VideoBridge 2160 (ES1-2160, Electro Scientific Instruments), and it was established that these three combinations provided the following values of capacitance: 155 nF, 266 nF and 533 nF. The capacitors were charged by a DC power supply (Glassman High Voltage, series EH, 60 kV) through a 0.5 MΩ charging resistor. The system was operated in a single-shot regime, high-voltage impulses being generated by closing a triggered spark-gap switch.

The high-voltage and ground electrodes were located in the middle of the water tank, ~ 500 mm below the water surface. Both electrodes were conical and made of stainless-steel, and five different inter-electrode distances were used in this study: 5 mm, 7 mm, 10 mm, 12 mm, and 15 mm.

The voltage and current waveforms were monitored using a NorthStar PVM-5 voltage probe (1000:1 division ratio, 80 MHz bandwidth) and a Samtech Ltd DE(CP)-01 resistive, low-inductance, current shunt (29.6 mΩ resistance). The voltage and current waveforms were recorded using a Tektronix TDS2024 digitising oscilloscope (200 MHz bandwidth, 2 GSamples/s sampling rate). A piezo-electric acoustic transducer, VP1093 Pinducer (Valpey Fisher), was used to obtain the acoustic impulses generated by the spark discharges. This probe was aligned with the mid-point of the inter-electrode gap, and was located 500 mm away from the spark-discharge source. The Pinducer probe was connected directly to a 1 MΩ input of a Tektronix TDS3054B digitising oscilloscope, with a bandwidth of 500 MHz and a sampling rate of 5 GSamples/s, in order to monitor the acoustic waveforms (assuming proportionality between voltage signal and acoustic pressure). A schematic diagram of the setup is shown in Fig. 1.

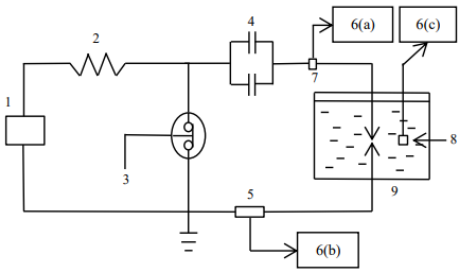

Fig. 1. Schematic diagram of the experimental setup; 1, DC power supply; 2, charging resistor; 3, spark-gap switch; 4, capacitor bank; 5, current shunt; 6(a), digitising oscilloscope for voltage monitoring; 6(b), digitising oscilloscope for current monitoring; 6(c), digitising oscilloscope for acoustic emission monitoring; 7, voltage probe; 8, acoustic probe; 9, water tank.

III. Results and Analysis

A. *Electrical and acoustic waveforms*

Spark discharges were generated in tap water (with conductivity of 0.05 μS/cm) at room temperature, using the pulsed-power circuit shown in Fig. 1. The nominal charging voltage was varied in the range from 20 kV to 35 kV in 5 kV steps. As described in Section II, three values of energy-storage capacitance were used: 155 nF, 266 nF and 533 nF. The inter-electrode gap was varied in the range from 5 mm to 15 mm. The transient voltage and current waveforms and the corresponding acoustic waveforms generated by plasma discharges were obtained using the diagnostic devices described in Section II. Fig. 2 shows typical voltage and current waveforms obtained following breakdown of a 10 mm gap.

The voltage and current waveforms obtained in this work are similar in form to the waveforms presented in [18]. The

decaying current and voltage oscillations indicate that the electrical behaviour of the pulsed-power system and the discharge channel can be described by under-damped sinusoidal oscillations, which are typical for an *R-L-C* circuit with a constant resistance. The validity of such an assumption has been verified in [18, 19]. In this model, the current is governed by:

$$I(t) = I_0 \exp(-\alpha t)\sin(\omega t) \qquad (1)$$

where

$$I_0 = V_{br} C\left(\frac{\alpha^2}{\omega} + \omega\right),\ \omega = \left(\frac{1}{LC} - \alpha^2\right)^{1/2},\ \alpha = \frac{R}{2L} \qquad (2)$$

In (1) – (2), I_0 is the current constant, which is close in value to the maximum current; V_{br} is the actual breakdown voltage as shown in Fig. 2(a); L and C are the total inductance and capacitance of the circuit, respectively; R is the total resistance; α is the damping factor; and ω is the angular velocity of the current oscillations.

According to [22, 23], the main obstacles to direct measurement of the dynamic plasma resistance are the transient behaviour of the voltage and current in the circuit, and significant reactive components in the plasma-channel impedance. However, the constant resistance approach provides good agreement between the modelled and experimentally-obtained hydrodynamic parameters as presented in [18]. This approach has been validated in the present study by assuming constant resistance and matching the experimental current waveforms with the analytical waveforms calculated using (1), as shown in Fig. 2(b). The analysis presented in this paper is therefore based on the assumption of constant resistance of the plasma channel.

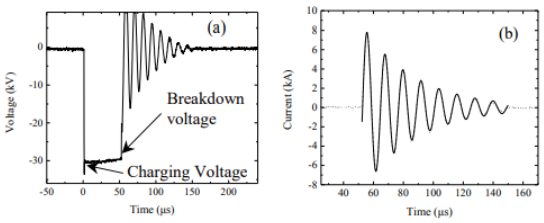

Fig. 2. (a) Voltage and (b) current waveforms for spark discharge with the following parameters: 10 mm gap, 533 nF energy-storage capacitance, 29.8 kV breakdown voltage (30 kV nominal charging voltage). The dotted line in (b) is the experimental $I(t)$, and the solid line is the analytical fitting by (1).

The circuit parameters (inductance, total resistance and constant plasma resistance) can be obtained using the experimental current waveforms and (1) - (2). The constant resistance of the spark plasma, R_{plasma}, can be obtained, using (3), as the difference between the total resistance of the circuit, R_{total}, and the resistance of the circuit without an underwater plasma channel, $R_{circuit}$ (obtained experimentally under short-circuit load conditions for similar values of peak current):

$$R_{plasma} = R_{total} - R_{circuit} \qquad (3)$$

The acoustic waveforms generated upon electrical breakdown between the electrodes were monitored using a Pinducer acoustic sensor and a separate digitizing oscilloscope. The characteristics of the acoustic signals were captured using two different oscilloscope time-base settings: one with a time-base of 200 ns/division to resolve the primary acoustic impulses generated by the expanding plasma cavity; and one with a time-base of 1000 μs/division to monitor the complete period of cavity oscillations, by registering the two acoustic impulses produced by the expansion and collapse of a cavity. Fig. 3 shows example acoustic waveforms generated upon breakdown of a 15 mm water gap. Fig. 3(a) demonstrates the primary acoustic impulse generated by the expanding plasma cavity (shorter timescale), and Fig. 3(b) demonstrates two acoustic signals generated during expansion and collapse of the plasma cavity (longer timescale). The time interval between the primary and secondary acoustic signals is the period of the cavity's oscillation.

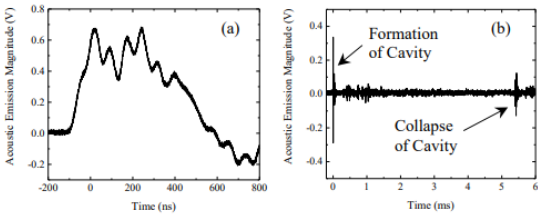

Fig. 3. Acoustic signals generated by the transient underwater plasma cavity. (a), Primary signal due to cavity expansion; (b) primary and secondary signals generated by expanding and collapsing cavity (5 mm gap, 34.4 kV breakdown voltage, 266 nF energy-storage capacitance).

The output transient voltage signal from the ultrasound transducer is proportional to the actual profile of the acoustic signal. However, the calibration coefficients for the acoustic sensor were not available from the manufacturer; therefore, the relative magnitudes of the acoustic signals in Volts were used in the present work. The magnitude of the first acoustic peak (Fig. 3(a)) was obtained and plotted as a function of different circuit parameters, representing the functional behaviour of the maximum pressure in the acoustic wave.

Fig. 3(b) shows two acoustic impulses generated by the same cavity during its expansion and collapse cycle. These signals were registered over a significantly longer time interval, ~ 4 ms, and they allow the total period of the cavity expansion-collapse cycle to be obtained. The lower-voltage peaks between the two major acoustic spikes represent reflections of the acoustic signal from the water-tank walls and the air/water surface. This longer observation timescale did not allow measurements of the magnitudes of the main peaks to be performed accurately, due to limitations in the digital sampling rate.

B. Analysis and discussion of the experimental results

1) Period of cavity oscillation

After completion of the initial, pre-breakdown stage of the discharge, the plasma-filled, post-breakdown cavity expands

with emission of the primary acoustic impulse, and then collapses under the external hydrostatic pressure. The maximum radius of the cavity and its period of oscillation depend on the energy deposited into this cavity in the transient, post-breakdown process. The cavity's dynamics (its radius as a function of time) are governed by the Rayleigh-Plesset equation [24], which can be integrated assuming that the viscosity and surface tension of the water can be neglected. Thus, an analytical link between the period of the cavity's oscillation, T_{cavity}, and its maximum radius, R_{max}, can be established for the ideal (no energy losses) case:

$$T_{cavity} = 1.83 R_{\max} \left(\rho_0 / p_\infty\right)^{1/2} \tag{4}$$

where ρ_0 is the density of water, and p_∞ is the ambient hydrostatic pressure.

The electrical energy released in the breakdown channel, W_{ch}, is converted in part into thermal plasma energy, W_t, resulting in cavity expansion:

$$W_t = (4\pi/3) R_{\max}^3 p_\infty \tag{5}$$

The combination of (4) and (5) leads to the following relation between the period of the cavity's oscillations and the thermal plasma energy:

$$T_{cavity} = 1.14 \sqrt{\rho_0}\, W_t^{1/3} p_\infty^{-5/6} \tag{6}$$

As a portion, γ, of the total electrical energy released in the plasma channel, W_{ch}, is converted into thermal energy in the plasma, W_t, the link between these energies can be expressed as:

$$\gamma W_{ch} = W_t \tag{7}$$

The electrical energy, W_{ch}, is also proportional to the energy stored in the capacitor bank of the pulsed-power system before breakdown:

$$W_{ch} \propto C V_{br}^2 / 2 \tag{8}$$

Therefore, the period of the cavity's oscillations is proportional to the breakdown voltage to the power 2/3, and to the capacitance to the power 1/3:

$$T_{cavity} \propto V_{br}^{2/3} C^{1/3} \rho_0^{1/2} p_\infty^{-5/6} \tag{9a}$$

In the case of known values of capacitance, fluid density and hydrostatic pressure, a proportionality coefficient, m, between T_{cavity} and V_{br} can be introduced:

$$T_{cavity} = m V_{br}^{2/3} \tag{9b}$$

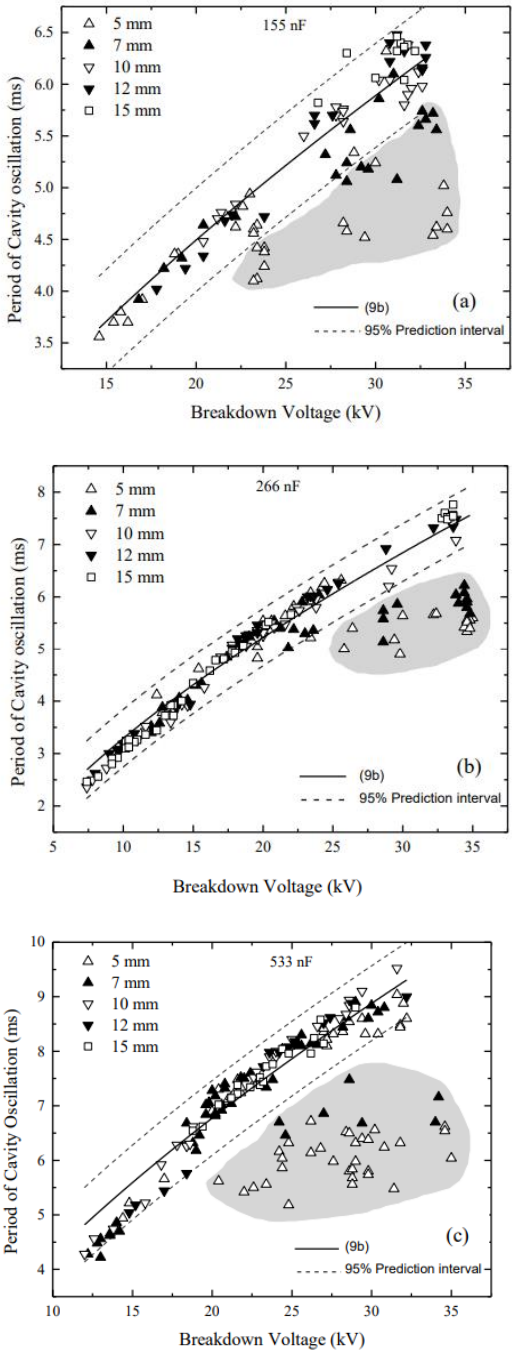

Fig. 4. Period of cavity oscillation as a function of the breakdown voltage for (a) 155 nF, (b) 266 nF and (c) 533 nF, with the fitting lines given by (9b). The dashed lines show the upper and lower boundaries of the 95% prediction

interval. The grey areas indicate those data points where $R_{plasma}<R_{circuit}$.

A systematic experimental study of the period of the cavity's oscillation as a function of the breakdown voltage was conducted using five different inter-electrode gaps: 5 mm, 7 mm, 10 mm, 12 mm, and 15 mm. Three energy-storage capacitances were used in these tests: 155 nF, 266 nF and 533 nF. The results of these measurements (the period of cavity oscillations as a function of breakdown voltage) are shown in Fig. 4, with each data point representing an individual breakdown event. It can be seen that the period of cavity oscillations increases with an increase in the breakdown voltage. However, each graph in Fig. 4 shows that, together with the main increasing trend in the period of oscillations, there are outlying clusters of data points which sit below the lower boundary lines of the 95% prediction intervals for breakdown voltages of ~ 20 kV and above. These clusters, highlighted in grey in Fig. 4, are comprised of data points obtained for shorter inter-electrode gaps (5 mm and 7 mm). Therefore, for these shorter gaps, an increase in the breakdown voltage results in a limited increase in the energy delivered into the plasma channel, despite the higher total energy available in the discharge. The plasma resistance affects the fraction of the stored energy - described by γ in (7) - which is delivered into the spark cavity; this resistance has been obtained for all discharges and will be discussed in Section III-B 3). The plasma resistance for all data points located in the outlying grey clusters in Fig. 4 is lower than the circuit resistance, $R_{plasma} < R_{circuit}$. Therefore, the deviation of T_{cavity} from the main trend for shorter gaps and higher breakdown voltages can be explained by the decrease in the efficiency of conversion of electrical energy ($CV_{br}^2/2$) into the thermal energy of the plasma, due to the change in the ratio between the plasma resistance and the remaining resistance of the pulsed-power circuit. This ratio reduces for higher voltages and shorter gaps.

Equation (9b) has been used to fit the experimental data for the period of the cavity oscillations, T_{cavity} (using data points located within the 95% prediction intervals in Fig. 4). The fitting procedure was implemented using Origin Pro 9 software. The proportionality coefficient, m, was used as a free fitting parameter, and the breakdown voltage, V_{br}, was in kV. The fitting lines obtained by (9b) are shown as solid lines in Fig. 4, while the dashed lines represent the lower and upper 95% prediction intervals. Numerical values of the fitting parameter, m, are given in TABLE I for all three values of capacitance used in these tests.

TABLE I
FITTING PARAMETER m FOR (9b)

C	155 nF	266 nF	533 nF
m	0.61	0.71	0.92
95% confidence interval	(0.61-0.62)	(0.70-0.72)	(0.91-0.93)

From (9a) and (9b), the coefficient m should be proportional to the capacitance to the power 1/3: $m \propto C^{1/3}$. A non-linear fit of the data in TABLE I led to the relationship $m \propto C^{0.34}$, which is in good agreement with the expected exponent value of 1/3.

Analysis of the graphs shown in Fig. 4 leads to the following conclusions. For breakdowns where the plasma resistance is greater than the resistance of the driving circuit, the behaviour of T_{cavity} with varying breakdown voltage follows that predicted by the scaling relationship (9b) for all tested inter-electrode gaps. The coefficient m increases with an increase in the energy-storage capacitance. For shorter gaps and higher breakdown voltages, where the plasma-channel resistance is less than the resistance of the driving circuit, the efficiency of conversion of electrical energy into thermal plasma energy is reduced, resulting in the clusters of data points which fall below the lower boundary lines of the 95% prediction intervals based on (9b).

2) Magnitude of acoustic impulses as a function of V_{br}

For practical development and application of plasma-acoustic sources, it is important to establish a relationship between the breakdown voltage of the water gap and the peak pressure in the primary acoustic impulse radiated by the expanding plasma cavity. This peak pressure is a function of the radius of the cavity, its expansion velocity and its acceleration. The hydrodynamic model described in [18] allows the peak pressure to be obtained as a function of the pulsed-power circuit parameters and plasma resistance. However, the use of phenomenological scaling relationships can be more convenient in engineering and scientific practice. For example, it was established in [25] that in the case of a chemical underwater explosion, the peak pressure in the radiated impulse is a function of the charge mass, M, and the distance between the charge and the observation point, ℓ:

$$P_{\max} \propto \left(M^{1/3}/\ell\right)^{\beta} \tag{10}$$

where an empirical constant β is found to be 1.13. As the energy provided to an explosively-driven system would be proportional to the mass of the explosive, it may be possible to adapt this phenomenological relationship to the case of a spark breakdown in water. It can be assumed that the charge mass, M, is proportional to the energy stored in the capacitor(s) of the pulsed-power system:

$$M \propto CV_{br}^2/2 \tag{11}$$

Thus, by combining (10) and (11), the peak acoustic pressure in the first acoustic impulse radiated by the plasma cavity at any known distance from the spark discharge (ℓ = constant) would be expected to be proportional to the product of the breakdown voltage to the power $2\beta/3$, and to the capacitance to the power $\beta/3$:

$$P_{\max} \propto C^{\beta/3}V_{br}^{2\beta/3} \tag{12a}$$

For a known value of capacitance, a coefficient of proportionality, k, between P_{max} and V_{br} can be introduced:

$$P_{\max} = kV_{br}^{2\beta/3} \tag{12b}$$

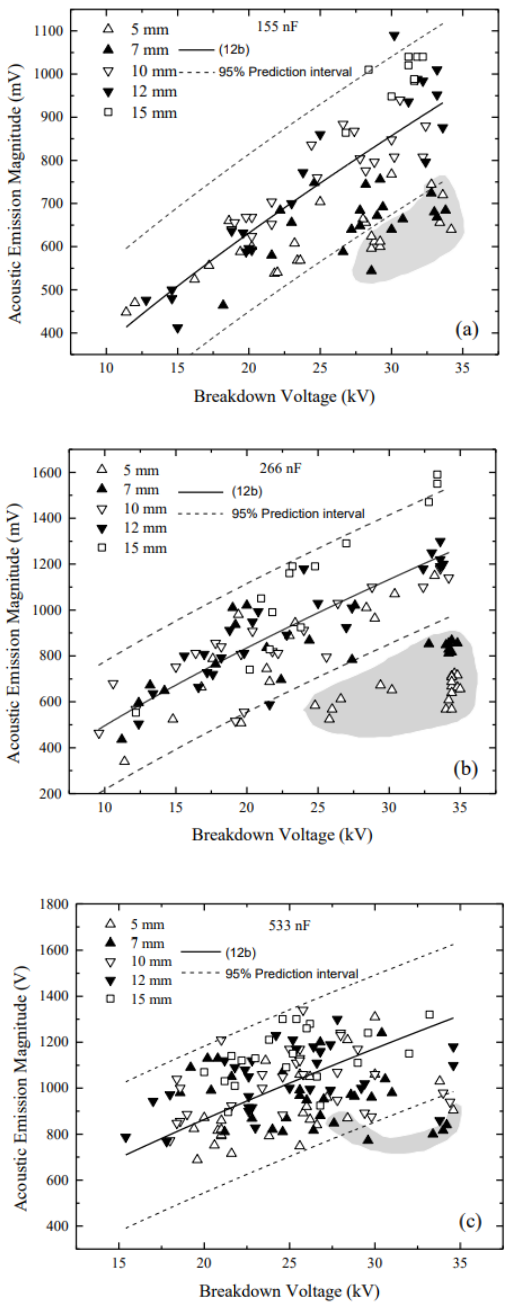

Fig. 5. Peak magnitude of the primary acoustic signal as a function of the breakdown voltage for (a) 155 nF, (b) 266 nF and (c) 533 nF, with the fitting lines given by (12b). The dashed lines show the upper and lower boundaries of the 95% prediction interval. The grey areas indicate those data points where $R_{plasma}<R_{circuit}$.

The maximum, peak pressure of the primary acoustic impulse emitted by the expanding cavity, P_{max}, has been obtained experimentally, and plotted as a function of the breakdown voltage, V_{br}, for all three capacitance values and for all five inter-electrode distances, Fig. 5. Each data point in Fig. 5 represents an individual measurement of the peak acoustic magnitude. The trends observed in Fig. 5 show that the maximum acoustic magnitude demonstrates the same functional behaviour as the period of cavity oscillations presented in Fig. 4. The peak pressure in the primary acoustic impulses increases with an increase in the breakdown voltage for all inter-electrode gaps. The solid lines in Fig. 5 represent the fitting lines obtained using (12b), with $\beta = 1.13$ for the main increasing trends in the peak pressure. The coefficient of proportionality, k, was a free parameter in this fitting procedure, which was performed using Origin Pro 9 software package. Numerical values of k (for the peak magnitude expressed in mV and the breakdown voltage expressed in kV) are given in TABLE II.

TABLE II
FITTING PARAMETERS k FOR (12b)

C	155 nF	266 nF	533 nF
k	66.18	87.44	90.45
95% confidence interval	(64.79-67.57)	(84.98-89.89)	(88.33-92.57)

As in the case of the period of cavity oscillations, there are data points for breakdown of the shorter gaps (5 mm and 7 mm) and for voltages higher than ~ 20 kV which have lower peak pressure than the points within the 95% prediction intervals. This data, denoted by the grey areas in Fig. 5, is again associated with breakdowns were the plasma resistance is lower than the resistance of the driving circuit, $R_{plasma} < R_{circuit}$, and the lower acoustic peak magnitudes can again be explained by a decrease in the proportion of the electrical energy which is converted into thermal plasma energy. It is also clear from the results shown in Fig. 5 that the peak acoustic magnitude is higher for higher values of energy-storage capacitance, at the same breakdown voltages.

The coefficient k in (12b) increases with an increase in the capacitance of the pulsed-power system. According to (12a) and (12b), $k \propto C^{0.37}$ - non-linear allometric fitting of the data in TABLE II gives a similar exponent value for C, ~ 0.3. This suggests that the scaling relation (12b) could be used for analysis of the functional behaviour of the acoustic magnitude. There is a significant spread in the peak acoustic magnitude as shown in Fig. 5, so (12b) should be used with a degree of caution, since it provides only the expected average value of the peak acoustic power. Nevertheless, this phenomenological scaling relation, which is based on (10), allows identification of the functional behaviour of P_{max}, which makes this relation a valuable tool in practical engineering and scientific applications.

3) Plasma resistance and dependency of the hydrodynamic parameters of cavity on R_{plasma}

The resistance of the plasma channel, R_{plasma}, is an important factor in the optimisation of plasma-acoustic systems. R_{plasma} defines the efficiency of conversion of the available electrical

energy into thermal plasma energy and, therefore, determines the hydrodynamic parameters of the plasma cavity and the characteristics of the acoustic impulses emitted by this cavity. Although the actual plasma resistance is a time-varying parameter, it changes very rapidly and in a time interval which is shorter than a quarter of the period of the current oscillation, the plasma resistance reaches its minimum value [26]. As discussed in Section II, the constant-resistance model has been selected in the present work for obtaining an effective resistance for the plasma cavities and the energy dissipated in the plasma channels. The resistances of the pulsed-power driving circuit, $R_{circuit}$, with three different capacitances were obtained by extracting α and ω values from the experimental current waveforms and solving (1)-(2). The plasma-generating electrodes were short-circuited in this case, and the voltage controlled so that the peak current magnitudes were similar to those observed during water breakdowns. Average values of these resistances, obtained using at least 4 current waveforms, together with the corresponding standard deviations are listed in TABLE III. The same methodology was used to obtain the total resistance of the circuit, R_{total}, including the resistance of the plasma cavities, R_{plasma}, from the waveforms measured for each breakdown event. Equation (3) was then used to calculate the effective resistance of the plasma channel for each breakdown event.

TABLE III
$R_{circuit}$ FOR DIFFERENT CIRCUIT CAPACITANCES, C

C (nF)	$R_{circuit}$ (mΩ)	Standard deviation (mΩ)
155	534	20
266	401	20
533	273	7

In Fig. 6, the period of cavity oscillations is plotted as a function of the calculated effective plasma resistance for the three values of the circuit capacitance, and for all five inter-electrode gaps. Each data point in Fig. 6 represents an individual measurement of the peak acoustic magnitude. The vertical lines in each graph show the corresponding values of the circuit resistance, $R_{circuit}$.

The effective plasma resistance values vary in a wide range, from 35 mΩ to 5.9 Ω. The plasma resistance generally increases with an increase in the inter-electrode gap length, as the length of the plasma channel also increases. Lower values of the effective plasma resistance can be attributed to higher energy levels delivered in the discharge and vice versa, lower energy levels result in lower values of the plasma resistance. Fig. 6 shows that the period of cavity oscillations initially increases with an increase in the plasma resistance, before reaching a maximum and then decreasing. This trend can be observed for all three values of capacitance in the pulsed-power circuit. The higher values of the plasma resistance have been registered in the case of 266 nF capacitance: for this capacitance, breakdown of longer gaps was achieved using a charging voltage of 30 kV, which was not possible in the case of 155 nF capacitance (where 35 kV charging voltage was required). Thus, such combination of the circuit parameters resulted in a longer "tail" in the period of cavity oscillation as a function of the plasma resistance.

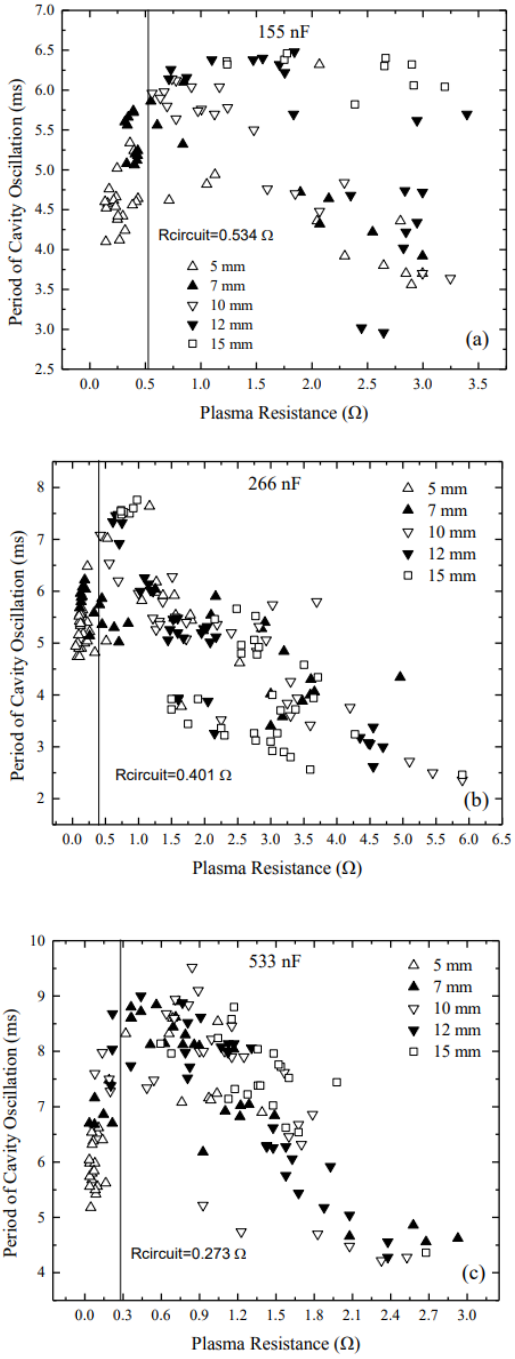

Fig. 6. Period of cavity oscillations as a function of the plasma resistance for (a) 155 nF, (b) 266 nF and (c) 533 nF. The straight vertical lines represent the calculated resistances of the pulsed-power driving circuits.

Theoretically, optimal energy transfer occurs when the resistance of the load is equal to that of the external driving circuit. However, Fig. 6 shows that the maximum oscillation periods are achieved for plasma resistances, R_{plasma}, greater than the circuit resistances, $R_{circuit}$. Calculated values of $R_{circuit}$ are shown by the vertical lines in Fig. 6, and it can be seen that the maximum values of the period of cavity oscillations are achieved at plasma resistances which are approximately twice as high as the pulsed-power circuit resistance: ~ 1 Ω for 155 nF; ~ 0.8 Ω for 266 nF; and ~ 0.6 Ω for 533 nF. The period of cavity oscillations reduces when the plasma resistance becomes lower or higher than these optimal values, this reduction being due to the smaller proportion of energy delivered into the plasma during the transient process, as compared with the total energy accumulated in the capacitor bank of the pulsed-power system. This reduction in the proportion of energy delivered into the plasma is also a possible reason for the saturation in the period of cavity oscillations for 5 mm and 7 mm gaps observed in Fig. 4 and Fig. 5.

Fig. 7 shows the relationship between the peak acoustic magnitude and the plasma resistance for all three values of the capacitance and for all five inter-electrode distances. As can be taken from Fig. 7, the functional behaviour of the peak acoustic magnitude for 155 nF and 266 nF capacitances is similar to that of the period of plasma oscillations shown in Fig. 6.

The peak acoustic magnitudes also tend to increase with an increase in the plasma resistance, and reach their maximum values at plasma resistances which are close to, but higher than, the calculated resistances of the pulsed-power circuit. However, the peak magnitudes behave more stochastically and do not show clear maxima at specific plasma resistances - only in the case of 266 nF is it reasonable to state that the optimal resistance is ~ 0.8 Ω. The functional behaviour of the peak acoustic magnitude in the case of 533 nF capacitance is not well defined: although the peak magnitude initially increases with increasing resistance and reduces at higher values of resistance, it is difficult to identify the optimal value of R_{plasma} for all tested inter-electrode gaps. For example, the majority of the peak acoustic magnitudes for the 5 mm gap lie along a horizontal line, which confirms saturation of the acoustic signal magnitude at higher energy levels.

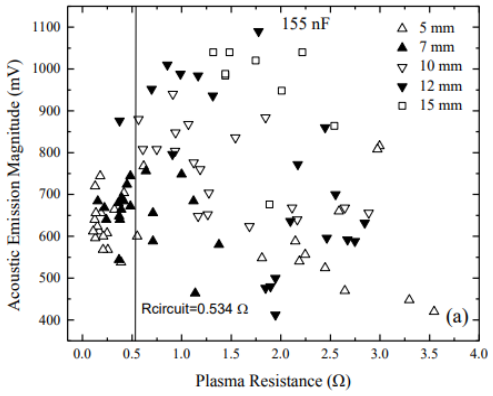

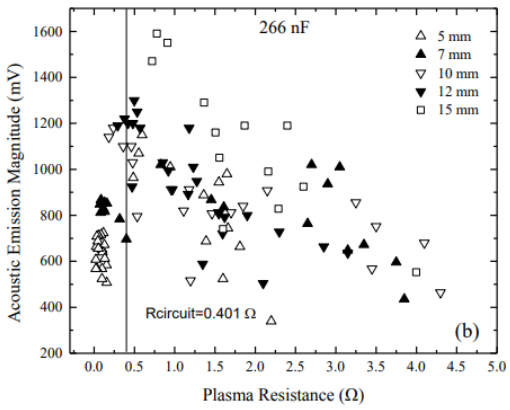

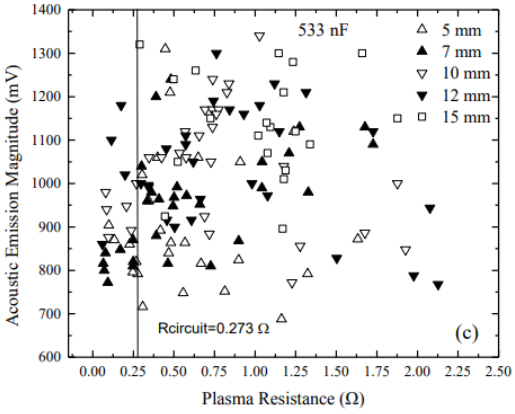

Fig. 7. Peak magnitude in the primary acoustic signal as a function of the plasma resistance for (a) 155 nF, (b) 266 nF, and (c) 533 nF. The straight lines represent the resistance of the pulsed-power circuit, $R_{circuit}$.

4) Energy dependency of hydrodynamic and acoustic parameters of the cavity

In Section III-B 2), the period of cavity oscillations and the peak acoustic pressure were obtained and presented as functions of the breakdown voltage. The phenomenological scaling relations established in Section III-B 2) are based on measurable or known circuit parameters, V_{br} and C, which make them useful for practical applications where the breakdown voltage is one of the main operating factors. However, in Section III-B 3), the plasma resistance associated with the breakdown channel was also obtained, which allows calculation of the energy delivered into the plasma channel to be made. Thus, it becomes possible to find a relationship between the energy dissipated in the plasma channel (eliminating pre-breakdown energy losses and losses in the pulsed-power circuit) and the hydrodynamic and acoustic parameters of the cavity.

In the present section, an analysis of the behaviour of the period of cavity oscillations and the peak acoustic magnitude as functions of the energy delivered into the plasma channel, W_{ch}, is presented. W_{ch} was obtained by integration of the product of the calculated constant plasma resistance, R_{plasma}, and squared values of the experimentally-measured current:

$$W_{ch} = R_{plasma} \int I^2(t) dt \qquad (13)$$

Using (6), the following scaling relationship between the period of oscillations, T_{cavity}, and the energy delivered into the plasma channel was obtained:

$$T_{cavity} \propto \gamma \rho^{1/2} p_{\infty}^{-5/6} W_{ch}^{1/3} \qquad (14a)$$

For known values of γ, ρ and p, a coefficient of proportionality, n, between T_{cavity} and W_{ch} can be introduced:

$$T_{cavity} = n W_{ch}^{1/3} \qquad (14b)$$

Fig. 8 shows the period of oscillations, T_{cavity}, as a function of W_{ch}, the energy delivered into the plasma channel, calculated using (13). Equation (14b) was used for fitting the experimental data points in Fig. 8. The proportionality coefficient, n, was a free parameter in the fitting procedure, which was conducted using Origin Pro 9 graphing software. In (14b), T_{cavity} is in ms and W_{ch} is in J. The fitting parameter n and its 95% confidence intervals are given in TABLE IV.

TABLE IV
FITTING COEFFICIENT n FOR SCALING RELATION (14b)

Capacitance	155 nF	266 nF	553 nF
n	1.69	1.68	1.59
95% confidence interval	(1.67 – 1.72)	(1.66-1.69)	(1.58-1.62)

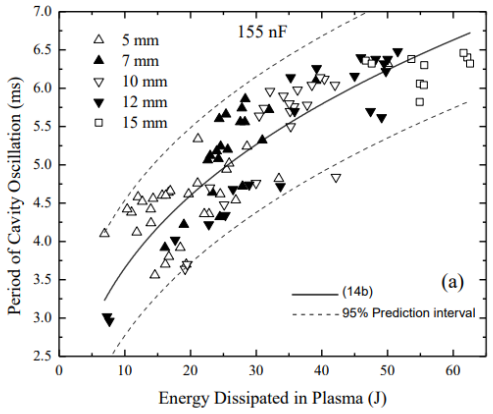

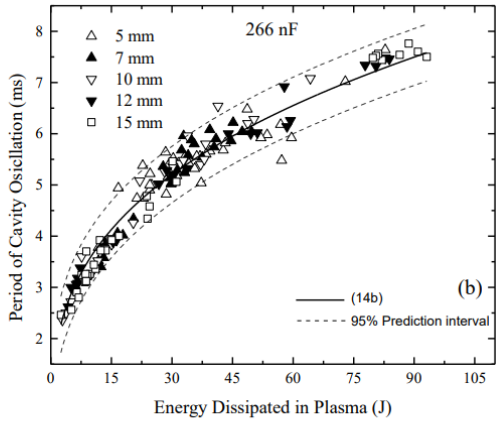

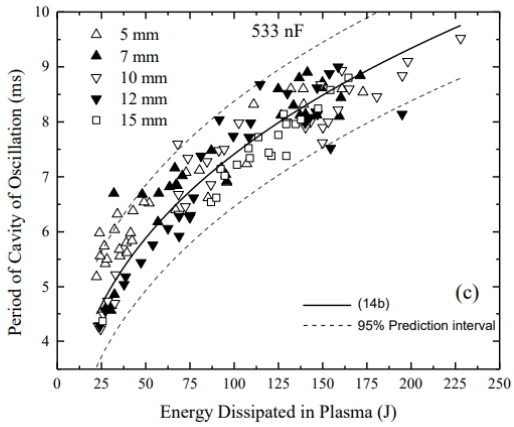

Fig. 8. Period of cavity oscillations as a function of the energy dissipated in the plasma channel for (a) 155 nF, (b) 266 nF and (c) 533 nF, with the fitting curves given by (14b). The dashed lines show the upper and lower boundaries of the 95% prediction interval.

The quality of the fits of (14b) to the experimental data shows that this phenomenological scaling relation reasonably describes the functional behaviour of the period of cavity oscillation, and can be used for calculation of the expected values of T_{cavity}.

In Section III-B 2), the functional dependency of the acoustic peak magnitude on the breakdown voltage was established. This scaling relation is helpful in practical applications in which the breakdown voltage can be readily obtained. However, if the resistance of the plasma channel is known and the discharge current waveform is available, the energy delivered into the plasma channel can also be calculated. It is important to investigate the relationship between this energy, W_{ch}, and the peak acoustic magnitude. The cumulative result of this analysis is shown in Fig. 9. This figure provides a cumulative graph, the natural logarithm of the peak acoustic magnitude as a function of the natural logarithm of the energy, W_{ch}, for all 3 capacitances and 5 inter-electrode distances.

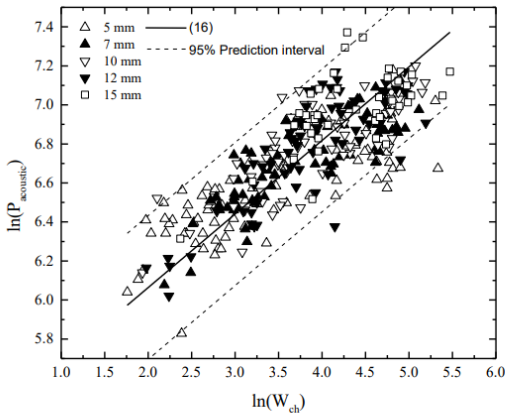

Fig. 9. Peak acoustic magnitude versus energy dissipated in the plasma channel, with the (solid) fitting line given by (16). The dashed lines show the upper and lower boundaries of the 95% prediction interval.

The phenomenological relation for the acoustic magnitude, $P_{acoustic}$, was obtained using (10) and assuming that $W_{ch} \propto M$:

$$P_{acoustic} = qW_{ch}^{\beta/3} \tag{15}$$

where q is a coefficient of proportionality between $P_{acoustic}$ (expressed in mV) and W_{ch} (expressed in J). Taking the natural logarithm of both sides of (15), one can obtain:

$$\ln(P_{acoustic}) = \ln(q) + (\beta/3)\ln(W_{ch}) \tag{16}$$

The solid line in Fig. 9 is a fitting line obtained by (16). The coefficient, $\ln(q)$, was a free parameter in this fitting procedure, and the power factor, β, was kept constant, $\beta = 1.13$. It can be seen that (15) and (16) describe well the functional behaviour of the peak acoustic magnitude, and thus this phenomenological scaling relation can be used in practical applications such as the development of underwater plasma-acoustic sources.

It is worthy of note that for lower discharge energies, [27] and [28] provide similar analytical relations between the peak acoustic magnitude and the discharge energy: $P_{max} \sim (W_{ch}^{\ b}/p)$, where p is the external/hydrostatic pressure and b is a fitting constant which is close to the value of $\beta/3$ used in this study. As in the case of (12), scaling relation (15) cannot be used for exact calculation of the peak acoustic magnitude, however this scaling relation helps to establish the functional behaviour of the peak magnitude, and can be used for prediction and evaluation of this magnitude as a function of the energy delivered into the underwater spark. Using (5) and (7), it is possible to evaluate the proportion of the electrical energy, γ, which is converted into the thermal plasma energy spent on cavity expansion. The values of γ have been obtained by plotting W_{ch} as a function of $R_{circuit}$ and using the fitting procedure in Origin Pro 9 software. It was found that γ for all tested capacitances is ~ 0.3; these values, together with their 95% prediction interval limits, are listed in TABLE V.

TABLE V
COEFFICIENT γ FOR DIFFERENT CAPACITANCES

Capacitance	γ	95% confidence interval
155 nF	0.32	(0.29 - 0.35)
266 nF	0.35	(0.34 - 0.36)
553 nF	0.25	(0.23 - 0.27)

IV. CONCLUSIONS

In this study, the functional behaviour of the hydrodynamic, electrical and acoustic parameters of underwater spark discharges has been investigated. The period of cavity oscillations, the peak magnitude of the acoustic impulses generated, and the resistance of the underwater plasma channels have been obtained as functions of the breakdown voltage, energy, circuit capacitance and inter-electrode distance.

It was shown that the period of cavity oscillations and the acoustic impulse magnitude increase with an increase in the breakdown voltage for discharges in all tested gaps. This increase can be described by the phenomenological scaling relations (9b) and (12b). However, for shorter gaps (5 mm and 7 mm) and higher breakdown voltages (~ 20 kV and above), there are clusters of data points which deviate from the main trend lines. These data are located below the lower boundary lines for the 95% prediction intervals of the main trends. It was found that the plasma resistance for all data points located in these outlying clusters is lower than the circuit resistance. Therefore, this deviation of T_{cavity} and P_{max} from the main trends can be explained by the less-efficient electrical to thermal energy conversion for these discharges.

The resistance of underwater plasma channels was obtained using the constant-resistance approach. The plasma resistance was found to vary from ~ 0.035 Ω to ~ 5.9 Ω for different energisation conditions and for different inter-electrode gaps. It was found that the period of cavity oscillations and the peak acoustic magnitude are non-linear functions of the plasma resistance; these values have their maxima when the resistance of the plasma is approximately twice higher than the resistance of the pulsed-power driving circuit.

The energy dissipated in the plasma channel was calculated using the experimental current waveforms and calculated constant plasma resistances. The period of cavity oscillations and the peak acoustic magnitude demonstrated a non-linear increase with an increase in the energy delivered into the plasma channel, and their functional behaviour is described by the phenomenological scaling relations (14b) and (15).

The results of this study will help in further understanding of the process of development of transient spark discharges in water, generation of acoustic impulses by such discharges, and in optimisation of plasma-acoustic sources, through tailoring of the pulsed-power circuit parameters to specific applications.

V. REFERENCES

[1] W. Stygar, M. Savage, T. Wagoner *et al*, "Dielectric-break down tests of water at 6 MV", *Physical Review Special Topics- Accelerators and Beams*, vol. 12, 01402, pp. 1-10, 2009.

[2] C. Chaussy, E. Schmiedt, "Extracorporeal shock wave lithotripsy (ESWL) for kidney stones, An alternative surgery?", *Urol. Radiol.*, vol. 6, no. 1, pp. 60-67, 1984.

[3] M. Wilson, L. Balmer, M. Given, S. MacGregor, I. Timoshkin, "An investigation of spark discharge parameters for material processing with high power ultrasound", *Minerals Engineering*, vol. 20, pp. 1159-1169, 2007.

[4] W. Carley-Macauly, J. Hitchen, N. Maroudas, "Energy consumption in electrohydraulic crushing", *Trans. Inst. Chem. Eng.*, vol. 44a, pp. T395-T404, 1966.

[5] K. Carley-Macauly, "Electrohydraulic crushing", *Chem. And Proc. Eng.*, vol. 49, no. 9, pp. 87-92, 1968.

[6] M. Wilson, L. Balmer, M. Given, S. MacGregor, J.Mackersie and I. Timoshkin, "Apploations of electric spark generated high power ultrasound to recover ferrous and non-ferrous metals from slag waste", *Minerals Engineering*, vol. 20, pp. 1159-1169, 2007.

[7] K. Chung S. Lee, Y. Hwang, C. Kim, "Modelling of pulsed spark discharge in water and its applications to well cleaning", *Current Applied Phys*., vol. 15, pp 977-986, 2015.

[8] E. Martin, "Experimental investigation of a high-energy, high-pressure arc plasma", *J. of Appl. Phys.,* vol. 31, pp. 255-267, 1960.

[9] S. Buogo, G. Canneli, "Implosion of an underwater spark-generated bubble and acoustic energy evaluation using the Rayleigh model", *J. Acout. Soc. Am.*, vol. 111, no. 6, pp. 2594-2600, 2002.

[10] V. Atrazhev, V. Vorob'ev, I. Timoshkin, M. Given, S. MacGregor "Mechanisms of impulse breakdown in liquid: the role of joule heating and formation of gas cavities", *IEEE Trans. on Plasma Sci.*, vol. 38, no. 10, pp. 2644-265, 2010.

[11] T. J. Lewis, "New electro-mechanical concepts for the primary mechanism of electrical breakdown in liquids", *12th Int. Conf. on Conduction and Breakdown in Dielectric Liquids*, Rome, Italy, pp. 272-278, 1996.

[12] B. S. Sommers, J.E. Foster, N.Y. Babaeva, M.J. Kushner, "Observations of electric discharge streamer propagation and capillary oscillations on the surface of air bubbles in water", *J. Appl. Phys D: Applied Physics*, vol. 44, 082001, pp. 1-6, 2011.

[13] J. Qian, P. Joshi, K. Schoenbach, G. Sarkisov, "Model analysis of self- and laser triggered electrical breakdown of liquid water for pulsed power applications", *IEEE Trans. On Plasma Science*, vol.34, no.5, pp.1680-1691, 2006.

[14] R. Joshi, S. Thagard, "Streamer-like electrical discharges in water: part I. fundamental mechanisms", *Plasma Chem. Process*., vol.33, pp.1-15, 2013.

[15] V. Y. Ushakov, V. Y. Klimkin, S. M. Korobeynikov, *Impulsive Breakdown of Liquids*. Berlin, Germany: Springer-Verlag, 2007.

[16] M. Shneider, "Dielectric fluid in inhomogeneous pulsed electric field", *Phys. Rev*., E87, 043004, 2013.

[17] Y. Seepersad, M. Pekker, M. Shneider, D. Dobrynin, "On the electrostrictive mechanism of nanosecond-pulsed breakdown in liquid phase", *J. Phys. D: Appl. Phys*., vol.46, 162001, pp. 1-6, 2013.

[18] I. Timoshkin, R. Fouracre, M. Given, S. MacGregor, "Hydarodynamic modeling of transient cavities in fluids generated by high voltage spark discharges", *J. Phys. D: Appl. Phys.*, vol. 39, pp. 4808-4817, 2006

[19] J. W. Mackersie, I. V. Timoshkin and S. J. MacGregor, "Generation of high-power ultrasound by spark discharge in water", *IEEE Trans. on Plasma Sci.*, vol. 33, no. 5, pp. 1715-1724, 2005.

[20] J. Cook, A. Gleeson, R. Roberts, "A spark-generated bubble model with semi-empirical mass transport", *J. Acoust. Soc. Am*., vol.101, no.4, 1908-1920, 1997.

[21] K. A. Naugol'nykh and N. A. Roi, "Spark discharges in water (a hydrodynamical description)", (Translation, Foreign Technology Division), Wright-Patterson AFB, Dayton, OH, USA, Tech. Rep., 1974.

[22] J. P. VanDevender, "The resistive phase of a high-voltage water spark", *J.Appl.Phys.*, vol. 49, pp 2616-2620, June, 1978.

[23] J. M. Lehr et al, "Multi-megavolt switching in water: considerations for the Z-R machine", in *Proc. Int. Conf. on Electrical Insulation and Dielectric Phenomenon,* Cancun, Mexico, pp. 554-557, 2002.

[24] T. G. Leighton, "The Acoustic Bubble", Academic Press, 1997.

[25] J. R. McGrath, "Scaling Underwater Exploding Wires", NRL Report 6266, Energy Conversion Branch, Electronic Division, US Naval Research Laboratory, Washington, 1965.

[26] K. B. Cunningham, A. J. Coleman, T. G. Leighton and P. R. White, "Characterizing in vivo acoustic cavitation during lithotripsy with time-frequency methods", *Acoust. Bull.*, vol. 26, no. 5, pp 10-16, 2001.

[27] G. Touya, T. Reess, L. Pecastaing, A. Gibert, and P. Domens, "Development of subsonic electrical discharges in water and measurements of the associated pressure waves," *J. Phys. D: Appl. Phys.*, vol. 39, no. 24, pp. 5236–5244, 2006.

[28] J. Martin, "Etude et caractérisation d'onde de pression générée par une décharge électrique dans l'eau," Ph.D. thèse, à l'Université de Pau et des Pays de l'Adour, La faculté des sciences et techniques, Pyrénées-Atlantiques, France, 2013.

Ying Sun was born in Shandong, China. He received the B.Eng degree in electronic and electrical engineering in 2012 and M.Sc degree in electrical power engineering with business in 2013 from University of Strathclyde, Scotland, United Kingdom. He is currently pursuing the Ph.D degree in high voltage technology at University of Strathclyde, Scotland, United Kingdom.

Igor V. Timoshkin (M'07-SM'14) received a degree in physics from the Moscow State University (Russia) in 1992, and the Diploma and the Ph.D. degree from the Imperial College of Science, Technology and Medicine, (London, UK) in 2001. After graduation from MSU he worked as a

Researcher at Moscow State Agro-Engineering University, and then at the Institute for High Temperatures of Russian Academy of Sciences before moving to ICSTM in 1997. He joined the Department of Electronic and Electrical Engineering of the University of Strathclyde (Glasgow, UK) in 2001 where he became a Reader in 2016. His research interests include properties of solid and liquid dielectric materials, electronics of plasma discharges in condensed media, practical applications of electro-hydraulic and high-power ultrasound pulses, bio-dielectrics and effects of electromagnetic fields on biological objects.

Martin J. Given (M'99-SM'11) is currently a Senior Lecturer in the Department of Electronic and Electrical Engineering at the University of Strathclyde. He received a degree in physics from the University of Sussex in 1981 and a PhD in electronic and electrical engineering from the University of Strathclyde in 1996. His research interests include, ageing processes and condition monitoring in solid and liquid insulation systems, high speed switching and pulse power.

Mark P. Wilson (M'10) was born in Stranraer, Scotland, in 1982. He received the B.Eng. (with honours), M.Phil., and Ph.D. degrees in electronic and electrical engineering from the University of Strathclyde, Glasgow, U.K., in 2004, 2007, and 2011, respectively. He is presently working as a Teaching Associate at the University of Strathclyde, where he continues to investigate surface flashover of solids immersed in insulating oil. Mark is a member of the IEEE Nuclear and Plasma Sciences Society, from whom he received a Graduate Scholarship Award in 2011, the IEEE Dielectrics and Electrical Insulation Society, and the IET.

Tao Wang received the B.Eng and M.Sc degrees from Northeast China Dianli University (China) in 1993 and 1996 respectively, and the Ph.D. degree from the University of Strathclyde (Glasgow, UK) in 2005. He then joined the Newland Entech as a research fellow developing high efficiency industrial ozone generator. He joined the department of Electronic and Electrical Engineering of University of Strathclyde as a lecturer in 2010. His research interests include non-thermal gas discharges and their applications in gas synthesis, water disinfection and advanced oxidation process in water.

Scott J. MacGregor (M'95-SM'14) received the B.Sc. and Ph.D. degrees from the University of Strathclyde, Glasgow, U.K., in 1982 and 1986, respectively. He became a Pulsed Power Research Fellow in 1986 and a Lecturer in pulsed-power technology in 1989. In 1994, he became a Senior Lecturer, with a promotion to Reader and Professor of High Voltage Engineering, in 1999 and 2001, respectively. In 2006 and 2010 he became Head of the Department of Electronic and Electrical Engineering and Executive Dean of the Faculty of Engineering, and has been the Vice-Principal of the University of Strathclyde since 2014. Professor MacGregor was the recipient of the 2013 IEEE Peter Haas Award, and he was appointed as an Associated Editor of the IEEE Transitions on Dielectrics and Electrical Insulation in 2015. His research interests include high-voltage pulse generation, high-frequency diagnostics, high-power repetitive switching, high-speed switching, electronic methods for food pasteurization and sterilization, generation of high-power ultrasound (HPU), plasma channel drilling, pulsed-plasma cleaning of pipes, and stimulation of oil wells with HPU.

Nelly Bonifaci graduated from University Joseph Fourier with a MEng degree in Physics in 1989. In 2008 she obtained the HDR Habilitation qualification from the University of J Fourier, Grenoble. Dr Bonifaci joined the Laboratory on Dielectric Materials and Electrostatics (now G2E laboratory) CNRS, France in 1989 where she became a 1st class researcher in 1997. In 2007 she was promoted to a position of a Senior Researcher/Team Leader. Dr Bonifaci research interests include breakdown in insulating liquids, plasma streamers in liquid dielectrics, pre-breakdown and plasma phenomena in dielectric liquids including corona discharges and electronic transport. Dr Bonifaci is an Editor of the IEEE Transactions of Dielectric and Electrical Insulation and a member of International Organising Committee of the IEEE Conference on Dielectric Liquids.

Appendix 2 Published journal paper on free spark discharges

Y. Sun, I. V. Timoshkin, M. J. Given, M. P. Wilson, T. Wang, S. J. MacGregor and N. Bonifaci, "Impulsive discharges in water: acoustic and hydrodynamic parameters," *IEEE T. Plasma Sci.*, vol. 44, no. 10, pp. 2156-2166, Jul. 2016.

Electrical and Acoustic Parameters of Wire-Guided Discharges in Water: Experimental Determination and Phenomenological Scaling

Y. Sun, I. V. Timoshkin, *Senior Member*, *IEEE,* S. J. MacGregor, *Senior Member, IEEE*, M. P. Wilson, *Member, IEEE,* M. J. Given, *Senior Member, IEEE*, T. Wang, N. Bonifaci

***Abstract*—The present paper is focused on investigation of the electrical, hydrodynamic and acoustic parameters of underwater plasma discharges, stabilized with thin copper wires. The experimental current and acoustic waveforms have been obtained using different combinations of the circuit capacitance, charging voltage and wire length. The resistances of plasma discharges have been calculated for all combinations of electrical and topological parameters, based on the constant resistance approach. Phenomenological scaling relationships that link the plasma resistance and the total energy delivered to the plasma, the period of discharge cavity oscillation and the peak magnitude of the acoustic impulse have been obtained. These relationships can be used in optimization of the acoustic output from the wire-guided discharges for different practical applications.**

***Index Terms*—Wire-guided underwater discharges, acoustic impulses, plasma resistance.**

I. Introduction

UNDERWATER spark discharges generate strong acoustic and pressure impulses that can be used in different practical applications, for example in mineral engineering [1], rock drilling operations [2], material recycling [3, 4], and for environmental applications such as removal of pollutants in water [5]. The breakdown field in water depends on the duration of the high voltage (HV) impulses applied to the electrode system. For shorter HV impulses, with duration of a few tens of nanoseconds, the breakdown field could be as high as ~1.5 MV/cm; with an increase in the impulse duration, the breakdown field reduces to ~0.1 MV/cm for HV impulses of microsecond duration [6]. Thus, for initiation of free spark discharges in water in centimeter-long gaps, significantly high applied voltages are required, which may lead to practical problems such as increased cost of dielectric insulation, increased overall size of the driving pulsed power systems and potential flashover problems. In the case of free discharges in water, there is limited control of the discharge path, and elevated conductivity of the water (for example, tap water or sea water) results in significant pre-breakdown energy losses due to Joule heating. Thus, the acoustic efficiency of free discharges in water is limited.

In order to minimise the pre-breakdown energy losses and to increase the acoustic efficiency of underwater spark discharges through the use of longer inter-electrode gaps, while maintaining lower levels of applied voltage, underwater spark discharges may be initiated with a thin conductive wire placed between the high voltage and ground electrodes.

A typical chain of events in the wire-guided discharge can be described as follows. The pulsed power circuit is closed by the thin conductor placed between the discharge electrodes, therefore significant conduction current starts to flow through the wire after application of the high voltage impulse. This current results in heating, melting and disintegration of the wire into fine droplets of the melted metal. After wire disintegration, the circuit becomes open, thus the conduction current collapses and the voltage across the entire inter-electrode gap increases until the eventual breakdown of the gas in this channel, which is filled with the droplets of melted metal. Upon breakdown, the energy stored in the pulsed power system is delivered into the plasma channel formed between the electrodes [7]. Typically, the energy required for wire heating, melting and disintegration constitutes only a small fraction of the total energy available in the discharge [8]. Therefore, the remaining energy is delivered into the breakdown channel formed by the disintegrated wire. The vaporised metallic wire defines the path of the post-breakdown plasma channel, which enhances the consistency and stability of such underwater discharges.

Wire-guided discharges in water can be utilised for different industrial applications and for research purposes. For example, fast electrical disintegration of metallic conductors in water can be used for fabrication of nanomaterials (metallic and metal oxide nanoparticles) [9], and for generation of high residual stresses in metallic parts [10]. Underwater wire-guided discharges are used in investigation of the conductivity and equations of state of warm dense matter [11, 12]. Water has low compressibility, which results in slow radial expansion of the plasma developed in the initial stage of the underwater wire discharge, ~10^5 cm/s. This expansion velocity is almost two orders of magnitude lower than the plasma expansion velocity in the case of a wire explosion in vacuum [11]. Therefore, due to the high current magnitude and high plasma density

This manuscript has been submitted for publication on 7 February 2017, in its final form on XX XXX 2017. I. Timoshkin is grateful for hospitality and support from G2E Laboratory, CNRS, France, which allowed for his research visits to G2E Laboratory in Grenoble in 2017.

Y. Sun, I. Timoshkin, M. Given, M. Wilson, S. MacGregor are with University of Strathclyde, Department of EEE, Glasgow, UK, G1 1XW, (e-mail: ying.sun@strath.ac.uk; igor.timoshkin@strath.ac.uk; m.given@strath.ac.uk; mark.p.wilson@strath.ac.uk, scott.macgregor@strath.ac.uk).

N. Bonifaci is with the G2E Laboratory, CNRS, Grenoble, France. (e-mail: nelly.bonifaci@g2elab.grenoble-inp.fr)

developed in an underwater plasma channel, the equation of state of the warm dense matter formed in the breakdown channel, and the electrical conductivity of this matter, can be obtained and investigated [12].

Although wire-guided underwater discharges have been intensively studied for several decades, there is a lack of understanding of the relationships between their electrical, hydrodynamic and acoustic parameters. Thus, it is important to investigate the functional behavior of the electrical, hydrodynamic and acoustic parameters of the wire-guided discharges, in order to optimise and to tailor their acoustic output for practical applications. As in the case of free breakdown in water, underwater wire-guided discharges generate strong pressure impulses. The primary pressure impulse is produced at a very early stage of expansion of the plasma generated by the breakdown in the channel filled with gas and metallic droplets formed by the heated and disintegrated wire. Intensive Joule heating of the plasma in this channel results in fast expansion of the plasma/gas-filled cavity, which continues until its kinetic energy is completely converted into potential energy accumulated in the surrounding water. At this stage, the external hydrodynamic pressure is significantly higher than the pressure inside the cavity, which leads to its collapse and the radiation of a secondary pressure impulse. This dynamic process is similar to the expansion-collapse process of a cavity formed by a free discharge in water. The functional behavior of the period of cavity oscillation, the acoustic magnitude of the pressure impulses generated, and the resistance of the underwater plasma generated by free spark discharges in water have been investigated in a number of papers, including [13, 14].

Also from the late 1960s, different scaling relationships for spark discharges in water have been proposed, however there is still a lack of a general phenomenological model(s) that would help researchers and engineers who are working in this area to predict and to optimize the hydrodynamic parameters of transient underwater cavities and the acoustic impulses generated by these cavities. In [15], for example a scaling relation between the peak acoustic magnitude and the product of the voltage and peak current in free discharges in water was obtained graphically. However, no investigation of the potential influence of different inter-electrode lengths on the peak acoustic magnitude was carried out. In [16], several models, including a model based on the energy balance equation for the plasma discharge in water, were discussed. Some of the approaches proposed in [16] have been tested and confirmed to be valid for free discharges in water which take place in relatively short (tens of millimeters) inter-electrode gaps. However, no model is given in [16] that could provide scaling relationships between the electrical, hydrodynamic and acoustic parameters for longer discharges initiated with thin conductive wires. It is important to address this issue and to development of phenomenological scaling relationships for such discharges which will link their electrical and acoustic parameters and will enable their optimisation and tailoring.

The present paper is focused on an experimental investigation of such parameters for underwater wire-guided discharges with different wire/gap lengths as the charging voltage and capacitance of the pulsed power supply was varied. The behavior of the following parameters has been analysed: the resistance of the plasma channel; the period of cavity oscillation; and the acoustic pulse magnitude (peak pressure). This has allowed phenomenological scaling relationships between the resistance of the plasma channel, the energy available in the discharge, the period of the cavity oscillation and the peak acoustic magnitude to be established. The obtained functional dependencies can be used for development and optimization of plasma-acoustic sources for specific practical applications.

II. Experimental Set-up

The experimental system consists of a pulsed driving circuit connected to electrodes submerged in water, and diagnostic devices for monitoring the electrical and acoustic parameters. This system is similar to the pulsed power system developed and used in [14] for studying free discharges in water. Several combinations of different HV capacitors (Maxwell Laboratories Ltd, USA) were used to achieve total (measured) energy-storage capacitances of 155 nF, 267 nF and 533 nF in the single-stage pulsed power system. The capacitance was charged to voltages of 25 kV, 30 kV and 35 kV by a DC power supply (Glassman High Voltage, series EH).

The conductive wire used to generate spark discharges was copper (99.9% Cu), with a diameter of 0.05 mm (Goodfellow Ltd). For each discharge, a length of copper wire was clamped by two stainless-steel crocodile clips, which were solidly mounted vertically opposite to each other on two stainless-steel rods, within a wire sample holder. The upper crocodile clip was connected to the output of the HV pulsed power system while the bottom crocodile clip was grounded. The electrode holder was placed in the middle of a large water tank with dimensions of 2 m (length) × 1 m (depth) × 1 m (width). The wire lengths (gap distances between the crocodile clips) were chosen as 15 mm, 45 mm and 75 mm.

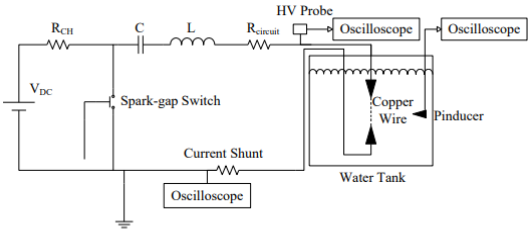

Fig.1. Schematic diagram of the experimental setup: V_{DC}, DC power supply; R_{CH}, charging resistor; C, capacitor bank; L, circuit inductance; $R_{circuit}$, circuit resistance.

The diagnostic devices used in the present study are also as described in [14]. A high voltage probe (NorthStar PVM-5, 1000:1 division ratio, 80 MHz bandwidth) and a resistive current shunt probe (Samtech Ltd DE(CP)-01, 29.6 mΩ) were used to capture the transient voltage and current waveforms, and the corresponding output signals were recorded by a Tektronix 2024 digitising oscilloscope with 2 GSample/s sampling rate and 200 MHz bandwidth. The acoustic signals were registered by a piezoelectric acoustic sensor, Valpey

Fisher Pinducer VP1093, and the output voltage signal from the Pinducer was transferred to a Tektronix 3054B digitising oscilloscope with 5 GSample/s sampling rate and 500 MHz bandwidth. The acoustic sensor was located 500 mm away from the wire-guided discharge source. A schematic diagram of the experimental setup is given in Fig. 1.

III. Electrical and Acoustic Waveforms

As described in Section II, the wire-guided spark discharges were initiated by a thin copper wire located between the HV and ground electrodes. Each combination of charging voltage (25 kV, 30 kV and 35 kV) and capacitance (155 nF, 266 nF and 533 nF) was used to generate discharges in tap water, stabilized by Cu wires with three different lengths: 15 mm; 45 mm and 75 mm. The transient voltage and current waveforms and corresponding acoustic output were recorded for each wire-guided discharge. Figure 2 shows an example of the discharge current waveform obtained with a 45 mm-long wire.

The initial sharp current spike in Fig. 2 indicates the process of copper wire melting and disintegration. Upon applying the high voltage impulse to the wire, the current through the wire placed between the electrodes rises over a few tens of nanoseconds (initial current spike, dotted line in Fig.2). Due to the injected electrical energy, the wire is heated, melted and disintegrated. The resistance between the electrodes increases and the current drops.

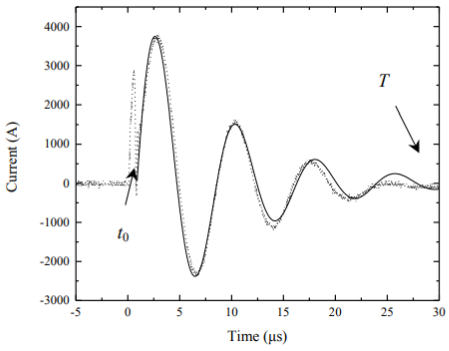

Fig.2. Current waveforms for wire-guided underwater spark discharge with the following parameters: 45 mm-long wire, 266 nF energy-storage capacitance, 17.5 kV peak impulse voltage. The dotted line is the experimental current waveform $I(t)$; the solid line is the analytical fitting by (1). Analytical fitting starts at time t_0 - the moment of the breakdown in the channel formed by the disintegrated wire. T indicates the end of the energy deposition phase.

Due to the high resistance now present across the gap, the inter-electrode voltage increases, causing breakdowns of a gaseous nature between the droplets of melted copper in the channel formed by the disintegrated wire, reclosing the inter-electrode gap. The current oscillations in the pulsed discharge circuit can now be described by under-damped oscillations in a *R-L-C* circuit (starting from time t_0 in Fig.2). By simplifying the discharge circuit to a lumped *R-L-C* circuit, and assuming that the resistance of the breakdown plasma channel is constant, the current oscillations after wire disintegration and the final breakdown of the channel formed by the disintegrated wire can be fitted with the function:

$$I(t) = I_0 \exp\left(-\frac{R_{total}}{2L}t\right)\sin\left(t\sqrt{\frac{1}{LC}-\left(\frac{R_{total}}{2L}\right)^2}\right) \qquad (1)$$

where I_0 is a fitting constant related to the maximum peak current in the transient process, and R_{total} is the total resistance of the experimental circuit, including the assumed constant resistance of the plasma channel, R_{pl}.

In Fig.2, the oscillations shown by the solid line indicates the current waveform obtained using (1), from the moment of the secondary breakdown in the channel, t_0, until the end of the energy deposition stage, T. The dotted line shows the obtained experimental current waveform. The match between the experimental waveform and the current waveform plotted using (1) provides validation of the use of the constant resistance approach in the analysis of the underwater discharges.

Using (1), the circuit inductance, L, and the total resistance, R_{total}, were obtained. The constant resistance of the plasma channel, R_{pl}, can be calculated by subtracting the derived circuit resistance, $R_{circuit}$, obtained from current waveforms, using (1), when the electrode gap was short circuited (no contribution from the spark discharge channel), from the total resistance, R_{total}, of the circuit with the spark discharge channel, also obtained using (1):

$$R_{pl} = R_{total} - R_{circuit} \qquad (2)$$

The acoustic waveforms emitted by the wire-guided discharges were monitored and recorded. The primary acoustic pressure impulse emitted by the expanding plasma cavity was registered by the Tektronix digitizing oscilloscope using a time base of 200 ns/division, while the acoustic signals generated by the first complete expansion-collapse cycle of the cavity were captured using a longer time base of 1 ms/division.

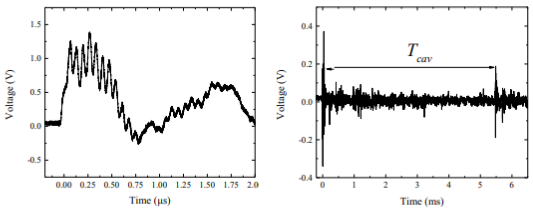

Fig.3. Acoustic signals generated by the underwater wire-guided discharge. (a), primary signal due to cavity expansion; (b) primary and secondary signals generated by expanding and collapsing cavity (15 mm length wire, 20.8 kV impulse voltage, 155 nF energy-storage capacitance). T_{cav} is the time interval between the primary pressure impulse due to cavity formation and the secondary pressure impulse due to cavity collapse (the period of cavity oscillation).

Fig.3 shows a typical example of the acoustic output registered from a 15-mm-long wire-guided discharge, with the

acoustic waveforms of the primary acoustic impulse generated by the formation of the cavity (Fig. 3(a), short timescale) and the primary and secondary acoustic impulses radiated by the formation and collapse of the cavity (Fig. 3(b), longer timescale). The magnitude of the primary acoustic impulses, P_{ac}, is measured as the direct output signal from the acoustic sensor in Volts, following the procedure established in [14]. In Fig. 3(b), the period of the cavity oscillation, T_{cav}, is read as the time interval between the formation and collapse of the cavity. These two parameters, P_{ac} and T_{cav}, are used in further investigation of the performance of the wire-guided discharges.

IV. Electrical, Hydrodynamic and Acoustic Parameters of Wire-Guided Discharges

The resistance of the plasma in the breakdown channel is a key factor defining the acoustic and hydrodynamic performance of the plasma channel. The relationship between the plasma resistance, R_{pl}, and the circuit resistance, $R_{circuit}$, determines the energy partition in the circuit and, thereby, the amount of electrical energy transformed into acoustic energy. In general, the plasma resistance of a channel is related to the length of the channel. The path of the wire-guided plasma channel is defined (stabilized) by the wire, and therefore follows the shortest distance between the electrodes. Thus, because of this gap stabilization, the plasma resistance is consistent for breakdown events under the same energisation conditions, and with the same gap length. Therefore, the correlation between the plasma resistance and other discharge parameters, such as energy available in the discharge, can be established and used in the analysis of the hydrodynamic and acoustic properties of wire-guided spark discharges. In this experimental study, it was found that the plasma resistance across all combinations of wire length, voltage and capacitance varied from 0.56 Ω to 2.29 Ω.

A. Electrical parameters

In the case of spark breakdown in fluids, the transient resistance of the breakdown channel demonstrates a highly dynamic behavior, and typically decreases during a few tens/hundreds of nanoseconds from its initial, relatively high, value, to a minimum value of a few tens/hundreds of milliohms [17, 18]. There are several models that describe this dynamic resistance of the spark breakdown channel as a function of time. For example, based upon the plasma energy balance equation in the breakdown channel, it has been shown that the transient resistance of the breakdown channel in a gas, $R(t)$, is inversely proportional to the integral of $I(t)^2$, and directly proportional to the length of the breakdown channel, ℓ:

$$R(t) = k \frac{\ell}{\left(\int_{t_0}^{t} I(t)^2 dt \right)^n} \qquad (3)$$

where n is a constant. According to the energy balance model developed by Rompe and Weizel (and discussed in [18]), n in (3) is equal to ½ and coefficient k (noted as k_{RW} for the Rompe – Weizel's model) is a function of different parameters of the plasma breakdown channel including electronic temperature, electronic mobility, and ionization potential. k_{RW} is typically considered as a constant for a specific range of the experimental parameters, [18]. In Vlastos's energy balance model, n = 3/5 [19] and coefficient k (noted as k_W in this model) is considered as a model constant which also depends on the plasma parameters and the initial radius of the plasma channel, [19]. The detailed analysis of coefficients k_{RW} and k_W is beyond the scope of this work, further details related to these coefficients and their numerical values for transient spark discharges in gas including discharges initiated with thin conductive conductors can be found in [18, 19, 20]. Popovic *et al*. generalised this approach in [21], by assuming that n is a phenomenological constant that can be obtained using the best fit between the calculated and experimental values of the breakdown channel resistances. It was shown in [21, 22] that using (3) with n = 1/2 and n = 3/5 provides reasonable agreement with the experimentally-obtained transient spark resistance in air. Moreover, it was found in [20] that (3) with n = 1/2 can be used for description of the transient resistance of the breakdown channel in liquids: Fuhr and Schmidt used (3) in their analysis of the transient breakdown resistance in liquid hydrocarbons. In the present paper, (3) is used to provide a link between the electrical and hydrodynamic parameters of the underwater wire-guided discharges. The phenomenological coefficient, n, was obtained for all combinations of the circuit capacitance, charging voltage and wire length, using the fitting procedure described later in this section.

After fast post-breakdown reduction, the plasma resistance remains almost constant until the end of the energy deposition process, which can last for a few tens of microseconds [18, 20]. Thus, in the case of the transient processes of such duration or longer, it is possible to substitute the transient resistance with an effective (constant) spark plasma resistance. For example, a constant plasma resistance was used to describe the transient current oscillations observed for short, sub-micrometer and millimeter air gaps [23], and for long, hundreds of centimeters, air gaps [24]. As shown in [20], the calculated resistance at the end of the transient process obtained using (3) is very close to the experimentally-obtained resistance of the breakdown channel. Therefore, it can be postulated that the efficient (constant) plasma resistance, R_{pl}, is proportional to the transient resistance, $R(T)$, at the end of current oscillation obtained using (3) at $t \rightarrow T$.

In the present work, it is assumed that the transient resistance of the breakdown channel at the end of the energy deposition phase is proportional to the constant resistance value of the plasma channel obtained by the fitting procedure based on (1):

$$R(T) \propto R_{pl} \qquad (4)$$

To provide a link between the acoustic and hydrodynamic parameters of the underwater wire-guided discharges, and the total energy deposited into the plasma channel, $W(T)$, the total energy has been calculated by integrating the current waveforms, using the values of R_{pl} obtained from (1) and (2):

$$W(T) = R_{pl}\int_{t_o}^{T} I(t)^2\,dt \qquad (5)$$

where the integration is conducted from t_0, the moment of the breakdown in the gas/liquid metal droplets channel formed by the disintegrated wire, until the end of the energy deposition phase, T, Fig.2. The total energy deposited into the plasma channel, $W(T)$, has been obtained for all combinations of the charging voltage, capacitance and wire length. The validity of the constant resistance approach to calculation of the energy deposited into the underwater breakdown channel has been discussed and justified in [13].

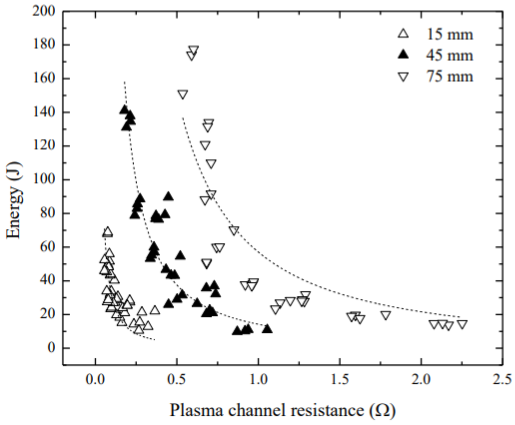

Fig.4. Plasma energy as a function of constant plasma resistance for all three capacitances and three gap distances. Dashed lines, analytical fitting using (6), $n = 0.41 \pm 0.03$.

Thus, one can obtain the link between the energy deposited into the plasma channel, $W(T)$, and the resistance of the plasma channel, R_{pl}, by combining (3), (4) and (5):

$$W(T) = a\left(\frac{\ell}{R_{pl}^{1-n}}\right)^{\frac{1}{n}} \qquad (6)$$

The total energy, $W(T)$, obtained using the experimental current waveforms was fitted with analytical current functions given by (6). Coefficient a in (6) is a phenomenological constant. The calculated values of $W(T)$ and the corresponding fitting lines are shown in Fig. 4 as functions of the plasma resistance, R_{pl}, for all wire lengths of wires and for all tested combinations of charging voltage and capacitance. The dashed lines in Fig. 4 represent analytical fittings of (6), obtained using Origin 8 graphing software with $n = 0.41 \pm 0.03$, and $a = (14.33 \pm 0.12) \times 10^{-3}$. Thus, this analytical fitting procedure demonstrates that the phenomenological relationships (4) and (6) can be used for satisfactory scaling of underwater wire-guided discharges.

B. Hydrodynamic parameters

The phenomenological scaling relationship between the period of cavity oscillation, T_{cav}, and the energy available in the discharge, W, has been tested in [14] for free discharges in water, and found to be valid for different combinations of electrical (breakdown voltage, energy-storage capacitance) and topological (inter-electrode distance) parameters:

$$T_{cav} \propto W^{\frac{1}{3}} \qquad (7)$$

Coefficient proportionality between T_{cav} and W in (7) is a model coefficient which is a function of hydrodynamic and energy parameters including a portion of the total electrical energy released in the breakdown plasma channel which is converted into thermal energy in the plasma, hydrostatic pressure and specific weight of liquid (water), [14].

Assuming the same functional dependency between the period of oscillations and the delivered energy, $W(T)$, for wire-guided discharges in water, the combination of (6) and (7) allows for establishment of the relationship between the period of cavity oscillations and the plasma resistance:

$$T_{cav} = b\left(\frac{\ell}{R_{pl}^{1-n}}\right)^{\frac{1}{3n}} \qquad (8)$$

where b is a phenomenological coefficient which is a function of the proportionality coefficients in (6) and (7).

The period of cavity oscillations, T_{cav}, has been obtained for all combinations of ℓ, C and charging voltage.

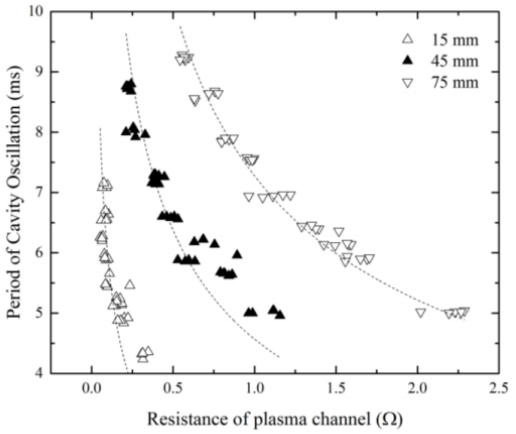

Fig.5. Period of cavity oscillation as a function of the plasma resistance for all three capacitances: 155 nF, 266 nF and 533 nF; and all three wire lengths: 15 mm, 45 mm, and 75 mm. Dashed lines represent analytical fitting lines according to (8), with $n = 0.41 \pm 0.04$.

Fig.5 presents the obtained period of cavity oscillation, T_{cav}, as a function of the plasma resistance, R_{pl}. It was found that the

period of cavity oscillation decreases as the plasma resistance increases for each specific length of wire, and the period of cavity oscillation is longer for either higher capacitance or longer wire length (longer inter-electrode gap). The dashed lines in Fig.5 represent the analytical fitting lines obtained using (8). The mean values of coefficients n and b in (8) that provides the best fit to all experimental data for all three wire lengths are $n = 0.41 \pm 0.04$ and $b = 0.22 \pm 0.01$. Thus, the close agreement in the value of n obtained for the fit of (6) to the data for energy deposition, and for the fit of (8) to the data for the oscillation period of the cavity, confirms the validity of the approach used to describe the electrical and hydrodynamic parameters of wire-guided discharges in water.

C. Acoustic parameters

The peak acoustic magnitude of the pressure impulses generated by the wire-guided discharges as a function of the plasma resistance was obtained for all combinations of capacitance, wire length and charging voltage. Fig. 6 shows the peak acoustic magnitude as a function of the plasma channel resistance - it was found that, for each specific wire length, the peak acoustic magnitude decreased with an increase in R_{pl}.

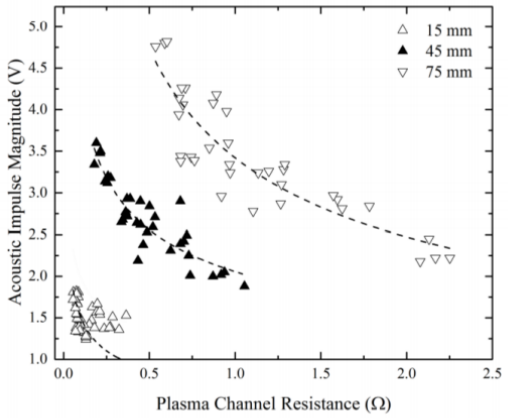

Fig.6. Acoustic emission magnitudes as a function of the plasma resistance for all three capacitances: 155 nF, 266 nF and 533 nF; and all three wire lengths. Dashed lines represent analytical fitting lines according to (9).

Fig.6 shows that, for the same plasma resistance, the peak magnitude of the acoustic signal generated with longer wires is larger than the acoustic magnitude generated by the discharges stabilized with shorter wires. However, for each wire length, the peak acoustic magnitude, P_{ac}, generated using all three tested capacitances and charging voltages, demonstrates similar functional dependency on the plasma resistance, R_{pl}, and the length of wire, ℓ: the peak acoustic magnitude is proportional to the length of wire, and inversely proportional to the plasma resistance to the power m:

$$P_{ac} = c_1 \frac{\ell}{R_{pl}^m} \qquad (9)$$

where c_1 and m are phenomenological constants that can be obtained by fitting (9) to the experimental data shown in Fig.6. Again using Origin Pro 8, the value of coefficients m and c_1 that provided the fit for all three wire lengths were $m = 0.37 \pm 0.07$ and $c_1 = (4.43 \pm 0.15) \times 10^{-2}$.

Thus, it is shown that in the case of stabilization of the discharge channel with a thin wire, the acoustic magnitude generated by the discharges is proportional to the length of the wire. This is in agreement with [25], where an analytical equation for the total acoustic energy in the pressure impulse generated by an underwater discharge was shown to be directly proportional to the integral of the squared pressure signal and the length of the wire, ℓ. Using (6) and (9), the link between the peak acoustic magnitude, P_{ac}, and the total energy deposited into the plasma channel, $W(T)$, can be derived:

$$P_{ac} = c_2 \left(\ell^{(1-n-m)} W(T)^{nm} \right)^{\frac{1}{1-n}} \qquad (10)$$

where coefficient c_2 is a function of coefficients c_1 and a, $c_2 = c_1 a^{nm/(n-1)}$. Inserting the obtained numerical values for the coefficients, $n = 0.41$, and $m = 0.37$, (10) can be represented as:

$$P_{ac} = c_2 \ell^{0.37} W(T)^{0.26} \qquad (11)$$

Equation (11) follows the form of the empirical relationship between the peak acoustic magnitude produced by a spark discharge in water and the corresponding energy available in the spark discharge used in [26], where it was shown that $P_{ac} \propto W^{\beta/3}$, with $\beta = 1.13$. It can be seen that the power coefficient, $\beta/3$, used in [26] is close to the power coefficient, 0.26, obtained in the present work.

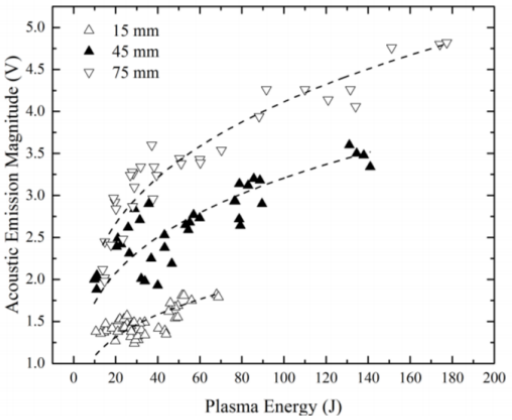

Fig.7. Acoustic emission magnitudes as a function of the energy available in discharges for all three capacitances: 155 nF, 266 nF and 533 nF; and for all three wire lengths: 15 mm, 45 mm, and 75 mm. Dashed lines represent analytical fitting lines according to (11).

Fig.7 shows experimental values of the peak acoustic magnitude plotted against the total energy available in the

wire-guided discharge for all three wire lengths, all capacitances and all charging voltages. The dashed lines represent the fitting obtained by (11), c_2 was a variable parameter, $c_2 = 0.22 \pm 0.02$, which confirms the value of $c_2 = 0.238$ obtained using combination of (6) and (9). The good fit between the experimental data and the behavior predicted by (11) confirms that the phenomenological scaling relationships proposed in the present work can satisfactorily describe the functional dependency of the acoustic magnitude on the energy delivered to the discharge and the plasma resistance. These relationships provide a mechanism for the optimization of practical acoustic wire-guided discharge sources.

V. Conclusions

The main objectives of the present paper include experimental determination of the electrical and acoustic parameters of the underwater wire-guided discharges, and the development of phenomenological scaling relationships for these discharges. A detailed experimental investigation of the behavior of wire-guided underwater discharges has been made over a range of wire/gap lengths, charging voltages and energy-storage capacitances. The electrical parameters: plasma resistance (assumed constant) and the energy delivered into the plasma channel, together with the period of cavity oscillation, a hydrodynamic parameter, and the magnitude of the acoustic impulses have been either measured or derived. The relationships between the total energy delivered into the plasma channel, the period of cavity oscillation, the acoustic magnitude and the plasma resistance have been investigated and fitted with phenomenological equations, based on the dependency of the plasma resistance on the integral of the current delivered to the plasma channel.

The present paper also is focused into the development of scaling relationships for wire-guided underwater discharges. It was shown that, based on basic relationships between the plasma resistance and its relationship with the current flowing in the discharge channel, it is possible to derive phenomenological scaling equations for wire-guided underwater discharges. These phenomenological equations have been shown to describe satisfactorily the main electrical, hydrodynamic and acoustic parameters of wire-guided discharges. The relationships include the wire/gap length as a parameter, together with the total energy delivered into the discharge, and the plasma resistance. Thus, the sensitivity of the discharge parameters to the length of wire has been captured in the proposed equations. The established scaling relationships have a different character than the corresponding relationships for free discharges in water [14]: the role of the inter-electrode gap in the free discharges is different, and it was shown that the main hydrodynamic and acoustic parameters of these discharges can be described by relationships which include the circuit parameters only as free variables. However, as has been shown in the present work, for longer inter-electrode gaps stabilized with conductive wires, the inter-electrode gap (the wire length) plays an independent role and must be included in the scaling relationships as a free parameter.

The obtained experimental results and the phenomenological scaling relationships will help in further optimization and development of practical applications of underwater wire-guided discharges.

References

[1] T. Parker, F. Shi, C. Evans, M. Powell, "The effects of electrical comminution on the mineral liberation and surface chemistry of a porphyry copper ore", *Minerals Engineering*, vol. 82, no.15 2015, pp. 101–106.

[2] I. Timoshkin, J. Mackersie, S. MacGregor, "Plasma channel miniature hole drilling technology", *IEEE Transactions on Plasma Science*, vol.32, no.5, pp. 2055-2061.

[3] H. Bluhm, W. Fre , H. Giese, P. Hoppe, C. Schultheis , R. Strassner, "Application of pulsed HV discharges to material fragmentation and recycling", *IEEE Trans. Dielectr. Electr. Insul*. vol.7, no.5, pp. 625–636, 2000.

[4] M. Wilson, L. Balmer, M. Given, S. MacGregor, I. Timoshkin, "An investigation of spark discharge parameters for material processing with high power ultrasound", *Minerals Engineering*, vol.20, n.12, pp. 1159-1169

[5] T. Dang, A. Denat, O. Lesaint, G. Teissedre, "Pulsed electrical discharges in water for removal of organic pollutants: a comparative study", *The European Physical Journal - Applied Physics*, vol.47, no.2 2009, 22818

[6] M. Hogg, I. Timoshkin, M. Given, M. Wilson, S. MacGregor, T. Wang, R. Fouracre, J. Lehr, "Impulse breakdown of water with different conductivities," *IEEE Transactions on Dielectrics and Electrical Insulation*, vol. 19, no. 5, pp. 1559-1568, 2012.

[7] "Exploding Wires", vol.2, Ed. by W. Chase and H. Moore, Plenum Press, NY, 1962

[8] L. Nelson, S. Hogelandb, T. Roth, "Aluminum-Enhanced Underwater Electrical Discharges For Steam Explosion Triggering", Sandia National Laboratories, Report SAND99-0796, 1999, https://www.osti.gov/scitech/servlets/purl/12653

[9] C. Peng, J. Wang, N. Zhou, G. Sun, "Fabrication of nano-powders by electrical explosion of a copper wire in water", *Current Appl. Phys*., vol. 16, pp.284-287, 2016

[10] I. Timoshkin, S. MacGregor, Rolls-Royce PLC (Patent applicant), "Apparatus and method for electric spark peening of gas turbine components", Patent No. 20100008786, 2010.

[11] Y. Krasik, S. Efimov, D. Sheftman, *et al*, "Underwater electrical explosion of wires and wire arrays and generation of converging shock waves", *IEEE Transactions on Plasma Science*, vol.44, no.4, pp. 412-431, 2016

[12] T. Sasaki , Y. Yano, M. Nakajima , T. Kawamura, "Warm-dense-matter studies using pulse-powered wire discharges in water", *Laser and Particles Beams*, vol. 24, no. 3, 2006, pp. 371-380

[13] I. Timoshkin, R. Fouracre, M. Given, S. MacGregor, "Hydrodynamic parameters of the transient underwater cavities" *J. Phys. D: Appl. Phys*. vol.39, n.22, pp.4808, 2006.

[14] Y. Sun, I. Timoshkin, M. Given, M. Wilson, T. Wang, S. MacGregor, N. Bonifaci, "Impulsive Discharges in Water: Acoustic and Hydrodynamic Parameters", *IEEE Transactions on Plasma Science*, vol. 44, no. 10, pp. 2156-2166, 2016.

[15] W. Guman, B. Humphrey Jr., "Studies on an electric discharge underwater sound source", Report No. FHR-2229-7, Fairchild Hiller Corp Farmingdale NY Republic Aviation Div, 1968, http://www.dtic.mil/cgi-bin/GetTRDoc?AD=AD0681862

[16] K. Naugol'nykh and N. Roi, "Spark discharges in water (A hydrodynamical description)", (Translation, Foreign Technology Division), Wright-Patterson AFB, Dayton, OH, USA, Tech. Rep., 1974.

[17] T. G. Engel, A. L. Donaldson, and M. Kristiansen, "The Pulsed Discharge Arc Resistance and its Functional Behavior," *IEEE Transactions on Plasma Science*, vol. 17, no. 2, pp. 323–329, 1989

[18] R. Montano, M. Becerra, V. Cooray, M. Rahman, P. Liyanage, "Resistance of Spark Channels," *IEEE Transactions on Plasma Science*, vol. 34, no. 5, pp. 1610–1619, 2006

[19] A. Vlastos, "The Resistance of Sparks," *J. Appl. Phys.*, vol. 43, no. 4, pp. 1987–1989, 1972

[20] P. Castera, P.-Q. Elias, "Resistance models applied to the return stroke phase of negative pulsed surface discharge in air", *IEEE Transactions on Plasma Science*, vol. 42, no. pp. 1922-1931, 2014

[21] M. M. Popovic, S. S. Popovic, M. M. Platisa, "Investigation of the beginning of high current discharges in pulsed arcs," in Proc. Of Third Int. Conf. on Gas Discharges, The Institution of Electrical Engineers (IEE), Publication no.118, London, 1974, pp. 32–36.
[22] J. Fuhr, W. Schmidt, "Spark breakdown of liquid hydrocarbons. II. Temporal development of the electric spark resistance in n-pentane, n-hexane, 2,2 dimethylbutane, and n-decane", *J. Appl. Phys.*, vol. 59, no. 11, pp. 3702-3708, 1986
[23] W. D. Greason, "Methodology to study the resistance of spark discharges", *IEEE Trans. Ind. Appl.*, vol. 35, no. 2, pp. 359-365, 1999
[24] F. Théberge, J.-F. Daigle, J.-C. Kieffer, F. Vidal, M. Châteauneuf, "Laser-guided energetic discharges over large air gaps by electric-field enhanced plasma filaments", *Sci. Rep.* vol.7, 40063; doi: 10.1038/srep40063, 2017
[25] A. Grinenko, V. Gurovich, Ya. Krasik, A. Sayapin, S. Efimov, J. Felsteiner, "Analysis of shock wave measurements in water by a piezoelectric pressure probe", *Review Of Scientific Instruments*, vol.75, no.1, 2004, pp.240-244.
[26] J. McGrath, "Scaling Underwater Exploding Wires", NRL Report 6266, Energy Conversion Branch, Electronic Division, US Naval Research Laboratory, Washington, 1965

Ying Sun was born in Shandong, China. He received the B.Eng degree in electronic and electrical engineering in 2012 and M.Sc degree in electrical power engineering with business in 2013 from University of Strathclyde, Scotland, United Kingdom. He is currently pursuing the Ph.D degree in high voltage technology at University of Strathclyde, Scotland, UK.

Igor V. Timoshkin (M'07-SM'14) received a degree in physics from the Moscow State University (Russia) in 1992, and the Diploma and the Ph.D. degree from the Imperial College of Science, Technology and Medicine, (London, UK) in 2001. After graduation from MSU he worked as a Researcher at Moscow State Agro-Engineering University, and then at the Institute for High Temperatures of Russian Academy of Sciences before moving to ICSTM in 1997. He joined the Department of Electronic and Electrical Engineering of the University of Strathclyde (Glasgow, UK) in 2001 where he became a Reader in 2016. His research interests include transient spark discharges in gases and liquids, environmental applications of non-thermal plasma discharges, plasma air-cleaning and bio-decontamination technologies.

Scott J. MacGregor (M'95-SM'14) received the B.Sc. and Ph.D. degrees from the University of Strathclyde, Glasgow, U.K., in 1982 and 1986, respectively. He became a Pulsed Power Research Fellow in 1986 and a Lecturer in pulsed-power technology in 1989. In 1994, he became a Senior Lecturer, with a promotion to Reader and Professor of High Voltage Engineering, in 1999 and 2001, respectively. In 2006 and 2010 he became Head of the Department of Electronic and Electrical Engineering and Executive Dean of the Faculty of Engineering, and has been the Vice-Principal of the University of Strathclyde since 2014. Professor MacGregor was the recipient of the 2013 IEEE Peter Haas Award, and he was appointed as an Associated Editor of the IEEE Transitions on Dielectrics and Electrical Insulation in 2015. His research interests include high-voltage pulse generation, high-frequency diagnostics, high-power repetitive switching, high-speed switching, electronic methods for food pasteurization and sterilization, generation of high-power ultrasound (HPU), plasma channel drilling, pulsed-plasma cleaning of pipes, and stimulation of oil wells with HPU.

Mark P. Wilson (M'10) was born in Stranraer, Scotland, in 1982. He received the B.Eng. (with honours), M.Phil., and Ph.D. degrees in electronic and electrical engineering from the University of Strathclyde, Glasgow, U.K., in 2004, 2007, and 2011, respectively. He is presently based in the High Voltage Technologies research group at the University of Strathclyde, where his research interests include interfacial surface flashover, nanodielectrics, and the practical applications of high power ultrasound, corona discharges, and pulsed electric fields. Mark is a member of the IEEE Nuclear and Plasma Sciences Society, from whom he received a Graduate Scholarship Award in 2011, the IEEE Dielectrics and Electrical Insulation Society, and the IET.

Martin J. Given (M'99-SM'11) is currently a Senior Lecturer in the Department of Electronic and Electrical Engineering at the University of Strathclyde. He received a degree in physics from the University of Sussex in 1981 and a PhD in electronic and electrical engineering from the University of Strathclyde in 1996. His research interests include, ageing processes and condition monitoring in solid and liquid insulation systems, high speed switching and pulse power.

Tao Wang received the B.Eng and M.Sc degrees from Northeast China Dianli University (China) in 1993 and 1996 respectively, and the Ph.D. degree from the University of Strathclyde (Glasgow, UK) in 2005. He then joined the Newland Entech as a research fellow developing high efficiency industrial ozone generator. He joined the department of Electronic and Electrical Engineering of University of Strathclyde as a lecturer in 2010. His research interests include non-thermal gas discharges and their applications in gas synthesis, water disinfection and advanced oxidation process in water.

Nelly Bonifaci graduated from University Joseph Fourier with a MEng degree in Physics in 1989. In 2008 she obtained the HDR Habilitation qualification from the University of J Fourier, Grenoble. Dr Bonifaci joined the Laboratory on Dielectric Materials and Electrostatics

(now G2E laboratory) CNRS, France in 1989 where she became a 1st class researcher in 1997. In 2007 she was promoted to a position of a Senior Researcher/Team Leader. Dr Bonifaci research interests include breakdown in insulating liquids, plasma streamers in liquid dielectrics, pre-breakdown and plasma phenomena in dielectric liquids including corona discharges and electronic transport. Dr Bonifaci is an Editor of the IEEE Transactions of Dielectric and Electrical Insulation and a member of International Organising Committee of the IEEE Conference on Dielectric Liquids.

Appendix 3 Accepted journal paper on air-bubble-stimulated discharges

Y. Sun, I. V. Timoshkin, M. J. Given, M. P. Wilson, T. Wang, S. J. MacGregor and N. Bonifaci, "Acoustic impulses generated by air-bubble stimulated underwater spark discharges", *IEEE T. Dielect. El. In.*, accepted for publication, 2018.

Acoustic Impulses Generated by Air-Bubble Stimulated Underwater Spark Discharges

Y. Sun, I. V. Timoshkin, M. J. Given, M. P. Wilson, T. Wang and **S. J. MacGregor**
Department of Electronic and Electrical Engineering
University of Strathclyde
Glasgow, United Kingdom

N. Bonifaci
CNRS, G2E Laboratory
Grenoble, France

ABSTRACT

Considerable research efforts have been expended in investigating and optimising the emission of acoustic pressure impulses by high power spark discharges in water. Several methods are typically used to generate transient underwater spark discharges, including breakdown of water by stressing electrode(s) with HV impulses, initiation of spark discharges with thin metallic wires placed between opposite electrodes and by injecting gas bubbles into the inter-electrode gap. This paper is aimed at the investigation of the acoustic, hydrodynamic and electrical characteristics of underwater spark discharges initiated by injected air-bubbles. At a constant applied voltage, the injection of air bubbles allows the inter-electrode gap to be increased thus producing stronger acoustic impulses. This paper reports on the impact of injected air bubbles on the characteristics of transient underwater plasma discharges and on the functional relationships between hydrodynamic and electrical parameters of such discharges, including breakdown voltage, plasma resistance, energy delivered into the plasma cavity and the period of gas/plasma cavity oscillation. An analytical model which relates the acoustic efficiency, plasma resistance and energy available in discharge has been developed which can be used for the optimisation and tailoring of underwater plasma-acoustic sources.

Index Terms — **Underwater spark discharges, acoustic emission, hydrodynamics.**

1 INTRODUCTION

AN underwater spark discharge (UWSD) formed between high voltage and ground electrodes generates an acoustic pressure impulse, which quickly becomes an acoustic wave that propagates away from the breakdown channel. The high degree of control, straightforward optimisation and tailoring of the emitted acoustic pressure impulses make plasma-acoustic sources and UWSD's an attractive solution for different technological applications. For example, pressure impulses generated by the UWSD's are used in material recycling and mineral processing [1], in water treatment operations, [2, 3], and in ultra-wideband sonar technology, [4].

Recently, a number of comprehensive studies characterising UWSD's and their associated pressure impulses have been conducted, [5-10]. It was found that the peak magnitude of the acoustic impulses strongly depends on the inter-electrode gap, i.e. an increase in the inter-electrode distance results in generation of stronger acoustic pressure impulses, [5, 7, 8, 9].

Manuscript received on 22 December 2017, in final form 31 May 2018, accepted 3 June 2018. Corresponding author: Y. Sun.

However, when using water with an elevated electrical conductivity (as compared with that of distilled water), for example in the case of UWSD's in tap water or sea water, the ionic conduction may cause a significant pre-breakdown drop in the voltage across the electrodes. In the case of free, un-triggered discharges in water with conductivity of 66 μS/cm the maximum inter-electrode distance, which was possible to break with 35 kV impulses, was 15 mm, [6]. It was not possible to achieve repeatable spark discharges in water with such conductivity with further increases in the inter-electrode gap. An increase in the applied voltage may help to achieve spark discharges in longer gaps, however in many technological applications it may not be practical from the point of view of insulation coordination.

The initial, pre-breakdown, stage of the development of a spark discharge in a liquid includes multiple complex processes, such as charge injection and field modification. A comprehensive study of the charge injection process in water and water/glycol solutions was conducted in [11-13], where it was shown that the injected charge modifies the electric field in the liquid near the electrodes, and can result in higher breakdown voltage and faster pre-breakdown voltage decay. Detailed analysis of such processes is beyond the scope of the

present paper, since it is focused on the post-breakdown characteristics of underwater spark discharges.

As reported in [8, 10], the use of a thin conductive wire placed between the electrodes allows the distance between the electrodes to be increased. However, this approach requires replacement of the initiating wire after each shot, thus such systems typically operate in a single shot/low frequency pulse regime. To increase the operating frequency and to minimise pre-breakdown ionic losses, gas bubbles can be injected into the inter-electrode gap. The injected gas bubbles help to reduce both the time to breakdown and the breakdown voltage, due to the lower breakdown strength of gases (as compared to that of the water), and the field enhancement within the bubbles (due to the permittivity mismatch between the water and the gas).

In [14], different gases (Ar, CO_2, CH_4, and C_3H_8) were used to form bubbles in distilled water to stimulate spark discharges and to keep the breakdown voltage at a relatively low level. In [15] nitrogen bubbles were injected between parallel-plane electrodes to facilitate the development of spark discharges. In [16], the influence of the dimension of the injected gas bubbles on the breakdown initiation process was studied. In [17, 18] the role of gas bubbles in the breakdown initiation process in water has been analysed. Thus, the injection of gas bubbles may provide a practical solution for triggering spark underwater spark discharges in longer gaps in water with elevated electrical conductivity.

In the present paper, air bubbles were injected into the inter-electrode gap to facilitate development of the transient (spark) plasma channels. This study is aimed at a comprehensive investigation of the hydrodynamic, acoustic and electrical parameters of air-bubble-stimulated UWSD's, including the acoustic magnitude, the period of cavity oscillation, the breakdown voltage, the plasma resistance and the energy delivered into the plasma.

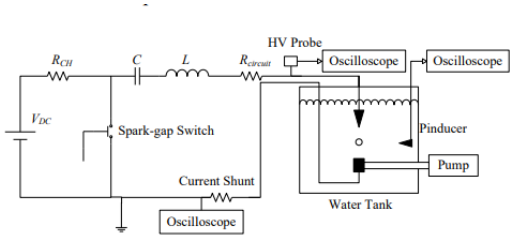

Figure 1. Schematic diagram of the pulse power system and the electrodes topology with an external pump: V_{DC}, DC generator; R_{CH}, charging resistance; C, energy storage capacitance; $R_{circuit}$, circuit resistance; L, circuit inductance.

An analytical model has been developed based on Gilmore's bubble oscillation model [5, 6], to obtain the time-dependent radius of the vapour/gas cavity formed by the spark discharge and the peak magnitude of the acoustic impulse generated by this transient cavity. The acoustic efficiency of UWSD's has been obtained as a function of their electrical parameters (the constant plasma resistance and the energy delivered into the plasma). The obtained functional dependencies of the hydrodynamic and electrical parameters of the UWSD's can be used for optimisation of the plasma-acoustic systems and tailoring their acoustic emission parameters for specific practical applications.

2 EXPERIMENTAL SET-UP

The experimental setup used in this work included an impulsive voltage generation system, a pair of electrodes with controllable separation and an external air pumping system. The air pump was used to inject a continuous flow of air bubbles into the inter-electrode gap. A schematic diagram of the setup is shown in Figure 1. The impulsive voltage generation system used in these tests was the same as the pulsed power system described in [7, 8]. It consists of a Glassman high voltage DC power supply (series EH), used to charge different combinations of HV capacitors from Maxwell Laboratories Ltd, USA. The pulsed power system is triggered by a manually controlled spark-gap switch.

The stainless steel electrodes were orientated vertically in the center of a large water tank filled with tap water, with dimensions of 2 m (length) × 1 m (width) × 1 m (height). The high voltage electrode was in a shape of cone with a 5 mm base radius and a tip radius of ~ 0.8 mm in order to enhance the electrical field in its vicinity. The lower, ground electrode was cylindrical in shape with a diameter of 15 mm, and had an embedded air flow channel. The air bubbles were injected into the inter-electrode gap through a 1 mm aperture of the gas channel formed in the lower, ground electrode, and the topology of this electrode is shown in Figure 2. Air was injected into the gas channel by an aquarium pump; the air flow in the system being controlled by gas regulators. The pump was kept on during the whole period of testing to generate a consistent flow of air-bubbles between the electrodes from shot to shot. The injected air bubbles will move vertically up, towards the upper conical electrode.

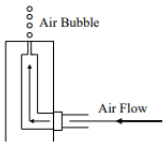

Figure 2. Ground electrode modified with air flow channel.

The transient voltage and current waveforms were obtained using a PVM-5 high voltage probe (North Star Ltd USA, with the following nominal parameters: 1000:1 division ratio, 80 MHz bandwidth, 400 MΩ input resistance, and 12 pF input capacitance, [19]) and a current shunt with the resistance of 29.6 mΩ, (Samtech Ltd, Scotland). These waveforms were recorded using a Tektronix 2054B digitising oscilloscope (500 MHz bandwidth, 2 GS/s sampling rate). The acoustic signals were obtained by using a piezo-electric acoustic sensor, Pinducer VP1093 (Valpey Fisher Ltd USA) and were recorded by a Tektronix 5034B digitising oscilloscope (350 MHz bandwidth, 5 GS/s sampling rate). Two different time bases were used to optimise the resolution of the acoustic signals emitted by the expanding and collapsing gas cavities. The magnitude of the acoustic impulse was captured with a 200 ns/division time-base, while two consecutive acoustic signals produced by the expanding and collapsing cavities were

obtained with a 2 ms/division time-scale in order to register the period of cavity oscillation.

3 RESULTS

A comprehensive investigation of the acoustic and hydrodynamic characteristics of the air-bubble-stimulated UWSD's was conducted. The relationships established between the acoustic, hydrodynamic and electrical parameters are presented and discussed in this section. The acoustic and hydrodynamic parameters include the peak acoustic magnitude, $P_{ac\text{-}max}$ and the period of the cavity's primary oscillation, T_{cav}. The electrical parameters are the breakdown voltage, V_{br}, the discharged current, I, the plasma resistance, R_{pl}, and the energy delivered into plasma, E_{pl}.

Different combinations of capacitance and charging voltages were used in the present work. Three values of energy-storage capacitance in the pulsed power circuit, C, were used: 155, 266 and 533 nF. The charging voltage levels, V_{ch}, were 25 kV, 30 kV and 35 kV. These levels of C and V_{ch} were chosen to provide a nominal stored energy, $0.5CV_{ch}^2$, in the range from ~ 48 J to ~ 326 J, while keeping charging voltages below 40 kV. Similar energies and charging voltage levels were used in several of the practical applications discussed in [1, 6, 20]. The charging voltages, capacitances and energies used in the present work are also close to those used in previous studies focused on free and wire-guided discharges in water, [5 - 8]. Thus, the results obtained in the present paper, for air-bubble stimulated underwater spark discharges, can be compared with previously-published data on the acoustic, hydrodynamic and electrical parameters of free and wire-guided underwater spark discharges.

Three inter-electrode distances, ℓ, (15 mm, 20 mm and 25 mm) were chosen for this study to allow comparison of the results obtained for the air-bubble-stimulated discharges with the results for free underwater spark discharges obtained for shorter gaps, ℓ<15 mm, in [7]. However, when using the 155 nF capacitance the success rate of spark breakdown events in long, 20 mm and 25 mm, gaps in tap water with conductivity of 66 µS/cm was low, less than 5%. Therefore, the acoustic and hydrodynamic data for C = 155 nF were obtained only for ℓ = 15 mm.

3.1 ELECTRICAL AND ACOUSTIC WAVEFORMS

By applying a HV impulse to a pair of electrodes in the water tank, breakdown can be initiated by injection of air bubbles into the inter-electrode gap resulting in formation of a low resistance plasma channel between the electrodes. Examples of typical post-breakdown voltage and current waveforms obtained for the air-bubble-stimulated discharges are shown in Figure 3. In Figure 3(a), the breakdown voltage, V_{br}, is read as -33.8 kV at the moment when the voltage starts to drop due to the formation of the plasma channel. At the same time, a conductive current appears in the circuit and under-damped current and voltage oscillations are observed in both waveforms.

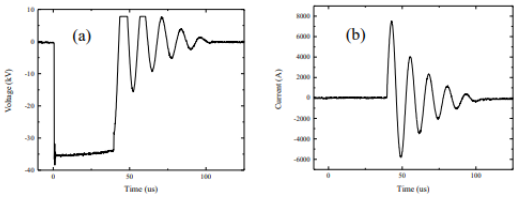

Figure 3. The example electrical waveforms: (a) voltage; (b) current, obtained from a discharge achieved in a 25 mm gap with 533 nF capacitance.

The profiles of the waveforms in Figure 3 are similar to those obtained in [7] for free spark discharges in water. In [7, 8], the general solution for the post-breakdown *R-L-C* circuit has been successfully verified to describe the dynamic oscillations of the circuit current:

$$I(t) = I_0 e^{-\alpha t} \sin(\omega t) \qquad (1)$$

where I_0 is a constant related to the peak current, α is the attenuation coefficient and ω is the angular frequency of the oscillations.

This approach assumes a constant plasma resistance. It is known that the resistance of the underwater spark channel significantly reduces during the first quarter-cycle of the oscillating current from a few Ωs to a few mΩs, [5]. The spark resistance remains in this range until the end of the first half-cycle of the oscillating discharge current. An equivalent constant value of resistance obtained from the oscillating current wave form can be used to represent the energy delivered to the spark channel. In [5] the validity of the constant plasma resistance approximation in the hydrodynamic modelling of underwater spark discharges was confirmed, and this approach was adopted in the present study.

The total resistance of the circuit, R_{total}, which includes the plasma channel resistance can be obtained by fitting the experimental current wave forms with equation (1). R_{total} includes all resistive elements in the pulsed power circuits and the resistance of the plasma channel, R_{pl}. Therefore, R_{pl}, is calculated as the difference between R_{total} and the resistance of the pulsed power driving circuit, $R_{circuit}$:

$$R_{pl} = R_{total} - R_{circuit} \qquad (2)$$

Based on the behavior of the circuit, at equivalent current levels, when the gap is short-circuited, ($R_{pl} = 0$), $R_{circuit}$, can be obtained. One the plasma resistance is known, the electrical energy delivered into the plasma channel, E_{pl}, can then be calculated:

$$E_{pl} = R_{pl} \int I(t)^2 dt \qquad (3)$$

Typical acoustic signals generated by an air-bubble-stimulated UWSD's are shown in Figure 4. Figure 4(a) shows the profile of the primary acoustic impulse, $P_{ac}(t)$. The value of the first peak in acoustic signal is used to represent the magnitude of the primary (first) acoustic impulse emitted by the spark discharge cavity, $P_{ac\text{-}max}$.

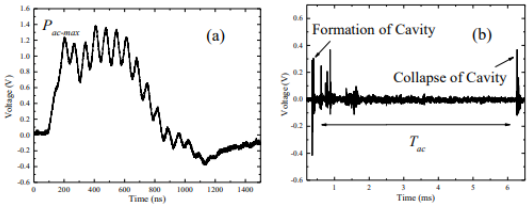

Figure 4. Acoustic signals generated by discharges in 20 and 25 mm gaps: (a) the profile of the acoustic magnitude, registered with a 200 ns/division time-base; (b) the primary and secondary acoustic impulses emitted at the formation and collapse of the cavity. $P_{ac\text{-}max}$ is the first peak of the impulse and T_{cav} indicates the time duration of the primary oscillation of the cavity.

Figure 4b shows two major (primary and secondary) acoustic impulses captured at the moments of formation and collapse of the spark discharge cavity, yielding the period of the cavity's oscillation, T_{cav}, as the time interval between these two impulses. Due to the unavailability of calibration for the acoustic sensor from the manufacturer, the sensor output in Volts was used to represent the magnitude and wave-shape of the acoustic signals. In the ideal case with no energy loss, the Rayleigh solution describes the dynamic oscillation of the cavity. This solution describes well both, the expansion and collapse stages of the cavity forming a complete cavity cycle, and it links the period of such an cavity oscillation cycle, T_{cav}, with the maximal radius of the cavity, r_{max}, [21-23]. The electrical energy transferred into the plasma is not only converted into acoustic energy and the internal energy of the plasma in the channel, but also into the energy of light emission and other potential energy losses due to the non-ideal spherical topology of the bubble, heat transfer across the plasma/gas-liquid interface, and other loss mechanisms. It was estimated that these energy losses only accounted for less than ~10 % of the total energy delivered into plasma, [5].

3.2 THE ROLE OF BREAKDOWN VOLTAGE

The period of cavity oscillation, T_{cav}, and the peak magnitude of the acoustic signal, $P_{ac\text{-}max}$, were obtained for all three inter-electrode distances under different energisation conditions. These data are shown in Figure 5 as functions of V_{br} with each point representing a single breakdown event stimulated by air bubbles.

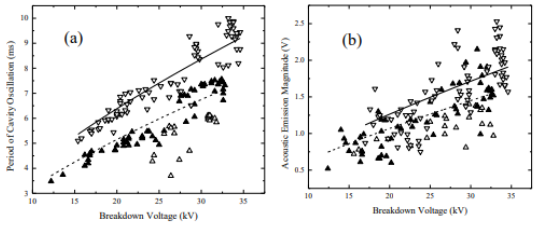

Figure 5. Relationships between: T_{cav} and V_{br}, (a); $P_{ac\text{-}max}$ and V_{br}, (b). Open upper triangle represents data for C=155 nF; closed upper triangle represents data for C=266 nF; open inverted triangle represents data for C=533 nF. Solid and dashed lines in (a) indicate the fitting of equation (4) and those in (b) indicate the fitting of equation (5).

It can be seen from Figure 5(a) that the period of cavity oscillation increases with breakdown voltage for all inter-electrode distances and the discharges achieved with higher values of C typically produce longer T_{cav} at the same breakdown voltage. Either large values of V_{br} or high C in Figure 5a correspond to a larger amount of energy available in the discharge which results in longer T_{cav}. In [7], a similar dependency of T_{cav} on V_{br} and C was observed for free UWSD's and a phenomenological equation was provided to describe this relation:

$$T_{cav} = aC^{1/3}{V_{br}}^{2/3} \qquad (4)$$

where a is a phenomenological fitting coefficient, T_{cav} is in ms, C is in μF and V_{br} is in kV.

Table 1. Coefficient a for Equation (4)

C	266 nF	533 nF
a	0.109 ± 0.002	0.107± 0.002

Equation (4) was fitted to the experimental T_{cav} values obtained for the air-bubble-triggered discharges (generated with 266 nF and 533 nF capacitances) by using OriginLab 9.0 graphing software. No fitting for the C = 155 nF case is provided as only a single inter-electrode distance, ℓ = 15 mm, was used for this value of C.

This fitting procedure provided the fitting coefficient, a, for the different values of C as given in Table 1; the analytical fitting curves are shown in Figure 5a. As indicated by the solid line (C = 533 nF) and the dashed line (C = 266 nF) in Figure 5a, equation (4) demonstrates a good agreement with the experimental data. The quality of the fitting obtained by equation (4) has been observed, for free discharges in [6] and for air-bubble stimulated discharges in the present work. Thus, it confirms that the post-breakdown functional behavior of T_{cav} is not affected by the discharge initiation mechanism. It is also worthy of note that the values of the proportionality coefficient, a, for both 266 and 533 nF cases are close to each other, indicating that the functional behavior of T_{cav} is not sensitive to ℓ for free and air-bubble-stimulated discharges.

Figure 5b shows the peak magnitude of the acoustic impulse as a function of the breakdown voltage. Similar to the relationship established for T_{cav} and V_{br}, $P_{ac\text{-}max}$ increases with an increase in V_{br} for all tested capacitances and inter-electrode distances; the discharges with larger C's also generate higher $P_{ac\text{-}max}$. As compared with Figure 5a, the data in Figure 5b show a higher degree of dispersion; thus discrimination between $P_{ac\text{-}max}$ for different values of C's is not as well defined as that for T_{cav}. This is due to the higher sensitivity of $P_{ac\text{-}max}$ to the choice of ℓ, which was observed in [8, 10, 24]. In [24], a phenomenological relation has been established which relates the intensity of the shock wave with the plasma channel length, ℓ: $P_m = 0.58\ell^{0.75}$. However, considering the limited range of the values of ℓ used in the present work, the relationship originally developed in [7] for free discharges was also used to describe $P_{ac\text{-}max}$ (V_{br}) in the case of air-bubble-stimulated discharges:

$$P_{ac-max} = bC^{\theta/3}{V_{br}}^{2\theta/3} \qquad (5)$$

where b is a fitting coefficient, $\theta = 1.13$, $P_{ac\text{-}max}$ is in V, C is in μF, and V_{br} is in kV.

By fitting Equation (5) to the experimental data shown in Figure 5(b) (excluding the 155 nF case), it was found that $b = (1.36 \pm 0.06) \times 10^{-2}$ for the 266 nF case and $b = (0.04 \pm 0.06) \times 10^{-2}$ for the 533 nF case. The results of this fitting procedure are shown as the solid and dashed lines, in Figure 5(b). The fitting curves in Figure 5(b) show a reasonable agreement with the experimental data, confirming that equation (5) can be used to describe the relation between $P_{ac\text{-}max}$ and V_{br} for air-bubble-stimulated discharges. This relationship can be used to predict the magnitude of the acoustic impulses generated for specific pulsed power circuit parameters.

3.3 THE ROLE OF ENERGY

The energy released in the plasma channel during the post-breakdown period is an important factor which can be used in the development and optimisation of the plasma-acoustic sources. By using Equations (1)–(2) together with the experimental current waveforms, the energy delivered into the plasma channel, E_{pl}, has been obtained for all combinations of the capacitances and inter-electrode distances.

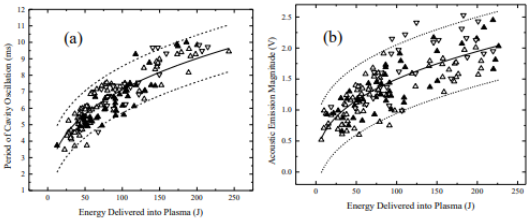

Figure 6. Relationships between: T_{cav} and V_{br}, (a); $P_{ac\text{-}max}$ and E_{pl}, (b). Open upper triangles represent data for ℓ =15 mm; closed triangles represent data for ℓ =20 mm; open inverted triangles represent data for ℓ = 25 mm. Solid line indicates the fitting of equation (6); dashed lines represent the 95% prediction intervals.

Figure 6 shows T_{cav} and $P_{ac\text{-}max}$ as functions of the energy delivered into the plasma, E_{pl}, for three values of C. It can be seen that both, T_{cav} and $P_{ac\text{-}max}$ increase with an increase in E_{pl}. In [7], the phenomenological relations for the dependency of T_{cav} and $P_{ac\text{-}max}$ on E_{pl} have been established for the free UWSD's. These phenomenological relationships can be applied to establish the functional behavior of T_{cav} and $P_{ac\text{-}max}$ for air-bubble-stimulated discharges:

$$T_{cav} = kE_{pl}{}^{1/3}, \quad P_{ac-max} = mE_{pl}{}^{\theta/3} \qquad (6)$$

where k and m are phenomenological fitting coefficients, T_{cav} is in μs, $P_{ac\text{-}max}$ is in V, and E_{pl} is in J.

The solid lines in Figure 6 show the fitting results obtained using Equations (6) and the dashed lines show the 95 % prediction intervals. It can be seen that both equations (6) provide a good agreement with the experimental data with most of T_{cav} and $P_{ac\text{-}max}$ data are located within the 95 % prediction range. These results confirm that the scaling relations (6) can be used in the case of air-bubble-stimulated discharges.

The proportionality coefficient, k, was obtained by the fitting procedure and found to be $k = 1.50 \pm 0.02$ for data shown in Figure 6a. This value is close to k = (1.6-1.7) obtained for free discharges in [7]. The proportionality coefficient, m, in equation (6) for $P_{ac\text{-}max}$ was found to be $m = 0.26 \pm 0.01$. The importance of equations (6) is not only in providing the effective prediction of the acoustic and hydrodynamic characteristics of UWSD's but also in helping to achieve specific properties of the acoustic emission by adjusting and optimising appropriate parameters of the pulsed power circuit.

In the present work, only the energy released into the post-breakdown plasma channel was considered; this energy defines the hydrodynamic and acoustic parameters of the spark breakdown gas/plasma cavities studied in this paper. The role of the energy in the pre-breakdown processes in insulating liquids is discussed in [25 - 27]. It was shown that the energy stored electrostatically in the electrode gap, or in an additional capacitor connected in parallel with the electrodes, may affect the gap breakdown voltage; in [27], it was postulated that this locally-stored energy permits "weaker initiating events to grow to a breakdown point". However, the capacitance of the electrode system used in the present work is in the range from ~14 pF (for a 15 mm gap) to ~30 pF (for a 25 mm gap), and the nominal capacitance of the HV probe connected in parallel with the water gap is 12 pF. These values are significantly lower than the energy-storage capacitances, 155, 266 and 533 nF. Therefore, in the experimental arrangements used herein, the energy stored electrostatically in the water gap is negligible compared to the energy stored in the capacitor(s) of the pulse-driving circuit. Thus, it can be assumed that the energy stored in the water gap does not significantly affect either the breakdown or post-breakdown characteristics of the underwater spark discharges studied in the present work.

3.4 ACOUSTIC EFFICIENCY

The acoustic energy, E_{ac}, indicates the amount of energy related to the pressure impulse generated by the formation of the gas-plasma cavity after breakdown. In this work, E_{ac} refers to the acoustic energy associated with the primary acoustic impulse (the first acoustic impulse emitted by the discharge cavity). The acoustic wave at a distance, d, which is significantly longer that the inter-electrode gap, $d >> \ell$, can be considered as a spherical wave and E_{ac} can be calculated as:

$$E_{ac} = 4\pi Z_{ac}{}^{-1} d^2 \int P_{ac}(t)^2 dt \qquad (7)$$

where $P_{ac}(t)$ is the time-dependent waveform of the acoustic pressure impulse at the specific observation point, d; Z_{ac} is the acoustic impedance of water (defined as $Z_{ac} = \rho_0 c_0$ where ρ_0 is the density of water, and c_0 is the local speed of sound in water). The energy losses during the acoustic impulse's propagation are neglected in this analysis, thus E_{ac} obtained at d represents the initial acoustic energy transferred from the energy delivered into the plasma, E_{pl} into the acoustic impulse.

If the acoustic energy is known, it is possible to obtain the acoustic efficiency for the air-bubble-stimulated underwater discharges. This is an important parameter which can be used in performance evaluation of the plasma-acoustic systems. The

acoustic efficiency, η_{ac}, can be defined as a ratio of the acoustic energy in the pressure impulse to the total energy delivered into the plasma channel:

$$\eta_{ac} = E_{ac}/E_{pl} \times 100\% \quad (8)$$

The energy delivered into the plasma, E_{pl}, can be obtained by equation (3). However, the exact calibration of the pressure sensor, Pinducer VP1093, used in the diagnostic system is not provided by the manufacturer. Therefore, an alternative way to obtain the pressure waveform $P_{ac}(t)$ was developed: an analytical model which linked the acoustic waveform $P_{ac}(t)$, to the hydrodynamic (the radius of the cavity, $r(t)$,) and the electrical parameters of the circuit. This model was used in order to calculate the profile of the acoustic impulse.

3.4.1 ENERGY BALANCE EQUATION

The developed analytical model is based on the energy balance equation which links the electrical energy, released in the plasma channel with the mechanical work done by the gas-plasma channel and the internal energy of the plasma:

$$P_i \frac{d(V_C)}{dt} + P_\infty \frac{dV_C}{dt} + \frac{1}{\gamma - 1}\frac{d(P_i V_C)}{dt} = P_{elt} \quad (9)$$

where P_i is the pressure inside the plasma channel, V_{ac} is the volume of the cavity, P_{elt} is the electrical power, $P_{elt} = R_{pl} \times I(t)^2$, and γ is the constant ratio of specific heats and the value of $\gamma = 1.3$ is chosen according to [6].

The first two terms in equation (9) represent the mechanical work done by the expanding cavity against the water and the potential energy stored in the surrounding water respectively. The third term is the thermal (internal) energy of the gas/plasma in the cavity, which is considered to behave like an ideal gas.

3.4.2 CAVITY DYNAMICS AND ACOUSTIC IMPULSE

Gilmore's cavity oscillation model based on the Kirkwood Bethe hypothesis [28, 29] was used to describe the dynamic behavior of the cavity. During the initial energy deposition stage of the spark discharge, the gas/water interface of the formed cavity experiences an intense acceleration, potentially resulting in compression of the water in the vicinity of the plasma channel. Thus, a modified version of Tait's equation of the state for water, [30], and the pressure-dependent speed of sound in water, c, were used in the developed model:

$$\frac{P_i + B}{P_\infty + B} = \left(\frac{\rho}{\rho_\infty}\right)^n, \; c = (c_\infty{}^2 + (n-1)H)^{\frac{1}{2}} \quad (10)$$

where P_i is the internal pressure of the formed cavity, P_∞ is the constant hydrostatic pressure, $B = 0.3$ GPa and $n = 7$ for water; ρ and ρ_0 are the density of the water with and without an external pressure disturbance respectively; c_∞ is the local speed of undisturbed water and H is the enthalpy of the water at the gas/water interface [22]:

$$H = \frac{n}{n-1}\frac{(\rho_\infty + B)^{\frac{1}{n}}}{\rho_\infty}\left[(P_i + B)^{\frac{n-1}{n}} - (\rho_\infty + B)^{\frac{n-1}{n}}\right] \quad (11)$$

Based on the hypotheses (10) and (11), Gilmore's model for the cavity's oscillation in a compressible liquid is given as:

$$\left(1 - \frac{\dot{r}}{c}\right) r\ddot{r} + \frac{3}{2}\left(1 - \frac{\dot{r}}{3c}\right)\dot{r}^2 = \left(1 + \frac{\dot{r}}{c}\right) H + \left(1 - \frac{\dot{r}}{c}\right)\frac{r}{c}\dot{H} \quad (12)$$

where $\dot{r}$ and $\ddot{r}$ are the first and second time derivatives of the cavity's radius, $r(t)$, respectively. Equation (12) describes the expansion and collapse of the discharge cavity.

The primary acoustic impulse, $P_{ac}(t)$, emitted by the expanding plasma channel is described by the following equation in the acoustic approximation:

$$P_{ac}(t) = P_\infty + \rho_\infty \left(\frac{1}{d}(r^2\ddot{r} + 2r\dot{r}^2) - \frac{r^4}{2d^4}\dot{r}^2\right)^2 \quad (13)$$

where $d = 0.5$ m in this study.

3.4.4 SIMULATION REUSLTS

Equations (9)-(13) were used in [5, 6], to model free underwater discharges, and it was confirmed that this approach satisfactorily describes the evolution of the cavity's radius. In this paper, equation (9)-(13) were solved in the Simulink (MatLab R2016a) environment for air-bubble-stimulated discharges. Four initial parameters were used in the model, I_0, R_{pl}, α and ω these parameters were obtained from the experimental current waveforms for each individual discharge. These initial conditions together with the other constants used in this model are listed in Table 2.

It was found that the model was not very sensitive to the choice of the initial parameters; the maximum change in the acoustic output was only ~4% for a ~900% change in the initial values of the cavity radius and its velocity. The cavity dynamics and the acoustic parameters are defined by the energy input rather than by the initial values (initial cavity radius and velocity).

Table 2. Initial Conditions for the Model

Parameter	Value
$r(0)$	0.0001 m
$\dot{r}(0)$	0.001 m/s^2
d	0.5 m
P_∞	10^5 Pa
ρ_∞	10^3 kg/m^3
c_∞	1483 m/s

By knowing $P_{ac}(t)$, the acoustic energy, E_{ac}, was obtained by the model and the acoustic efficiency, η_{ac}, was calculated by using Equation (9) for all tests conducted in this paper. The relationship between η_{ac} and R_{pl}, and between η_{ac} and E_{pl} are given in Figure 7.

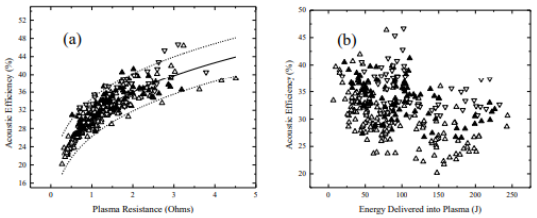

Figure 7. The acoustic efficiency as a function of (a) the plasma resistance; and (b) the energy delivered in plasma for all inter-electrode distances. Open upper triangles represent data for ℓ=15 mm; closed triangle represent data for ℓ =20 mm; open inverted triangles represent data for ℓ =25 mm. Solid line indicates the fitting of equation (14), dashed lines demonstrate the 95% prediction bands.

Figure 7a shows the functional behavior of the acoustic efficiency η_{ac} with the plasma resistance for all inter-electrode distances. It can be seen that η_{ac} is in the range from 20 % to 47 %, which is close to the values of the acoustic efficiency obtained in [31] for the free UWSD's, 23-30 %. η_{ac} increases with an increase in R_{pl} for all tested ℓ's, however, η_{ac} demonstrate variable sensitivity to the different inter-electrode gaps. The air-bubble-stimulated discharges with longer ℓ have higher plasma resistances, R_{pl}, thus the highest η_{ac} was obtained for the 20 mm and 25 mm cases. However, η_{ac} for ℓ =15 mm concentrate at lower levels, Figure 7b For the same value of R_{pl} (Figure 7a), the discharges with longer ℓ, especially for the 25 mm case, always generate higher η_{ac} due to the enhanced values of $P_{ac\text{-}max}$ for longer ℓ's. Data in Figure 7(a) can be fitted with a phenomenological scaling relation:

$$\eta_{ac} = sR_{pl}{}^{x} \qquad (14)$$

where s and x are fitting coefficients, and R_{pl} is in Ohms.

The fitting of Equation (14) to the experimental data is shown as a solid line in Figure 7a; the dashed lines indicate the 95 % prediction intervals. Coefficient s was found to be 30.41 ± 0.22 and the power coefficient, x, is 0.24 ± 0.01. Equation (14) provides a satisfactory fitting as the 95 % prediction interval includes most of the data points.

Figure 7b shows the variation of the acoustic efficiency with the energy delivered into the plasma channel for all inter-electrode distances. It can be seen that η_{ac} decreases slowly with an increase in E_{pl} which is confirmed by the finding that relative changes in E_{pl} and E_{ac}, lead to a decrease in the energy ratio, E_{ac} /E_{pl}. Figure 7(b) also shows that η_{ac} is higher for longer ℓ, for the same energy delivered into the plasma.

Based on the established dependency of η_{ac} on ℓ, C, R_{pl} and E_{pl}, it can be concluded that the increase in E_{ac}, especially obtained by an increase in C and V_{br}, does not necessarily lead to an enhanced acoustic efficiency, η_{ac}. Therefore, it is not possible to achieve an increase in both, E_{ac} and η_{ac} by simply injecting more energy into the plasma.

The results shown in Figure 7 show that discharges with longer ℓ and lower C provide higher acoustic efficiency as compared with discharges with shorter ℓ and higher C (providing that these discharges produce the same acoustic peak magnitude). Thus, this study stresses the importance of the breakdown mechanism in the optimisation of acoustic parameters of the plasma-acoustic sources: air-bubble-stimulated discharges can be developed in longer inter-electrode gaps at lower energisation levels. This finding is important for different practical applications and allows for optimisation of both, acoustic magnitude and acoustic efficiency of UWSD's by selecting the appropriate combinations of the electrodes topology, energisation and circuit parameters.

4 CONCLUSION

A comprehensive investigation of the characteristics of the underwater spark discharges initiated by injecting air bubbles into the inter-electrode gap has been conducted. It was shown that in the case of air-bubble-initiated UWSD's the inter-electrode gaps could be significantly increased compared to those for free discharges. The inter-electrode gap used in this study was increased from 15 mm to 25 mm under the same electrical parameters (capacitance and charging voltage) as used in the case of free discharges in [6]. The main advantage provided by longer inter-electrode gaps, is an increase in the peak magnitude of the emitted acoustic impulses and an increase in the acoustic efficiency.

Two phenomenological scaling relations, (4) and (5), were developed to describe the link between the acoustic and hydrodynamic parameters of the air-bubble-stimulated UWSD's, $P_{ac\text{-}max}$ and T_{cav}, and V_{br}. The increase in C and V_{br} resulted in an increase in both, T_{cav} and $P_{ac\text{-}max}$ generated by these discharges. It was also shown that both, T_{cav} and $P_{ac\text{-}max}$ increase with an increase in the energy delivered into plasma, E_{pl}. These relationships are due to an inverse proportionality between R_{pl} and E_{pl}, which was established in [8]. The relationship between T_{cav} and E_{pl}, and the link between $P_{ac\text{-}max}$ and E_{pl} are provided by equations (6).

The model which describes the dynamics of post-breakdown gas/plasma cavities and the acoustic impulses generated by these cavities was developed based on the Gilmore's bubble oscillation model in a compressible liquid, and the energy balance equation. The model provides a good agreement between the experimental and calculated values for the period of the cavity oscillation, T_{cav}. The modelled acoustic impulses were used to calculate the acoustic efficiency, η_{ac} of the air-bubble-stimulated UWSD's.

The dependencies of $P_{ac\text{-}max}$, and η_{ac} on R_{pl} have been obtained and it was shown that for these experimental conditions η_{ac} increases with an increase in plasma resistance. However, it was found that η_{ac} decreases with an increase in the total energy delivered into the plasma. High values of η_{ac} were obtained for either lower E_{pl} or longer ℓ. Therefore, the optimal conditions to achieve high η_{ac} and high $P_{ac\text{-}max}$ should include the use of lower capacitance in the pulsed power circuit, C, together with a longer inter-electrode distance. These requirements are difficult to achieve in free discharges in conducting water therefore the stimulation of the development of the discharges, for example by injecting air bubbles, in order to achieve successful breakdown in longer inter-electrode gaps is required. Also, air-bubble-stimulated discharges allows for higher pulse repetition rates as compared with the wire-guided discharges, [8]. The results obtained in this study will help in

the optimisation of the plasma acoustic sources and in tailoring of the acoustic wave-forms generated by the underwater spark discharges.

5 REFERENCES

[1] M. Wilson, L. Balmer, M. Given, S. MacGregor, I. Timoshkin, "An investigation of spark discharge parameters for material processing with high power ultrasound", Min. Eng., vol. 20, pp. 1159–1169, 2007.

[2] K. Chung, S. Lee, Y. Hwang, C. Kim, "Modeling of pulsed spark discharge in water and its applications to well cleaning", Curr. Appl. Phys., vol. 15, pp. 977–986, 2015.

[3] T. H. Dang, A. Denat, O. Lesaint, G. Teissedre, "Pulsed electrical discharges in water for removal of organic pollutants: a comprehensive study", Eur. J. Appl. Phys., vol. 47, no. 22818, 2009.

[4] http://woodshole.er.usgs.gov/operations/sfmapping/sparker.htm.

[5] I. Timoshkin, R. Fouracre, M. Given, S. MacGregor, "Hydarodynamic modeling of transient cavities in fluids generated by high voltage spark discharges", J. Phys. D: Appl. Phys., vol. 39, pp. 4808-4817, 2006.

[6] J. W. Mackersie, I. V. Timoshkin and S. J. MacGregor, "Generation of high-power ultrasound by spark discharge in water", IEEE Trans. on Plasma Sci., vol. 33,no. 5, pp. 1715-1724, 2005.

[7] Y. Sun, I. Timoshkin, M. Given, M. Wilson, T. Wang, S. J. MacGregor, "Impulsive discharges in water: acoustic and hydrodynamic parameters," IEEE Trans. on Plasma Sci., vol. 44, pp. 2156–2166, 2016.

[8] Y. Sun, I. Timoshkin, M. Given, M. Wilson, T. Wang, S. J. MacGregor, "Electrical and Acoustic Paramters of Wire-Guided Discharges in Water: Experimetnal Determination and Phenomenological Scaling", IEEE Trans. on Plasma Sci., vol. 45, pp. 2648–2655, 2017.

[9] R. M. Roberts, J. A. Cook, R. L. Rogers, "The energy partition of underwater sparks", J. Acoust. Soc. Amer., vol. 99, No. 6, pp. 3465–3475, 1996.

[10] I. Timoshkin, S. MacGregor, M. Given, R. Fouracre, "High power ultrasound impulses induced by wire-guided spark discharges in water", *IEEE 16th Int. Pulsed Power Conf.*, 2007, pp. 33-36.

[11] M. Zahn, S. Voldman, T. Takada, D. Fenneman, "Charge injection and transport in high voltage water/glycol capacitors", J. Appl. Phys., vol.54, pp.315-325, 1983.

[12] M. Zahn, Y. Ohki, K. Rhoads, M. LaGasse, H. Matsuzawa, "Electro-Optic Charge Injection And Transport Measurements In Highly Purified Water And Water/Ethylene Glycol Mixtures", IEEE Electr. Insul., vol. EI-20, no.2, pp.199-211, 1985.

[13] M. Zahn, Y. Ohki, D. Fenneman, R. Gripshover, V. Gehman, "Dielectric Properties of Water and Water/Ethylene Glycol Mixtures for Use in Pulsed Power System Design", Proc. of the IEEE, vol. 74, no.9, pp.1182-1221, 1986.

[14] A. Hamdan, M. S. Cha, "The effects of gaseous bubble composition and gap distance on the characteristics of nanosecond discharges in distilled water", J. Phys. D: Appl. Phys., vol. 49, no. 24, 2016.

[15] V. Stelmashuk, "Microsecond electrical dischagre in water in plate-to-plate configuration with nitrogen bubble injection", IEEE Trans. on Plasma Sci., vol. 44, no.4, pp 702-707, 2016.

[16] N. Y. Babaeva, D. V. Tereshonok, G. V. Naidis, "Initiation of breakdown in bubbles immersed in liquids: pre-existed charges versus bubble size", J. Phys. D: Appl. Phys., vol. 48, no. 35, 2016.

[17] B. S. Sommers and J. E. Foster, "Plasma formation in underwater gas bubbles", J. Phys. D: Appl. Phys., vol. 23, no. 1, 2014.

[18] Y. Hayashi, N. Takada, H. Kanda, M. Goto, "Effect of fine bubbles on electrical discharge in water", Plasma Source Sci., vol. 24, no. 5, 2015.

[19] Voltage Probe Manual and Data North Star High Voltage, Inc. Rev January 2016, http://www.highvoltageprobes.com/high-voltage-probe

[20] I.V. Timoshkin J.W. Mackersie, S.J. MacGregor, "Plasma channel miniature hole drilling technology", IEEE Trans.Plasma Science., vol. 32, no. 5, pp. 2055-2061, 2004.

[21] S. Buogo, J. Plocek, K. Vokurka, "Efficiency of energy conversion in underwater spark discahrges and associated bubble oscillations: experimental results", ACTA , vol. 95 46-59, pp. 46-59, 2009.

[22] C. E. Brennen, *Fundamentals of Multiphase Flows*, Cambridge University Press, Pasadena California, Ch. 4, 2005.

[23] L. A. Crum, T. J. Mason, J. L. Reisse, *Sonochemistry and Sonoluminescence*, Kluwer Academic Publishers, New Haven, pp. 183-190, 1999.

[24] Y. Liu, Y. Z. Li, D. X. Li, W. S. Liu, Y. G. Zhou, C. F. Lin, "Intensity improvement of shock waves induced by liquid electrical discharges", Phys. of Plasmas, vol. 24, no. 043510, 2017.

[25] M. G. Danikas, "Breakdown of Transformer Oil", IEEE Electr. Insul. Mag., vol. 6, no. 5, pp.27-34, 1990.

[26] A. Jaksts, J. D. Cross, "High Speed Streak Photography Of The Breakdown Of Transformer Oil And The Dependence Of Its Nature On Local Stored Energy", IEEE Trans. Electr. Insul, vol. EI-18, no.6, pp.599-604, 1983.

[27] J. D. Cross, "A physical explanation of the effects of electrode area on the breakdown of liquid dielectrics", Can. Elec. Eng. J., vol 7, no 2, pp.28-30, 1982.

[28] T. G. Leighton, *The Acoustic Bubble*, Academic Press Inc., London, Ch. 4, 1994.

[29] A. Ziolkowski, "Measurement of air-gun bubble oscillation", Geophysics, vol. 63, no. 6, pp. 2009-2024, 1998.

[30] F. R. Gilmore, "The growth or collaspe of a shperical bubble in a viscous compressble liquid", Hydrodynamics Lab., Report No. 26-4, 1952.

[31] Y. Liu, Y. Z. Li, D. X. Li, Y. G. Zhou, H. Li, Q. Zhang, C. F. Lin, "Energy transfer efficiency improvement of liquid pulsed current discharge by plasma channel length reualgtion mode", IEEE Trans. Plasma Sci., vol.45, no. 12, pp. 3231 – 3239, 2017.

Ying Sun was born in Shandong, China. He received the B.Eng degree in electronic and electrical engineering in 2012 and M.Sc degree in electrical power engineering with business in 2013 from University of Strathclyde, Scotland, United Kingdom. He is currently pursuing the Ph.D degree in high voltage technology at University of Strathclyde, Scotland, UK.

Igor V. Timoshkin (M'07-SM'14) received a degree in physics from the Moscow State University (Russia) in 1992, and the Diploma and the Ph.D. degree from the Imperial College of Science, Technology and Medicine, (London, UK) in 2001. After graduation from MSU he worked as a Researcher at Moscow State Agro-Engineering University, and then at the Institute for High Temperatures of Russian Academy of Sciences before moving to ICSTM in 1997. He joined the Department of Electronic and Electrical Engineering of the University of Strathclyde (Glasgow, UK) in 2001 where he became a Reader in 2016. His research interests include transient discharges in condensed media, practical applications of electro-hydraulic and high-power ultrasound pulses, bio-dielectrics and effects of electromagnetic fields on biological objects.

Martin J. Given (M'99-SM'11) is currently a Senior Lecturer in the Department of Electronic and Electrical Engineering at the University of Strathclyde. He received a degree in physics from the University of Sussex in 1981 and a PhD in electronic and electrical engineering from the University of Strathclyde in 1996. His research interests include, ageing processes and condition monitoring in solid and liquid insulation systems, high speed switching and pulse power.

Mark P. Wilson (M'10) was born in Stranraer, Scotland, in 1982. He received the B.Eng. (with honours), M.Phil., and Ph.D. degrees in electronic and electrical engineering from the University of Strathclyde, Glasgow, U.K., in 2004, 2007, and 2011, respectively. He is presently based in the High Voltage Technologies research group at the University of Strathclyde, where his research interests include interfacial surface flashover, nanodielectrics, and the practical applications of high power ultrasound, corona discharges, and pulsed electric fields. Mark is a member of the IEEE Nuclear and Plasma Sciences Society, from whom he received a Graduate Scholarship Award in 2011, the IEEE Dielectrics and Electrical Insulation Society, and the IET.

Tao Wang received the B.Eng and M.Sc degrees from Northeast China Dianli University (China) in 1993 and 1996 respectively, and the Ph.D. degree from the University of Strathclyde (Glasgow, UK) in 2005. He then joined the Newland Entech (China) as a research fellow developing high efficiency industrial ozone generator. He joined the department of Electronic and Electrical Engineering of University of Strathclyde as a lecturer in 2010. His research interests include non-thermal gas discharges and their applications in gas synthesis, water disinfection and advanced oxidation process in water.

Scott J. MacGregor (M'95-SM'14) received the B.Sc. and Ph.D. degrees from the University of Strathclyde, Glasgow, U.K., in 1982 and 1986, respectively. He became a Pulsed Power Research Fellow in 1986 and a Lecturer in pulsed-power technology in 1989. In 1994, he became a Senior Lecturer, with a promotion to Reader and Professor of High Voltage Engineering, in 1999 and 2001, respectively. In 2006 and 2010 he became Head of the Department of Electronic and Electrical Engineering and Executive Dean of the Faculty of Engineering, and has been the Vice-Principal of the University of Strathclyde since 2014. Professor MacGregor was the recipient of the 2013 IEEE Peter Haas Award, and he was appointed as an Associated Editor of the IEEE Transitions on Dielectrics and Electrical Insulation in 2015. His research interests include high-voltage pulse generation, high-frequency diagnostics, high-power repetitive switching, high-speed switching, electronic methods for food pasteurization and sterilization, generation of high-power ultrasound (HPU), plasma channel drilling, pulsed-plasma cleaning of pipes, and stimulation of oil wells with HPU.

Nelly Bonifaci graduated from University Joseph Fourier with a MEng degree in Physics in 1989. In 2008 she obtained the HDR Habilitation qualification from the University of J Fourier, Grenoble. Dr Bonifaci joined the Laboratory on Dielectric Materials and Electrostatics (now G2E laboratory) CNRS, France in 1989 where she became a 1st class researcher in 1997. In 2007 she was promoted to a position of a Senior Researcher/Team Leader. Dr Bonifaci research interests include breakdown in insulating liquids, plasma streamers in liquid dielectrics, pre-breakdown and plasma phenomena in dielectric liquids including corona discharges and electronic transport. Dr Bonifaci is an Editor of the IEEE Transactions of Dielectric and Electrical Insulation and a member of International Organising Committee of the IEEE Conference on Dielectric Liquids.